N° d'ordre : 4567

THÈSE

Présentée à

L'UNIVERSITÉ BORDEAUX 1

École doctorale des sciences chimiques

par

INDRANI BHOWMICK

Pour obtenir le grade de

DOCTEUR

SPÉCIALITÉ : Physico-Chimie de la Matière Condensée

Synthèse et caractérisation de matériaux moléculaires magnétiques incorporant des ions métalliques 3*d* et 4*d*/5*d* connectés par des ponts cyanures

---

Soutenue le 6 Septembre 2012

En attente de l'avis de:	M. Marius Andruh	Rapporteur
	M. Marc Fourmigué	Rapporteur

Devant la commission d'examen formée de :

M. Marius Andruh	Professeur, Universitatea din Bucureşti	Rapporteur
M. Marc Fourmigué	Directeur de recherches, CNRS	Rapporteur
M. Rodolphe Clérac	Chargé de recherches, CNRS	Directeur de thèse
M. Guillaume Rogez	Chargé de recherches, CNRS	Examinateur
M. Jean-Baptiste Verlhac	Professeur, Université Bordeaux 1	Examinateur
M. Philippe Richetti	Directeur de recherches, CNRS	Examinateur

- 2012 -

To my parents....especially to my mother

I passed three years of PhD and finally achieved what I wished. But this achievement is only possible for the hearty contributions of many persons. Here I want to express my gratitude to them for their support which made my path comfortable for last three years.

Firstly, thank to ***M. Philippe Richetti*** *for welcoming me at the Centre of Research Paul Pascal as a PhD scholar and also for being Jury member of my thesis committee. I am grateful to* ***Prof. Marius Andruh*** *and* ***Dr. Marc Fourmigué*** *for dedicating their precious time to review the thesis. I would also like to thank to* ***Dr. Guillaume Rogez*** *and* ***Prof. Jean-Baptiste Verlhac*** *for participating in the thesis Jury committee and having special comments on the manuscript.*

I am most grateful to my supervisor, ***Dr. Rodolphe Clérac****. Whatever words I can say for him to express my gratitude is not enough to honour his contribution to my PhD and life as well. His guidance, unique style of motivation and intelligence always inspired me to develop a productive research work. He not only introduced me to the field of molecular magnetism, but also taught me many things about this subject. His way of teaching was very good to make a bridge between chemists and physicist; so that even I had chemistry background, I learned a lot of physical aspects of coordination complexes. Rodolphe is very patient to listen all problems and therefore to find out the best possible solution; his extreme optimistic attitude to all aspects always helped me to overcome the hurdles during these three years. From his excellent organizing capability I learned a lot about how to develop the scientific viewpoint, also helped to develop the scientific communication skill in a group. As he is very dynamic with a high energy level, it always charged up the activity of our group including me. His logical and innovative ideas helped me to learn to diversify the scientific thoughts. It is only because of him I learned to be independent in work and also to be more confident and bold. Bunches of thanks to Rodolphe; he is one of my most admirable persons.*

I must say many thanks to ***Dr. Elizabeth Hillard*** *who is in our group since January 2012 and the environment of the group just bloomed with her unique charm. She helped me a lot to develop writing skill of scientific language for the articles and this thesis. With her skills and intellects she just took a week to involve deeply to my research. Elizabeth spent a lot of her precious time to help me in organization of the research work. She takes only a second to be a friend and it was same with me. It was always nice to talk with her whatever be the topic, scientific or non-scientific. She has the magic power which always prompts me to talk with her very intimately, as if I am talking with my close friend. I was mostly attracted to her energy, enthusiasm and fast communication skill; I am inspired to be strong and always smiling. I am kind of fond of her.*

Many thanks to ***Prof. Claude Coulon****; he was the first person to make molecular magnetism understandable and interesting to me. He constructed my basement of the physical knowledge on the*

arena of molecule based magnetic materials, which was extremely helpful to interpret the properties of my compounds in PhD. I am very grateful to him for his pedagogic way of teaching. From him I have learned how to present a complicated thing in a systematic way to make it easy; and I think it is one of the most important skill one researcher should have. Without his teaching I would never be satisfied about my learning in my PhD.

I thank ***Dr. Pierre Dechambenoit*** *for his immense contribution to teach me many scientific skills from the chemistry laboratory to data analysis. He was deeply involved to my research work; he always welcomed me to have constructive scientific discussion, help to solve many problems, passionately found out new ideas and strategies helpful to my research work. From him I have learned how much perfection one should posses in every step to be a good and skilled researcher. His patients and perfections are two of most important quality that I must learn to be a good scientist. If Pierre was not there I would never succeed to posses many skills in these three years.*

I would like to thank ***Prof. Corine Mathonière*** *for her caress. Her nice presence was always an inspiration to our group and me as well. I like her pedagogic style of scientific discussion. I would like to thank* ***Mathieu Rouzieres*** *from whom I learned to use the SQUID and I always liked his cordial wishes.*

Dr. Céline Pichon *was my lab-mate for two year. I am very thankful to her for the nice time I spent with. I was very impressed with her simplicity, friendly attitude. She had a special care for everyone, immense patients to help somebody for any problem of life. I bothered her several times for several reasons, and she was always there. I was really touched with the goodness of her heart.*

I give a lot of thanks to ***Dimitri Mitcov****, my office-mate, lab-mate and friend, for his inspiration and sincerity. He is as good as in friendly discussion and scientific discussion. He was never annoyed to listen many of my demands, like spend time to find chemicals, bring chemicals from bunker, take photographs, listen presentation practice for hours, find locations on map etc etc...he is a very nice person and he is one of them who helped me to overcome the dullness of foreign life. I wish the best for his PhD.*

Thanks to ***Mihail Secu*** *and* ***Sergiu Calancea*** *for their friendship, well wishes, and nice time that I will always clip in my memory. Both of them always inspired me to be more patient, determined and bold; I am very happy for the greetings I always received from them and I was impressed with their purity of heart. I wish a very bright future for both of them.*

Thanks to ***Ie-Rang Jeon*** *and* ***Vivien Pianet*** *for the memorable moments I spent with them. Ie-Rang is very intelligent and her management power is a quality to learn to be successful. I wish a*

deserving future for her. The systematic pedagogic way of Vivien's work is an art to make good scientific skill; my well wishes are with him for his bright career.

I am also thankful to the former PhD-mates ***Diana Siretanu****,* ***Oleg Palamarciuc*** *and* ***Rodica Ababei*** *for the nice time I spent with them,... visiting places, taking photographs and many more. The suggestions from Rodica and Diana were especially very helpful for me to understand organization of PhD, and how to do the time estimation in these three year span. From their way of guidance I felt like a younger sister of them. Even I was sometimes stressed; their inspirations and good wishes never let me feel lost in hardness. I know those days would be much tougher without Diana and Rodica.*

Thanks to many other persons I mate for short time but always enjoyed their presence: ***Dr. Marguerite Kalisz,*** ***Dr. Dalice Piñero-Cruz,*** ***Kasper Steen Pedersen*** *and* ***Pascaline Patureau****. I heartily appreciate the charming presence of Pascaline during my writing of manuscript.*

I must thank to my collaborators from Berkeley, California USA: ***Prof. Jeffrey R. Long*** *and* ***Dr. T. David Harris****. David helped me lot to obtained the rhenium based compound that I have extensively used in my research work.*

I express my gratitude to the people from all departments of CRPP: service informatique, mission, gestion, accueil et bâtiment, cellule chimie et instrumentation, atelier mécanique. I would like to thank ***Nadine Laffargue*** *for her help for my bibliographic work. I show gratitude to* ***Stephane Gineste*** *and* ***Mbolotiana Rajaoarivelo*** *for their finding the required chemicals quickly. I would never be able to make a PhD without their helpful hands.*

I like to say thousands of thanks my friend ***Sri Bharani Sekar****. We are very close friend for almost last one year and her presence is one strength for me to pass the hardest time of PhD: the last six months. Her intimacy, cares and inspiration always reminded me my family, but never let me miss it. She is very understanding, bold to face the hurdles and has a impressive positive attitude to the life. Her presence is always refreshing and keeps its foot prints on mind. We have bunches of nice moments together: shopping a lot, cooking new recipes, eating in restaurants, roaming in the city... I know how hard and dull would be my past days without Sri Bharani; I am extremely grateful to her...but most unfortunately I cannot be with her when she is just now beginning her hardest period of PhD... Indeed I have best wishes for her life.*

Finally, my heartiest gratitude and love are dedicated to my family. A most special thanks to my mother ***Bipasha Bhowmik (Sarkar)****; she is the most admirable person of my life. I can never finish to tell how much extraordinary she is. I honour all the sleepless nights she spent for me, I honour her patients and perseverance to guide me in every step of life. It was only her determination, motivation*

and love that reached me here today. I used to say 'if I have achieved any reward in my life, my mother deserves it'. The unique mixture of softness and boldness in my mother is the inspiring spirit throughout my life. Thanks to my father ***Ashis Bhowmik****, for strong support me in all my wishes and giving the special freedom to make my career as my will. He always motivated me to be strong in hard competition, bold enough to reach the apex. I learned discipline from him, and he is the person who taught me to say 'no' to the impossible. My father deeply wanted me to come in CRPP, and is one of the biggest reasons I am here; I got the opportunity to discover the hearty presence of many persons; I got the chance of learning many skills and important aspects of life. I am very thankful to my loving, supportive, encouraging, and charming sister,* ***Prantika Bhowmik****. She is a big part of my life, and nothing would be beautiful without her. She is my "best friend" and I always missed her presence in last three years. I am very proud to have a sister like her and wish her a very happy and bright life.*

Thank you all – Merci à tous

Indrani Bhowmick
Pessac, September, 2012

CONTENTS

GENERAL INTRODUCTION

Magnetism is one of Nature's most fascinating phenomena. Magnetism was first discovered in the form of the mineral magnetite, also called lodestone, which is comprised of iron oxide. Even though the history of magnetism is controversial, the ancient Greeks are supposed to be the first to use lodestone (600 B.C.) and call it "magnet". The earliest Chinese literature reference to magnetism lies in the 4th century B.C. writings of Wang Xu: "The lodestone attracts iron."[1a] Chinese as early as 300-200 B.C. knew that an iron rod which had been brought near of these natural magnets would acquire and retain the magnetic property and the rod when suspended from a string would align itself in a north-south direction. Thus the ancient Chinese are known to use the loadstone as compass, a navigational instrument.[1b] Stories of magnetism was also found in the writings of Gaius Plinius Secundus (A.D. 23-79, Roman), know as Pliny the Elder.[2] Pierre Pelerin de Maricourt, writes *Epistola de Magnete* (1269), the first general study of magnetism.[3]

Magnetic materials are used ubiquitously in the modern world; for example, in electrical energy transport, high-power electro-motors, generators, telecommunication systems, navigation equipment, aviation and space operations, micromechanical automation, magnetocaloric refrigeration, computer science, high density recording, non-destructive testing of materials, medical devices (X-rays and MRI machines etc) and in many other applications. Over time, magnet based materials have become indispensable in daily household life also, playing a role in computer and television monitors, microphones, switches, sensors, bank and identification cards, data storage devices, door latches, toys etc. In other words, the magnets are almost everywhere.

The Englishman William Gilbert (1544 –1603) was the first person to carry out a systematic scientific investigation on magnetism. He also discovered Earth to be a weak magnet[4] which was further illustrated by Carl Friedrich Gauss (1777-1855). A quantitative study of magnetism was initiated in the 18th Century. Danish physicist Hans Christian Ørsted (1777-1851) first suggested a link between electricity and magnetism. Later on, André-Marie Ampère (1775-1836) and Michael Faraday (1791-1867) provided both the experimental and theoretical foundation of electromagnetism. Two of Faraday's great discoveries were electromagnetic induction and diamagnetism (1845). Italian physicist Francesco Zantedeschi (1797-1873) performed experiments on closed electrical circuit upon presence and withdrawal of magnetic field. James Clerk Maxwell (1831-1879) extended the work of Faraday to give the mathematical expressions of classical electromagnetic theory (1865).[5] Pierre Curie (1859-1906) and Pierre Ernest Weiss (1865-1940) contributed hugely to the investigation of magnetic phenomena in condensed matter. Pierre Curie examined the effect of temperature on magnetic materials and Weiss proposed the theory of the magnetic domain in ferromagnetic materials (1906).[6]

Niels Bohr (1885-1962) identified the underlying physics from which paramagnetism is associated with localized unpaired electron (1913). In the 20th century, magnetism was put on a firm theoretical basis through the work of people like John Hasbrouck Van Vleck (1899-1980). Van Vleck

established elemental relations between the quantum theory of magnetism and crystal field theory.[7] His work provided experimentalists useful tools to compute the energy levels of the compound, the magnetic properties and to analyse magnetic data.[7] Consequently, quantum chemists and physicists developed wide quantum studies on molecular systems like wave function (1920s-1930s), molecular orbitals (between 1930s-1950s)[8] and ligand field theory,[9] spin-orbit coupling, zero field splitting, radical phenomena and among others. Researchers began to accumulate the magnetic susceptibility data of various materials to investigate the phenomena on the molecular level. The "anomalous" magnetic behaviour of copper acetate[10] was quantified by a singlet-triplet gap by Bleaney and Bowers in 1952.[11] Molecular magnetism is a relatively recent scientific field where chemists and physicists intensively collaborate to design and characterise molecule-based magnetic materials. Many considers the work of Bleaney and Bowers[11] as the birth of the molecular magnetism.

At the beginning of the 1970s, the field of magnetochemistry or molecular magnetism achieved an important theoretical basis when physicists took into account chemical bonding and exchange interactions in their magnetic approach to molecules. The work of Goodenough, [12] Kanamori [13] and Anderson [14] was significant to this approach. Hoffmann and Kahn provided a description of the interaction between unpaired electrons in a molecule.[15,16] Their work gave synthetic chemists clear directions towards the design of molecules with expected interactions and magnetic properties. Thus in the field of molecule-based magnets the scientific language between the two communities, chemists and physicists, started to become more and more common. The first well-known molecular compound displaying a ferromagnetic ground state was described by Wickman et al. in 1967.[17] In 1987, Miller and Epstein reported the first example of a molecule based ferromagnet containing an organic building block, TCNE (TCNE = tetracyanoethylene).[18] The next year, Kahn, Pei and Verdaguer contributed one more milestone in this field with the first design of a molecule based ferrimagnet, based on copper(II) and manganese(II).[19] Molecular magnetism was furthermore fueled by the discovery of a Single Molecule Magnet (SMM), where the molecule itself behaved as magnet. It was first reported in 1991[20] that the $[Mn_{12}O_{12}(O_2CMe)_{16}(H_2O)_4]$ complex ($Mn_{12}Ac$ was first synthesized in 1980)[21] exhibits slow relaxation of the magnetization at low temperatures and thus represents a molecular approach to nanomagnets. The magnetic bistability observed in the SMMs indicates potential applications for these types of materials in information storage devices, where a single molecule can act as the smallest unit of magnetic memory.[22] Later, in 2001, A. Caneschi et al. reported the magnetic relaxation dynamics in an one dimensional coordination network.[23] Thus the one dimensional molecular magnets, named Single Chain Magnets[24] further enlarged the field of molecular magnetism.

This thesis is devoted to the synthesis of new molecule based magnetic materials and their characterization. We mainly focused on the systems with magnetic *d*-block transition metals and their organization in low dimensional architectures. Such transition metal ions possess variety of oxidation

states, often yielding unpaired electrons, and the anisotropy around such metal centers is tunable through the ligand field. Notably 4*d* and 5*d* metal ions possess often large magnetic anisotropy due to their significant spin-orbit coupling. Therefore the *d*-block (3*d*, 4*d* and 5*d*) transition metal ions have become one of the key design elements in molecule based magnetic materials.

In this research work, we are intended to synthesize low dimensional molecule-based magnetic materials (like SMM and SCMs) incorporating the magnetic interactions between the 3*d* and 4*d*/5*d* transition metal ions via cyanido bridging. Therefore, in one hand, we selectively used the *d*-block transition metal precursors in which we can control the dimensionality of the final compound. Indeed, coordination chemistry is the main tool for the synthesis of such materials, allowing chemists to adjust the oxidation states of the metal centers and the magnetic interactions of their unpaired electrons. On the other hand, our work focused on the synthesis of cyanido bridged transition metal compounds, because the cyanido group is known to support significant magnetic exchange between the metal ions.[25] Moreover the cyanido ligand has a different coordination environment on either end, so that it can selectively bind to different metal ions through the carbon and nitrogen atoms, and is therefore appropriate for the design of heterometallic magnetic systems.

Herein, we will report both zero (molecular) and one dimensional molecule-based magnetic species with an extensive discussion of their properties. Chapter I contains a general discussion of the characteristics of molecule-based magnets with suitable examples from both theoretical and chemical point of view. Moreover in Chapter I, we discussed why the cyanido ligand was used as a heterometallic bridging unit (section I.4). The Chapter II will introduce the reader to the building blocks used for designing molecular magnets in this work. This chapter described the strategy to design of low dimensional molecule-based magnets using 3*d* and cyanido based 4*d*/5*d* transition metal ions and also justifies the choice of different molecular precursors in this research work. The rest of the chapters (chapter III, IV and V) of this thesis contain the descriptions of the newly obtained materials from both a chemical and a magnetic point of view. At the end of each chapter a "conclusions and perspectives" section is introduced which is not only a summarized overview of the work, but will also help the reader to understand some of the problems we faced during the research work. Finally, we will provide a conclusion to this work and emphasize future perspectives to enrich the arena of molecule-based magnetism. At the end of the thesis, one will find an Annex section describing the byproducts and partially characterized compounds we have obtained during this work.

[1] (a) http://www.gutenberg.org/cache/epub/7209/pg7209.html . (b) Lowrie and William, *Fundamentals of Geophysics*. London: Cambridge University Press., **2007**, p. 281.

[2] (a) Pliny the Elder, *Naturalis Historia* (*Natural History*), **AD 77–79**. (b) Pliny the Younger (61 AD – ca. 112 AD), *Epistulae (Letters)*.

[3] Pierre Pelerin de Maricourt, *Epistola de Magnete*, **1269**.

[4] W. Gilbert, *De Magnete, Magneticisque Corporibus, et de Magno Magnete Tellure*, **1600**.

[5] James Clerk Maxwell, *A Dynamical Theory of the Electromagnetic Field*, Philosophical Transactions of the Royal Society of London, **1865**, 155: 459–512.

[6] (a) P. Weiss, *La variation du ferromagnetisme du temperature*, *Comptes Rendus*, **1906**, 143, p. 1136-1149. (b) C. Cullity, D. Graham. *Introduction to Magnetic Materials, 2nd ed.*, **2008**, P-116.

[7] J. H. Van Vleck, *The Theory of Electric and Magnetic Susceptibility*, Oxford University Press, Oxford, **1932**.

[8] (a) http://www.nobelprize.org/nobel_prizes/chemistry/laureates/1966/mulliken-lecture.pdf . (b) G. G. Hall, *The Molecular Orbital Theory of Chemical Valency. VI. Properties of Equivalent Orbitals*, *Proc. Roy. Soc. A*, **1950,** 202(1070): 336–344.

[9] H. L. Schläfer, G. Gliemann, *Basic Principles of Ligand Field Theory*, Wiley Interscience: New York, **1969**.

[10] B. C. Guha, *Proc. R. Soc. London*, **1951**, A206: 353.

[11] B. Bleaney, K. D. Bowers, *Proc. Roy. Soc. (London) Ser*., **1952**, A214, 451.

[12] J. B. Goodenough, *Magnetism and the Chemical Bond*, Interscience Publishers, New York **1963**.

[13] J. Kanamori, *Magnetism*, *Vol. 1*, (Eds.: G. T. Rado, H. Suhl), Acad. Press, New York **1963**.

[14] P. W. Anderson, B. I. Halperin, C. M. Varma, *Philos. Mag.* **1972,** 25, 1.

[15] P. J. Hay, J. C. Thibeault, R. H. Hoffmann, *J. Am. Chem. Soc.*, **1975,** 97, 4884.

[16] O. Kahn, B. J. Briat, *J. Chem. Soc. Faraday Trans. II*, **1976**, 72, 268.

[17] H. H. Wickman, A. M. Trozzlo, H. J. Williams, G. W. Hull, F. R. Merritt, *Phys. Rev. B*, **1967**, 155, 563.

[18] J. S. Miller, J. C. Calabrese, H. Rommelmann , S. Chittapeddi, J. H. Zhang, W. M. Reiff, A. J. Epstein, *J. Am. Chem. Soc.*, **1987**, 109, 769.

[19] O. Kahn, Y. Pei, M. Verdaguer, J.-P. Renard, J. Sletten, *J. Am. Chem. Soc.*, **1988**, 110*,* 782.

[20] A. Caneschi, D. Gatteschi, R. Sessoli, A. L. Barra, L.C. Brunel, M. Guillot, *J. Am. Chem. Soc*., **1991**, 113, 5873.

[21] T. Lis, *Acta Crystallogr.*, **1980**, B36, 2042.

[22] R. Sessoli, D. Gatteschi, A. Caneschi, M. A. Novak, *Nature*, **1993**, 365, 141.

[23] A. Caneschi, D. Gatteschi, N. Lalioti, C. Sangregorio, R. Sessoli, G. Venturi, A. Vindigni, A. Rettori, M. G. Pini, M. A. Novak, *Angew. Chem. Int. Ed*., **2001**, 40, 1760.

[24] R. Clérac, H. Miyasaka, M. Yamashita, C. Coulon, *J. Am. Chem. Soc.*, **2002**, 124, 12837.

[25] References number 53-68 in chapter I of this thesis.

CHAPTER I

Physicochemical approach to molecular magnetic materials

I. Introduction

Magnets are extremely important to our modern life. Magnet based materials have become indispensable in common tools such as microphones, switches, sensors, motors, generators, data storage devices, medical devices and many more. The majority of the conventional magnetic materials used in current technology, such as Fe, Fe_2O_3, Cr_2O_3, $SmCo_5$, $Nd_2Fe_{14}B$, etc. are all metal-based inorganic two- or three-dimensional arrays. The preparation/processing of such materials require high-temperature metallurgical methodologies. Moreover, optimization of information storage techniques requires the miniaturization of the size of magnetic materials. The traditional magnetic materials exhibit their limitations towards size reduction by losing their magnetic properties.[1]

In contrast to traditional magnetic materials, molecule-based magnets are organic or inorganic/organic hybrid materials, comprised of spin units of either metal or organic radicals.[2,3a] Employing self-assembly methods, it is possible to engineer a bulk molecular material at much lower temperature with a better control over the magnetic properties, size and dimensionality. Chemical synthesis provides immense flexibility towards the design of new magnetic materials from a variety of molecular precursors, which carry the magnetic centers or spins. Besides the versatile application of molecular magnets mainly in information storage technology,[4] they also provide an ideal opportunity to explore the physics behind magnetism.[3b] On one hand, such materials allow theoreticians to investigate the coexistence of quantum and classical effects; on the other hand, they motivate chemists to combine the magnetic centers in desired direction with the aim of improved characteristics.

For chemists the chemical tools to build all such metal-based magnetic materials can be found in coordination chemistry, that corresponds to the study of metal-organic molecular compounds.[5] The cationic metal centers interact with electron donors (like C, N, O, Cl, S etc) with various ligands, and therefore satisfy their coordination sphere according to the ligand field. The main objective of chemists is to exploit these phenomena to obtain complexes with interesting magnetic characteristics, such as strong magnetic interaction and high spin and/or anisotropy. Therefore, the design of molecule-based magnetic materials involves focusing not only the metal ions possessing unpaired electrons, but also on the coordination capability of various ligands and their qualitative and quantitative influence in magnetic exchange.[5]

In the last two decades, major scientific achievements have been made at the atomic, molecular and macromolecular levels towards the synthesis of nanometer scale magnetic systems.[5] This worldwide research effort towards magnetic materials categorize molecular systems in different families, such as Single Molecule Magnets (SMMs),[4,6] Single Chain Magnets (SCMs),[7] photo-magnets[8] etc. These magnets fabricated from molecules are unique; they exhibit all the phenomena observed in conventional transition-metal and rare earth-based magnets, further accompanied by many

other chemical and physical properties such as supramolecular interactions,[9] liquid crystal phase,[10] chirality,[11] conductivity,[12] solubility,[13] spin-crossover,[14] negative magnetization,[15] photo-induced magnetization/ switching,[16] and many more.[17]

In this research work, the goal was rational synthesis of new cyanido bridged heterometallic molecule-based magnetic materials using the *d*-block transition metal precursors. The role of cyanido ligand in the heterometallic magnetic exchange will be discussed later in this chapter (section I.4). A variety of magnetic properties displayed in new heterometallic complexes, including SCM behavior and long-range magnetic ordering, will be extensively described in this thesis. In the present chapter, we will describe the theory behind the magnetic behavior expected from zero- and one-dimensional systems, which will serve as the basis for understanding the magnetic molecule-based species reported further in this thesis.

I.1. Basic theory behind magnetism

In order to design materials with interesting magnetic properties it is necessary to understand how bulk magnetism arises in matter. Movement of an electrical charge (which is the basis of electric currents) generates a magnetic field in a material. Therefore magnetic characteristics in materials arise from entirely electronic origin. At the atomic level, magnetism is the result of motion by electrons, and their mutual combination of orbital motion and spin motion along the electrons' own axes. Both types of movement create a magnetic force field between electrons, and as a result the electron takes on the properties of a tiny bar magnet with a north pole and south pole. In most atomic orbital the electrons are paired and their individual magnetic fields cancel out each other resulting in no total magnetic moment. But when the electron(s) are unpaired in their atomic orbitals, the magnetic forces around them line up to create a net magnetic dipole, and most of the transition metals with unpaired electron in *d* and *f* atomic orbitals fall in this category. In presence of an external magnetic field these unpaired electrons interact with the field and their orbital motion is influenced.

Magnetic susceptibility is one of the key parameters to be investigated in the behavior of a magnetic sample. The magnetic susceptibility can give information about the electronic structure, magnetic exchange interactions and oxidation state of transition metal complexes. A detailed account of magnetic susceptibility can be found in the text books of Carlin,[18a] Kahn,[3b] Mabbs and Machin,[18b] Kittel,[18c] Boca[18d] and many others.

Magnetic susceptibility: In electromagnetism, the magnetic susceptibility is a quantitative measure of the extent of magnetization (*M*) of a material in response to an applied magnetic field (*H*). The magnetization *M* is a function of *H* acting through the second rank tensor susceptibility, χ:

$M = [\chi]H$ **Eq.I.1**

For an isotropic system the expression of the tensor susceptibility becomes a scalar number $\chi_\delta = \frac{|M|}{|H|}$ (or $\chi_\delta = \mu_0 \frac{|M|}{|H|}$ in SI). The magnetic susceptibility in the remainder called static susceptibility is denoted as χ_δ. But in practice the relation between M and H is not linear in all ranges of the magnetic field and thus we introduce the dynamic susceptibility χ_d (also known as differential magnetic susceptibility) expressed as:

$$\chi_d = {}^{\partial|M|}/_{\partial|H|} \quad \textbf{Eq.I.2}$$

Strictly speaking, this ratio is the volume susceptibility, because magnetization essentially involves a certain measure of magnetism (magnetic moment) per unit volume. More usefully, magnetic susceptibility can be expressed in terms of the molar mass of the material and hence the molar magnetic susceptibility is written as χ, with units of $m^3 \cdot mol^{-1}$ (SI) or $cm^3 \cdot mol^{-1}$ (CGS) and defined as,

$$\chi = \frac{M_m}{\rho} \chi_\delta \quad \textbf{Eq. I.3}$$

where M_m is the molar mass and ρ is the density of the sample.

As we have already discussed above, the genesis of the magnetic moments is due to the coupling of spin and orbital magnetic moments associated with the motion of electrons. There are three principal origins for the magnetic moment of a free atom in presence of external magnetic field. First, the spin magnetic moment is due to the precession of the electrons about their own spinning axis. Second, the orbital magnetic moment is due to the motion of electrons around the nucleus, and finally, the change in the orbital moment induced by an applied magnetic field. The first two effects give rise to paramagnetic contributions and the latter produces a diamagnetic contribution. Thus, χ is often a simple algebraic sum of the two contributions:

$$\chi = \chi^D + \chi^P \quad \textbf{Eq. I.4}$$

where χ^D and χ^P represent the diamagnetic and paramagnetic contribution of susceptibilities, respectively, where χ^D is negative and χ^P is positive. The net magnetic response of a system depends on the dominance of one of these susceptibilities over the other. When χ^D dominates, the sample is diamagnetic with the magnetization opposite to the applied magnetic field, whereas if χ^P dominates, the sample is paramagnetic with the magnetization in the direction of the applied magnetic field.

I.2. Types of magnetic properties

The best way to introduce the different kinds of magnetism is to describe the response of the susceptibility in an applied magnetic field.

Diamagnetism: Diamagnetism arises due to the interaction of the magnetic field with the motion of electrons in their orbitals. Diamagnetism is a fundamental property of matter which is always present, but is sometimes masked by other magnetic properties like paramagnetism. Diamagnetic susceptibility χ^D is usually independent of the temperature and the strength of the applied field. Diamagnetic behavior is characterized by a repulsion of the substance out of an applied magnetic field which interacts with molecular or atomic orbitals containing paired electrons. Therefore the substance having localized electrons with negative magnetic susceptibility is always diamagnetic.

Paramagnetism: This behavior arises as a result of an interaction between the applied magnetic field and unpaired electrons in atomic or molecular orbitals. These substances are attracted into a magnetic field due to partial alignment of the atomic magnetic moments in the direction of the field resulting in positive magnetization and positive magnetic susceptibility. Paramagnets do not retain any magnetization in the absence of an externally applied magnetic field because thermal motion causes the spins to become randomly oriented. Thus the total magnetization will drop to zero when the applied field is removed. In paramagnetic substances with localized spin, χ^P overcomes χ^D.

In order to investigate the nature of magnetic properties in a substance, the temperature dependence of magnetic susceptibility is a very useful tool. The magnetic susceptibility of a diamagnetic substance does not vary with temperature, whereas the magnetic susceptibility of paramagnet is inversely related to temperature. Pierre Curie showed that,[19a] for paramagnetic substances with isolated magnetic sites, the magnetization follows a Curie law to the approximation:

$$M = C.H/T \qquad \textbf{Eq. I.5}$$

where M is the resulting magnetization, H is the applied field, T is absolute temperature and C is Curie constant. This leads to the expression known as Curie Law:

$$\chi = C/T \qquad \textbf{Eq. I.6}$$

I.2.1. Magnetic interactions

In most paramagnetic substances, the magnetic properties originate entirely from the individual magnetic centers, and the interactions between them. When the interaction is negligible,

these materials are qualified as "magnetically diluted". However, there are some paramagnetic substances in which a magnetic interaction exists between neighboring magnetic centers. Such substances are referred to as "magnetically concentrated". Therefore for a more quantitative understanding of these interactions in the magnetic materials, we need an appropriate estimation of magnetic coupling. The word "magnetic coupling" in a wide sense signifies the interaction of individual magnetic moments in a substance. In the cases of such magnetically concentrated systems, Curie's law is no longer valid and the magnetic exchange between spin carriers needs to be included in the model. To describe the interaction between the two adjacent magnetic moments (having spin S) the following Hamiltonian is used:

$$\mathcal{H} = -2J \sum_{<i,j>} \vec{S}_{\mathrm{i}} \,.\, \vec{S}_{\mathrm{j}} + g\mu_{\mathrm{B}} \sum_i \vec{H} \cdot \vec{S_i} \qquad \textbf{Eq. I.7}$$

where $2J$ is the exchange coupling between two neighboring spin, g is the "spectroscopic splitting factor" (Landé g factor) and μ_{B} is the Bohr magneton. When J > 0, ferromagnetic interactions are present between the spin pairs and when J < 0 the interaction is antiferromagnetic. In order to describe the thermal behavior of such magnetic material with interactions the Curie-Weiss law becomes applicable. According to the Curie-Weiss law[19b] the expression of magnetization becomes:

$$\chi = {}^{M}/_{H} = \frac{NS(S+1)g^2\mu_{\mathrm{B}}^2}{3k_{\mathrm{B}}T - 2zJS(S+1)} = \frac{C_{\mathrm{s}}}{T-\theta} \qquad \textbf{Eq. I.8}$$

where the temperature T is in Kelvin, N is Avagadro's number and k_{B} is the Boltzman constant. C_{S} is known as Curie constant having the expression, $C_{\mathrm{S}} = g^2N^2\mu_{\mathrm{B}}{}^2S(S+1)/3k_{\mathrm{B}}$ and the Weiss constant is $\theta = 2zJS(S+1)/3k_{\mathrm{B}}$. Here, z is a whole number which denotes the total number of neighbors around one spin S in the material. The value of the Weiss constant, θ, can be obtained directly by plotting $1/\chi$ versus T. The positive and negative intercept on the temperature axis respectively indicate the presence of dominant ferromagnetic ($\theta > 0$), and antiferromagnetic ($\theta < 0$), interactions in the magnetic material.

I.2.2. Magnetic Phase transition

A magnetic phase transition occurs when the interaction energy between the magnetic moments of a material are of the order of the thermal energy ($k_{\mathrm{B}}T$). Therefore as the thermal energy provided to a paramagnetic substance decreases, the ferro- or antiferromagnetic ordered phases can be stabilized below a critical temperature (T_C). In a ferromagnetic compound below this T_{C} the magnetic moments align parallel to each other (figure I.1a.). For an antiferromagnetic compound this critical

temperature is known as Néel temperature (T_N) where below T_N spins align antiparallel to each other, (figure I.1b.).

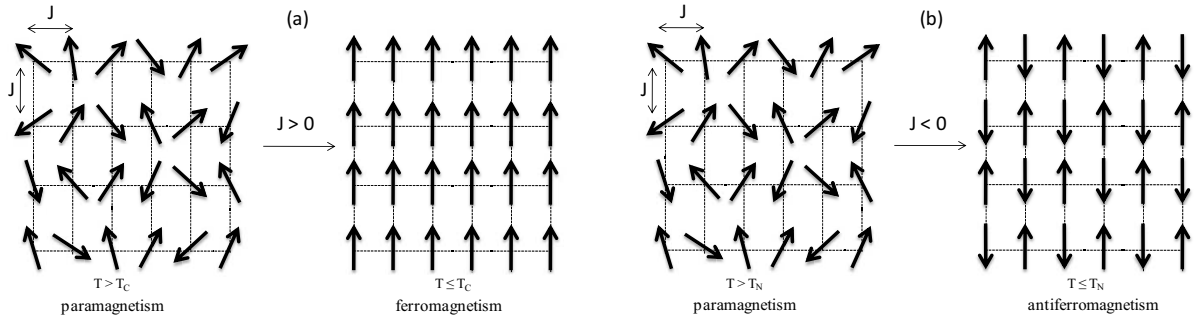

Figure I.1. Schematic representation of the orientation of the spins of a material during the transition from a paramagnetic state to a (a) ferromagnetic state and (b) antiferromagnetic state.

The T_C and T_N can be determined by susceptibility measurements and this magnitude of T_C and T_N can be estimated by applying the mean field approximation to the system. This Mean Field Theory is mostly applicable where the accurate determination of individual interactions is very complicated. The basic idea behind the Mean Field Theory is to replace all of the interactions inside a system with an average effective interaction, as if an effective field acting on each spin. For 3D systems, the mean field approximation is the appropriate method to determine the magnitude of magnetic exchange. At the mean field approximation the values of T_C or T_N are equal to $2|zJ|S(S+1)/3k_B$.

Phase transition in antiferromagnetic substances: In antiferromagnetic substances the paramagnetic to antiferromagnetic phase transition occurs below the Néel temperature (T_N). When a magnetic field is applied parallel to the direction of the magnetic moments, it provides the system with the energy to overcome the antiparallel orientations below T_N. Therefore an H(field) vs. T(temperature) phase diagram can be constructed for such antiferromagnetic systems (figure I.2) to investigate the phase transition phenomenon. In case of an antiferromagnet with low anisotropy with increasing field strength the magnetic moments orient perpendicular to the applied field and the material enters a new intermediate phase called the "spin-flop" phase. The further increase of H moves the whole system into a paramagnetic phase. Figure I.2a. exhibits a phase diagram of an ideal antiferromagnet where the (T, H) values correspond to the maximum magnetic susceptibility are plotted as a function of temperature. We find these maximum values of magnetic susceptibility from the dM/dH vs. T points. In the area below T_N and the H_{SF} line, the material is in an antiferromagnetic behavior, where H_{SF} corresponds to the critical field required to enter into the spin flop phase. Therefore beyond the region of T_N and the H_C line the magnetic moment of the substance is in a paramagnetic state. The axial anisotropy of a spin allows the spin to orient in a particular direction where the system experiences the minimum energy. With the increase of the anisotropy in the system

the "spin-flop" phase minimizes. In the case where the anisotropy is quite high, the spin flop state no longer exists. In such a compound the critical field H_C corresponds to transition from an antiferromagnetic to paramagnetic phase (figure I.2b). This kind of material is also known as a "metamagnet".

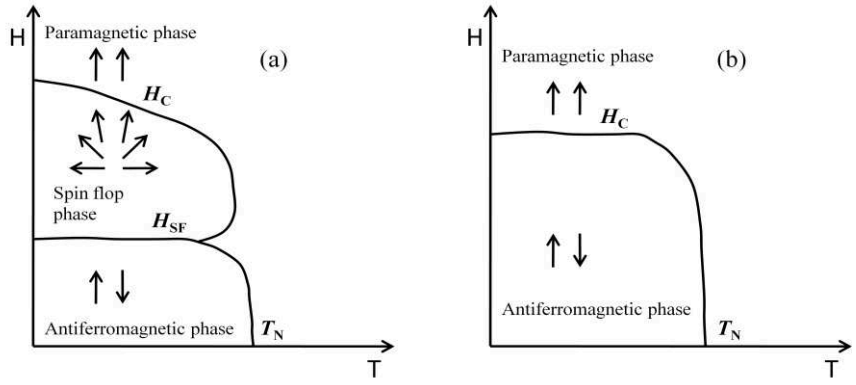

Figure I.2. Phase diagram of antiferromagnetic materials, (a) for an antiferromagnet with low anisotropy, (b) for a metamagnet (antiferromagnet with high anisotropy).

Canted antiferromagnetic phase: In some cases, the minimization of energy leads to an antiferromagnetic phase where the magnetic spins are not exactly antiparallel; and there exists a tilt angle between the spins in the ordered phase. A schematic representation of such orientation of spins is shown in figure I.3a. Therefore the system also possesses a phase diagram like antiferromagnetic system, where the phase is denoted as a canted antiferromagnetic phase. In such a compound the total magnetization of the system is not cancelled in the antiferromagnetic phase, and thus can exhibit some residual magnetization (weak ferromagnetism)[19c] in zero field.

Ferrimagnetic phase: In some cases, the magnetic moments of a substance align in an antiparallel fashion with decrease of temperature, but the spins do not entirely cancel one another. We call it ferrimagnetic phase. The ferrimagnetic behavior thus qualitatively resembles that of ferromagnetism. In figure I.3b the orientations of the spins of a ferrimagnetic state are schematically represented.

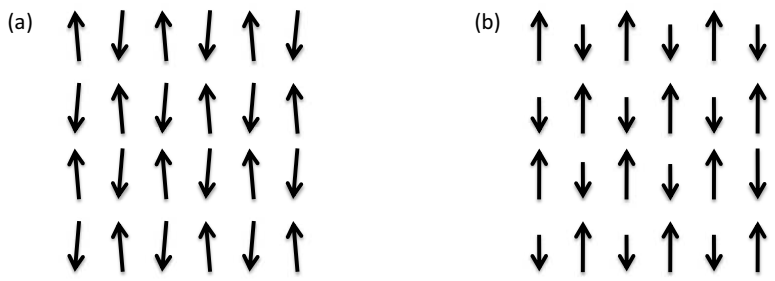

Figure I.3. Schematic representation of the orientation of the spins of a material having (a) canted antiferromagnetic state and (b) ferrimagnetic state.

I.3. Molecule based magnetic materials

Most of the commonly used magnets exhibit long range ferromagnetic or ferrimagnetic order. But with an increasing demand for small information storage devices, the importance of developing smaller and smaller grain magnetic materials has increased proportionally. Below a critical size, such magnetic materials become a single domain magnetic entity. But the reduction in size of these kind of materials has its own limitation. With the decrease of the size, the system loses magnetic anisotropy (that is proportional to the volume), and at the point where the anisotropy energy barrier becomes comparable to the thermal energy, there is a very fast relaxation of magnetization. The thermal energy easily provides randomness to the system and the retentivity to magnetization of the material decreases. Therefore, the minimization of the size of the magnetic grain leads to a superparamagnetic phase where the material no longer has the potential to store data.[1] In this context, the discovery of single molecule magnets (SMMs) [4,6] is extremely significant. A SMM is a zero-dimensional, single domain highly anisotropic magnetic entity in the nanometer scale where each molecule can store information. The macroscopic substances built with non-interacting SMMs resemble paramagnetic substances. The long relaxation time of the single molecule magnets originates from the high spin ground state and strong unidirectional anisotropy in the molecule. Later, a new class of one dimensional nano-magnets was discovered and called single chain magnets (SCMs)[7] by analogy to SMMs. These materials are composed of isolated magnetic chains which can be individually magnetized. Such one dimensional magnets are built with short range interactions between the magnetic centers and therefore do not display long range magnetic order at a finite temperature. SCMs also display large uniaxial anisotropy and a long relaxation time compatible with applications in information storage.

I.3.1. Single Molecule Magnets (SMMs)

A single molecule magnet (SMM) is a molecule that shows slow relaxation of the magnetization of purely molecular origin. It can be magnetized in a magnetic field and will remain magnetized even after switching off the magnetic field. The prerequisites for such a system are (a) a high-spin ground state (S_T), (b) a high uniaxial magnetic anisotropy with a magnetic easy axis and (c) negligible magnetic interactions between molecules. These characteristics were first observed in the manganese-based poly-metallic complex $[Mn_{12}O_{12}(O_2CCH_3)_{16}(H_2O)_4]$,[4] later known as Mn_{12}-Ac. This discovery opened a new window to the chemist to make numerous SMMs based on transition metal ions and coordinating ligands. Metal-organic complexes with 3*d,* 4*d,* 5*d*, 4*f*, and 5*f* metals exhibiting SMM properties are myriad in the literature.[3a,6c,e,20-36] The manganese-based single molecule magnets

significantly enriched the SMM family due to its various stable oxidation states depending on the coordination environment (like Mn_2,[20] Mn_3,[21] Mn_4,[22,23] Mn_5,[24] Mn_6,[25] Mn_7,[26] Mn_8,[27] Mn_9,[27] Mn_{12},[4] Mn_{19},[28] Mn_{30},[29] Mn_{84},[30]). Furthermore, one can find other homo-metallic SMMs with iron,[31] nickel,[32] cobalt,[33] lanthanides,[34] actinides[35] and even many hetero-metallic SMMs based on *d* and *f* block transition metals.[36]

I.3.1.1 Theoretical aspects of SMMs

In an SMM, each molecule consists of metal ions (spin carriers) bound to various organic ligands. The intramolecular magnetic exchange between metal centers through the ligands is significantly larger than the intermolecular interactions. Therefore the macroscopic magnetic properties of the material basically reflect the properties of a single molecule. These molecular systems have a large number of well-defined energy levels, populated according to Boltzmann statistics. At low temperature, when the magnetic coupling energy is larger than the thermal energy, the large spin ground state (S_T), the magnetic anisotropy (D) with $\mathcal{H} = DS_{T_z}^2$ and the large ratio of intra to intermolecular interactions lead the system to be trapped in its minimum energy level. The spin anisotropy manifests itself as an energy barrier Δ_A that must be overcome for the spins to switch from an "all up" alignment to an "all down" alignment (Figure I.4). Therefore an energy barrier Δ_A is followed by separation of the two lowest energy levels of $m_S = \pm S_T$, where m_S correspond to the spin projection quantum number. In the $m_S = 0$ state there is no energy cost to reverse the direction of the total spin. The energy difference Δ_A between the states of lowest energy and those of maximum energy is defined as,

$$\Delta_A = |D|S_T{}^2 \qquad \textbf{Eq. I.9}$$

where S_T is the total spin state and D is the zero-field splitting parameter originating from the anisotropy of the system. When S_T is a half integer (due to an odd number of unpaired electron in a molecule) this energy barrier is $\Delta_A = |D|(S_T^2 - ¼)$. Thus for a molecule to behave as a SMM, it should have a Ising-like anisotropy which indicates that the maximum m_S state is the ground state. Theoretically the higher the barrier, the longer a material remains magnetized in the absence of an applied field. At a given temperature high barrier is obtained when the molecule contains many unpaired electrons and also when its zero-field splitting value is large.

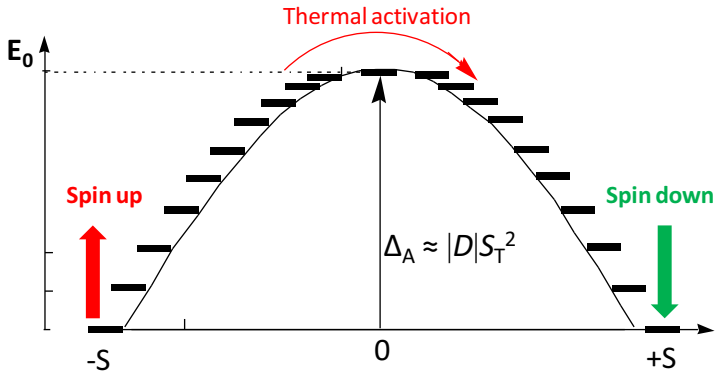

Figure I.4. Schematic energy diagram of a SMM with total spin ground state S and where M_S = -S and M_S = +S is the total spin ″up″ (red) and ″down″ (green) ground state respectively.

We here illustrate SMM properties with the help of the well known Mn_{12}-Ac compound.[4] Each Mn_{12}-Ac molecule contains 12 manganese atoms with 8 Mn^{III} (S = 2) and 4 Mn^{IV} (S = 3/2) (figure I.5a.). The central $Mn^{IV}{}_4O_4$ cube is surrounded by a ring of 8 Mn^{III} units connected through bridging oxido ligands. The large spin ground state S_T = 10 arises from magnetic exchange interactions between metal ions in the molecular core which indicates that the total number of unpaired electron is 20.

Magnetic properties in absence of external field:

The SMM behavior at low temperature is defined by the following Hamiltonian,

$$\mathcal{H} = DS_{T_z}^2 + E\,(S_{T_x}^2 - S_{T_y}^2) \qquad \textbf{Eq. I.10}$$

where $S_{T_x}^2$, $S_{T_y}^2$ and $S_{T_z}^2$ are spin operators along the three principal directions of magnetization (x is hard, y is intermediate and z is the easy axis) and D and E are respectively the easy axis and transverse anisotropy parameters of the molecule. The parameter E arises due to the geometrical deviation of the molecule from the ideal uniaxial environment. When D is negative and much larger than E ($|D| >> E$) the Hamiltonian can be simplified and reduced to $\mathcal{H} = DS_{T_z}^2$. In this approximation the spin energy levels can thus be expressed as $E_{m_S} = Dm_S^2$. Therefore, for Mn_{12}-Ac as S_T = 10, one can find the spin splits in total of 21 discrete energy levels with a strong uniaxial anisotropy barrier (Δ_A) on the order of 70 K. For D < 0 the states for which $|m_S|$ are the largest will have the lowest energy. Thus Mn_{12}-Ac exhibits a doubly degenerate m_S = ±10 spin ground state. In this situation, the equilibrium state at low temperature and without a magnetic field, half of the sample molecules is in the m_S = + 10 level ("spin up") and the other half is in the m_S level m_S = -10 ("spin down") so that the total magnetization of the sample is zero. At higher temperatures the thermal energy will allow the population of other m_S levels and to eventually overcome the energy barrier between positive and negative m_S states.

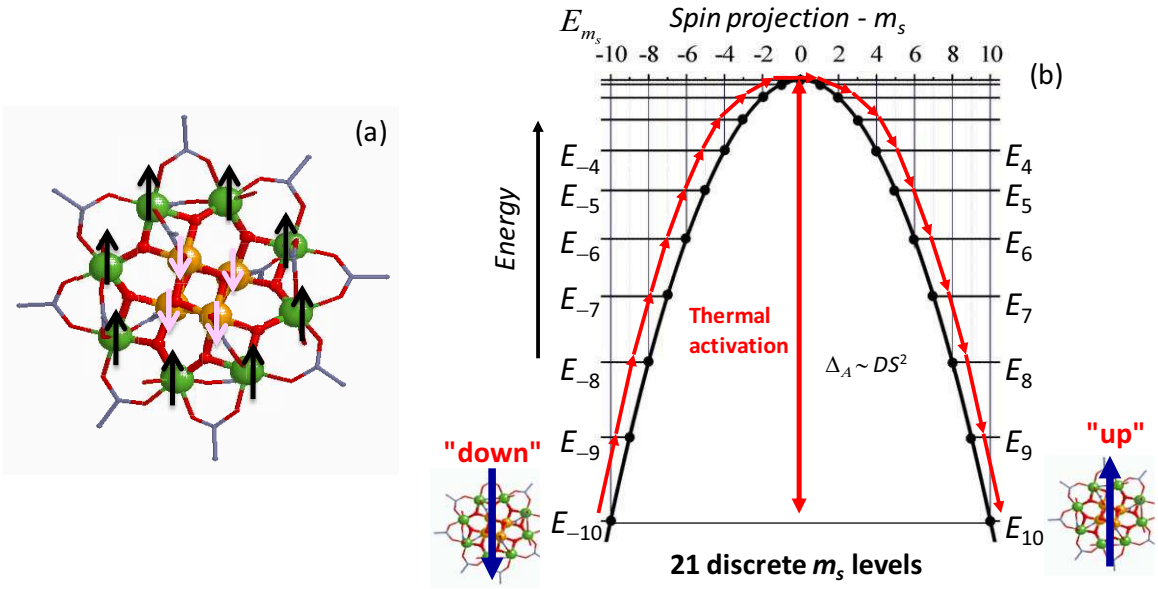

Figure. I.5. (a) Spin alignments in the ground state of Mn_{12}-Ac complexes that gives their $S_T = 10$ ground states where Mn^{IV} in yellow, Mn^{III} in green and O in red. (b) Potential-energy diagram for Mn_{12}-Ac at zero external magnetic field with an $S_T = 10$ ground state experiencing axial zero-field splitting, $\Delta_A = |D| \cdot S_T^2$. At low temperature SMM are blocked in the fundamental state $m_S = \pm 10$.

***Magnetic properties in longitudinal magnetic field*:**

For a SMM in the presence of an applied magnetic field the previous Hamiltonian (Eq. I.10) is changed in case of a uniaxial anisotropy to:

$$\mathcal{H} = DS_{T_z}^2 - g\mu_B \vec{S}_T . \vec{H} \qquad \textbf{Eq. I.11}$$

where the last term is the Zeeman effect contribution. This Zeeman effect originates from the interaction of spin $\vec{S}_T$ with the external magnetic field $\vec{H}$. If the field is applied along the easy axis of magnetization the longitudinal field H_Z splits the spin sublevels according to the Zeeman coupling (figure I.6a):

$$E_{m_S} = Dm_S^2 - g\mu_B m_S . H_Z \qquad \textbf{Eq. I.12}$$

Therefore, the spin levels with $m_S > 0$ are stabilized in the parallel orientation with the external longitudinal field and the spin level $m_S < 0$ are destabilized. Thus all spins will align parallel to the field creating a magnetization $M \neq 0$, and the $m_S = +10$ would be the most stable spin state over the all other spin states (figure I.6b).

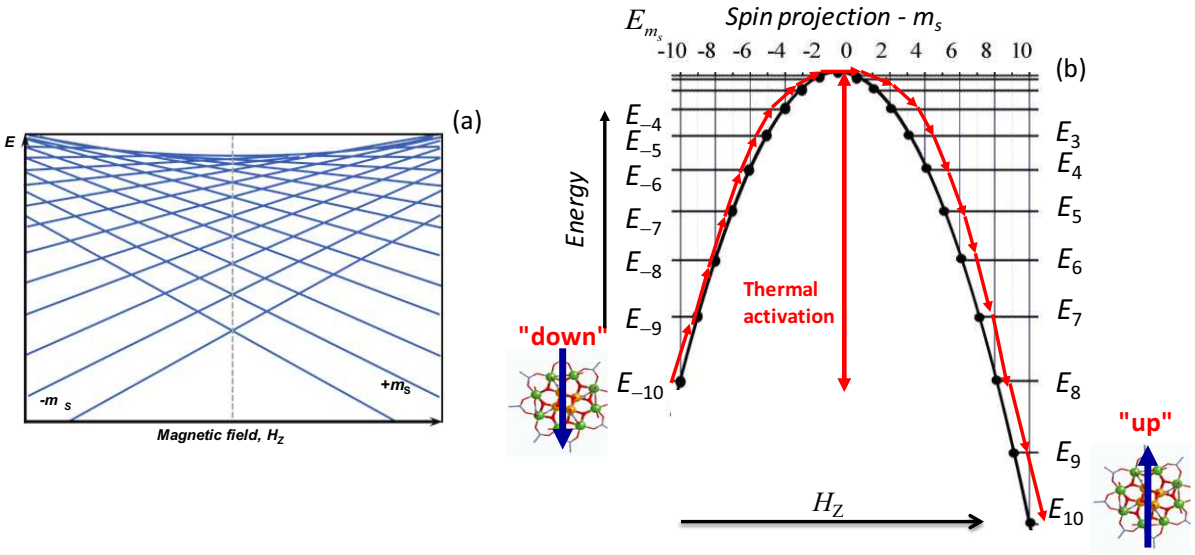

Figure I.6. (a) Zeeman diagram as a function of the external field H_Z applied along the easy axis. (b) The potential diagram of Mn_{12}-Ac in the presence of a longitudinal magnetic field H_Z where the spins are parallel to the external field in its ground state. It leads to the stabilization of $m_S > 0$ states and the destabilization of the $m_S < 0$ states.

I.3.1.2. Magnetic relaxation

Due to the anisotropy barrier, schematized in figure I.4, SMMs display a slow relaxation of their magnetization. After magnetizing the system with an applied field, the external field is switched off and the system will relax with time to restore its thermodynamically favored energy levels. Therefore we see the slow relaxation of magnetization is a phenomenon dependent on time and temperature in the absence of magnetic field. The more time it takes to lose the magnetization, the more efficient is the SMM behavior. At a fixed temperature the magnetization M of a SMM decreases exponentially with time and follows the relation,

$$M(t) = M_0 . exp\ (^{-t}/_{\tau}) \qquad \textbf{Eq. I.13}$$

where M_0 is the saturation magnetization at time $t = 0$, $M(t)$ is the magnetization as a function of time and τ is the relaxation time. The temperature dependent relaxation time follows the Arrhenius law,

$$\tau(T) = \tau_0 . exp\ (^{\Delta_A}/_{k_B T}) \qquad \textbf{Eq. I.14}$$

where Δ_A is the anisotropic energy barrier, k_B is the Boltzmann constant, and τ_0 is the pre-exponential factor, which is intrinsic to the SMM and can be determined through experiment. In the case of Mn_{12} complexes, τ_0 varies in the range of 10^{-8} – 10^{-10} s. As the temperature increases the rate of relaxation also becomes faster. The low temperature dynamics of magnetization including the relaxation time are

experimentally estimated by alternative current (*ac*) magnetic measurements with a weak oscillating field typically between 1 and 5 Oe. Here the magnetic susceptibility of a sample is measured using a weak magnetic field that switches direction at a fixed frequency (ν_{exp}). Thus the characteristic time of the experiment τ_{exp} is defined as $\tau_{exp} = (2\pi\nu_{exp})^{-1}$. The alternative magnetic susceptibility consists of two parts: an in-phase, or real, component χ' and an out-of-phase, or imaginary, component χ'':

$$\chi_{ac} = \chi' + i\chi'' \qquad \textbf{Eq. I.15}$$

The χ' component is the magnetic susceptibility in a low field and the χ'' component relates to the dissipative processes of the magnetization in the sample. Thus the magnetic relaxation is evaluated from the variation of χ' and χ'' with frequency. At low enough *ac* frequency when $\tau(T)$ is smaller than τ_{exp} the magnetization vector oscillates with the *ac* field and the measurement is quite similar to the *dc* magnetic measurements. In such a situation relaxation dynamics are not observed and one can only observe the χ' component which is equal to the *dc* magnetic susceptibility. But at higher frequency, when the relaxation time exceeds τ_{exp} the magnetization curve no longer follows the *dc* pathway due to the dynamics of the system and the magnetization of the sample delay behind the driving force. This is why the *ac* susceptibility of a system if often called the dynamic susceptibility.

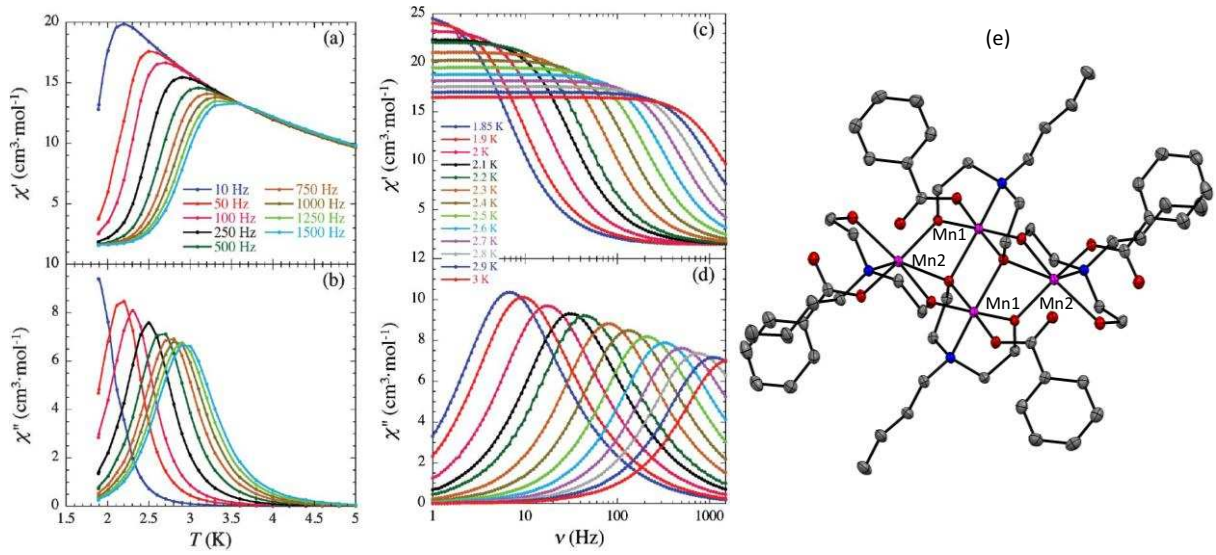

Figure I.7. Zero *dc* field *ac* susceptibility measurements for $[Mn^{II}_2Mn^{III}_2(bdea)_2(bdeaH)_2(O_2CPh)_4]$ as a function of the temperature at different frequencies (a) in-phase and (b) out-of phase signals; as a function of the frequency at different temperatures (c) in-phase and (d) out-of-phase signals. (e) ORTEP type view of the crystal structure of $[Mn^{II}_2Mn^{III}_2(bdea)_2(bdeaH)_2(O_2CPh)_4]$. The magenta, grey, red and blue spheres represents the Mn, C, O and N atom respectively. The H atoms are omitted due to clarity.[37]

If the barrier to magnetization relaxation is significant in comparison to the thermal energy, then χ' begins to diminish and χ'' increases. Thus in the *ac* measurements both χ' and χ'' are measured either as function of temperature at a particular frequency or as a function of frequency at fixed

temperature. As an example, the nature of the *ac* component is shown for a Mn_4 SMM, $[Mn^{II}_2Mn^{III}_2(bdea)_2(bdeaH)_2(O_2CPh)_4]$[37] ($bdeaH_2$ = N-butyldiethanolamine) in figure I.7. In the figure we see that below 4 K the *ac* susceptibilities become frequency dependent, where the $\chi'(T)$ tends to decrease and the $\chi''(T)$ increases at higher frequency. The figure I.7c and I.7d exhibits the significant frequency dependence of χ' and χ'' at different temperatures below 3 K. This behavior solely indicates the slow relaxation of magnetization in $[Mn^{II}_2Mn^{III}_2(bdea)_2(bdeaH)_2(O_2CPh)_4]$.

The temperature or frequency where χ'' reaches its maximum value corresponds to the so-called blocking temperature (T_B), or blocking frequency (ν_B) of the system respectively. Above the blocking temperature, χ'' is small and χ' resembles the *dc* magnetic susceptibility. Since T_B depends on the measurement frequency, the peak in χ'' vs. T occurs at different temperatures for different frequencies. The relaxation time (τ) can therefore be deduced from the maxima of $\chi''(T)$ and/or $\chi''(\nu)$ curves at T_B and ν_B according to the relation $\tau(T_B) = (2\pi\nu_B)^{-1}$. These τ values are plotted against the inverse of the temperature on a logarithmic scale (see inset of figure I.8b. where the solid red dots corresponds to the τ measured in *ac*). The slope of the corresponding line is a direct measurement of the thermal activation energy Δ_A for the SMM. In figure I.8 the corresponding plots of the relaxation phenomenon of the SMM $[Mn_4(hmp)_6(H_2O)_2(NO_3)_2](NO_3)_2.2.5H_2O$ (Hhmp = 2-hydroxymethylpyridine) are represented.[23f] In this SMM, the T_B is observed above 1.8 K and in this temperature range τ is temperature dependent with $\Delta_A/k_B = 20.9$ K and $\tau_0 = 6.7 \times 10^{-9}$ s.

In order to study the relaxation behavior in a larger range of temperatures, the micro-SQUID measurements[38] on a single crystal at very low temperature (below 2 K) are an effective tool. In this magnetic measurement a large *dc* field is initially applied to the system at fixed temperature to saturate the magnetization in the easy direction. Thereafter the field is switched off and the magnetization is measured as a function of time. In this way the direct current (*dc*) magnetization decay data are obtained at different temperatures. Thus the experiment is performed at multiple temperatures, but always with the same duration, which exhibits different values of magnetization at time $\tau = 0$ depending on the temperature (figure I.8a.). As the magnetic relaxation is exponentially related with time at fixed temperature, the relaxation time τ can be extracted at each experimental temperature by taking τ = t when the magnetization reaches 1/e (see Eq. I.13). Therefore the $M(t)/M_S(t = 0)$ with time plot is transformed to a $\tau(T)$ vs. $1/T$ plot (according to the Arrhenius law in Eq. I.14, signified by solid blue dots in figure I.8b) to compare with the *ac* relaxation (solid red dots in figure I.8b). Indeed at low enough temperature, a very important phenomenon in molecular magnetism, quantum tunneling of the magnetization (QTM), can be experimentally observed as it becomes faster than the thermally activated relaxation involving Δ_A (figure I.8b). The temperature where the quantum tunneling of the magnetization begins is signified as T_{QTM}.

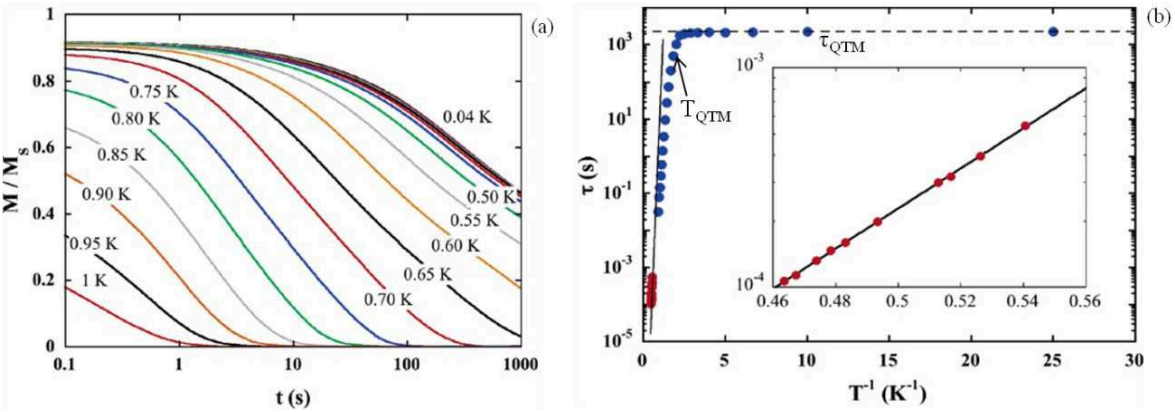

Figure. I.8. (a) Relaxation of the magnetization of $[Mn_4(hmp)_6(H_2O)_2(NO_3)_2](NO_3)_2.2.5H_2O$ at different temperatures. The data are normalized to the saturation magnetization (M_S) at 1.4 T. (b) τ vs. T^{-1} plot determined by *dc* (blue) and *ac* (red) techniques. Inset: τ vs. T^{-1} plot using *ac* data. The solid line represents the Arrhenius fit. Quantum Tunneling of Magnetization (QTM) regime is observed below T_{QTM} = 0.34 K with a characteristic time of τ_{QTM} = 2300 s (dotted line).[23f]

Origin of tunneling effect:

To explain the experiments in particular for $T < T_{QTM}$, we must introduce a more general expression of the anisotropy including transverse anisotropy E in addition to the axial anisotropy D. These terms lead to a transverse degeneracy followed by breaking of level at the crossings of m_S states (figure I.6a). The energy values of the m_S states are no longer equal, and there is a repulsion of levels called the anti-crossing, where the eigen states are mixed. The energy gap between the two states (figure I.9c) is known as tunnel gap or the tunneling splitting (Δ_{LZ}). In such an anti-crossing zone, the passage of one spin state (m_S) to another (m_S') has some probability to occur through quantum tunneling. When two m_S microstates on either side of the energy barrier have similar energies, then there is an increased probability of QTM and the population of the spin belonging to one $+m_S$ state does not need to overcome an energy barrier to move to another degenerated $-m_S$ state. Therefore spin reversal may occur from one state to another by tunneling in zero field (figure I.9a.). This tunneling is possible also in presence of an applied magnetic field, particularly when the degeneracy is observed in the m_S energy levels. Under a field when two m_S levels cross, quantum tunneling occurs, known as quantum resonant relaxation. This resonant quantum tunneling occurs at a particular field, $\mu_0 Hz^{(n)} \approx nD/(g\mu_B)$ where n is an integer (figure I.9b.).

Like classical magnets, SMMs exhibit magnetic hysteresis loops below the blocking temperatures. The form of the hysteresis curves depend on the sweep rate of the magnetic field and become wider with decreasing temperature. A series of steps are also observed in these hysteresis loops due to the effect of quantum tunneling. In figure I.9d the magnetic hysteresis loop of $[Mn_4(hmp)_6(H_2O)_2(NO_3)_2](NO_3)_2.2.5H_2O$ is shown, where the observed steps in the hysteresis loop correspond to a faster magnetization relaxation when the energy levels on opposite parts of the double-well potential are the same.[23f] In fact, QTM is the phenomena that leads the molecular magnetic

systems to relax faster than thermodynamically necessary. Part of the magnetization of the sample has relaxed by tunneling in zero field by going directly from the $m_S = -S_T$ to $m_S = +S_T$ state (figure I.9a), here in the present example it is the states $m_S = -9$ to $m_S = +9$ state (figure I.9d, denoted as $H_Z^{(1)}$). Now in the presence of an applied field H_Z (field along the z direction) the $m_S > 0$ quantum states are stabilized. For some values of H_Z (at $\mu_0 Hz^{(n)} \approx nD/(g\mu_B)$ i.e., at the resonant field) two of the m_S states of both side of potential well possess equal energy and thus QTM takes place followed by further relaxation of the spin to the minimum energy level (figure I.9b). From the hysteresis loop (figure I.9d) the quantum passage of the spin between $m_S = -9$ to $m_S = 8$ (denoted by $H_Z^{(2)}$), $m_S = -9$ to $m_S = 7$ (denoted by $H_Z^{(3)}$) and $m_S = -9$ to $m_S = 6$ (denoted by $H_Z^{(4)}$) are clearly identified. These different characteristic fields are also shown in the Zeeman diagram (figure I.9e) where we can find that the $m_S = -9$ state successively cross the $m_S = 8$, 7 and 6 states where the QTM take place.

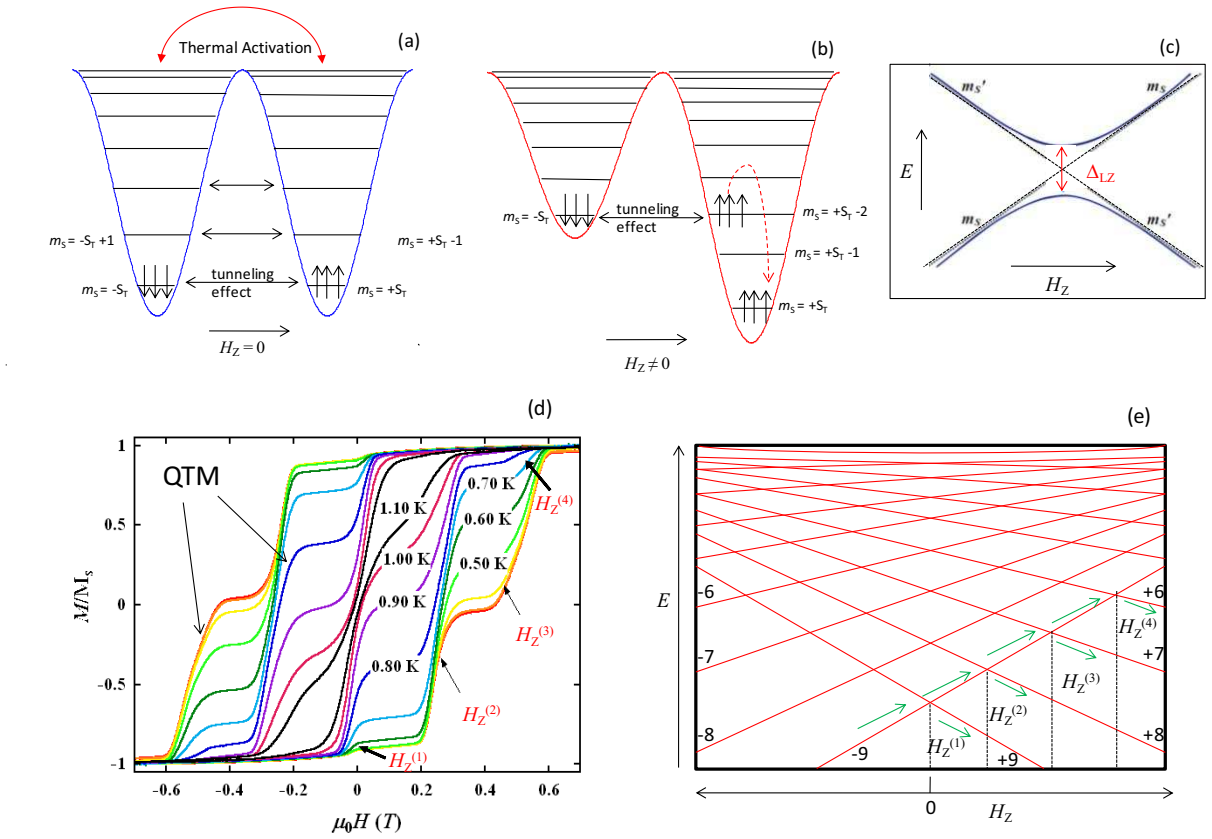

Figure I.9. (a) Schematic potential well diagram at zero field where quantum tunneling of magnetization is possible between two degenerate m_S states. (b) In the presence of field H_Z, at a certain field when $\mu_0 H_Z^{(n)} \approx nD/(g\mu_B)$ and the energy of the two new m_S states are equal quantum tunneling of magnetization occurs between the two levels. The spins follow the usual relaxation procedure to the most stable ground state (red dotted arrow). (c) the zoom of the Zeeman diagram where the m_S and the m_S' states mix in the presence of an H_Z field (d) The magnetic hysteresis loop (at 0.07 T/s sweep rate) of $[Mn_4(hmp)_6(H_2O)_2(NO_3)_2](NO_3)_2.2.5H_2O$ exhibiting steps due to QTM. (e) The Zeeman energy diagram representing the QTM effect for $[Mn_4(hmp)_6(H_2O)_2(NO_3)_2](NO_3)_2.2.5H_2O$ with spin ground state $S_T = 9$.[23f]

I.3.2. Single Chain Magnets (SCMs)

By the name single chain magnets (SCMs) are quite analogous to single molecule magnets. However, the theoretical approach to understanding SCMs is very different. These materials are composed of magnetically isolated chains, each with a finite magnetization which can be ″trapped″ in the absence of an applied magnetic field. They are able to exhibit slow relaxation of their magnetization at low temperature. In these systems, this slow relaxation is observed not for isolated anisotropic entities like SMMs, but rather for a sequence of elementary magnetic units, each carrying a spin with an anisotropic environment and strongly interacting with each other along the chain. In order to obtain an efficient SCM, the constituent anisotropic elemental units of the chain must be oriented along an easy axis of magnetization as much as possible. Thus the total uniaxial anisotropy is increased along the chain and leads to enhanced magnetic correlation which favors slow relaxation phenomena.

Chemists have synthesized a large number of quasi-one-dimensional systems, where the interactions between spins are restricted mostly to one dimension, but which usually undergo a 3D transition at very low temperatures where the weak inter-chain interactions are no longer negligible. The first experimental evidence of slow relaxation of the magnetization in a one-dimensional compound was observed in 2001 by the group of Prof. D. Gatteschi.[39] This compound consists of $[Co^{II}(hfac)_2(NITPhOMe)]$ (hfac = hexafluoroacetylacetonate, NITPhOMe = 4-methoxy-phenyl-4,4,5,5-tetramethylimidazoline-1-oxyl-3-oxide) units, where $[Co(hfac)_2]$ and the organic radical NITPhOMe are arranged alternately to form a helical chain with antiferromagnetic intrachain interactions. In 2002, an one dimensional complex was reported composed of $\{[Mn_2(saltmen)_2][Ni(pao)_2(py)_2](ClO_4)_2\}$ ($saltmen^{2-}$ = *N, N′*- (1,1,2,2 -tetramethylethylene) bis(salicylideneiminate), pao^- = pyridine-2-aldoximate and py = pyridine)[7b] repeating unit exhibiting slow magnetic relaxation dynamics and first designated by the name Single Chain Magnet. Later on numerous examples of one-dimensional complexes exhibiting SCM properties have enriched this arena.[40-46] In most cases bridging organic ligands with an oxygen or nitrogen donor have been used to develop short range interactions between the spin carriers (transition metal ions). Furthermore, counter ions and solvent molecules have played an important role in separating the individual chains and thus diminishing the interchain magnetic interactions and preserving the one dimensional magnetization.

I.3.2.1. Theoretical aspects of SCMs

Theoretically, in the case of the 1D system, only short range interactions (between the neighboring spin carriers) dominate and thus in such a system long-range magnetic order does not take

place at a finite temperature. The low temperature magnetic properties of the chain compound are strongly influenced by the extent of magnetic correlation. In 1963, R. J. Glauber described a theoretical approach toward 1D chain behavior considering chains of ferromagnetically coupled Ising spins.[47] The chain composed of $\{[Mn_2(saltmen)_2][Ni(pao)_2(py)_2](ClO_4)_2\}$ and the analogous 1D systems[7b,40] were supportive to this model. The magnetic exchange found in those 1D systems have been nicely explained adapting the theory proposed by Glauber. For such systems the chains are composed of a sequence of elementary magnetic units, each bearing a strongly interacting anisotropic spin. The Hamiltonian that describes the magnetic interactions between the elementary anisotropic magnetic units in a chain is,

$$\mathcal{H} = -2J \sum_{-\infty}^{+\infty} \vec{S}_{\mathrm{T}i,z} . \vec{S}_{\mathrm{T}i+1,z} + D \sum_{-\infty}^{+\infty} \vec{S}^2_{\mathrm{T}i,z} \qquad \textbf{Eq. I.16}$$

where S_T is the spin of repeating anisotropic entities (with D as anisotropic parameter), J is the interaction between them and $\Delta_A = |D|S_T^2$ is the anisotropy energy of one magnetic unit of the chain.

The determination of the correlation length ξ is very important for a ″Ising type″ SCM in order to estimate the extent of magnetic exchange. This parameter is intrinsic for a chain system and actually signifies the number of magnetic entities taking part in an exchange correlation; 2ξ may also be considered as the domain length in 1D magnet. Practically, these chains can not possess an infinite length due to chemical or physical defects that are always present in the crystal. Thus a nonmagnetic defect results a finite length (L) of a chain which must be considered to describe the phenomena more clearly. The magnetic correlation length ξ is a temperature dependent parameter and increases exponentially (for Ising-like one dimensional systems) with decreasing temperature. At low temperatures when $D/J > 4/3$, the large oriented domains are separated by sharp domain walls (figure I.10) and the energy necessary to create one of these domains is $\Delta_\xi = 4|J|S_T^2$. In this situation, the low temperature magnetic susceptibility is expressed as,

$$\chi T/C \approx \exp(\Delta_\xi/k_B T) \qquad \textbf{Eq. I.17}$$

where C is the effective Curie constant belonging to each magnetic entity in the chain. The value of ξ is calculated with the equivalence relation $\chi T/C \approx 2\xi/a$, where a is the unit cell parameter signifying the distance between two successive interacting magnetic centers. Thus the experimental plot of $ln(\chi T)$ as a function of $(1/T)$ will give a straight line with the Δ_ξ as the slope. In contrast when $D << J$ (Heisenberg limit), the domain walls are no longer sharp and the correlation energy becomes $\Delta_\xi \approx 4S^2\sqrt{|JD|}$.[48]

The relaxation of the magnetization for a chain is thermally dependent ($\tau = \tau_0\, exp(\Delta_\tau/k_BT)$) on both Δ_A (energy to reverse the spin direction) and Δ_ξ (energy to break the domain walls). When the physical length of the chain is higher than the magnetic correlation length (i.e., $L > 2\xi$ and the chains are designated as infinite) the total energy involved in the relaxation of magnetization, Δ_τ, is expressed as $\Delta_\tau = \Delta_A + 2\Delta_\xi$. The relaxation involves the diminution of two sides of domain walls and so $2\Delta_\xi$ is the contribution to the relaxation energy barrier (see figure I.10a). This expression is always true for any SCM at high enough temperature. With the lowering of temperature the magnetic domains (2ξ) start to expand and thus at a particular temperature $T = T^*$, a crossover occurs as $L \approx 2\xi$. When $T < T^*$, 2ξ becomes larger than L and the chains are in the finite regime. Considering the contribution of magnetic correlations in the finite chain case, the expression of the relaxation barrier becomes $\Delta_\tau = \Delta_A + \Delta_\xi$ (see figure I.12b). Therefore, in the case of narrow domain walls ($D/J > 4/3$) and for single-ion anisotropy, the expression of the relaxation time becomes,

$$\tau(T) = \tau_0.exp\left(\frac{\Delta_A + 2\Delta_\xi}{k_BT}\right) = \tau_0.exp\left(\frac{|D|S_T^2 + 8JS_T^2}{k_BT}\right) \quad \text{for infinite chain regime} \qquad \textbf{Eq.I.18}$$

and

$$\tau(T) = \tau_0.exp\left(\frac{\Delta_A + \Delta_\xi}{k_BT}\right) = \tau_0.exp\left(\frac{|D|S_T^2 + 4JS_T^2}{k_BT}\right) \quad \text{for finite chain regime} \qquad \textbf{Eq.I.19}$$

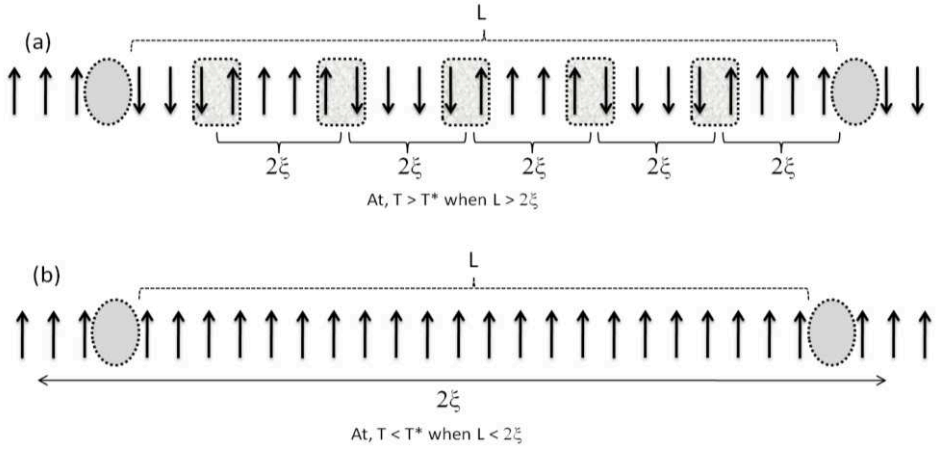

Figure I.10. Schematic diagram of the SCM on the basis of correlation length ξ, L corresponds to the physical length of chain between two successive crystal defects (signified by the gray oval); (a) infinite regime where $L > 2\xi$, and (b) finite regime where $L < 2\xi$.

The logarithmic plot of $\tau(T)$ vs. $1/T$ gives a straight line where the relaxation energy barrier Δ_τ is deduced from the slope. If the T^* of a SCM system lies within the experimentally accessible temperature region, a crossover between two straight lines is observed at T^* where the straight line with the lower slope indicates the relaxation of finite regime and the other straight line corresponds to the infinite regime.

A very nice example of an Ising-like SCM is the 1D network of $\{[Mn_2(saltmen)_2][Ni(pao)_2(py)_2](ClO_4)_2\}$ where the individual chains are well separated to exhibit unidimensional magnetization.[7b] Each chain is composed of the repeating trinuclear unit [Mn-Ni-Mn] (figure I.11), which is strongly anisotropic with total spin $S_T = 3$ ($S_{Mn} = 2$, $S_{Ni} = 1$) and the direction of total spin of all the trinuclear units is along the chain direction. The fitting (using the Heisenberg model) of the experimental magnetic susceptibility above 30 K indicates an antiferromagnetic interaction between Mn and Ni of *ca.* J/k_B = -21 K. The [Mn-Ni-Mn] trinuclear units interact ferromagnetically *via* the weak Mn-Mn ferromagnetic exchange, and the mean field approximation quantifies this interaction at *ca.* J'/k_B = 0.77 K. Above 6 K, the linear increase of $ln(\chi T)$ versus $1/T$ confirms the one dimensional nature of the system and the Ising-type anisotropy (figure I.12a).[49] From the slope of the linear region of $ln(\chi T)$ versus $1/T$ the correlation energy is deduced as $\Delta_\xi/k_B = 28$ K which is in good agreement with the inter-trinuclear interaction of J'/k_B = 0.77 K ($4S_T^2J'/k_B$ = 27.7 K). Below 5 K, the saturation of $ln(\chi T)$ versus $1/T$ is due to a crystal defect present within the magnetic correlation length ($L < 2\xi$).

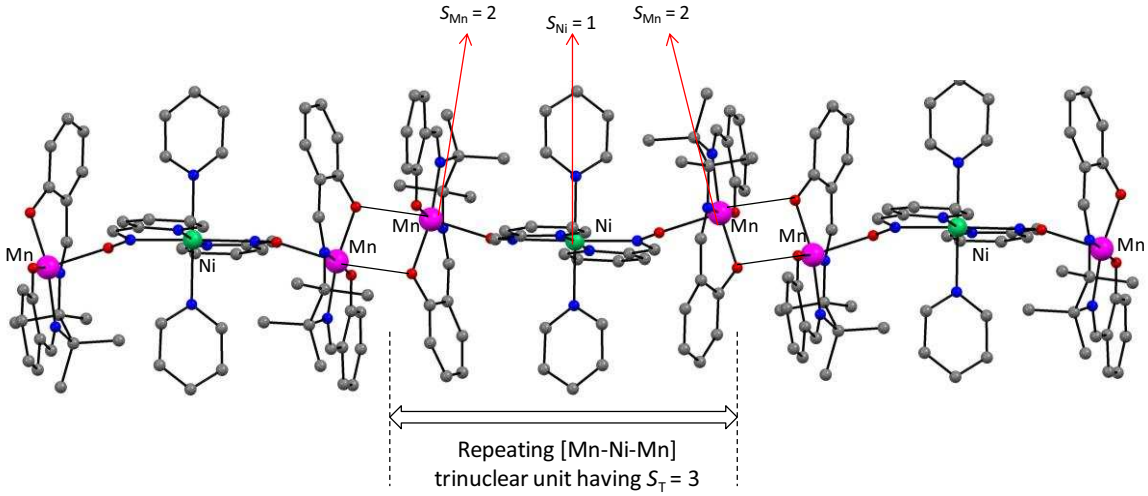

Figure I.11. One dimensional crystallographic view of the $\{[Mn_2(saltmen)_2][Ni(pao)_2(py)_2](ClO_4)_2\}$ emphasizing the repeating trinuclear unit [Mn-Ni-Mn] with total spin $S_T = 3$ ($S_{Mn} = 2$, $S_{Ni} = 1$) due to Mn^{III}-Ni^{II} strong antiferromagnetic interaction.[7b]

When the magnetic field is applied in the easy direction of a single crystal, there are large magnetic hysteresis loops with the coercive field reaching 2.75 T below 0.4 K.[40a] The relaxation time of magnetization was studied using combined *ac* measurements (temperature and frequency dependence of the *ac* susceptibility) and *dc* measurements (dependence of the magnetization with time). Both thermally activated infinite and finite regimes are observed in the Arrhenius plot of the temperature dependence of relaxation time (figure I.12b) with the crossover $T^* = 2.7$ K. Therefore the relaxation energies are found to be $\Delta_{\tau 1}/k_B = 74$ K ($\tau_0 = 3.5\times10^{-11}$ s) for the infinite regime, and $\Delta_{\tau 2}/k_B$ =

55 K (τ_0 = 2.5×10^{-8} s) for the finite regime. These relaxation energy barriers yield the anisotropy energy Δ_A/k_B = 23 K when Δ_ξ/k_B = 28 K.

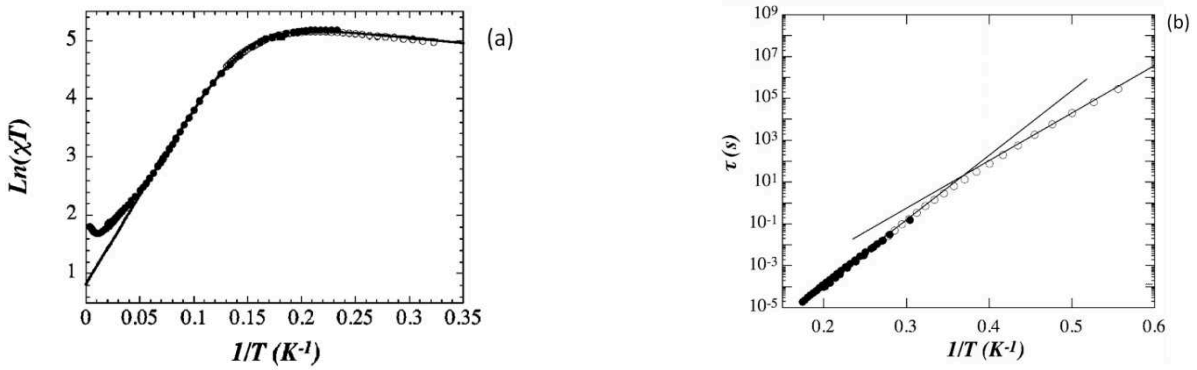

Figure I.12. (a) Semilog plot of $ln(\chi T)$ vs. $1/T$ (χ is given in emu/mol). The full and open dots were obtained from *ac* and *dc* measurements, respectively. Solid lines correspond to the fit with the equation $\chi T/C \approx \exp(\Delta_\xi/k_B T)$, and the straight line region indicates the linear correlation in Ising limit. (b) Semilog plot of the relaxation time τ vs. $1/T$. The full and open dots were obtained from *ac* and *dc* measurements, respectively. The temperature corresponding to the crossover (T*) of the two straight line represents the critical temperature of the system (where L ≈ 2ξ).

I.3.2.2. Influence of magnetic phase transition on SCMs

In order to obtain an ideal SCM system the inter-chain magnetic interaction should be absent in all temperature ranges; but in practice this aim is not easy to achieve. Often at low temperature inter-chain antiferromagnetic interactions are present and thus leads to an antiferromagnetic ground state of the system. Consequently, in such compounds a paramagnetic to antiferromagnetic phase transition is possible with metamagnet type behavior. A field/temperature (T, H) phase diagram can be constructed to investigate the ordered phase. Slow relaxation of the magnetization can still be observed in the antiferromagnetic phase, with a maximum relaxation time close to the antiferromagnetic-paramagnetic phase transition.[50] Therefore, such an ordered state is an important element towards the design of high temperature molecular magnets using SCM-based materials and could be generalized to other slow relaxing systems like SMMs.

I.4. Chemical aspects of molecule based magnets

In order to obtain molecule based magnets we need to consider the nature of two chemical entities: the magnetic centers i.e., the metals with unpaired electrons, and ligands which will connect the metal centers and promote the magnetic interactions. The *f* and *d* block transition metals with

unpaired electrons in a high spin ground state are attractive in conception of molecule based magnetic materials. For example, manganese with its multiple oxidation states and high spin ground states serves as one of the leading elements to synthesize molecule based magnets especially SMM and SCM compounds.[4,20-30] Chelating ligands and bridging ligands having N, O, S etc donor atoms centers, as well as halido (Cl, Br, F etc) bridges are largely used to organize the metal centers to form of SMMs or SCMs. For example, in the previously-discussed SMM Mn_{12}-Ac (figure I.5a) the oxido donors belonging to the chelating acetate help to associate the twelve manganese ions (four Mn^{IV} of $S = 3/2$ and eight Mn^{III} of $S = 2$) giving $S_T = 10$.[4] In the $[Mn_4(hmp)_6]^{4+}$ SMM family, the pyridine nitrogen atoms and the alcoholic oxygen atoms of the hmp ligand bind the four individual magnetic centers (two Mn^{II} of $S = 5/2$ and two Mn^{III} of $S = 2$) to form a complex with $S_T = 9$ (see figure I.13a).[22]

Single chain magnet compounds are obtained by binding the magnetic centers chemically in one dimension. Therefore bridging ligands like azido (N_3^-), cyanido (CN^-), thiocyanido (SCN^-), halido and some others play a very important role in organizing the metal centers in one dimension. Furthermore this kind of bridging ligand also can arrange preformed SMMs in one dimension when the SMM possesses a suitable ligand substitutable site, for example the azido bridged Mn_4 SMM[51] where the two Mn^{II} have an available coordination site to accept electron density from azido bridge. Two and three dimensional arrangements of Mn_4 SMMs are also possible with other suitable linkers dicyanamide or from a reaction with $[Pt^{III}(mnt)_2]^{2-}$ moiety.[52] In the figure I.13b, an one dimensional arrangement of the $[Mn_4(hmp)_6(MeCN)_2]^{4-}$ through $[Pt(mnt)_2]^{n-}$ units is shown.

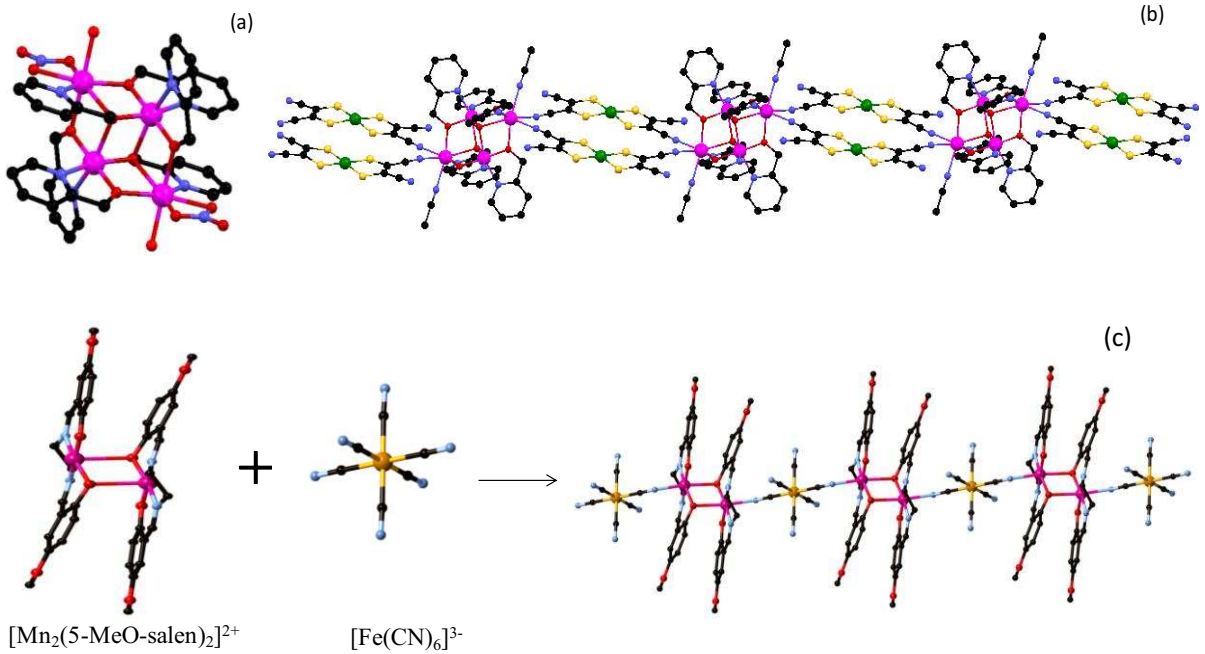

Figure I.14. (a) The crystal structure of $[Mn_4(hmp)_6(NO_3)_2(H_2O)_2]$ where hmp^- and the NO_3^- act as the chelating ligands. (b) The one dimensional arrangement of the Mn_4 SMM in one dimension through the $[Pt(mnt)_2]^{n-}$ anions.[52c] (c) Crystal structure view of $(Et_4N)[Mn_2(5\text{-MeO-salen})_2Fe(CN)_6]$. In all these structures the pink, orange, red, blue, black and green atoms are the manganese, iron, oxygen, nitrogen, carbon and platinum atoms. The hydrogen atoms are removed for clarity.[53]

Besides these diamagnetic bridging ligand and building block, some paramagnetic molecules with suitable donor atoms can organize SMMs in one dimension towards the formation of SCMs. In the already discussed example of the SCM $[Mn_2(saltmen)_2][Ni(pao)_2(py)_2](ClO_4)_2$[7b] the $[Mn_2(saltmen)_2]^{2+}$ moiety itself has SMM properties with $S_T = 4$ ground state[20] and $[Ni(pao)_2(py)_2]$ is an $S = 1$ paramagnetic building block having oximato donor atoms available on the ligand pao^-. Two oximato oxido groups of pao^- coordinate to the axial position of two $[Mn_2(saltmen)_2]^{2+}$ resulting in the alternative arrangement of $[Mn_2(saltmen)_2]^{2+}$ and $[Ni(pao)_2(py)_2]$ in one dimension. In the SCM, $(Et_4N)[Mn_2(5\text{-MeO-salen})_2Fe(CN)_6]$, the $[Mn_2(5\text{-MeO-salen})_2]^{2+}$ SMM alternates with the $[Fe(CN)_6]^{3-}$ building block through the cyanido bridging between Mn^{III} and Fe^{III} centres (figure I.13c).[53]

The nature and magnitude of the magnetic interaction in a molecule based magnet solely depend on the mutual distances, orbital overlaps and orientations of the magnetic centres. Therefore we always look for chelating or bridging ligands which are capable to keeping the magnetic centres sufficiently close to one another in order to promote the strong magnetic exchange through the super exchange phenomenon. Consequently, oxido bridges between metal centres are very common in molecule based magnetic materials, as there is only one atom (oxygen) between the two magnetic centres.

Hetero-bimetallic one dimensional system would be expected to yield to SCMs with a ferromagnetic arrangement, when the two metals have different spins. In order to obtain heterometallic coordination systems, both zero or one dimension, we should select the bridging ligands that have different coordination environment at the two sites. In this context the cyanido group is one of the widely used bridging ligands. The cyanido group is also very useful for the synthesis of molecule based magnets due to its linearity and strong coordination capacity with different binding modes that help to promote strong magnetic coupling. In the present thesis, we have extensively used cyanido group to bridge the magnetic centres, so we now turn our attention to the nature of the magnetic exchange through the cyanido bridge.

Cyanido bridges as potential mediators for magnetic exchange

Ever since the mixed valence complex Prussian blue, $Fe^{III}_4[Fe^{II}(CN)_6]_3$, was found by a Berlin painter in 1704,[54] the chemistry of cyanido-bridged complexes has grown to be a major research effort in coordination chemistry. Over the years, scientists have utilized the structural rigidity and predictability of the cyanido ligand to create numerous structure types, including multinuclear cyanido-bridged complexes [55,56] and extended solids exhibiting one-, two-, and three-dimensional frameworks.[57] Accordingly, the cyanido ligand has shown an excellent ability to mediate magnetic superexchange, strongly influencing the properties of molecule based magnets.

One of the key characteristics of the cyanido group is its ability to link two different metal ions when acting as a bridge, a quality which is related to its asymmetric character. The π* anti bonding orbital of cyanido is mainly involved in the magnetic exchange interaction.[55a, 58] The mode of metal-metal interactions through the cyanido mediator is based on the symmetry of the orbitals containing the unpaired metal electrons. Assuming an octahedral coordination geometry for both metal centers connected by a cyanido ligand, unpaired electrons in orbitals of compatible symmetry (t_{2g} + t_{2g} or e_g + e_g) will couple the metal ion spins antiferromagnetically, while those in orthogonal orbitals (t_{2g} + e_g) will couple then ferromagnetically. The strength of the exchange interaction depends critically upon the degree of overlap between the metal- and cyanido-based orbitals. When the radially-extended *d* orbitals of low-valent early transition metals are involved the extent of magnetic exchange is high. Antiferromagnetic exchange is typically stronger than the ferromagnetic interaction, and dominates the superexchange in a competitive situation. In figure I.14, a scheme demonstrates the orbital overlap of transition metals through cyanido ligand.

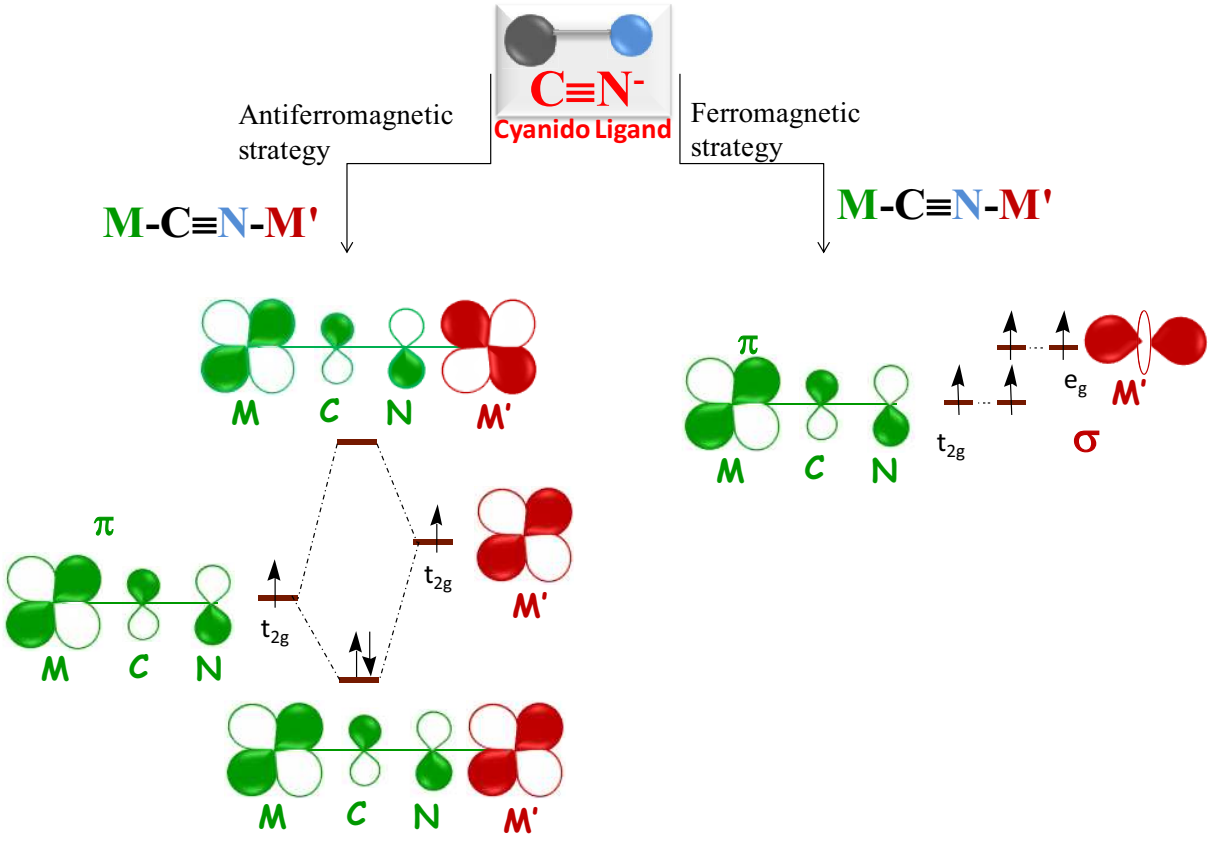

Figure I.14. Schematic diagram of orbital interactions across a bridging cyanido ligand is shown giving rise to magnetic superexchange. The t_{2g} orbitals interact through cyanido π* orbitals due to the symmetry compatibility, resulting in antiferromagnetic coupling. In case is the ferromagnetic coupling the unpaired electrons of e_g orbitals are overlapped orthogonally through a σ bond due to the symmetry incompatibility.[55a]

For example, between $Ni^{II}(t_{2g}^6 e_g^2)$ and $Cr^{III}(t_{2g}^3 e_g^0)$, ferromagnetic coupling is expected to arise from t_{2g}^3–e_g^2 interaction, whereas $Cr^{III}(t_{2g}^3 e_g^0)$ and $Mn^{II}(t_{2g}^3 e_g^2)$ interacts antiferromagnetically through

the cyanido bridge via a t_{2g}^3–t_{2g}^3 interaction, which is stronger than the t_{2g}^3–e_g^2 ferromagnetic interaction. In the SCM, $(Et_4N)[Mn_2(5\text{-MeO-salen})_2Fe(CN)_6]$,[53] the $Mn^{III}(t_{2g}^3 e_g^1)$ ion couples ferromagnetically with the low spin $Fe^{III}(t_{2g}^5 e_g^0)$.

The hexacyanidometallates based on transition metal ions, $[M(CN)_6]^{3-}$ (M = Fe^{III}, Mn^{III}, Cr^{III}, Ru^{III}, Os^{III}, Mo^{III} etc) have played a very important role in the preparation of a variety of molecule based magnets, including SMMs and SCMs.[53,59] Recently our group in collaboration with Hitoshi Miyasaka has reported a series of SCMs based on Mn^{III}-Schiff bases and 3*d* metal hexacyanido building block with the general molecular formula $[Mn^{III}(5\text{-TMAMsalen})M^{III}(CN)_6]\cdot 4H_2O$ (M = Fe, Mn, Cr, and 5-TMAMsalen^{2-} = *N, N'*- ethylenebis (5-trimethylammoniomethylsalicylideneiminate), see figure I.15).[70] There also exists many more penta, tetra and tri cyanido based paramagnetic building blocks of 3*d* transition metals like $[Fe^{III}(1,Me\text{-imidazole})(CN)_5]^{2-}$,[60a] $[M^{III}(L)(CN)_4]^-$ (M = Fe and Cr , L = bipy, phen etc),[60d,61d] *mer* or *fac*-$[Fe^{III}(L)(CN)_3]$ [60c] (L = a tridentate capping ligands, other tridentate ligand like bpca, Tp etc) which produced a variety of magnetic coupling in the molecules.[60,61]

The 4*d* and 5*d* metal ions like $Mo^{III/V}$, $Re^{III/IV}$, $W^{III/IV}$, Nb^{IV} etc has higher ionic radius and therefore they can exhibit more than six coordination number. So some other cyanido based paramagnetic units like $[Mo^{III}(CN)_7]^{4-}$,[61] $[Re^{IV}(CN)_7]^{3-}$,[62] $[Mo^{V}(CN)_8]^{3-}$,[63] $[W^{V}(CN)_8]^{3-}$,[64] $[Nb^{IV}(CN)_8]^{4-}$,[65] etc are also exhibited variety of interesting magnetic properties when they are used are molecular precursors for different magnetic materials. In order to synthesise preferably the one dimensional magnetic systems the use of *cis*- or *trans*-dicyanidometallate systems are more chemically convenient to control over the direction of the cyanido coordination. In his context, molecular precursors like *cis*-$[Fe^{III}(bpy)_2(CN)_2]^+$,[66] *trans*-$[Ru^{III}(acac)_2(CN)_2]^-$,[67] *trans*-$[M^{III}(salen)(CN)_2]^-$ (M = Ru, Os),[68] *trans*-$[Re^{IV}Cl_4(CN)_2]^{2-}$,[57(r)] are also found in the literature. One of the advantages of the use of the cyanidometallate based molecular precursors is their stability in solution and also they are quite preventive towards the redox phenomena in solution. But the literature implies that the control over the chemistry of 4*d* and 5*d* based cyanometallates is more complex than the 3*d* one. Many of the heavy metal cyanido complexes are sensitive to the external influences like oxygen, water, temperature, light etc. For example, a trace amount of oxygen can oxidize the metal ions of the $[Mo^{III}(CN)_6]^{3-}$ to Mo^{IV}, the aqueous solution of $[Ru^{III}(CN)_6]^{3-}$ are prone to reduce into $[Ru^{II}(CN)_6]^{4-}$ which is diamagnetic.

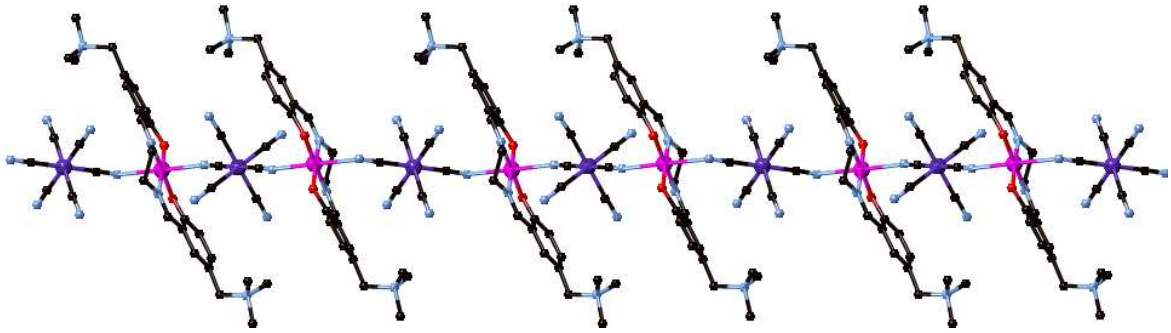

Figure I.15. The $[M^{III}(CN)_6]^{3-}$ (M = Fe, Cr, Mn) and Mn^{III}-Schiff base based SCMs where the pink, black, blue, red and violet atoms are the Mn, C, N, O and M. the hydrogen atoms are not displayed for clarity.[70]

4d and 5d transition metal ions in molecule based magnetic materials:

The comparative study of molecule based magnetic materials reveals that the heavier metal ions possessing 4*d* and 5*d* unpaired electron significantly contribute to the magnetic properties of paramagnetic compounds.[69a] Enhanced magnetic interactions are expected for heavier transition metal ions due to the greater diffuseness of the *4d* and *5d* orbitals when compared to the 3*d* ones, and these characteristics also result in a greater amount of spin-orbit coupling. One of the most important characteritics of the *4d* and *5d* based molecular species is their high degree of magnetic anisotropy. In such materials the genesis of this anisotropy is not only the influence of the ligand field on the metal ions but also the local anisotropy arising from the metal ion itself.[69] Therefore the *g* factor of 4*d* and 5*d* based molecular species is strongly anisotropic as well followed by high values of uniaxial anisotropy *D*. As we already discussed, in molecule based magnets like SMMs and SCMs we always try to enhance the higher uniaxial anisotropy in order to obtain high blocking temperature (T_B). In this context the 4*d* and 5*d* based molecular precursors undoubtedly have a strong impact in the synthesis of SMM and SCMs.

In the present research work, we have synthesized compounds with 3*d*-4*d* and 3*d*-5*d* heterometallic magnetic exchanges through cyanido bridge. The 3*d* metals, that we used, are Mn^{III} ($3d^4$, $S = 2$), Mn^{II} ($3d^5$, $S = 5/2$), Fe^{II} ($3d^6$, $S = 2$), Ni^{II} ($3d^8$, $S = 1$) and Cu^{II} ($3d^9$, $S = ½$) as the electron acceptor ions from the *trans*-cyanido-M complexes (M = Ru^{III} ($4d^5$ metal) and Re^{IV} ($5d^3$ metal)).

The Mn^{III} are widely used in this research work as the Mn^{III}-Schiff base molecular precursor using $salen^{2-}$ type tetradentate Schiff bases, where all of the four equatorial coordination sites of Mn^{III} ion is occupied by the nitrogen and the oxygen atoms originated from the Schiff base ligands. The axial positions possess the solvents, suitable for the substitution by the cyanido group. Due to such ligand field effect the crystal field of this octahedral coordinated Mn^{III} ions experience remarkable axial elongation (Jahn- Teller effect) which results to the generation of high anisotropy in the Mn^{III}-

Schiff base unit and the easy axis of the magnetisation is the Jahn-Teller axis. When the Mn^{III}-schiff base complexes is in the dinuclear form the two Mn^{III} experiences a weak ferromagnetic interaction resulting a molecule of $S_T = 4$ ground state and itself behave as a SMM; the easy axes of both of the Mn^{III} are mutually parallel which introduce a better uniaxial anisotropy to the dimer. In this molecule the one of the axial positions are still free to display the substitution through cyanido ligand.[20, 7a, 53] In the chapter II we have discussed about the properties of these Mn^{III} precursors.

The Ni^{II}, Cu^{II}, Mn^{II} and Fe^{II} ions are used as the $[M(macrocycle)]^{2+}$ ($M = Ni^{II}$, Cu^{II}, Mn^{II}, Fe^{II}) where the metal ions reside in the cavity of the macrocyclic ligands and the N and O atoms coming from the macrocyclic ligand help to fulfil the equatorial coordination sites of the metal ion. Thus the axial coordination sites of the $[M(macrocycle)]^{n+}$ moiety can exhibit suitable substitution through the cyanido ligand.

Reasonably, as we have discussed earlier, the cyanido based molecular precursors that we used throughout the entire research work of this thesis contains 4*d* and 5*d* metal ions. Therefore, in the present thesis we have focussed on two *trans*-cyanido building block: *trans*-$[Ru^{III}(salen)(CN)_2]^-$ [68a] where the Ru^{III} is a low spin $4d^5$ metal ion ($S = ½$) and *trans*-$[Re^{IV}Cl_4(CN)_2]^{2-}$ [57r] where the Re^{IV} is a $5d^3$ metal ions ($S = 3/2$). These anisotropic building blocks are extensively used in our research to coordinate with the axial positions of the above mentioned 3*d* metal based molecular precursors through the cyanido bridge. In these building blocks the carbon atoms are coordinated with the 4*d*/5*d* metal ions and therefore the nitrogen end of the cyanido ligand can donate electron density to the 3*d* metal ions of the above mentioned precursors. Also we have synthesized *trans*-$[Ru^{III}$(5-Cl-saltmen)$(CN)_2]^-$ building block analogous to *trans*-$[Ru^{III}(salen)(CN)_2]^-$ adapting similar method.

The chapter II of this thesis contains more details about the purpose of choosing the above mentioned *d*-block transition metal ions. The properties and characterization of these compounds are also discussed extensively in chapter II. During our research work we have also synthesized the $[Re^{IV}Cl_4(CN)_2]^{2-}$ building block, which also made cyanido bridged compounds (discussed in the Annex) with the Mn^{III}-Schiff base complexes.

I.5. Motivation behind this research work

The design, synthesis and study of molecule based magnets with various properties are the main objectives of our research group. In the literature one can find that the synthesis of various SMMs and their characterization has been extensively done. Therefore one of our ambitions to contribute to the field of molecular magnets is to organize SMMs in one dimension via paramagnetic

linkage leading to SCMs properties. Additionally, another goal is to find new heterometallic one dimensional and molecular (zero dimensional) systems with interesting magnetic characteristics.

Throughout the discussion in this chapter, it is very clear that the estimation of magnetic exchange between two successive magnetic centers is one of the most important information to understand in these molecule based magnet systems. As discussed earlier, the cyanido ligand is a very efficient unit to preserve heterometallic strong magnetic coupling with the predictable coordination behavior. Therefore in our synthesis of magnetic materials we have exclusively used cyanido as a bridging ligand.

In the present thesis, the goal is to use *trans*-cyanido transition metal building blocks with high anisotropy as paramagnetic linkers to organize SMMs and other metal-organic moieties in one dimension followed by their magnetic characterization. On the other hand, we have also synthesized some new cyanido-bridged heterometallic molecules in addition to the one dimensional systems.

The chemical strategy behind the design of such systems involves simple donor-acceptor coordination chemistry, which is mostly performed at ambient temperature using organic solvents and water. The *trans*-cyanido metal building blocks, *trans*-$[Ru^{III}(salen)(CN)_2]^-$ and *trans*-$[Re^{IV}Cl_4(CN)_2]^{2-}$ play the role of the donor moiety via the nitrogen donor site on the cyanido ligand; whereas the other 3*d* metal-organic precursors or SMMs (mononuclear and the dinuclear Mn^{III}-Schiff bases, $M(macrocycle)]^{n+}$ where M = Ni^{II}, Cu^{II}, Fe^{III}; macrocycle = cyclam, cyclic-LN_3O_3; n = 2 or 3) reside in the acceptor class with easily substitutable coordination sites on the metal centers.

In chapter II the detailed introduction to the molecular precursors is given along with the reasoning behind their selection and the selection of reaction schemes. Chapter II also contains a few literature examples of the molecular precursors we have used in our research work, supportive to our idea to use them as the building block of molecule-based magnets. Chapter III and chapter IV contain the discussion of the synthesis, structure and magnetic properties of the compounds prepared using the *trans*-$[Re^{IV}Cl_4(CN)_2]^{2-}$ building block. In the chapter III we will discuss about the Mn^{III}-Re^{IV} systems which have variety of complexes: Mn^{III}/Re^{IV} salts without cyanido bridge, and with cyanido bridge few Mn^{III}-Re^{IV}-Mn^{III} trimers, an phenoxido bridged pair of Mn^{III}-Re^{IV}-Mn^{III} trimer and one dimensional $Mn^{III}{}_2Re^{IV}$ polymers. Chapter IV contains the story of Re^{IV}-M^{II}(macrocyclic) (M = Ni^{II}, Cu^{II}, Mn^{II}, Fe^{II}) one dimensional compounds having significantly different magnetic properties. The compounds synthesized using the *trans*-$[Ru^{III}(salen)(CN)_2]^-$ and the Mn^{III}-Schiff base precursors are illustrated in the chapter V. The characterization of all new magnetic materials will be thoroughly described in all those chapters. At the end of the each chapter one conclusive section is added as a brief summary of the chapter which also contains the difficulties and limitations we faced during the synthesis of the heterometallic compounds.

In this thesis our ambition is not only to enrich the arena of molecular magnetism with new magnetic materials, but also to illustrate future perspective towards enhanced molecular magnets. Therefore in the "General Conclusion and Future Perspectives" part, we will discuss many possibilities. At the end of the thesis we have added an annexed part to discuss some by-products/new materials that we have obtained during the research work. This annexed part of the thesis contains the note of the compounds having partial characterizations, problems of reproducibility, or discovered as an undesired byproduct of a reaction.

I.6. References

[1] V. Skumryev, S. Stoyanov, Y. Zhang, G. Hadjipanayis, D. Givord, J. Nogués, *Nature*, **2003,** 423, 850.

[2] D. W. Bruce, D. O'Hare, R. I. Walton, *Molecular Materials*, Inorganic Materials Series, John Wiley and Sons, UK, **2010**.

[3] (a) D. Gatteschi, R. Sessoli, J. Villain, *Molecular Nanomagnets*, Oxford University Press, **2006**. (b) O. Kahn, *Molecular Magnetism*, VCH, New York, **1993**.

[4] R. Sessoli, D. Gatteschi, A. Caneschi, M. A. Novak, *Nature*, **1993**, 365, 141.

[5] (a) E. Coronado, K. R. Dunbar, *Inorg. Chem.*, **2009**, 48, 3293 and references therein. (b) O. Kahn, *Acc. Chem. Res.*, **2000**, 33, 10, 647. (c) R. Sessoli, A. K. Powell, *Coord. Chem. Rev.*, **2009**, 253, 2328. (d) D. Gatteschi, *Adv. Mater.* **1994,** 6, 9, 635.

[6] (a) A. Caneschi, D. Gatteschi, R. Sessoli, A. L. Barra, L. C. Brunel, M. Guillot *J. Am. Chem. Soc.*, **1991**, 113, 5873. (b) R. Sessoli, H. L. Tsai, A. R. Schake, S. Y. Wang, J. B. Vincent, K. Folting, D. Gatteschi, G. Christou, D. N. Hendrickson *J. Am. Chem. Soc*., **1993,** 115, 1804. (c) G. Christou, D. Gatteschi, D. N. Hendrickson, R. Sessoli, *MRS Bull*., **2000**, 25, 66. (d) M. N. Leuenberger, D. Loss, *Nature*, **2001**, 410, 789. (e) G. Aromí, E. K. Brechin. *Struct. Bond.*, (Berlin), **2006**, 122: 1-69 and references therein. (f) J. D. Rinehart, J. R. Long, *Chem. Sci.*, **2011**, 2, 2078.

[7] (a) C. Coulon, H. Miyasaka, R. Clérac, *Struct. Bond.*, **2006**, 122, 163-206. (b) R. Clérac, H. Miyasaka, M. Yamashita, C. Coulon, *J. Am. Chem. Soc.*, **2002**, 124, 12837.

[8] (a) S. Decurtins, P. Gütlich, C. P. Köhler, H. Spiering, *Chem. Phys. Lett*., **1984**, 105, 1. (b) O. Sato, T. Iyoda, A. Fujishima, K. Hashimoto, *Science*, **1996**, 272, 704. (c) S. i. Ohkoshi, K. Imot, Y. Tsunobuchi, S. Takano, H. Tokoro, *Nature Chemistry*, **2011**, 3, 564.

[9] (a) O. Kahn, (ed.) *Magnetism: A supramolecular function*, NATO ASI Series C (Dordrecht: Kluwer), **1996,** Vol. 484. (b) W. Wernsdorfer, N. Aliaga-Alcalde, D. N. Hendrickson, G. Christou, *Nature*, **2002**, 416, 406.

[10] (a) Y. Molard, A. Ledneva, M. Amela-Cortes, V. Cıfcu, N. G. Naumov, C. Mériadec, F. Artzner, S. Cordier, *Chem. Mater*, **2011**, 23, 5122. (b) E. Terazzi, C. Bourgogne, R. Welter, J.-L. Gallani, D. Guillon, G. Rogez, B. Donnio, *Angew. Chem. Int. Ed*., **2008**, 47, 490. (c) R. Chico, C. Domınguez, B. Donnio, S. Coco, P. Espinet, *Dalton Trans*., **2011**, 40, 5977.

[11] (a) C. Train, R. Gheorghe, V. Krstic, L. M. Chamoreau, N. S. Ovanesya, G. L. J. A. Rikken, M. Gruselle, M. Verdagure, *Nat. Matter*., **2008**, 7, 729. (b) G. L. J. A. Rikken, E. Raupach, *Nature*, **1997**, 390, 493. (c) G. L. J. A. Rikken, E. Raupach, Nature, **2000**, 405, 932. (d) G. L. J. A. Rikken, E. Raupach, *Phys. Rev. E,* **1998**, 58, 5081. (d) E. Coronado, C. J. Gómez-García, A. Nuez, F. M. Romero, J. C. Waerenborgh, *Chem. Mater.*, **2006**, 18, 2670.

[12] (a) A. Kobayashi, H. Kobayashi, *Charge Transfer Salts, Fullerenes and Photoconductors* in: H. S. Nalwa Ed., Handbook of Conductive Molecules and Polymers, vol. 1, Wiley, Chichester, **1997**. (b) C. Rovira, *Chem. Rev.*, **2004**, 104, 5289. (c) L. Valade, D. De Caro, M. Basso-Bert, I. Malfant, C. Faulmann, B. G. De Bonneval, J.-P. Legros, *Coord. Chem. Rev*., **2005**, 249, 1986. (d) R. Llusara, C. Vicent, *Coord. Chem. Rev*., **2010**, 254, 1534. (e) E. Coronado, P. Day, *Chem. Rev.*, **2004**, 104, 5419.

[13] (a) E. Sinn, G. Sim, E. V. Dose, M. F. Tweedle, L. J. Wilson, *J. Am. Chem. Soc.*, **1978**, 100, 3375. (c) M. F. Tweedle, L. J. Wilson, *J. Am. Chem. Soc.*, **1976**, 98, 4824. (c) H. Kobayashi, A. Kobayashi, P. Cassoux, *Chem. Soc. Rev.*, **2000**, 29, 325.

[14] (a) J. Krober, E. Codjovi, O. Kahn, F. Groliere , C. Jay, *J. Am. Chem. Soc.*, **1993**, 115, 9810. (b) S.-I. Ohkoshi, K. Imoto, Y. Tsunobuchi, S. Takano, H. Tokoro, *Nature Chemistry*, **2011**, 3, 564. (c) A. B. Gaspar, V. Ksenofontov, M. Seredyuk, P. Gütlich, *Coord. Chem. Rev*., **2005**, 249, 2661. (d) J. A. Real, A. B. Gaspar, V. Niel, M. C. Muñoz, *Coord. Chem. Rev*., **2003**, 236, 121.

[15] (a) C. Mathonière , S. G. Carling, D. Yusheng, P. Day, *J. Chem. Soc. Chem. Commun*., **1994**, 1551. (b) A. Kumar, S. M. Yusuf, L. Keller, J. V. Yakhmi, *Phys. Rev. Lett.*, **2008**, 101, 207206. (c) S. A. Chavan, R. Ganguly, V. K. Jain, J. V. Yakhmi. *J. Appl. Phys.*, **1996**, 79, 5260.

[16] (a) K. Hashimoto, S. Ohkoshi., *Philos. Trans. R. Soc. London.*, **1999**, A357, 2977. (b) M. D. Sastry, M. K. Bhide, R. K. Kadam, S. A. Chavan, J. V. Yakhmi, O. Kahn, *Chem. Phys. Lett.*, **1999**, 301, 385. (c) D. A. Pejakovic, C. Kitamura, J. S. Miller, A. J. Epstein, *Phys. Rev. Lett*., **2002**, 88, 057202.

[17] (a) J. S. Miller, A. J. Epstein, *Angew. Chem. Int. Ed.*, **1994**, 33, 4, 385. (b) F. Xu, C. M. Wu, V. Rengarajan, T. D. Finley, H. O. Keles, Y. Sung, B. Li, U. A. Gurkan, U. Demirci, *Adv. Mater.*, **2011**, 23, 4254. (c) E. Chelebaeva, J. Larionova, Y. Guari, R. A. Sa´Ferreira, L. D. Carlos, F. A. Almeida Paz, A. Trifonov, C. Guérin, *Inorg. Chem*., **2008**, 47, 775. (d) H.-B. Duan, X.-M. Ren, L.-J. Shen, W.-Q. Jin, Q.-J. Meng, Z.-F. Tian, S.-M. Zhou, *Dalton Trans.*, **2011**, 40, 3622.

[18] (a) R. L. Carlin. *In Magnetochemistry*. Springer-Verlag, New York, **1986**. (b) F. E. Mabbs, D. J. Machin, *Magnetism and Transition Metal Complexes*, Chapman and Hall, **1973**. (c) C. Kittel, *Introduction to Solid State Physics, 2*nd *Ed*., J. Wiley and Sons, New York, **1953**. (d) R. Boča, *Theoretical foundations of molecular magnetism*, *1*st *Ed*., Elsevier Science, **1999**.

[19] (a) C. Kittel, *Introduction To Solid State Physics*, *7th Ed.*, John Wiley & Sons, Inc., New York **1996**, p- 422-423. (b) C. Kittel, *Introduction To Solid State Physics*, *7th Ed*., John Wiley & Sons, Inc., New York **1996**, p- 444. (c) T Moriya, *Magnetism I*, Academic Press, New York and London, **1963**, p- 85.

[20] (a) H. Miyasaka, R. Clérac, W. Wernsdorfer, L. Lecren, C. Bonhomme, K. Sugiura, M. Yamashita, *Angew. Chem. Int. Ed.*, **2004**, 43, 2801. (b) H. Miyasaka, R. Clérac, T. Ishii, H. Chang, S. Kitagawa, M. Yamashita, *J. Chem. Soc. Dalton Trans.*, **2002**, 1528.

[21] (a) R. Inglis, L. F. Jones, G. Karotsis, A. Collins, S. Parsons, S. P. Perlepès, W. Wernsdorfer, E. K. Brechin, *Chem. Commun.*, **2008**, 5924. (b) R. Inglis, L. F. Jones, C. J. Milios, S. Datta, A. Collins, S. Parsons, W. Wernsdorfer, S. Hill, S. P. Perlepès, S. Piligkos, E. K. Brechin, *Dalton Trans*., **2009**, 3403. (c) R. Inglis, A. D. Katsenis, A. Collins, F. White, C. J. Milios, G. S. Papaefsthiou, E. K. Brechin, *Cryst. Eng. Comm*., **2010**, 12, 2064.

[22] (a) S. M. J. Aubin, N. R. Dilley, M. W.Wemple, M. B. Maple, G. Christou, D. N. Hendrickson, *J. Am. Chem. Soc.*, **1998**, 120, 839. (b) S. M. J. Aubin, N. R. Dilley, L. Pardi, J. Krzystek, M. W. Wemple, L.-C. Brunel, M. B. Maple, G. Christou, D. N. Hendrickson, *J. Am. Chem. Soc.*, **1998**, 120, 4991. (c) S. Wang, K. Folting, W. E. Streib, E. A. Schmitt, J. K. McCusker, D. N. Hendrickson, G. Christou, *Angew. Chem. Int. Ed.*, **1991**, 30, 305. (d) L. Lecren, Y. G. Li, W. Wernsdorfer, O. Roubeau, H. Miyasaka, R. Clérac, *Inorg. Chem. Commun.*, **2005**, 8, 626.

[23] (a) O. Roubeau, R. Clérac, *Eur. J. Inorg. Chem*., **2008**, 4325. (b) E.-C. Yang, N. Harden, W. Wernsdorfer, L. Zakharov, E. K. Brechin, A. L. Rheingold, G. Christou, D. N. Hendrickson, *Polyhedron*, **2003**, 22, 1857. (c) M. W. Wemple, D. M. Adams, C. J. Adams, K. Folting, D. N. Hendrickson, G. Christou, *J. Am. Chem. Soc*., **1995**, 117, 7275. (d) N. Aliaga-Alcalde, R. S. Edwards, S. O. Hill, W. Wernsdorfer, K. Folting, G. Christou, *J. Am. Chem. Soc*., **2004**, 126, 12503. (e) D. Li, H. Wang, S. Wang, Y. Pan, C. Li, J. Dou, Y. Song, *Inorg. Chem*., **2010**, 49, 3688. (f) L. Lecren, W. Wernsdorfer, Y. G. Li, O. Roubeau, H. Miyasaka, R. Clérac, *J. Am. Chem. Soc*., **2005**, 127, 11311.

[24] (a) B. S. Tsukerblat, A. V. Palii, S. M. Ostrovsky, S. V. Kunitsky, S. I. Klokishner, K. R. Dunbar, *J. Chem. Theory Comput.*, **2005**, 1, 668. (b) S. I. Klokishner, S. M. Ostrovsky, A. V. Palii, K. R. Dunbar, *J. Mol. Struct.*, **2007**, 838, 144.

[25] (a) C. J. Milios, A. Vinslava, A. Whittaker, S. Parsons, W. Wernsdorfer, G. Christou, S. P. Perlepes, E. K. Brechin, *Inorg. Chem.*, **2006**, 45, 5272. (b) C. J. Milios, R. Inglis, R. Bagai, W. Wernsdorfer, A. Collins, S. Moggach, S. Parsons, S. P. Perlepès, G. Christou, E. K. Brechin, *Chem. Commun.*, **2007**, 3476. (c) C. J. Milios, A. Vinslava, W. Wernsdorfer, S. Moggach, S. Parsons, S. P. Perlepès, G. Christou, E. K. Brechin. *J. Am. Chem. Soc.*, **2007**, 129, 2754.

[26] (a) T. C. Stamatatos, K. M. Poole, D. Foguet-Albiol, K. A. Abboud, T. A. O'Brien, G. Christou, *Inorg. Chem.*, **2008**, 47, 6593. (b) T. C. Stamatatos, D. Foguet-Albiol, K. M. Poole, W. Wernsdorfer, K. A. Abboud, T. A. O'Brien, G. Christou, *Inorg. Chem.*, **2009**, 48, 9831. (c) T. Taguchi, W. Wernsdorfer, K. A. Abboud, G. Christou, *Inorg. Chem.*, **2010**, 49, 199.

[27] (a) W. Wernsdorfer, N. Aliaga – Alcade, D. N. Hendrickson, G. Christou, *Nature*, **2002**, 416, 406. (b) C. Boskovic, W. Wernsdorfer, K. Folting, J. C. Huffman, D. N. Hendrickson, G. Christou, *Inorg. Chem.*, **2002**, 41, 5107. (c) D. Procissi, B. J. Suh, A. Lascialfari, F. Borsa, A. Caneschi, A. Cornia, *J. Appl. Phys*., **2002**, 91, 7173.

[28] A. M. Ako, I. J. Hewitt, V. Mereacre, R. Clérac, W. Wernsdorfer, C. E. Anson, A. K. Powell, *Angew. Chem., Int. Ed.*, **2006**, 30, 4926.

[29] M. Soler, W. Wernsdorfer, K. Folting, M. Pink, G. Christou, *J. Am. Chem. Soc*., **2004**, 126, 2156.

[30] A. J. Tasiopoulos, A. Vinslava, W. Wernsdorfer, K. A. Abboud, G. Christou, *Angew. Chem., Int. Ed.*, **2004**, 43, 2117.

[31] (a) D. E. Freedman, W. H. Harman, T. D. Harris, G. L. Long, C. J. Chang, J. R. Long, *J. Am. Chem. Soc.*, **2010**, 132, 1224. (b) W. H. Harman, D. T. Harris, D. E. Freedman, H. Fong, A. Chand, J. D. Rinehart, A. Ozarowski, M. T. Sougrati, F. Grandjean, G. J. Long, J. R. Long, C. J. Chang, *J. Am. Chem. Soc.*, **2010**, 132, 18115. (c) A. L. Barra, A. Caneschi, A. Cornia, F. Fabrizi de Biani, D. Gatteschi, C. Sangregorio, R. Sessoli, L. Sorace, *J. Am. Chem. Soc.*, **1999**, 121, 5302. (d) K. Wieghardt, K. Pohl, I. Jibril, G. Huttner, *Angew. Chem., Int. Ed. Engl.*, **1984**, 23, 77. (e) C. D. Delfs, D. Gatteschi, L. Pardi, R. Sessoli, K. Wieghardt, D. Hanke, *Inorg. Chem.*, **1993**, 32, 3099. (f) A.-L. Barra, P. Debrunner, D Gatteschi, C. E. Schulz, R. Sessoli, *Europhys. Lett.*, **1996**, 35, 133. (g) K. L. Taft, S. J. Lippard, *J. Am. Chem. Soc.*, **1990**, 112, 9629. (h) K. L. Taft, C. D. Delf, G. C. Papaefthymiou, S. Foner, D. Gatteschi, S. J. Lippard, *J. Am. Chem. Soc.*, **1994**, 116, 823. (i) H. J. Eppley, H. L. Tsai, N. de Vries, K. Folting, G. Christou, D. N. Hendrickson, *J. Am. Chem. Soc*., **1995**, 117, 301.

[32] (a) C. Boskovic, E. K. Brechin, W. E. Streib, K. Folting, J. C. Bollinger, D. N. Hendrickson, G. Christou, *J. Am. Chem. Soc*., **2002**, 124, 3725. (b) E. C. Yang, W. Wernsdorfer, S. Hill, R. S. Edwards, M. N. Hendrickson, *Polyhedron*, **2003**, 22, 1727.

[33] M. Soler, W. Wernsdorfer, K. Folting, M. Pink, G. Christou, *J. Am. Chem. Soc*., **2004**, 126, 2156.

[34] (a) N. Ishikawa, M. Sugita, T. Ishikawa, S. Koshihara, Y. Kaizu, *J. Am. Chem. Soc.*, **2003**, 125, 8694. (b) N. Ishikawa, M. Sugita, N. Tanaka, T. Ishikawa, S. Y. Koshihara, Y. Kaizu, *Inorg. Chem.*, **2004**, 43, 5498. (c) N. Ishikawa, M. Sugita, W. Wernsdorfer, *Angew. Chem., Int. Ed.*, **2005**, 44, 2931. (d) S. D. Jiang, B. W. Wang, G. Su, Z. M. Wang, S. Gao, *Angew. Chem., Int. Ed.*, **2010**, 49, 7448.

[35] (a) J. D. Rinehart, J. R. Long, *J. Am. Chem. Soc.*, **2009**, 131, 12558. (b) J. D. Rinehart, K. R. Meihaus, J. R. Long, *J. Am. Chem. Soc.*, **2010**, 132, 7572.

[36] (a) D. Li, S. Parkin, G. Wang, G. T. Yee, R. Clérac, W. Wernsdorfer, S. M. Holmes, *J. Am. Chem. Soc.*, **2006**, 128, 4214. (b) D. Li, S. Parkin, R. Clérac, S. M. Holmes, *Inorg. Chem.*, **2006**, 45, 7569. (c) C. M. Zaleski, E. C. Depperman, J. W. Kampf, M. L. Kirk, V. L. Pecoraro, *Angew. Chem., Int. Ed*., **2004**, 43, 3912. (d) J. Rinck, G. Novitchi, W. Van den Heuvel, L. Ungur, Y. Lan, W. Wernsdorfer, C. E. Anson, L. F. Chibotaru, A. K. Powell, *Angew. Chem., Int. Ed.*, **2010**, 49, 7583.

[37] A. M. Ako, V. Mereacre, I. J. Hewitt, R. Clérac, L. Lecren, C. E. Anson, A. K. Powell, *Journal of Materials Chemistry*, **2006**, 16, 2579.

[38] (a) W. Wernsdorfer, *Adv. Chem. Phys.* **2001**, 118, 99. (b) W. Wernsdorfer, *Supercond. Sci. Technol.*, **2009**, 22, 064013.

[39] A. Caneschi, D. Gatteschi, N. Lalioti, C. Sangregorio, R. Sessoli, G. Venturi, A. Vindigni, A. Rettori, M. G. Pini, M. A. Novak, *Angew. Chem. Int. Ed*., **2001**, 40, 1760.

[40] (a) H. Miyasaka, R. Clérac, K. Mizushima, K.–I. Sugiura, M. Yamashita, W. Wernsdorfer, C. Coulon, *Inorg. Chem*., **2003**, 42, 8203. (b) H. Miyasaka, T. Nezu, K. Sugimoto, K. Sugiura, M. Yamashita, R. Clérac, *Inorg. Chem*., **2004**, 43, 5486. (c) H. Miyasaka, T. Nezu, K. Sugimoto, K. Sugiura, M. Yamashita, R. Clérac, *Chem. Eur. J*., **2005**, 11, 1592. (d) H. Miyasaka, R. Clérac, *Bull. Chem. Soc. Jpn.*, **2005**, 78, 1725. (e) H. Miyasaka, A. Saitoh, S. Abe, *Coord. Chem. Rev*., **2007**, 251, 2622. (f) H. Miyasaka, A. Saitoh, M. Yamashita, R. Clérac, *Dalton Trans*., **2008**, 2422. (g) H. Miyasaka, M. Julve, M. Yamashita, R. Clérac, *Inorg. Chem*., **2009**, 48, 3420.

[41] (a) T. C. Stamatatos, K. A. Abboud, W. Wernsdorfer, G. Christou, *Inorg. Chem*., **2009**, 48, 807. (b) R. Lescouëzec, J. Vaissermann, C. Ruiz–Pérez, F. Lloret, R. Carrasco, M. Julve, M. Verdaguer, Y. Dromzee, D. Gatteschi, W. Wernsdorfer, *Angew. Chem. Int. Ed*., **2003**, 42, 1483. (c) L. M. Toma, R. Lescouëzec, F. Lloret, M. Julve, J. Vaissermann, M. Verdaguer, *Chem. Commun*., **2003**, 1850. (d) L. M. Toma, F. S. Delgado, C. Ruiz–Pérez, R. Carrasco, J. Cano, F. Lloret, M. Julve, *Dalton Trans*., **2004**, 2836. (e) L. M. Toma, R. Lescouëzec, S. Uriel, R. Llusar, C. Ruiz–Pérez, J. Vaissermann, F. Lloret, M. Julve, M. Verdaguer, *Dalton Trans*., **2007**, 1850.

[42] (a) S. Wang, J. L. Zuo, S. Gao, Y. Song, H. C. Zhou, Y. Z. Zhang, X. Z. You, *J. Am. Chem. Soc*., **2004**, 126, 8900. (b) S. W. Choi, H. Y. Kwak, J. H. Yoon, H. C. Kim, E. J. Koh, C. S. Hong, *Inorg. Chem*., **2008**, 47, 10214. (c) D. Visinescu, L. M. Toma, F. Lloret, O. Fabelo, C. Ruiz–Pérez, M. Julve, *Dalton Trans*., **2008**, 4103. (d) V. Costa, R. Lescouëzec, J. Vaissermann, P. Herson, Y. Journaux, M. H. Araujo, J. M. Clemente-Juan, F. Lloret, M. Julve, *Inorg. Chim. Acta*, **2008**, 361, 3912. (e) J. F. Guo, X. T. Wang, B. W. Wang, G. C. Xu, S. Gao, L. Szeto, W. T. Wong, W. Y. Wong, T. C. Lau, *Chem. Eur. J*., **2010**, 16, 3524. (f) T. D. Harris, M. V. Bennett, R. Clérac, J. R. Long, *J. Am. Chem. Soc*., **2010**, 132, 3980.

[43] (a) T. F. Liu, D. Fu, S. Gao, Y. Z. Zhang, H. L. Sun, G. Su, Y. J. Liu, *J. Am. Chem. Soc*., **2003**, 125, 13976. (b) X. T. Liu, X. Y. Wang, W. X. Zhang, P. Cui, S. Gao, *Adv. Mater*., **2006**, 18, 2852. (c) H. B. Xu, B. W. Wang, F. Pan, Z. M. Wang, S. Gao, *Angew. Chem. Int. Ed*., **2007**, 46, 7388. (d) H. L. Sun, Z. M. Wang, S. Gao, *Chem. Eur. J*., **2009**, 15, 1757. (e) E. Pardo, R. Ruiz-García, F. Lloret, J. Faus, M. Julve, C. Ruiz-Pérez, *Adv. Mater*., **2004**, 16, 1597.

[44] (a) E. Pardo, R. Ruiz-García, F. Lloret, J. Faus, M. Julve, Y. Journaux, M. A. Novak, F. S. Delgado, C. Ruiz- Pérez, *Chem. Eur. J.*, **2007**, 13, 2054. (b) E. Coronado, J. R. Galán-Mascarós, C. Martí-Gastaldo, *J. Am. Chem. Soc*., **2008**, 130, 14987. (c) Y. Z. Zheng, M. L. Tong, W. X. Zhang, X. M. Chen, *Angew. Chem. Int. Ed*., **2006**, 45, 6310. (d) Y. Z. Zheng, W. Xue, M.–L. Tong, X. M. Chen, S. L. Zheng, *Inorg. Chem*., **2008**, 47, 11202. (e) Y. L. Bai, J. Tao, W. Wernsdorfer, O. Sato, R.-B. Huang, L. S. Zheng, *J. Am. Chem. Soc.*, **2006**, 128, 16428. (f) X. J. Li, X. Y. Wang, S. Gao, R. Cao, *Inorg. Chem*., **2006**, 45, 1508. (g) S. Hu, L. Yun, Y. Z. Zheng, Y. H. Lan, A. K. Powell, M. L. Tong, *Dalton Trans*., **2009**, 1897.

[45] (a) Z. M. Sun, A. V. Prosvirin, H. H. Zhao, J. G. Mao, K. R. Dunbar, *J. Appl. Phys*., **2005**, 97, 10B305. (b) A. V. Palii, S. M. Ostrovsky, S. I. Klokishner, O. S. Reu, Z. M. Sun, A. V. Prosvirin, H. H. Zhao, J. G. Mao, K. R. Dunbar, *J. Phys. Chem. A*, **2006**, 110, 14003. (c) A. V. Palii, O. S. Reu, S. M. Ostrovsky, S. I. Klokishner, B. S. Tsukerblat, Z. M. Sun, A. V. Prosvirin, H. H. Zhao, K. R. Dunbar, *J. Am. Chem. Soc*, **2008**, 130, 14729. (d) K. Bernot, J. Luzon, R. Sessoli, A. Vindigni, J. Thion, S. Richeter, D. Leclercq, J. Larionova, A. Vander Lee, *J. Am. Chem. Soc*, **2008**, 130, 1619. (f) H. Miyasaka, T. Madanbashi, K. Sugimoto, Y. Nakazawa, W. Wernsdorfer, K. I. Sugiura, M. Yamashita, C. Coulon, R. Clérac, *Chem. Eur. J*., **2006**, 12, 7028. (g) L. Bogani, C. Sangregorio, R. Sessoli, D. Gatteschi, *Angew. Chem. Int. Ed*., **2005**, 44, 5817. (h) K. Bernot, L. Bogani, A. Caneschi, D. Gatteschi, R. Sessoli, *J. Am. Chem. Soc*., **2006**, 128, 7947. (i) K. Bernot, J. Luzon, A. Caneschi, D. Gatteschi, R. Sessoli, L. Bogani, A. Vindigni, A. Rettori, M. G. Pini, *Phys. Rev. B*, **2009**, 79, 134419.

[46] H. L. Sun, Z. M. Wang, S. Gao, *Coord. Chem. Rev.*, **2010**, 254, 1081.

[47] R. J. Glauber, *J. Math. Phys*. **1963**, 4*,* 294.

[48] B. Barbara, *J. Phys.*, **1973**, 34, 1039.

[49] C. Coulon, R. Clérac, L. Lecren, W. Wernsdorfer, H. Miyasaka, *Phys. Rev. B*, **2004**, 69, 132408.

[50] (a) C. Coulon, R. Clérac, W. Wernsdorfer, T. Colin, H. Miyasaka, *Phys. Rev. Lett.*, **2009**, 102, 167204. (b) H. Miyasaka, K. Takayama, A. Saitoh, S. Furukawa, M. Yamashita, R. Clérac, *Chem. Eur. J.*, **2010**, 16, 3656.

[51] L. Lecren, O. Roubeau, C. Coulon,Y. G. Li, X. F. Le Goff, W. Wernsdorfer, H. Miyasaka, R. Clérac, *J. Am. Chem. Soc.*, **2005,** 127, 17353.

[52] (a) H. Miyasaka, K. Nakata, L. Lecren, C. Coulon, Y. Nakazawa, T. Fujisaki, K. Sugiura, M. Yamashita, R. Clérac, *J. Am. Chem. Soc.*, **2006**, 128, 3770. (b) H. Miyasaka, K. Nakata, K. Sugiura, M. Yamashita,R. Clérac, *Angew. Chem. Int. Ed*., **2004**, 43, 707. (c) H. Hiraga, H. Miyasaka, K. Nakata, T. Kajiwara, S. Takaichi, Y. Oshima, H. Nojiri, M. Yamashita, *Inorg. Chem.*, **2007**, 46, 9661.

[53] M. Ferbinteanu, H. Miyasaka, W.Wernsdorfer, K. Nakata, K. Sugiuran, M. Yamashita, C. Coulon, R. Clérac, *J. Am. Chem. Soc*., **2005**, 127, 3090.

[54] (a) Anonymous, *Misc. Berlinensia Incrementum Scientarium (Berlin)*, **1710**, 1, 377. (b) J. Woodward, *Phil. Trans.*, **1724**, *33*, 15. (c) J. Brown, *Phil. Trans.*, **1724**, 33, 19. (d) H. M. Powell, *Proc. Chem. Soc*., **1959**, 73.

[55] (a) J. R. Long, *Molecular Cluster Magnets In Chemistry of Nanostructured Materials*; P. Yang, Ed.; World Scientific: Hong Kong, **2003**; p- 291-315, and references therein. (b) L. M. C. Beltran, J. R. Long *Acc. Chem. Res.*, **2005**, 38, 325. (c) M. Shatruk, C. Avendano, K. Dunbar, *In Progress in Inorganic Chemistry*; K. D. Karlin Ed.; *John Wiley & Sons: Amsterdam*, **2009**, 56, pp 155, and references therein.

[56] (a) T. Mallah, C. Auberger, M. Verdaguer, P. Veillet, *Chem. Commun*., **1995**, 61. (b) R. J. Parker, D. C. R. Hockless, B. Moubaraki, K. S. Murray, L. Spiccia, *Chem. Commun.*, **1996**, 2789. (c) Z. J. Zhong, H. Seino, Y. Mizobe, M. Hidai, A. Fujishima, S. -i. Ohkoshi, K. Hashimoto, *J. Am. Chem. Soc.*, **2000**, 122, 2952. (d) V. Marvaud, C. Decroix, A. Scuiller, C. Guyard- Duhayon, J. Vaissermann, F. Gonnet, M. Verdaguer, *Chem. Eur. J.*, **2003**, 9, 1677. (e) D. Li, S. Parkin, G. Wang, G. T. Yee, A. V. Prosvirin, S. M. Holmes, *Inorg. Chem.*, **2005**, 44, 4903. (f) Z. H. Ni, H. Z. Kou, L. F. Zhang, C. Ge, A. L. Cui, R. J. Wang, Y. Li, O. Sato, *Angew. Chem. Int. Ed.*, **2005**, 44, 7742. (g) T. D. Harris, J. R. Long, *Chem. Commun.*, **2007**, 1360. (h) M. Shatruk, A. Dragulescu Andrasi, K. E. Chambers, S. A. Stoian, E. L. Bominaar, C. Achim, K. R. Dunbar, *J. Am. Chem. Soc*., **2007**, 129, 6104. (i) X. Y. Wang, A. V. Prosvirin, K. R. Dunbar, *Angew. Chem. Int. Ed.*, **2010**, 122, 5135.

[57] (a) D. F. Shriver, S. A. Shriver, S. E. Anderson, *Inorg. Chem*., **1965**, 4, 725. (b) H. J. Buser, D. Schwarzenbach, W. Petter, A. Ludi, *Inorg. Chem.*, **1977**, 16, 2704. (c) T. Mallah, S. Thiebaut, M. Verdaguer, P. Veillet, *Science*, **1993**, 262, 1554. (d) V. Gadet, T. Mallah, I. Castro, M. Verdaguer, P. Veillet, *J. Am. Chem. Soc.*, **1992**, 114, 9213; (e) S. Ferlay, T. Mallah, R. Ouahes, P. Veillet, M. Verdaguer, *Nature*, **1995**, 378, 701. (f) W. R. Entley, G. S. Girolami, *Science*, **1995**, 268, 397. (g) K. R. Dunbar, R. A. Heintz, *Prog. Inorg. Chem.*, **1997**, 45, 283, and references therein. (h) J. Larionova, R. Clérac, J. Sanchiz, O. Kahn, S. Golhen, L. Ouahab, *J. Am. Chem. Soc.*, **1998**, 120, 13088. (i) M. Verdaguer, A. Bleuzen, V. Marvaud, J. Vaissermann, M. Seuleiman, C. Desplanches, A. Scuiller, C. Train, R. Garde, G. Gelly, C. Lomenech, I. Rosenman, P. Veillet, C. Cartier, F. Villain, *Coord. Chem. Rev.*, **1999**, 190, 1023, and references therein. (j) J. Larionova, O. Kahn, S. Golhen, L. Ouahab, R. Clérac, *Inorg. Chem*., **1999**, 38, 3621. (k) J. Larionova, O. Kahn, S. Golhen, L. Ouahab, R. Clérac, *J. Am. Chem. Soc.*, **1999**, 121, 3349. (l) S. M. Holmes, G. S. Girolami, *J. Am. Chem. Soc.*, **1999**, 121, 5593. (m) O. Hatlevik, W.

E. Buschmann, J. Zhang, J. L. Manson, J. S. Miller, *AdV. Mater.*, **1999**, 11, 914. (n) Y. Liao, W. W. Shum, J. S. Miller, *J. Am. Chem. Soc.*, **2002**, 134, 9336. (o) M. Verdaguer, G. Girolami, *In Magnetism: Molecules to Materials V*, J. S. Miller, M. Drillon, *Eds. Wiley-VCH: Weinheim*, **2005**, p 283. (p) K. Tomono, Y. Tsunobuchi, K. Nakabayashi, S. –i Ohkoshi, *Inorg. Chem.*, **2010**, 49, 1298. (q) J. H. Her, P. W. Stephens, C. M. Kareis, J. G. Moore, K. S. Min, J. W. Park, G. Bali, B. S. Kennon, J. S. Miller, *Inorg. Chem.*, **2010**, 49, 1524. (r) T. D. Harris, M. V. Bennett, R. Clérac, J. R. Long, *J. Am. Chem. Soc*., **2010**, 132, 3980

[58] (a) H. Weihe, H. U. Güdel, "*Magnetic exchange across the cyanide bridge"*, *Comments On Inorganic Chemistry, Taylor* & Francis**, 2000**, 22, 1-2, p 75-103. (b) W. E. Entley, G. S Girolami. *Science,* **1995**, 268, 397.

[59] (a) H. B. Zhou, J. Wang, H. S. Wang, Y. L. Xu, X. J. Song, Y. Song, X. Z. You, *Inorg. Chem.*, **2011**, 50, 6868; (b) M. Ohba, N. Usuki, N. Fukita, H. O. Åkawa, *Angew. Chem. Int. Ed.*, **1999**, 38, 12, 1795. (c) H. J. Choi, J. J. Sokol, J. R. Long, *Inorganic Chemistry***, 2004**, 43, 5, 1607. (d) V**.** Gadet, T. Mallah, I. Castro, M. Verdaguer, *J. Am. Chem.* Soc., **1992**, 114*,* 9214. (e) B. N. Figgis, E. S. Kucharski, M. Vrtisl, *J. Am. Chem. Soc*., **1993**, 115*,* 176. (f) T. Shiga, H. Ohkawa, S. Kitagawa, M. Ohba, *J. Am. Chem. Soc.*, **2006***,* 128, 16426. (g) H. Z. Kou, J. K. Tang, D. Z. Liao, S. Gao, P. Cheng, Z. H. Jiang, S. P. Yan, G. L. Wang, B. Chansou, J. P. Tuchagues, *Inorg. Chem.*, **2001**, 40*,* 4839. (h) M. Ohba, N. Usuki, N. Fukita, H. Ohkawa, *Inorg. Chem.*, **1998**, 37*,* 3349. (i) K.V. Langenberg, S. R. Batten, K. J. Berry, D. C. R. Hockless, B. Moubaraki, K. S. Murray *Inorg. Chem.* **1997**, 36*,* 5006. (j) F. Yan, Z. Chen, *J. Phys. Chem. A*, **2000**, 104, 6295. (k) M. Ohba, H. Ohkawa, N. Fukita, Y. Hashimoto, *J. Am. Chem. Soc.*, **1997**, 119*,* 1011. (l) M. Ohba, N. Mamono, H. ohkawa, T. Enoki, J. M. Latour, *J. Am. Chem. Soc.*, **1994**, 114, 11566. (m) H. Z. Kou, S. Gao, C. H. Li, D. Z. Liao, B. C. Zhou, R. J. Wang, Y. Li, *Inorg. Chem.*, **2002**, 41, 18, 4756. (n) H. Z. Kou, B. C. Zhou, D. Z. Liao, R. J. Wang, Y. Li, *Inorg. Chem.*, **2002**, 41, 25, 6887. (o) A. V. Palii, S. M. Ostrovsky, S. I. Klokishner, B. S. Tsukerblat, C. P. Berlinguette, K. R. Dunbar, J. R. Galan-Mascaros, *J. Am. Chem. Soc.*, **2004**, 126, 16860. (p) P. L. W. Tregenna-Piggott, D. Sheptyakov, L. Keller, S. I. Klokishner, S. M. Ostrovsky, A. V. Palii, O. S. Reu, J. Bendix, T. Brock-Nannestad, K. Pedersen, H. Weihe, H. Mutka, *Inorg. Chem.*, **2009**, 48, 1, 128. (q) K. S. Pedersen, J. Dreiser, J. Nehrkorn, M. Gysler, M. Schau-Magnussen, A. Schnegg, K. Holldack, R. Bittl, S. Piligkos, H. Weihe, P. Tregenna-Piggott, O. Waldmann J. Bendix, *Chem. Commun*., **2011**, 47, 6918. (r) L. G. Beauvais and J. R. Long, *J. Am. Chem. Soc.*, **2002**, 124, 2110. (s) V. S. Mironov, Dokl. *Phys. Chem*., **2006**, 408, 130.

[60] (a) D. Zhang, H. Wang, Y. Chen, Z. H. Ni, L. Tian, J. Jiang, *Inorg. Chem.*, **2009**, 48, 11215. (b) R. lescoüezec, L. M. Toma, J. Vaissermann, M. Verdaguer, F. S. Delgado, C. Ruiz-P´erez, F. Lloret, M. Julve, *Coord. Chem. Rev.*, **2005**, 249, 2691 and references therein. (c) S. Wang, X. H. Ding, J. L. Zuo, X. Z. You, W. Huang, *Coord. Chem. Rev.*, **2011**, 255, 1713 and references therein. (d) D. Visinescu, L. M. Toma, J. Cano, O. Fabelo, C. R. Pérez, A. Labrador, F. Lloret*,* M. Julve, *Dalton Trans.*, **2010**, 39, 5028.

[61] (a) V. S. Mironov, L. F. Chibotaru, A. Ceulemans, *J. Am. Chem. Soc.*, **200**3, 125, 9750. (b) O. Kahn, J. Larionova, L. Ouahab, *Chem. Commun.*, **1999**, 945 and references therein. (c) J. Larionova, J. Sanchiz, S. Golhen, L. Ouahab, O. Kahn, *Chem. Commun.*, **1998**, 953. (d) R. Lescoue1zec, F. Lloret, M. Julve, J. Vaissermann, M. Verdaguer, *Inorg. Chem.*, **2002**, 41, 818.

[62] (a) D. E. Freedman, D. M. Jenkins, A. T. Iavarone , J. R. Long, *J. Am. Chem. Soc.*, **2008**, 130, 2884, (b) J. M. Zadrozny, D. E. Freedman, D. M. Jenkins, T. D. Harris, A. T. Iavarone, C. Mathonière, R. Clérac, J. R. Long, *Inorg. Chem.*, **2010**, 49, 8886.

[63] (a) J. Larionova, M. Gross, M. Pilkington, H. Andres, H. Stoeckli- Evans, H. U. Güdel, S. Decurtins, *Angew. Chem., Int. Ed*., **2000**, 39, 1605; (b) F. Bonadio, M. Gross, H. Stoeckli-Evans, S. Decurtins, *Inorg. Chem.,* **2002**, 41, 5891. (c) M. Pilkington, S. Decurtins, *Chimia*, **2001**, 55, 1014. (d) H. Xu, O. Sato, Z. Li, J. Ma*, Inorg. Chem. Commun.*, **2012**, 15, 311.

[64] (a) Y. Song, P. Zhang, X. M. Ren, X. F. Shen, Y. Z. Li, X. Z. You, *J. Am. Chem. Soc.,* **2005**, 127, 3708. (b) J. H. Lim, J. H. Yoon, H. C. Kim, C. S. Hong, *Angew. Chem., Int. Ed.*, **2006**, 45, 7424. (c) M. G. Hilfiger, H. H. Zhao, A. Prosvirin, W. Wernsdorfer, K. R. *Dunbar, Dalton Trans*., **2009**, 5155.

[65] (a) M. Arai, W. Kosaka, T. Matsuda, S. Ohkoshi, *Angew. Chem., Int. Ed*., **2008**, 47, 6885. (b) M. Pilkington, S. Decurtins, *Chimia*, **2000**, 54, 593. (c) W. Kosaka, K. Hashimoto, S. –i Ohkoshi, *Bull. Chem. Soc. Jpn.*, **2008**, 81, 992; (d) T. S. Venkatakrishnan, S. Sahoo, N. Bréfuel, C. Duhayon, C. Paulsen, A. L. Barra, S. Ramasesha, J. -P. Sutter, *J. Am. Chem. Soc.*, **2010**, 132, 6047.

[66] H. Oshio, O. Tamada, H. Onodera, T. Ito, T. Ikoma, S.T. Kubota, *Inorg. Chem*., **1999**, 38, 5686.

[67] (a) W. F. Yeung, W. L. Man, W. T. Wong, T. C. Lau, S. Gao, *Angew. Chem., Int. Ed.*, **2001**, 40, 3031. (b) W. F. Yeung, P. H. Lau, T. C. Lau, H. Y. Wei, H. L. Sun, S. Gao, Z. D. Chen, W. T. Wong, *Inorg. Chem.*, **2005**, 44, 6579. (c) L. M. Toma, L. D. Toma, F. S. Delgado, C. Ruiz-Pérez, J. Sletten, J. Cano, J. M. Clemente-Juan, F. Lloret and M. Julve, *Coord. Chem. Rev.*, **2006**, 250, 2176. (d) J. F. Guo, X. T. Wang, B. W. Wang, G. C. Xu, S. Gao, L. Szeto, W. T. Wong, W. Y. Wong, T. C. Lau, *Chem. Eur. J*., **2010**, 16, 3524. (e) W. F. Yeung, T. C. Lau, X. Y. Wang, S. Gao, L. Szeto, W. T. Wong, *Inorg. Chem*., **2006**, 45, 675. (f) D. Zhang, L. F. Zhang, Y. Chen, H. Wang, Z. Hai Ni, W. Wernsdorfer, J. Jiang, *Chem. Commun.*, **2010**, 46, 3550.

[68] (a) J. H. Yoon, H. S. Yoo, H. C. Kim, S. W. Yoon, B. J. Suh, Chang Seop Hong, *Inorg. Chem*., **2009**, 48, 3, 816. (b) J. F. Guo, W. F. Yeung, P. H. Lau, X. T. Wang, S. Gao, W. T. Wong, S. S. Y. Chui, C. M. Che, W. Y. Wong, T. C. Lau, *Inorg. Chem*., **2010**, 49, 1607.

[69] (a) X-Y Wang, C. Avendañoa, K. R. Dunbar, *Chem. Soc. Rev.*, **2011**, 40, 3213. (b) J. M. D. Coey, *Magnetism and Magnetic Materials*, Cambridge University Press, New York, **2009**.

[70] H. Miyasaka, T. Madanbashi, A. Saitoh, N. Motokawa, R. Ishikawa, M. Yamashita, S. Bahr, W. Wernsdorfer, R. Clérac, *Chem. Eur. J*., **2012**, 18, 13, 3942.

CHAPTER II

The molecular precursors of the magnetic materials

II.1. Introduction and synthetic strategy

In this chapter our discussion is mainly focused on the metal-organic molecular precursors used in this present research work to obtain the molecule-based magnets discussed in chapters III, IV and V. We will discuss not only why we rationally chose these precursors but also emphasize our objective with suitable examples found in the literature.

The magnetic properties of molecule-based magnetic materials originate entirely from the interactions between the individual magnetic moments in the building blocks used to synthesize the material. Therefore a rational synthetic approach is very important to obtain a material with premeditate and interesting magnetic properties. The selection of metal ions with unpaired electrons and the proper ligand environment are the basic parameters to consider while building a molecular magnet. In particular, the coordination environment of these metal ions will help us to introduce strong anisotropy in the system. As we have already mentioned in chapter I, we extensively used the cyanido ligand to bridge the magnetic metal ion, and thus our chemical strategy to synthesize these magnetic materials involved simple donor acceptor coordination chemistry. In our synthetic strategy, we assembled two types of systems, (i) the cyanido based donors and (ii) acceptors parts. The donor-type molecular precursors possess the cyanido ligand coordinated with the metal centre through the carbon atom and the electron density is transferred through the nitrogen end of the cyanido to the acceptor metal ion. On the other hand, the acceptor molecular precursors contain electron poor metal centers that can accept electron density from the cyanido group. Therefore the acceptor molecular precursors must contain an available coordination site on the metal ions.

As mentioned earlier in chapter I, we are interested in making low dimensional magnetic materials, such as zero or one dimensional systems, and this has lead us to be more selective towards the suitable molecular precursors. We need to initially find molecular precursors that can exhibit a predictable directionality during coordination so that we can tune the final compound using a proper reaction strategy.

In general, our ambition in this research work is to use the cyanido ligand to link 3*d* metal ions and 4*d* or 5*d* metal ions and thus obtain new magnetic materials with dimensionality restricted to zero or one. This is why we have chosen the *trans*-dicyanido building blocks *trans*-$[Ru^{III}(salen)(CN)_2]^-$ and *trans*-$[Re^{IV}Cl_4(CN)_2]^{2-}$ which can coordinate with only two metal ions in a *trans* fashion (figure II.1a and II.1b). These building blocks also can introduce an appreciable amount of magnetic anisotropy to a molecular system, due to the spin orbit coupling experienced by such 4*d* and 5*d* metal ions. On the other hand, the 3*d* metal based molecular precursors $[Mn^{III}(SB)(solvent)_2]^+$ or $[Mn^{III}{}_2(SB)_2(solvent)_2]^{2+}$ (SB = Schiff bases), $[Ni^{II}/Cu^{II}(cyclam)]^{2+}$ and $[Fe^{II}/Mn^{II}(LN_3O_2)]^{2+}$ were used as the acceptor moieties. All of the ligands, whether Schiff bases, cyclam or LN_3O_2 occupy the equatorial plane of the metal

ions and thus the axial positions are available for coordination with the cyanido group of the donor moiety (figure II.1c, II.1d, II.1e). Due to Jahn-Teller distortion, these building blocks (in particular Mn^{III} complexes) can also introduce significant uniaxial anisotropy to the molecular magnetic materials.

Furthermore, the combination of these molecular precursors should not lead to such systems where the spins of the compound cancel one other, thus leading to a diamagnetic system. An antiferromagnetic interaction between two equal spins leads to the mutual cancellation of their magnetic moments and such a situation is undesirable. Therefore we should select starting materials of different spin ground states so that the synthesized molecules possess residual total spin. We used Mn^{III} ($3d^4$, high spin $S = 2$), Ni^{II} ($3d^8$, $S = 1$), Cu^{II} ($3d^9$, $S = ½$), Mn^{II} ($3d^5$, high spin $S = 5/2$) and Fe^{II} ($3d^6$, high spin $S = 2$) to synthesize the electron acceptor molecular precursors. It is theoretically possible to obtain systems ranging from dinuclear to one dimensional depending on the number of acceptor and donor units that coordinate together.

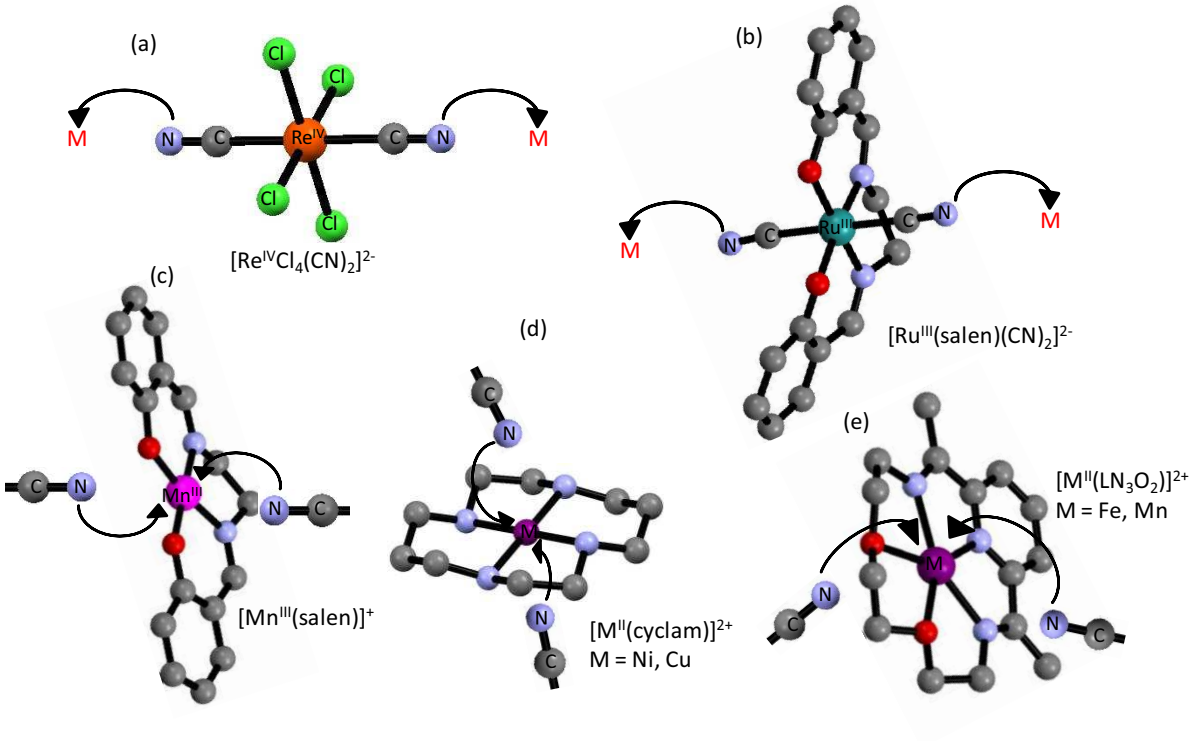

Figure II.1. Coordination modes of the molecular precursors through the cyanido bridge. The *trans*-dicyanido (a) 4*d* and (b) 5*d* building blocks act as electron donor moieties where M is the electron accepting metal ion. (c), (d) and (e) The 3*d* metal building blocks with axial positions available for coordination with the cyanido ligand.

Here, in the following parts of this chapter, we will illustrate the synthesis, crystal structures and magnetic properties of all the molecular precursors we have used. Additionally we will extend our discussion with pertinent literature examples.

All starting materials were synthesized and thoroughly characterized before using them to build the molecule-based magnetic materials. The detailed characterizations of these molecular precursors are described in section II.4. Some of the advantages of the syntheses of these starting materials are the purity of the obtained products, good yields and their good solubility in commonly used organic solvents like MeOH, MeCN, $MeNO_2$ etc.

II.2. 3*d* complexes acting as acceptor units

The 3*d* metal based molecular precursors, that we have used, have the general formula $[Mn^{III}(SB)(solvent)_2]^+$, $[Mn^{III}{}_2(SB)_2(solvent)_2]^{2+}$ (SB = salen type tetradentate chelating Schiff bases^{2-}, solvent = MeOH or H_2O occupying the axial positions of Mn^{III}), $[Ni^{II}/Cu^{II}(cyclam)]^{2+}$, $[Fe^{II}/Mn^{II}(LN_3O_2)]^{2+}$ (cyclam and LN_3O_2 being neutral tetradentate and pentadentate macrocyclic ligands respectively). The ligands in such molecular precursors occupy the four possible equatorial coordination sites and therefore the axial sites remain either vacant or coordinated with solvents. Thus these molecules are well adapted to coordinate with the electron donor cyanido group, either directly with a vacant position or through substitution of axial solvent molecules.

In the following parts of this chapter, we will discuss the properties of the 3*d* metal based molecular precursors used later in the thesis, followed by their quantitative and qualitative characterization (section II.4.2, II.4.3 and II.4.4). Additionally, examples found in the literature will help to illustrate the coordination behavior and the magnetic exchange of these molecules.

II.2.1. Mn^{III}-Schiff base complexes

The Mn^{III}-Schiff bases[1] are paramagnetic complexes with unique properties like large spin ground state (S = 2) and large magnetic anisotropy, which are fundamental requirements to synthesize molecule-based magnetic materials like SMMs and SCMs. Furthermore each of these complexes possesses two available coordination sites on the manganese ion, where other paramagnetic moiety can be connected through different bridging atoms/ligands. The environment around the Mn^{III} ion is not stereochemically hindered, and thus the axial positions are suitable for ligand substitution. Therefore the Mn^{III}-Schiff base complexes are one of the most widely used molecular precursors in the arena of molecule-based magnets.

In general the organic compound having imino group (C=N-R, where R is some aromatic or aliphatic moiety) is called a Schiff base ligand. The Schiff base ligands used here are tetradentate planar ligands obtained from the reaction between two equivalents of salicylaldehyde (or substituted salicylaldehyde) and one equivalent of a primary diamine. Condensation of two leads to the H_2salen-type (salen^{2-} = *N, N′*-bis(salicylidene)ethylenediamine) ligands (figure II.2a) where the two imino nitrogen (-C=N) atoms and the two oxygen atoms of the phenoxido groups are the donor atoms. The equatorial positions of the Mn^{III} ion are occupied by these four atoms of the Schiff base ligand, with a rigid, stable, planar geometry, while the axial coordination sites are usually occupied by solvent molecules coming from the reaction medium.

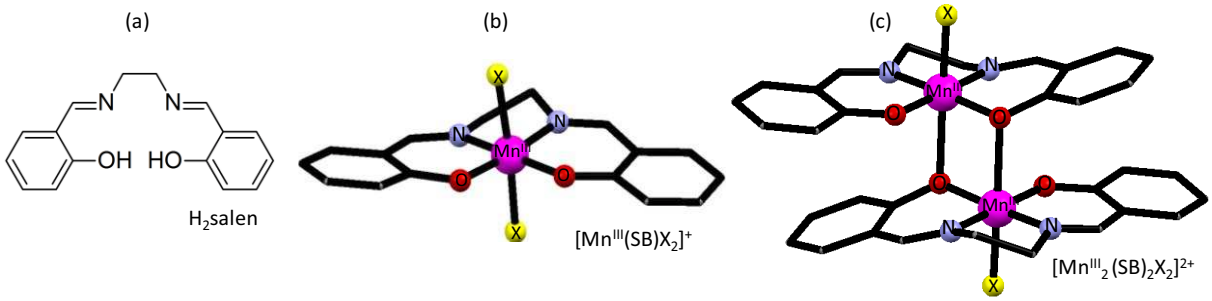

Figure II.2. (a) The H_2salen ligand; the substitution on the aromatic ring or the change of primary diamines results variation of Schiff base ligands (b) $[Mn^{III}(salen)X_2]^+$ and (c) the $[Mn^{III}_2(salen)_2X_2]^{2+}$ where the X is either a solvent molecule (or occasionally a counter anion like Cl^-, Br^-, etc.).

These Mn^{III}-Schiff base complexes can exhibit both mononuclear and dinuclear forms ($[Mn^{III}(SB)]^+$ and $[Mn_2^{III}(SB)_2]^{2+}$) depending upon the Schiff base functionalization and the used solvent (figure II.2b and Figure II.2c).[2] In the dinuclear form, one of the two axial positions of the Mn^{III} ions is coordinated with the phenoxido oxygen atom of the neighboring Mn-Schiff base moiety, and in most of the cases they experience a Mn^{III}-Mn^{III} ferromagnetic exchange through this phenoxido bridge.[1a] These Mn^{III}-Schiff base dimers are known to be one of the smallest molecules exhibit SMM properties, with significant uniaxial magnetic anisotropy and a large spin ground state S_T = 4.[3] The remaining two axial positions of $[Mn_2^{III}(SB)_2]^{2+}$ are available for substitution with ligands which could lead to a controlled organization of SMMs.[6-9]

II.2.1.1. Magnetic anisotropy of the dinuclear and mononuclear Mn^{III}-Schiff base complexes

The origin of the anisotropy of the Mn^{III}-Schiff base complexes is the Mn^{III} ion, which experiences a large Jahn-Teller effect in this weak ligand field. The free Mn^{III} ion has a spin state S = 2, as it has four unpaired electrons and the energies of the *d* orbitals are degenerate. When the free

Mn^{III} ion is placed in an octahedral ligand field, the five orbitals partition into two energy levels, and thus the *d* orbitals split into two sets (figure II.3a), (i) t_{2g} set containing the degenerated d_{xy}, d_{xz} and d_{yz} orbitals and (ii) e_g set containing the degenerated d_{x2-y2} and d_{z2} orbitals.

The ligand field environment in the presence of a Schiff base and axial solvent molecules contributes a large Jahn-Teller effect on the octahedral environment of the Mn^{III} ion. This results into the breaking of degeneracy of its electronic state. The structural deformation tends to lower the local symmetry of each atom in order to minimize the energy of the system. In the octahedral crystal field, the Jahn-Teller effect is more prominent when the e_g level contains an odd number of electrons because these energy levels are directly involved in ligand coordination. In the present case, the Mn^{III} ion in an octahedral crystal field is high spin and thus possesses one unpaired electron in an e_g level orbital. Jahn-Teller distortion leads to the distortion along z direction with further stabilization of the tetragonal geometry (D_{4h} geometry). In this case, the energies of *d*-orbitals with z factor (i.e., d_{z2}, d_{xz}, d_{yz}) are lowered as the bonds along the z-axis are elongated. It further split of the t_{2g} set into two levels where d_{xz} and d_{yz} are degenerated and stabilized and d_{xy} is destabilized (see figure II.3a). On the other hand, the e_g set splits into two levels stabilizing the d_{z2} over d_{x2-y2} (figure II.3a).

The octahedral symmetry of Mn^{III} ions generates two spectroscopic terms, the higher energy $^5T_{2g}$ and the lower energy ^5E_g (figure II.3b). In case of the Mn^{III} ion, the tetragonal elongation (in D4 symmetry) splits the spectroscopic terms as $^5Eg \rightarrow {}^5A_{1g} + {}^5B_{1g}$ and $^5T_{2g} \rightarrow {}^5B_{2g} + {}^5E_g$ which results in a maximum stabilization of $^5B_{1g}$ level and thus it becomes the ground state term of the system. Furthermore, the system experiences zero field spitting (ZFS) arising from both spin-spin and spin–orbit coupling, which further relieves the spin degeneracy of the ground state.[4a] The ZFS effect splits the ground state into $m_S = \pm 2, \pm 1, 0$ where the total energy gap between the ground state $m_S = \pm 2$ and the excited state $m_S = 0$ is $4D$ ($|D|S^2$, with $S = 2$) where D is the ZFS parameter, and the $^5B_{1g}$ ground state results in a negative value of D. (The Hamiltonian used to express ZFS energy is $H = DS^2$).[4]

The zero field splitting in the Mn^{III}-Schiff base complexes results in axial elongation of the octahedral geometry with a negative *D* value (figure II.3b). This is termed axial Ising-type anisotropy, where *D* is also known as anisotropic parameter.[5] The elongated axis (or anisotropic axis) corresponds to the easy axis of magnetization in the Mn^{III}-Schiff base complexes (figure II.3c).

In the dinuclear Mn^{III}-Schiff base complexes, i.e. in $[Mn^{III}_2(SB)_2]^{2+}$, the magnetic exchange between the two Mn^{III} ions is generally ferromagnetic and both anisotropic axes belonging to the two manganese atoms are parallel to each other (figure II.3d); thus the total anisotropy of the molecule is enhanced. This results in uniaxial Ising-type anisotropy of the molecule and therefore this dinuclear molecule can behave like a SMM.[1a,3]

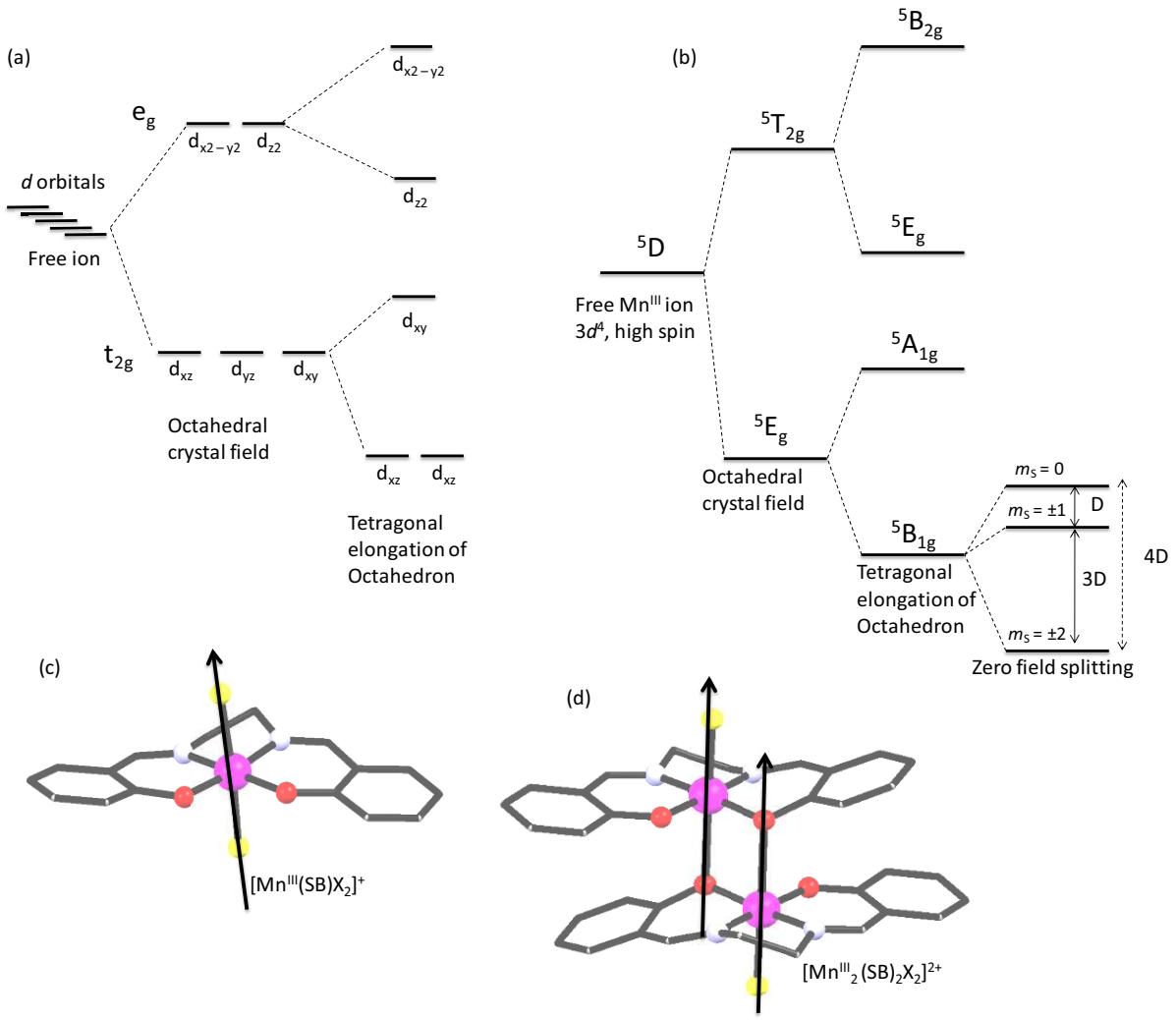

Figure II.3. (a) The orbital splitting of Mn^{III} (d^4) ions in the tetragonal elongation of octahedron. (b) Splitting of the ^5D term by octahedral and tetragonal (axially elongating) ligand fields and by second-order spin–orbit coupling (zero-field splitting) for the Mn^{III} ion. (c) The orientation of the anisotropic axis of $[Mn^{III}(SB)]^+$ along the axial coordination sites. (d) The parallel orientation of the anisotropic axes of $[Mn^{III}_2(SB)_2]^{2+}$.

Here we illustrate the SMM properties of the $[Mn^{III}_2(SB)_2]^{2+}$ dimer with the example of $[Mn^{III}_2(saltmen)_2(ReO_4)_2]$ ($saltmen^{2-}$ = *N, N′*-(1,1,2,2-tetramethylethylene)bis(salicylideneiminate)).[3a] This out-of plane Mn^{III} dimer (figure II.4a) possesses an $S_T = 4$ spin ground state and exhibits slow relaxation of its magnetization at low temperatures (figure II.4.b), which is the signature of its SMM behavior. The best fit of the magnetic susceptibility data yields $g = 2.00(1)$, $J/k_B = +2.65(5)$ K, and $D_{Mn}/k_B = -4.0(2)$ K, where g is the Landé factor of the Mn^{III} ion and k_B is the Boltzmann constant. Figure II.4c exhibits the temperature dependence of the relaxation time of this SMM. Between 4 and 1.9 K, the relaxation follows the Arrhenius law ($\tau = \tau_0 \, exp(\Delta_A/k_BT)$) with an activation energy Δ_A of 16 K and a pre-exponential factor $\tau_0 = 8 \times 10^{-9}$ s. Below 1.9 K, τ reaches saturation and becomes temperature independent at 1.9×10^{-4} s below 0.6 K. This feature indicates the presence of quantum tunnelling of the magnetization (QTM) in the $[Mn^{III}_2(saltmen)_2(ReO_4)_2]$ SMM.

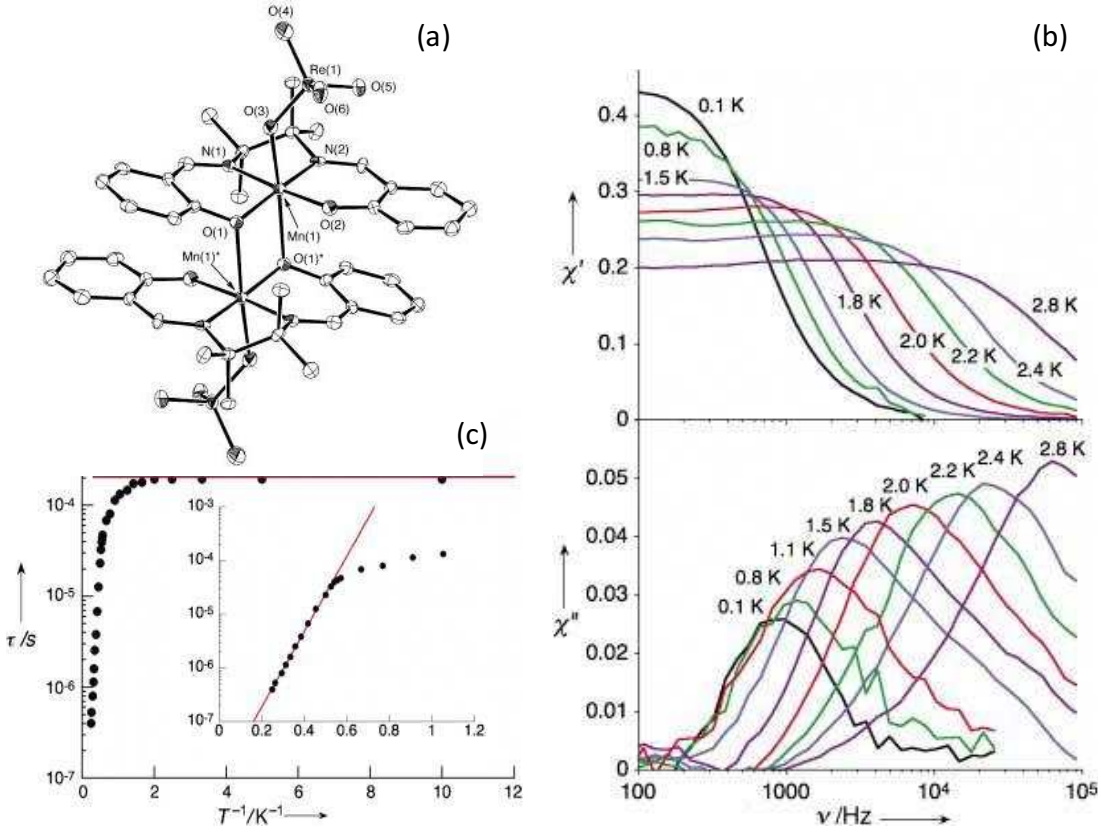

Figure II.4. (a) An ORTEP type view of $[Mn^{III}_2(saltmen)_2(ReO_4)_2]$ (thermal ellipsoids at 50% probability) Mn(1)···Mn(1)* distance is 3.330(1). The hydrogen atoms have been omitted for clarity. (b) The frequency dependence of the in-phase (χ') and out-of-phase (χ'') *ac* magnetic susceptibility of $[Mn^{III}_2(saltmen)_2(ReO_4)_2]$ at temperatures below 2.8 K at zero *dc* field and with an *ac* field amplitude of 5 Oe. (c) Plot of the relaxation time τ vs. $1/T$ for $[Mn^{III}_2(saltmen)_2(ReO_4)_2]$; Inset: Expanded view of the high-temperature region of the plot to emphasize the Arrhenius behaviour.

II.2.1.2. Control of the anisotropy of Mn^{III}-Schiff base complexes in one dimension

In SMMs and SCMs, the magnetic anisotropy is one of the key parameters responsible for the slow relaxation behavior. Therefore chemists must be able to control the orientation of the anisotropy axes in the assembled structures of molecular magnets. In the present research work, we focused on low dimensional magnetic materials and so our concern is solely related to the development of significant uniaxial magnetic anisotropy in the molecular systems. An SCM will be obtained if all the anisotropic axes of the mononuclear or the dinuclear Mn^{III}-Schiff base moieties can be oriented more or less in the same direction. Such SCMs have been obtained using paramagnetic building blocks like $[Fe^{III}(CN)_6]^{3-}$, $[Ni^{II}(pao)(pyridine)_2]$, etc. which organized the dinuclear $[Mn^{III}_2(SB)_2]^{2+}$ in one dimension.[6,7] In these one dimensional compounds, the Jahn-Teller axis of all the $[Mn^{III}(SB)]^{+}$ units (corresponding to the easy axis of magnetization) are parallel to each other. Moreover the

mononuclear Mn^{III}-Schiff base complexes have also been organized in one dimension using $[M^{III}(CN)_6]^{3-}$ (M = Fe, Cr, Mn), which can also exhibit SCM properties.[8] In figure II.5 we have illustrated how the anisotropic axes of the dinuclear and mononuclear Mn^{III}-Schiff base building blocks are aligned in the same direction in the SCMs $(NEt_4)[Mn^{III}_2(5\text{-MeOsalen})_2Fe^{III}(CN)_6]$ (5-MeOsalen^{2-} = *N, N′*-bis(5-methoxy-salicylidene)ethylenediamine) (figure II.5a) and $[Mn^{III}(5\text{-TMAMsalen})M^{III}(CN)_6]\cdot 4H_2O$ (M = Fe, Cr, Mn and 5-TMAMsalen^{2-} = *N, N′*-ethylenebis(5-trimethylammoniomethylsalicylideneiminate)) (figure II.5b).

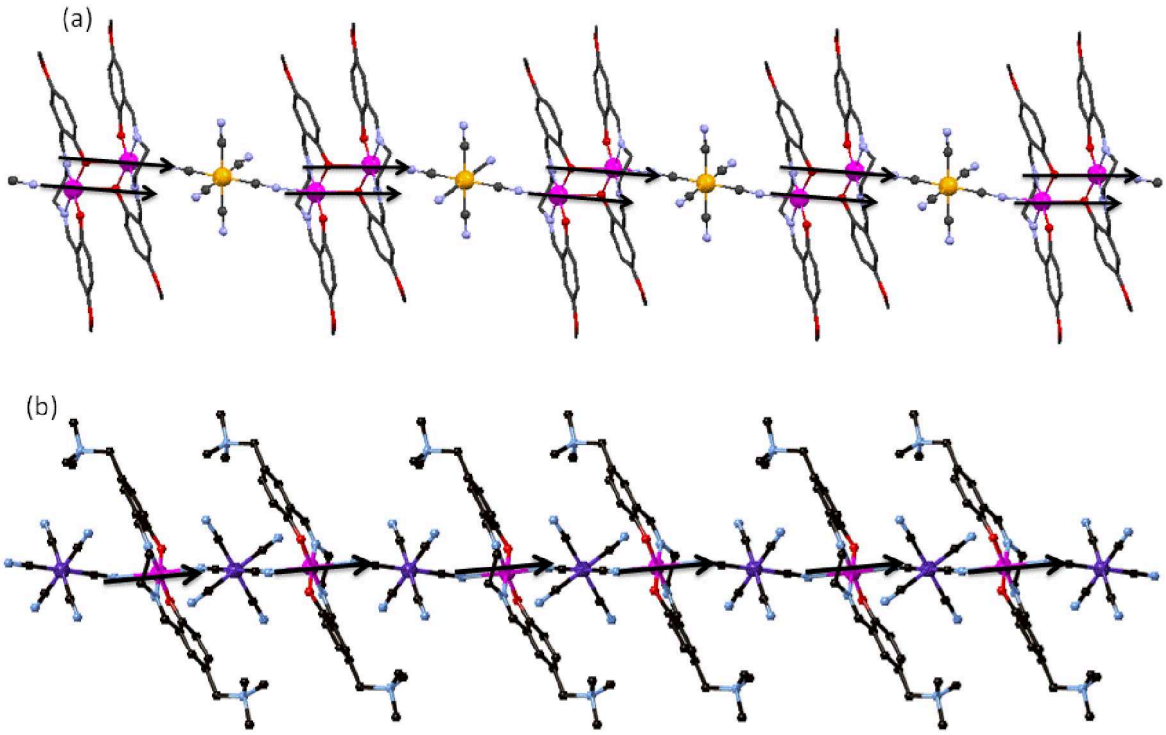

Figure II.5. The one dimensional arrangement of the Jahn–Teller axes of Mn^{III}-Schiff base complexes in (a) $(NEt_4)[Mn^{III}_2(5\text{-MeOsalen})_2Fe^{III}(CN)_6]$ (5-MeOsalen^{2-} = N,N'-bis(5-methoxy-salicylidene)ethylenediamine) and (b) in $[Mn^{III}(5\text{-TMAMsalen})M^{III}(CN)_6]\cdot 4H_2O$ (M = Fe, Cr, Mn and 5-TMAMsalen^{2-} = *N, N′*-ethylenebis(5-trimethylammoniomethyl salicylideneiminate)).[7,8]

Beside such one dimensional complexes, there are innumerable 2D and 3D complexes and discrete molecules made with salen type Mn^{III}-Schiff base precursors showing variety of magnetic properties.[9] For example the trinuclear *rac*-$(NEt_4)[\{Mn^{III}(salmen)(MeOH)\}_2\{Fe(CN)_6\}]$complex contains a Mn^{III}-NC-Fe^{III}-CN-Mn^{III} core and tetragonally elongated coordination around the Mn^{III} centers.[10,7] The ferromagnetic exchange of Mn^{III} with Fe^{III} give rise to the spin ground states $S = 9/2$ for the trinuclear complex and it also possess strong uniaxial anisotropy leading to SMM properties. A cyanido bridged $Fe^{III}_2Mn^{III}_2$ SMM has been reported having the molecular formula $[(Tp^{Me,mt4})Fe(CN)_3]_2[Mn(L)]_2$ ($Hpz^{Me3,mt4}$ = 3-methyl-4,5,6,7-tetrahydroindazole, $Tp^{Me,mt4}$ = $HB(pz^{Me3,mt4})_3^-$; H_2L = *N, N′*-bis(5-bromo-2- hydroxyacetophenylidene)-1,2-diaminopropane).[10b] This

compound has a phenoxido bridged dinuclear $[Mn^{III}(SB)]_2$ core blocked by the *tris*-cyanido Fe^{III} building block.

II.2.1.3. The Mn^{III}-Schiff base complexes used in the thesis

In this section we will only mention the salen-type Schiff base Mn^{III} complexes synthesized as acceptor-type precursors during our research work. Some of the compounds crystallize in a mononuclear form and some of them in a dinuclear form. In table II.1 all of the Mn^{III}-Schiff base complexes are listed, mentioning if they are mono or dinuclear as determined by the single crystal X-ray structure. The detailed synthesis, the infrared spectra and the crystallographic characterization of all these Mn^{III} precursors are discussed in sections II.4.1 and II.4.2. We have not performed the magnetic characterization of all of the Mn^{III} complexes due to the time limitation of the research work.

Table II.1. Mn^{III}-Schiff base complexes used in the thesis

Crystallized in the mononuclear form	*Crystallized in the dinuclear form*
$[Mn(3\text{-MeO-saltmen})(CH_3OH)(H_2O)](ClO_4)$	$[Mn^{III}_2(saltmen)_2(H_2O)_2](ClO_4)_2$
$[Mn^{III}(5\text{-F-saltmen})(H_2O)_2](ClO_4)$	$[Mn^{III}_2(5\text{-Cl-saltmen})_2(H_2O)_2](ClO_4)_2$
$[Mn^{III}(salphen)(CH_3COO)]$	$[Mn^{III}_2(5\text{-Cl-salmen})_2(H_2O)_2](ClO_4)_2.2H_2O$
$[Mn^{III}(4\text{-MeO-saltmen})(H_2O)_2](ClO_4).2H_2O$	$[Mn^{III}_2(5\text{-}^t\text{Bu-saltmen})_2(H_2O)_2](ClO_4)_2.2H_2O$
$[Mn^{III}(5\text{-MeO-salpen})(H_2O)_2](ClO_4)$	$[Mn^{III}_2(5\text{-Me-saltmen})_2(H_2O)_2](ClO_4)_2$
$[Mn^{III}(5\text{-MeO-salen})(H_2O)_2](ClO_4)$	$[Mn^{III}_2(5\text{-MeO-saltmen})_2(H_2O)_2](ClO_4)_2$
$[Mn^{III}(4\text{-HO-saltmen})(H_2O)_2](ClO_4).2H_2O$	$[Mn^{III}_2(5\text{-Me-salpen})_2(H_2O)_2](ClO_4)_2$

All the tetradentate Schiff base ligands were synthesized via a nucleophilic substitution reaction of salicylaldehyde and salicylaldehyde derivatives (with substitution on the aromatic ring) with aliphatic or aromatic primary diamines, resulting imine (R-C=N-) complexes. The general syntheses of all Schiff base ligands are quite similar except in terms of the reaction time and the yield of the product. After the synthesis of the Salen-type ligand most of the Mn^{III}-Schiff base complexes were synthesized as the perchlorate salt in a one step reaction using commercially available manganese (III) acetate hydrate.

II.2.2. Metal-macrocycle complexes

The metal macrocyclic complexes used in this thesis work were made with neutral macrocyclic ligands like cyclam (or substituted cyclam) and pentadentate LN_3O_2 ligands where cyclam = 1,4,8,11-tetraazacyclotetradecane (figure II.5a and II.5b) and LN_3O_2 = 3,12,18-triaaza-6,9-dioxabicyclo[12.3.2]octadeca-1(18),14,16-triene (figure II.5c). All these cyclic ligands contain the metal ions in their cavity via satisfying the equatorial coordination positions of the metal ions. The

axial positions of the metal ions are occupied with solvent molecules or counter anions. Therefore the axial positions remain available for substitution with bridging cyanido ligands.

II.2.2.1. Cyclam based metal complexes used in this thesis

Cyclam is a tetradentate cyclic ligand where the cycle is composed of 14 atoms (four nitrogen and 10 carbon) (figure II.5.a). The secondary amino-type nitrogen atoms act as donor atoms to the metal ions. The ligand can stabilize both *cis* and *trans* conformations of M(cyclam) complexes depending upon the metal ions used and reaction protocol. In the present work we focused on cyclam-based 3*d* metal complexes (Ni^{II}, Cu^{II}) having a *trans*-geometry so that we can control the dimensionality of the resulting magnetic molecules. We have also used the methyl substituted cyclam-type ligand 1,8-dimethyl-1,4,8,11-tetraazacyclotetradecane (figure II.5b). By using commercially available perchlorate salts of Ni^{II} and Cu^{II} we have synthesized three acceptor type precursors: $[Ni^{II}(cyclam)](ClO_4)_2$, $[Cu^{II}(cyclam)(ClO_4)_2]$ and $[Cu^{II}(1,8\text{-dimethyl-cyclam})(ClO_4)_2]$ by adapting literature methods.[11] Details of these precursors, such as their synthesis, spectroscopic characterization and crystallographic structures are given in section II.4.3.

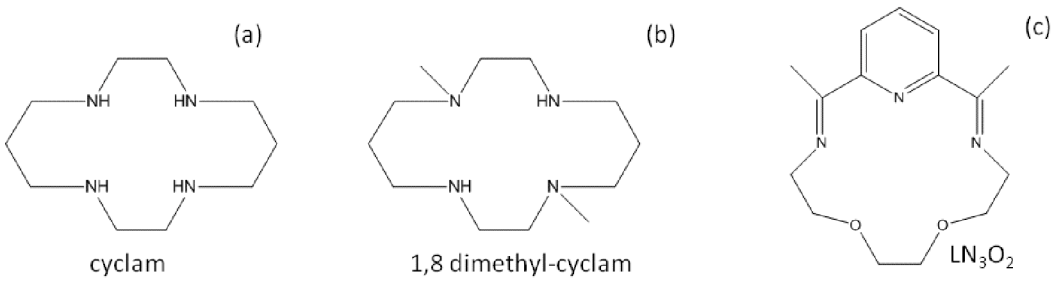

Figure II.5. The used neutral macrocyclic ligands: (a) cyclam = 1,4,8,11-tetraazacyclotetradecane, (b) 1,8-dimethyl cyclam = 1,8-dimethyl-1,4,8,11-tetraazacyclotetradecane and (c) LN_3O_2 = 3,12,18-triaaza-6,9-dioxabicyclo[12.3.2]octadeca-1(18),14,16-triene.

II.2.2.1.1. Magnetic properties

Although we have not performed detailed magnetic measurements on the Ni^{II}/Cu^{II} cyclam precursors, the X-ray crystallographic structures and literature reports of these complexes[11] give us a clear idea about their electronic configuration and magnetic properties. The Ni^{II} and Cu^{II} possess d^8 and d^9 electrons respectively in their valence shell.

In $[Ni^{II}(cyclam)](ClO_4)_2$, Ni^{II} is in a square planar ligand environment and the axial coordination sites remain vacant. Therefore the d_{x2-y2} energy level is sufficiently destabilized to force all the eight electrons to reside in the other orbitals i.e., d_{xy}, d_{xz}, d_{yz} and d_{z2}. Thus all the electrons are paired and in this ligand field environment, the Ni^{II} ion displays a diamagnetic behavior. However, when the axial positions of $[Ni^{II}(cyclam)]^{2+}$ are coordinated by ligands, the Ni^{II} ion experiences an octahedral environment, resulting in a $t_{2g}^6e_g^2$ electronic configuration such that each of the d_{x2-y2} and d_{z2} orbitals possess one unpaired electron. Thus octahedral Ni^{II} has as $S = 1$ spin ground state.

In $[Cu^{II}(cyclam)(ClO_4)_2]$ and $[Cu^{II}(1,8\text{-dimethyl-cyclam})(ClO_4)_2]$, the Cu^{II} ion remains in the octahedral ligand field where it is equatorially coordinated with the four nitrogen atoms originating from the cyclam ligand and the axial positions are weakly coordinated with two oxygen atoms coming from the ClO_4^- counter ion. Having d^9 electrons, the Cu^{II} ion in this geometry possesses a $t_{2g}^6e_g^3$ electronic configuration and one unpaired electron in the d_{x2-y2} orbital. Therefore the spin ground state of the Cu^{II} ion is $S = ½$. In these compounds the axial Cu^{II}-O bond distances are quite longer (about 0.5Å) than the average equatorial Cu^{II}-N bonds, which indicates the presence of a Jahn-Teller effect and significant tetragonal elongation.

II.2.2.1.2. Examples of low dimensional complexes

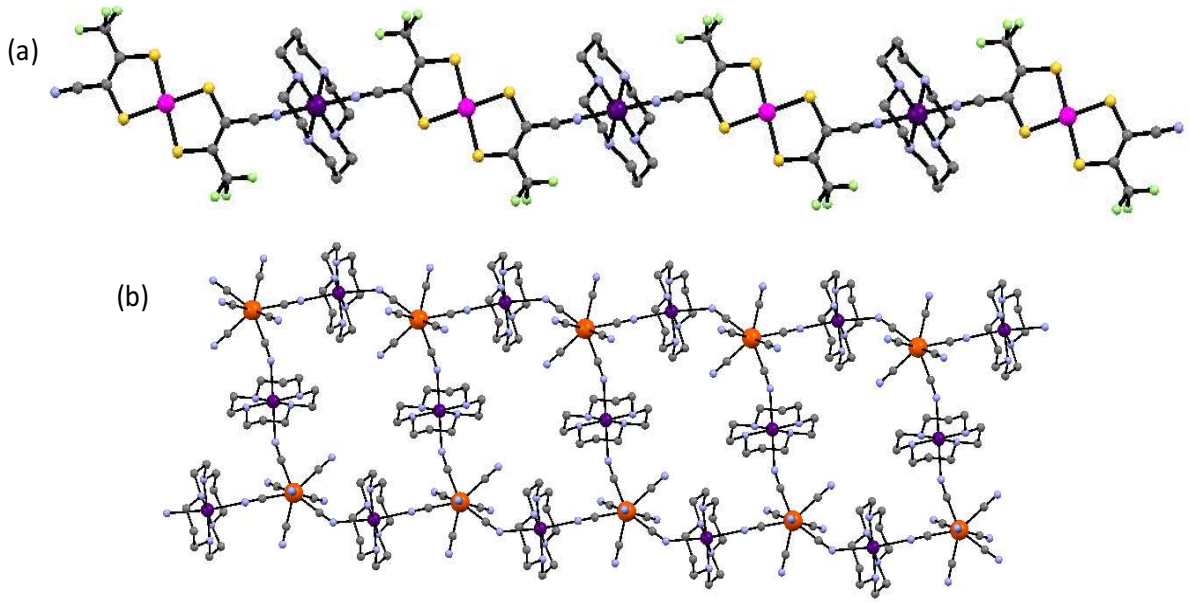

Figure II.6. (a) $[Ni^{II}(cyclam)][Cu^{II}(tfadt)_2]$ where the magenta, violet, pale green, blue, yellow, grey spheres represent the Cu, Ni, F, N, S and C atoms. The H atoms are omitted for clarity.[15] (b) The ladder type one dimensional compound $[Cu^{II}(cyclam)]_3[Mo^{V}(CN)_8]_2$ where the orange, violet, blue, grey spheres represent the Mo, Ni, N and C atoms. The H atoms are omitted for clarity.[16]

The axial positions of the $[M^{II}(cyclam)]^{2+}$ (M = Ni, Cu) complexes easily coordinate with donor-type ligands like cyanido and thus can form one dimensional arrangement of the $[M^{II}(cyclam)]^{2+}$ units via para- or diamagnetic linkers. For example, the reaction between $[Ni^{II}(cyclam)](ClO_4)_2$ and *trans*-$Na[Ru^{III}(salen)(CN)_2]$ forms a one dimensional chain compound having a ferromagnetic interaction between the Ni^{II} and Ru^{III}.[12] The Ni^{II} ion accepts electron density from the nitrogen atom of the cyanido ligand where the carbon of the cyanido ligand is connected to the Ru^{III}. The trinuclear compound $\{Ni^{II}(cyclam)[Ru^{III}(acac)_2(CN)_2]_2\}\cdot 2CH_3OH\cdot 2H_2O$ exhibits also a ferromagnetic interaction between the Ni^{II} and Ru^{III} ions of +4.6(2) cm^{-1} (+6.6 K, $H = -2J(S_{Ru1}\cdot S_{Ni} + S_{Ni}\cdot S_{Ru2})$).[13] Using the K_2CrO_4 precursor, a chain compound *catena*-(μ-CrO_4-O,O´)$[Ni^{II}(cyclam)]\cdot 2H_2O$ was reported with an ferromagnetic interaction between the Ni^{II} ions within the chain through the diamagnetic $[CrO_4]^{2-}$ bridge.[14] Using the copper dithiolene complex based on the tfadt ligand (tfadt = 3-trifluoromethylacrylonitrile-2,3-dithiolate) and $[Ni^{II}(cyclam)]^{2+}$ one can obtain the chain-like compound $[Ni^{II}(cyclam)][Cu^{II}(tfadt)_2]$ (figure II.6a) where the interaction between the Ni^{II} (S = 1) and Cu^{II} (S = ½) ions is ferromagnetic with J/k_B = +5.0(2) K.[15] The $[Cu^{II}(cyclam)]^{2+}$ unit has also been organized in a ladder-type one dimensional compound with the $[Mo^{V}(CN)_8]^{3-}$, having the molecular formula $[Cu^{II}(cyclam)]_3[Mo^{V}(CN)_8]_2.5H_2O$ where the magnetic exchange between the Cu^{II} and Mo^{V} is ferromagnetic (figure II.6b).[16]

II.2.2.2. $[M(LN_3O_2)]^{2+}$ macrocyclic complexes used in this thesis

Using the LN_3O_2 neutral macrocyclic ligand, we have synthesized two molecular precursors $[Fe^{II}(LN_3O_2)(H_2O)Cl]Cl$ and $[Mn^{II}(LN_3O_2)(H_2O)Cl]Cl$.[17,18] $[Fe^{II}(LN_3O_2)(H_2O)Cl]Cl$ was prepared with a slight modification of the synthetic procedure for $[Fe^{II}(LN_5)(H_2O)_2]Cl_2.4H_2O$ where LN_5 (2,13-dimethyl-3,6,9,-12,18-pentaazabicicylo[12.3.1]octadeca-1(18),2,12,14,16-pentaene) is a similar type pentadentate macrocyclic ligand.[17] The detailed synthesis, spectroscopic characterization and single crystal X-ray crystallographic characterization of these two complexes are described in section II.4.4. The Fe^{II} and Mn^{II} ions are hepta-coordinated, while the LN_3O_2 ligand coordinates with five equatorial positions of the metal ions and the two axial positions are occupied with water molecules or chlorido counter ions.

II.2.2.2.1. Magnetic properties

We have not measured the magnetic properties of $[Fe^{II}(LN_3O_2)(H_2O)Cl]Cl$ and $[Mn^{II}(LN_3O_2)(H_2O)Cl]Cl$ as literature allows us to understand the magnetic properties of these paramagnetic molecules.[17-19] In the hepta coordinated environment the Fe^{II} and the Mn^{II} ions are both

high spin with $S = 2$ (for $3d^6$ electrons) and $S = 5/2$ (for $3d^5$ electrons) spin ground states respectively. The quasi-C_{5v} symmetry of the Fe^{II} and Mn^{II} ions can promote strong axial anisotropy, one of the major ingredients of molecule based magnetic materials such as SMMs and SCMs.[17, 19] The crystal field environment of $[Fe^{II}(LN_3O_2)(H_2O)Cl]Cl$ are quite similar to those of $[Fe^{II}(LN_5)(H_2O)_2]Cl_2.4H_2O$ which exhibits a high magnetic anisotropy around 24.5 K.[17]

II.2.2.2.2. Examples of low dimensional coordination systems

The axial positions of both of the $[Fe^{II}(LN_3O_2)(H_2O)Cl]Cl$ and $[Mn^{II}(LN_3O_2)(H_2O)Cl]Cl$ molecular precursors can be substituted with bridging ligands or other electron donor moieties.

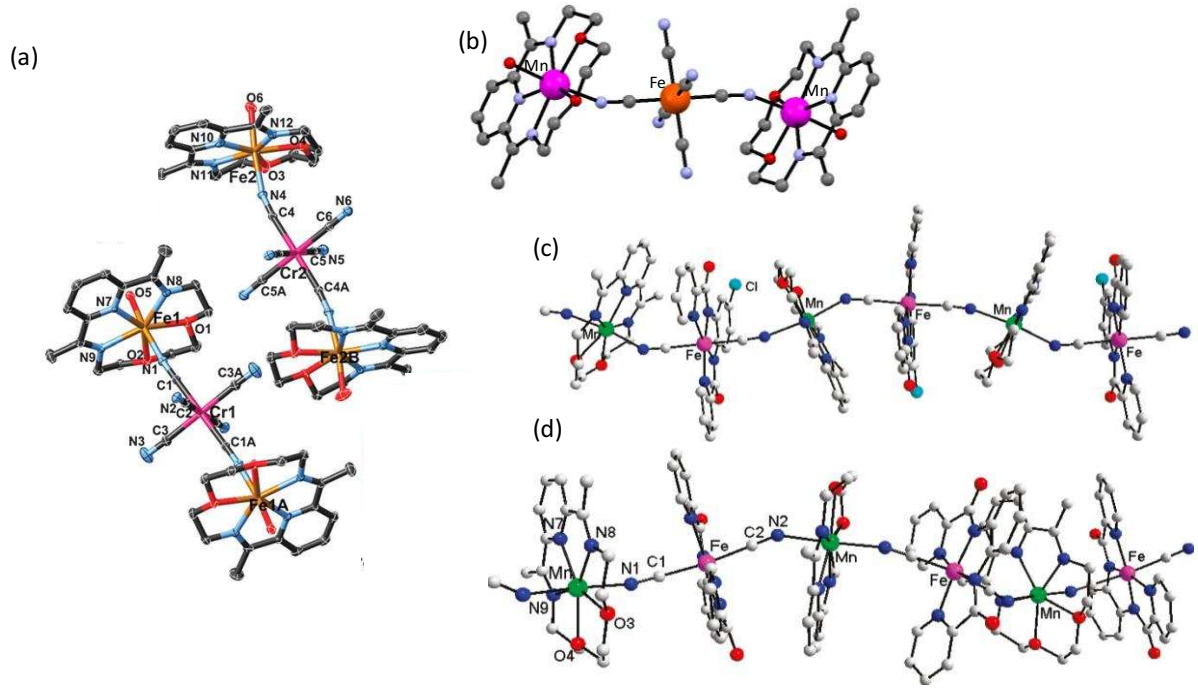

Figure II.7. (a) The trinuclear $\{[Fe^{II}(LN_3O_2)(H_2O)]_2[Cr^{III}(CN)_6]\}^+$ SMM; (b) The trinuclear $\{[Mn^{II}(LN_3O_2)(H_2O)]_2[Fe^{II}(CN)_6]\}^+$ complex where the blue, red and the grey spheres are the Mn, Fe, O, N and C atoms. (c) The one dimensional chain $[Mn^{II}(LN_3O_2)][Fe^{III}(bpClb)(CN)_2]^+$; (d) The one dimensional chain $[Mn^{II}(LN_3O_2)][Fe^{III}(bpb)(CN)_2]^+$; for all the figures the H atoms, the counter anions (in all the cases ClO_4^-) and the solvent molecules (solvents of crystallization) are omitted for clarity.

In the trinuclear molecule $\{[Fe^{II}(LN_3O_2)(H_2O)]_2[Cr^{III}(CN)_6]\}(ClO_4).3H_2O$, one of the axial coordination sites of the Fe^{II} ions is occupied by the nitrogen atom of the cyanido group of $[Cr^{III}(CN)_6]^{3-}$ moiety (figure II.7a).[19] The magnetic exchange between the Fe^{II} and the Cr^{III} ions is ferromagnetic through the cyanido bridge. This trinuclear molecule has a spin ground state $S_T = 11/2$ and exhibits a magnetic hysteresis loop below 1.8 K, as well as frequency-dependent *ac* magnetic susceptibilities. Therefore this compound is a Single Molecule Magnet with a spin reversal energy

barrier of 41 K. Another example of a trinuclear compound is $\{[(Mn^{II}LN_3O_2)(H_2O)]_2[Fe^{II}(CN)_6]\}\cdot MeOH\cdot 10H_2O$ where two $[Mn^{II}(LN_3O_2)]^{2+}$ fragments are connected through a $[Fe^{II}(CN)_6]^{4-}$ complex via the cyanido bridge (figure II.7b).[20] In this compound the Mn^{II} ions experience ferromagnetic interactions through the diamagnetic $[Fe^{II}(CN)_6]^{4-}$ linker. Moreover, the $[Mn^{II}(LN_3O_2)]^{2+}$ moiety coordinated to $[Cr^{III}(CN)_6]^{3-}$ through a cyanido bridge results in a one dimensional chain-like compound *n*-$\{[Mn^{II}(LN_3O_2)][Cr^{III}(CN)_6]\}^-$ where the Mn^{II} and Cr^{III} alternate in the chain.[20] The counter cation of crystallization of this negatively charged chain is the trinuclear compound $\{[Mn^{II}(LN_3O_2)(H_2O)]_2[Cr^{III}(CN)_6]\}^+$ where the two $[Mn^{II}(LN_3O_2)]^{2+}$ moieties are again bridged with $[Cr^{III}(CN)_6]^{3-}$ through the cyanido ligand. The nature of the magnetic interaction between the Mn^{II} and Cr^{III} ions was found to be ferromagnetic in this compound. The reaction between $[Mn^{II}(LN_3O_2)]^{2+}$ and $[Fe^{III}(bpb)(CN)_2]^-$ (bpb^{2-} = 1,2-bis(pyridine-2-carboxamido)benzenate) or $[Fe^{III}(bpClb)(CN)_2]^-$ ($bpClb^{2-}$ = 1,2-bis(pyridine-2-carboxamido)-4-chorobenzenate) results in 1:1 one dimensional compounds (figure II.7c and II.7d). The temperature dependence of the magnetic susceptibility of these chain compounds with antiferromagnetic coupling between the Mn^{II} and Fe^{III} spin carriers through the cyanido bridge.[18a]

II.3. 4*d* and 5*d* complexes acting as donor precursors

In the first chapter, we mentioned our preference for 4*d* and 5*d* metal-based molecular precursors due to their high anisotropic character coming from spin orbit coupling. Therefore in order to synthesize magnetic molecules with the control over the dimensionality, we have selected two kinds of *trans*-cyanido paramagnetic molecules: *trans*-$(Bu_4N)_2[Re^{IV}Cl_4(CN)_2]\cdot 2DMA$ (Re^{IV} has $5d^3$ electronic configuration and $S = 3/2$) and *trans*-$Ru^{III}(CN)_2$-Schiff base complexes (low spin Ru^{III} has $4d^5$ electrons and $S = 1/2$, where the Schiff bases are salen type chelating ligands). The *trans*-$[Re^{IV}Cl_4(CN)_2]^{2-}$ and the *trans*-$Ru^{III}(CN)_2$-Schiff base units are electron donors through the nitrogen end of the cyanido ligand (figure II.1a and II.1b) and therefore can coordinate with a maximum of two electron acceptor metal ions. The magnetic properties and the literature examples of these molecular precursors are shown below.

II.3.1. The tetrabutylammonium salt of *trans*-$[Re^{IV}Cl_4(CN)_2]^{2-}$

The *trans*-$[Re^{IV}Cl_4(CN)_2]^{2-}$ building block was synthesized as the tetrabutylammonium salt using commercially available $Re^{V}Cl_5$ following a literature method.[21a] The detailed synthesis,

spectroscopic characterization and single crystal X-ray structure of the *trans*-$(Bu_4N)_2[Re^{IV}Cl_4(CN)_2]\cdot 2DMA$ are given in section II.4.5.

II.3.1.1. Magnetic properties of *trans*-$(Bu_4N)_2[Re^{IV}Cl_4(CN)_2]\cdot 2DMA$

In *trans*-$(Bu_4N)_2[Re^{IV}Cl_4(CN)_2]\cdot 2DMA$ the Re^{IV} ion adopts a high spin $5d^3$ electronic configuration, and in the octahedral crystal field the three unpaired electrons reside in the t_{2g} energy level. In figure II.8a the temperature dependence of the magnetic susceptibility of *trans*-$(Bu_4N)_2[Re^{IV}Cl_4(CN)_2]\cdot 2DMA$ is plotted as χT vs. T collected under a 1000 Oe *dc* magnetic field.[21a] The magnetic susceptibility data of the compound yields a value of χT = 1.27 cm^3K/mol at 300 K, corresponding to an S = 3/2 spin ground state with g = 1.65. In lowering the temperature, the χT product remains almost constant until 70 K, and a further decrease of temperature results in a significant decrease of the χT values. This low temperature decrease of the magnetic susceptibility is the indication of the presence of magnetic anisotropy in the system. Additionally, the plot of the reduced magnetization reveals a series of non-superimposable isofield curves, which also indicates the presence of significant anisotropy in this paramagnetic complex (figure II.8b). The quantification of this isofield data yields the zero field splitting parameter D = - 14.4 cm^{-1} (D/k_B = 20.2 K) and g = 1.66. The high value of the D parameters implies that the heavy Re^{IV} center possesses large values of spin orbit coupling. But there is a controversy about how to describe the magnetic anisotropy of this Re^{IV} precursor. High-field electron paramagnetic resonance spectroscopy reveals the presence of a rhombic anisotropy with a large transverse component, E, in this compound.[21c] The complete understanding of the magnetic anisotropy of this compound is still lacking.

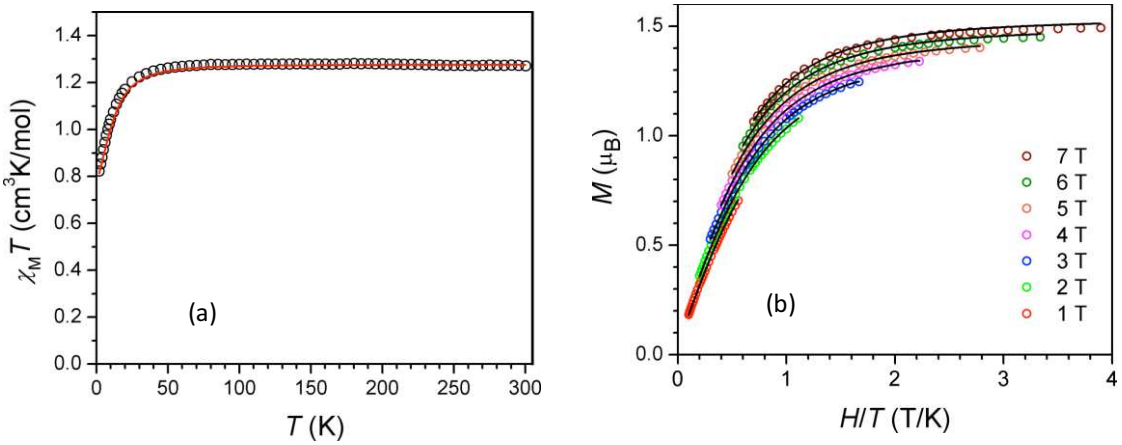

Figure II.8. (a) Variable-temperature magnetic susceptibility data collected for *trans*-$(Bu_4N)_2[Re^{IV}Cl_4(CN)_2]\cdot 2DMA$ under an applied *dc* field of 1000 Oe. The hollow black circles are the experimental data and the solid red line is the fit of the experimental data yielding the parameters D = -14.4 cm^{-1} (~20.2 K) and g = 1.66. (b) Low-temperature magnetization data for *trans*-$(Bu_4N)_2[Re^{IV}Cl_4(CN)_2]\cdot 2DMA$ collected under various applied *dc* fields. The black lines represent fits to the data.[21a]

II.4.1.2. Literature examples containing the *trans*-$[Re^{IV}Cl_4(CN)_2]^{2-}$ unit

The *trans*-$[Re^{IV}Cl_4(CN)_2]^{2-}$ unit has two axially coordinated cyanido groups which can coordinate with electron acceptor metal ions. This molecular precursor can make one dimensional compounds with an alternative arrangement of $[M^{II}(DMF)_4]^{2+}$ (M = Fe, Mn, Ni, Co) having the molecular formula $[(DMF)_4M^{II}Re^{IV}Cl_4(CN)_2]_\infty$. These chain compounds show Single Chain Magnet properties (figure II.9a).[21a] In these one dimensional systems, the S = 3/2 Re^{IV} spin shows ferromagnetic interactions with the Fe^{II}, Ni^{II} and Co^{II} magnetic centers whereas the magnetic exchange between Re^{IV} and Mn^{II} is antiferromagnetic.

Moreover, $(Bu_4N)[TpCu^{II}Re^{IV}Cl_4(CN)_2].1.33CH_3CN$ is a one dimensional chain compound (figure II.10a) where the Re^{IV} and the Cu^{II} spin carriers exhibit a huge ferromagnetic exchange of +41(2) K (figure II.10b).[21b] This compound orders antiferromagnetically below 11 K with a metamagnet type behavior induced by significant interchain antiferromagnetic interactions.

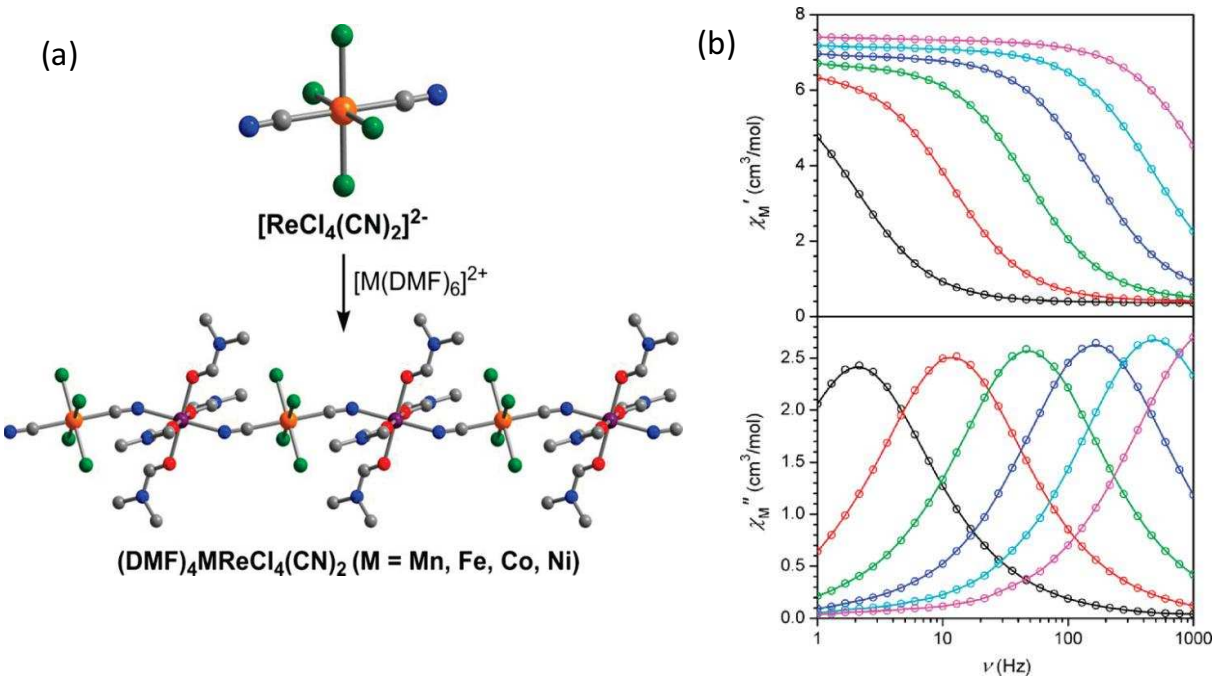

Figure II.9. $(DMF)_4M^{II}Re^{IV}Cl_4(CN)_2$ Single Chain Magnets (M = Ni, Co, Fe, Mn) (a) the one dimensional chain; orange, purple, green, red, blue, and gray spheres represent Re, M, Cl, O, N, and C atoms, respectively; H atoms have been omitted for clarity. (b) Variable-frequency in-phase (top) and out-of-phase (bottom) *ac* magnetic susceptibility data for $(DMF)_4Mn^{II}Re^{IV}Cl_4(CN)_2$, collected in a 4 Oe *ac* field at temperatures of 2.2 (black), 2.4 (red), 2.6 (green), 2.8 (blue), 3.0 (cyan), and 3.2 K (magenta).

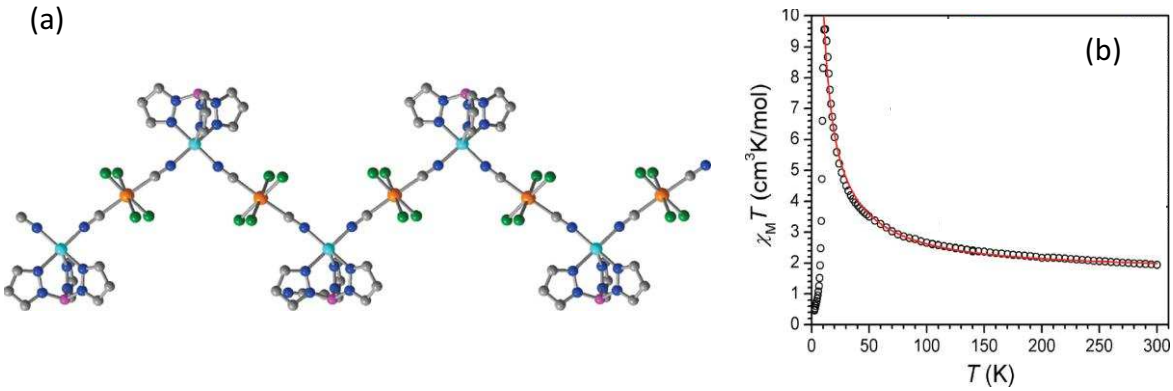

Figure II.10. (a) One dimensional chain of $(Bu_4N)[TpCuReCl_4(CN)_2].1.33CH_3CN$, Orange, cyan, green, purple, gray, and blue spheres represent Re, Cu, Cl, B, C, and N atoms, respectively; H atoms are omitted for clarity. (b) Variable-temperature magnetic susceptibility of $(Bu_4N)[TpCuReCl_4(CN)_2].1.33CH_3CN$ plotted as χT vs. T collected under a *dc* field of 1000 Oe.

II.3.2. *Trans*-$Ru^{III}(CN)_2$-Schiff base complexes

The *trans*-$Ru^{III}(CN)_2$-Schiff base complexes were synthesized using commercially available $Ru^{III}Cl_3$ and salen-type Schiff base ligands following globally the method of Leung and Che.[22a] The Ru^{III} ion is in an octahedral ligand field where the equatorial coordination sites are occupied with the two imino nitrogen atoms and the two phenoxo oxygen atoms from the salen-type chelating Schiff base ligands. The carbon atom of two cyanido ligands satisfies the remaining two axial coordination sites. This type of building block acts like an electron donor type moiety and therefore can coordinate with different metal centers through the nitrogen end of cyanido ligand (figure II.1b).

II.3.2.1. Literature examples containing the *trans*-$Ru^{III}(CN)_2$-Schiff base unit

The *trans*-$[Ru^{III}(salen)(CN)_2]^-$ building block has been combined with different molecular precursors to make zero to two dimensional compounds. The reaction between the $Na[Ru^{III}(salen)(CN)_2]$ and $[Ni^{II}(cyclam)](ClO_4)_2$ results into a one dimensional compound of molecular formula $[Ru^{III}(salen)(CN)_2][Ni^{II}(cyclam)](ClO_4)$ where the Ni^{II} and the Ru^{III} alternate in the chain (inset of figure II.11a).[22b] The temperature dependent magnetic susceptibility reveals a ferromagnetic interaction between the Ru^{III} and Ni^{II} in this one dimensional system (figure II.11a).

Using *trans*-$(Bu_4N)[Ru^{III}(salen)(CN)_2]$, one trinuclear compound $[Mn^{II}(CH_3OH)_4][Ru^{III}(salen)(CN)_2]_2{\cdot}6CH_3OH{\cdot}2H_2O$ and a two dimensional sheet-like compound of molecular formula $\{Mn^{II}(H_2O)_2[Ru^{III}(salen)(CN)_2]_2{\cdot}H_2O\}$ has been reported where the magnetic

exchange between the Ru^{III} and Mn^{II} were found to be weakly antiferromagnetic.[23] Another one dimensional complex has been reported having the molecular formula $[Ru^{III}(salen)(CN)_2][Mn^{III}(L)]$ (L = *N, N′*-(1- methylethylene)bis(2-hydroxynaphthalene-1-carbaldehydene iminate) dianion) where the Mn^{III} and Ru^{III} ions are alternatively arranged in the chain bridged by the cyanido group (figure II.11b).[23b] The magnetic exchange between the Ru^{III} and the Mn^{III} in this compound is ferromagnetic in nature. In this compound, we also see that the low temperature *ac* magnetic susceptibilities (χ' and χ'') are slightly frequency dependent, which is a signature of a glassy magnetized state probably reminiscent of SCM-like behavior or spin canting.

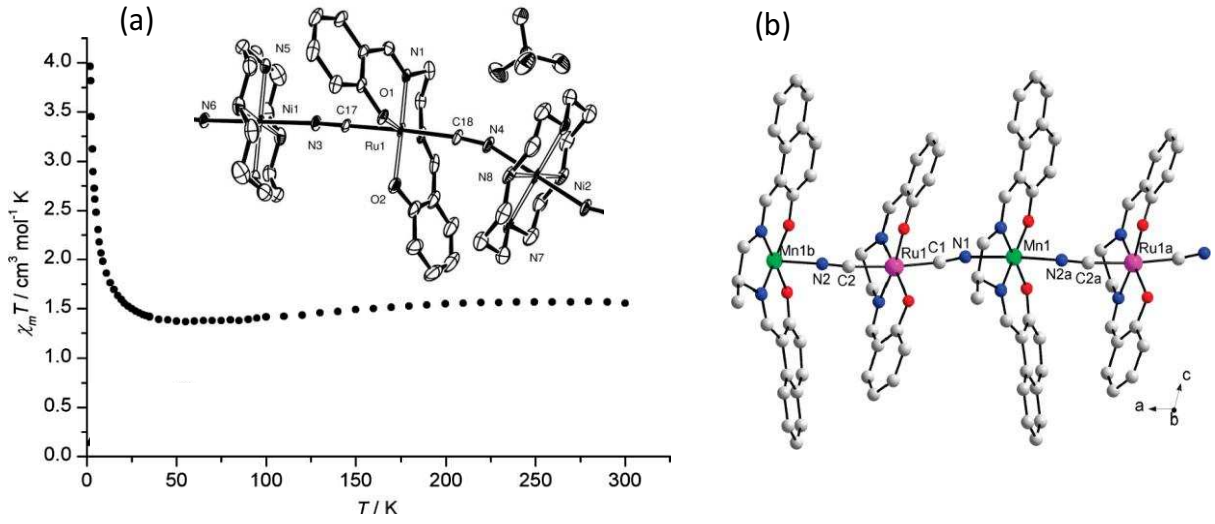

Figure II.11. (a) The temperature dependence of the χT product of the chain $[Ru^{III}(salen)(CN)_2][Ni^{II}(cyclam)](ClO_4)$ (the ORTEP figure with 50% thermal ellipsoid is in the inset).[22b] (b) The one dimensional chain $[Ru^{III}(salen)(CN)_2][Mn^{III}(L)]$ (L = *N, N′*-(1-methylethylene)bis(2-hydroxynaphthalene-1-carbaldehydeneiminate) dianion).[23]

II.3.2.2. The *trans*-$Ru^{III}(CN)_2$-Schiff base complexes used in this thesis

In the present research work, we have synthesized two types of *trans*-$Ru^{III}(CN)_2$-Schiff base molecular precursors having the molecular formula *trans*-$(Ph_4P)[Ru^{III}(salen)(CN)_2]\cdot MeOH\cdot H_2O$ and *trans*-$(Bu_4N)[Ru^{III}(5\text{-Cl-saltmen})(CN)_2]$ where $salen^{2-}$ = *N, N'*-bis(salicylidene)-ethylenediamine dianion and 5-Cl-$saltmen^{2-}$ = *N, N′*-bis(5-chloro-salicylidene)-1,1,2,2-tetramethylethylenediamine dianion. The detailed synthesis, infrared spectra and the single crystal X-ray crystallographic characterization of both of these Ru^{III} precursors are provided in section II.4.6. The synthesis and the characterization of the Schiff base ligands are described in section II.4.1.

II.3.2.3. The magnetic properties of the *trans*-$Ru^{III}(CN)_2$-Schiff base complexes

The Ru^{III} ion has a $4d^5$ electronic configuration and the *trans*-$Ru^{III}(CN)_2$-Schiff base complexes are low spin, i.e. with an $S = ½$ spin ground state.[13,22,23] In our thesis project, we have measured the magnetic properties of *trans*-$(Ph_4P)[Ru^{III}(salen)(CN)_2]\cdot MeOH\cdot H_2O$ to ensure the spin states of the Ru^{III} ion. The temperature dependence of the magnetic susceptibility of *trans*-$(Ph_4P)[Ru^{III}(salen)(CN)_2]\cdot MeOH\cdot H_2O$ was measured at 1000 Oe between 1.8 and 290 K.

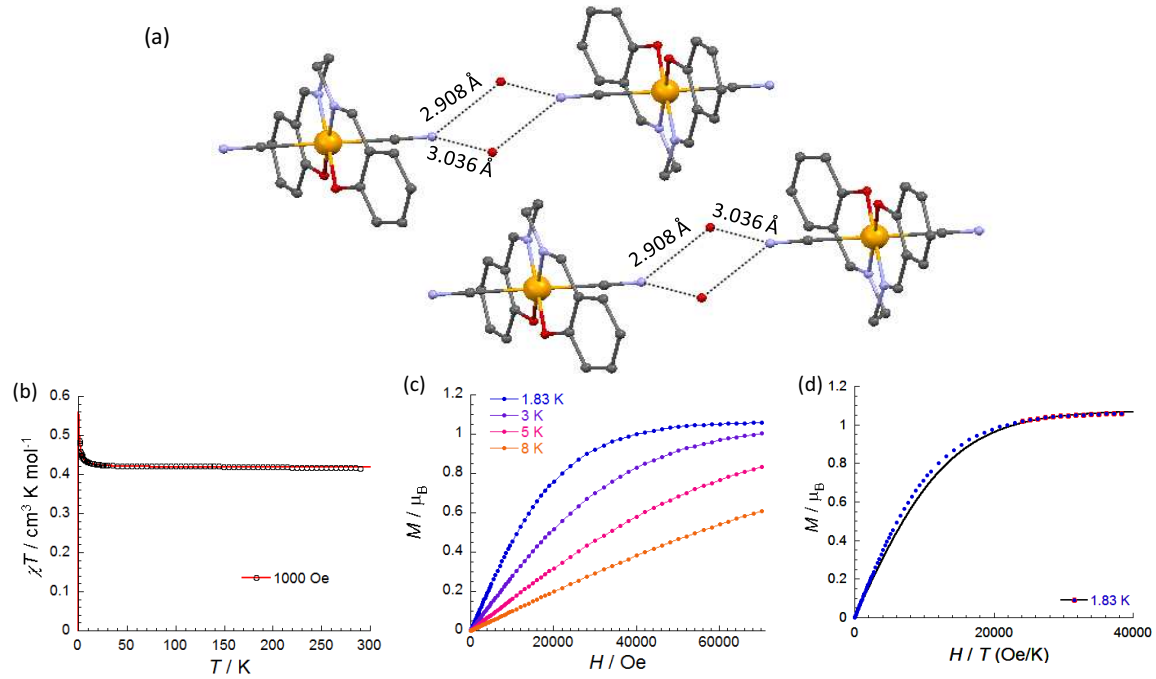

Figure II.12. (a) The H bonding interaction between the pair like $[Ru^{III}(salen)(CN)_2]$ units in crystal packing of *trans*-$(Ph_4P)[Ru^{III}(salen)(CN)_2]\cdot MeOH\cdot H_2O$. The orange, grey, blue and red spheres respectively represent the Ru, C, N and O atoms. (b) The temperature dependence of χT for *trans*-$(Ph_4P)[Ru^{III}(salen)(CN)_2]\cdot MeOH\cdot H_2O$ measured at 1000 Oe. The solid red line corresponds to the fit of experimental data with the equation $\chi T = (Ng^2\mu_B{}^2/k_B)(3+\exp(-2J/k_BT))^{-1}$. (c) The $M(H)$ plots of *trans*-$(Ph_4P)[Ru^{III}(salen)(CN)_2]\cdot MeOH\cdot H_2O$ at different temperatures between 1.83-8 K. (d) The fit (solid black line) of M vs. H/T data at 1.83 K for a $S = ½$ Brillouin function corresponds only a few experimental values (circled with red) at high field.

As shown in figure II.12a, at room temperature the χT product is 0.42 cm^3K/mol corresponding to the theoretical value expected for an one isolated $S = 1/2$ Ru^{III} center with $g = 2.10(6)$. Decreasing the temperature, the χT product remains unchanged in magnitude until 35 K, where it increases to reach 0.49 cm^3K/mol at 1.8 K. This increase of the χT product at low temperature originates from a small ferromagnetic interaction between two $[Ru^{III}(salen)(CN)_2]^-$ moieties in the crystal packing. In the crystal structure of *trans*-$(Ph_4P)[Ru^{III}(salen)(CN)_2]\cdot MeOH\cdot H_2O$, we can see that two of $[Ru^{III}(salen)(CN)_2]^-$ molecules form pairs with hydrogen bonding short contacts via a water molecule and one of the cyanido nitrogen atoms of each (figure II.12a, a more detail crystal structure

description of this complex is in the section II.4.6.3). This supramolecular interaction gives rise to ferromagnetic exchange inside the pair of $[Ru^{III}(salen)(CN)_2]^-$ moieties. The χT vs. T product was fitted with the Heisenberg model $H = -2JS_1.S_2$ where $S_1 = S_2 = ½$ for two Ru^{III} centers and J is the magnetic exchange between them. This model yields the magnetic susceptibility as: $\chi T = (Ng^2\mu_B^2/k_B)(3+\exp(-2J/k_BT))^{-1}$ per Ru^{III} site, and the fit of the data (solid red line in figure II.12b) gives $g = 2.11(3)$ and $J/k_B = + 0.64(3)$ K. Furthermore, the field dependence of the magnetization has also been measured in the temperature range 1.83-8 K (figure II.12c) and shows that the magnetization is saturated at 7 T at 1.83 K providing a value of 1.1 μ_B which is expected for a $S = 1/2$ paramagnetic material. The M vs. H/T data at 1.83 K were not well reproduced with $S = ½$ Brillouin function (figure II.12d) in order to estimate the Landé factor ($g = 2.14$) due to the presence of the weak ferromagnetic interactions in the $[Ru^{III}(salen)(CN)_2]^-$ pairs.

II.4. Experimental details for all the molecular precursors

In this part of the chapter, we will detail the synthetic methods used to obtain all the precursors along with their infrared (IR) spectroscopic characterization. As far as possible, these metal precursor compounds have also been characterized by single crystal X-ray crystallography. All the chemical reagents and solvents are used as received from the suppliers without further purification. The synthesis and characterization were done at room temperature unless otherwise mentioned.

II.4.1.The Schiff base ligands

All the tetradentate Schiff base ligands were synthesized from a nucleophilic substitution reaction of salicylaldehyde or salicylaldehyde derivatives (with substitution on the aromatic ring) with aliphatic or aromatic primary diamines. This condensation results in the formation of di-imine (R-C=N-) type molecules. The name of the different salicylaldehydes and the primary diamines used in this thesis to synthesize the Schiff base ligands are listed below in table II.2. All the diamines except 1,1,2,2-tetramethylethylenediamine are commercially available and were obtained from chemical suppliers**.**

Table II.2. The list of the salicylaldehydes and primary diamines used in this thesis to synthesize the Schiff base ligands

Salicylaldehyde derivatives		**Primary diamines**
Salicylaldehyde	5-Cl-salicylaldehide	Ethylenediamine
3-MeO-salicylaldehyde	5-F-salicylaldehide	1,1,2,2-tetramethylethylenediamine
4-MeO-salicylaldehyde	5-^{t}Bu-salicylaldehyde	*o*-Phenylenediamine
5-MeO-salicylaldehyde	4-HO-salicylaldehyde	Propylenediamine
5-Me-salicylaldehyde		1,3-Diaminopropane

II.4.1.1. Synthesis of the Schiff base ligands

The general synthesis of all Schiff base ligands is quite similar except for the reaction time and the final yield of the product. While stirring, 1 equivalent of diamine was added slowly to a solution of 2 equivalents of the salicylaldehyde derivative in absolute ethanol, instantly resulting in a yellow solution. The reaction mixture was heated at about 70° C and stirred continuously for 2-6 hours to obtain a yellow crystalline precipitate of the Schiff base ligand. The reaction mixture was cooled at room temperature and the ligand was collected by filtration and dried in air. The yield of the product can be increased by collecting the rest of the ligand in the filtrate either after decreasing its volume through evaporation or by the addition of excess water.

Figure II.13 presents the general scheme of the synthesis of these salen type Schiff base ligands. Figure II.14 shows some Schiff base ligands used in this thesis with their commonly used names.

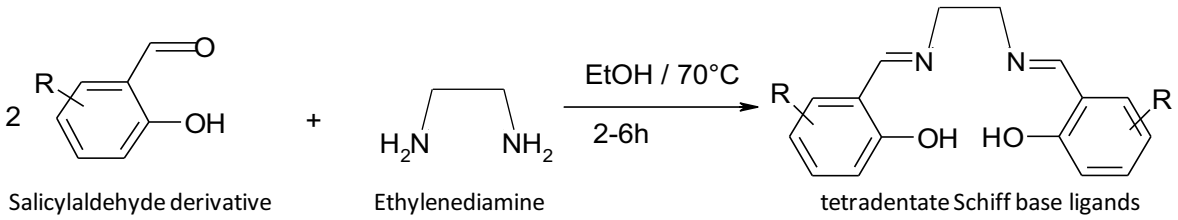

Figure II.13. Synthesis of salen-type tetradentate Schiff base ligands.

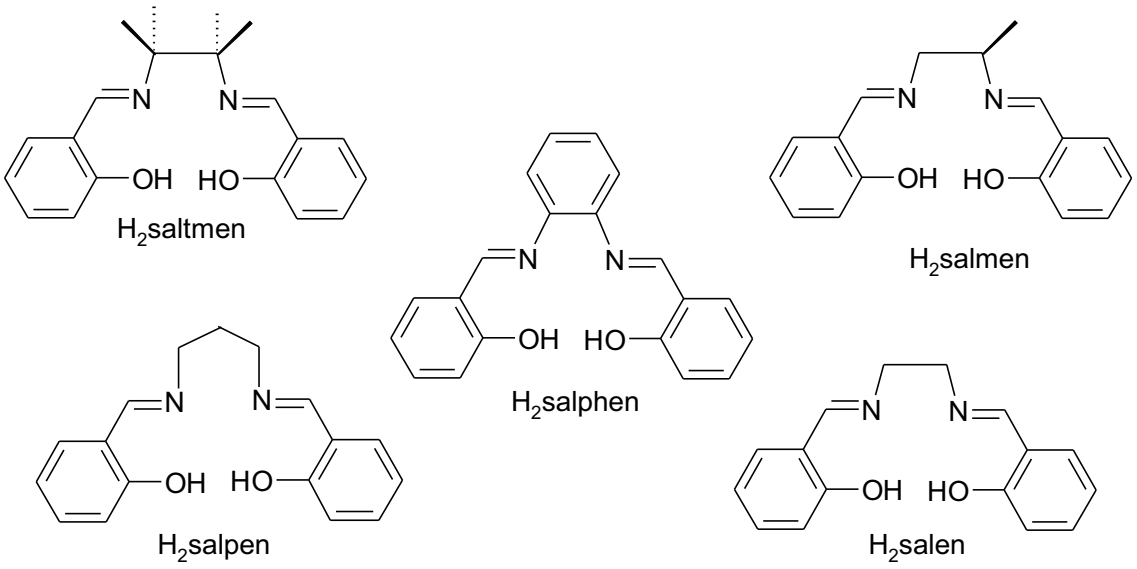

Figure II.14. Different Schiff base ligands (without showing the substituent on the aromatic ring) [(H_2salen = *N, N′*-bis(salicylidene)-ethylenediamine, H_2salmen = *N, N′*-bis(salicylidene)-1-methylethylenediamine, H_2salpen = *N, N′*-bis(salicylidene)-propylenediamine, H_2saltmen = (*N, N′*-bis(salicylidene)-1,1,2,2-tetramethylethylenediamine, H_2salphen = *N ,N′*-phenylenebis(salicylideneimine)]

The 1,1,2,2-tetramethylethylenediamine is not commercially available. Thus we have synthesized it according to the following method.[24] Figure II.15 represents the reaction scheme of the synthesis of this diamine.

Synthesis of 1,1,2,2-tetramethylethylenediamine: In a flask, 9.815 g of 2,3-dimethyl-2,3-dinitrobutane and 85 mL of concentrate hydrochloric acid were stirred together for 20 minutes at 60° C at reflux. Then Sn (99 % powder, 57.67 g) was slowly added over one hour with constant stirring to avoid the coagulation of the tin powder as much as possible. The whole mixture was refluxed for 6 hours. In this strong reducing environment, the dinitro complex converted to the diamine (1,1,2,2-tetramethylethylenediamine) with the nascent hydrogen generated from the oxidation of tin to tin chloride by concentrated HCl. After refluxing for 6 hours, the solution was cooled to room temperature and filtered. To the aqueous solution, 100 mL of diethyl ether was added followed by vigorous shaking, the solution was then allowed to stand for a complete separation of the organic phase containing the unreacted 2,3-dimethyl-2,3-dinitrobutane. The organic phase was discarded and this process was repeated for 3-4 times to remove all the dinitro precursors from the reaction mixture. While stirring, a very concentrated aqueous solution of 40 g sodium hydroxide was added to the aqueous solution very slowly drop by drop, for an hour to make it strongly basic (pH = 13-14). The addition of sodium hydroxide is very exothermic; hence a great attention should be taken during this addition. To avoid the rise of temperature of the reaction mixture, the addition of base may be done using an ice bath. After stirring the whole mixture during 3 hours at room temperature, the clear aqueous solution was filtered and the 1,1,2,2-tetramethylethylenediamine was extracted five times with 40 mL of dichloromethane. The organic layer was recovered and evaporated under vacuum resulting a white crystalline solid of 1,1,2,2-tetramethylethylenediamine (yield 60% on basis of dinitro compound).

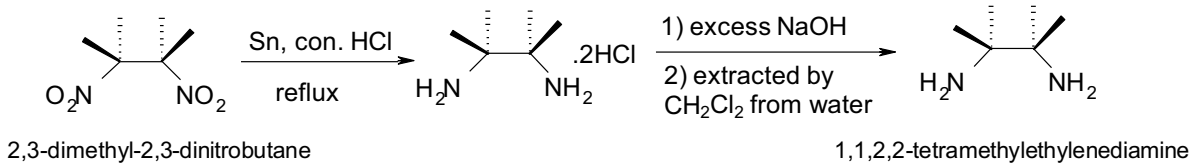

Figure II.15. Synthesis of the 1,1,2,2-tetramethylethylenediamine.

II.4.1.2. Infrared spectroscopic characterization

All the Schiff base ligands were characterized with FT-IR spectroscopic analysis. The formation of the imine bond (-C=N-) can be confirmed by the C=N stretching vibration frequency in the range of 1600-1640 cm^{-1}. Table II.3 lists the important characteristic stretching vibrations like $\bar{\nu}_{C=N}$, $\bar{\nu}_{C-O}$, $\bar{\nu}_{C-H}$, $\bar{\nu}_{C=C}$, $\bar{\nu}_{C-Cl}$, and $\bar{\nu}_{C-F}$ for all of the Schiff base ligands used in this thesis.

Table II.3. Some important infrared stretching vibrations of the Schiff base ligands used in this thesis.

The Schiff base	Stretching vibrations frequencies ($\bar{\nu}$) in cm^{-1}					
	$\bar{\nu}_{C=N}$	$\bar{\nu}_{C-O}$	$\bar{\nu}_{C-H}$	$\bar{\nu}_{C=C}$	$\bar{\nu}_{C-Cl}$	$\bar{\nu}_{C-F}$
$SaltmenH_2$	1624	1278	2982	1581		
3-MeO-$SaltmenH_2$	1621	1256	2984, 2941	1571		
4-MeO-$SaltmenH_2$	1616	1282	2982, 2940	1577		
5-MeO-$SaltmenH_2$	1629	1268	2987, 2938	1592		
5-Me-$SaltmenH_2$	1623	1277	2993, 2941, 2918	1589		
5-Cl-$SaltmenH_2$	1627	1276	2978, 2956	1568	695	
5-F-$SaltmenH_2$	1630	1272	2977	1586		767
5-^{t}Bu- $SsaltmenH_2$	1624	1268	2952, 2901	1587		
4-HO-$SaltmenH_2$	1630	1273	2986	1585		
$SalphenH_2$	1609	1275		1584, 1560		
5-Cl-$SalmenH_2$	1632	1278	2941, 2987	1576, 1590	695	
5-MeO-$SalpenH_2$	1631	1266	2902, 2930	1587		
5-Me-$SalpenH_2$	1633	1280	2915	1586		
$SalenH_2$	1608	1281	2901	1576		
5-MeO-$SalenH_2$	1636	1274	2937, 2959	1585		

II.4.2. Mn^{III}-Schiff base complexes

All of the Mn^{III}-Schiff base complexes have been synthesized using a similar reaction procedure using the tetradentate Schiff base ligands and commercially available manganese (III) acetate precursors.

II.4.2.1. Synthetic details of the Mn^{III}-Schiff base complexes

The Mn^{III}-Schiff base complexes (except Mn^{III}(salphen)(CH_3COO)) were synthesized as the perchlorate salts in a one step reaction (Caution! Perchlorates are explosive, should be used in small quantity). 5 mmol of the previously synthesized Schiff base ligands is dissolved in 40 mL of MeOH, warming (40-50° C) if necessary to dissolve the solid. Then a 20 mL methanol solution containing 5 mmol manganese (III) acetate (1.34 g) was added. The brown solution was heated to 50° C while stirring for 30 minutes. Then 0.61 g (5 mmol) of solid sodium perchlorate was added to the stirred hot solution. The heating was continued for five more minutes followed by addition of 50 mL boiling water and then filtered. The filtrate was left to stand for one to two days at room temperature. Dark brown crystals (in some cases greenish brown) were collected by suction filtration, washed with a minimum amount of water and dried in air. The yield of the product is above 80 % for most of the Mn^{III}- Schiff base precursors.

Mn^{III}(salphen)(CH_3COO) was synthesized by adding 5 mmol of manganese (III) acetate (1.34 g) to a 30 mL of hot (50° C) methanol solution containing 5 mmol of H_2salphen under stirring.

Subsequent cooling of the solution results in the precipitation of the product. Mn^{III}(salphen)(CH_3COO) was then crystallized from MeOH.

II.4.2.2. Infrared spectroscopic characterization

Table II.4 contains a list of the FT-IR stretching vibrations $\bar{\nu}_{Cl-O}$, $\bar{\nu}_{C=N}$, $\bar{\nu}_{C-O}$ and $\bar{\nu}_{O-H}$ for all the Mn^{III}-Schiff base compounds. The strong and broad $\bar{\nu}_{Cl-O}$ stretch (1030-1150 cm^{-1}) from the perchlorate ion is characteristic of these Mn^{III}-Schiff bases complexes. The broad band in the 3350-3450 cm^{-1} region is an indication of O-H stretching coming from the coordinated water molecule in the Mn^{III}-Schiff base complexes. The imine (C=N) stretching bands $\bar{\nu}_{C=N}$ shift to lower wavenumber than in the free ligand, due to the formation of Mn-N bonds. The C-O stretching frequency shifts to higher wavenumber compared to the free Schiff base ligands, which is a confirmation of the formation of the new Mn-O-C bonds. The [Mn^{III}(salphen)(CH_3COO)] precursor showed no perchlorate infrared peaks, but rather a broad peak near 1651 cm^{-1} corresponding to $\bar{\nu}_{C=O}$ i.e., the stretching of the carbonyl bond originating from the acetate ligand. The $\bar{\nu}_{C=N}$ of this compound is at 1590 cm^{-1}, and the $\bar{\nu}_{C-O}$ are at 1257, 1284 cm^{-1}.

Table II.4. List of characteristic FT-IR stretching vibrations for Mn^{III}-Schiff base complexes

Mn^{III}-Schiff base complexes	Stretching vibrations frequencies ($\bar{\nu}$) in cm^{-1}			
	$\bar{\nu}_{Cl-O}$	$\bar{\nu}_{C=N}$	$\bar{\nu}_{C-Ophen}$	$\bar{\nu}_{O-H}$
$[Mn^{III}_2(saltmen)_2(H_2O)_2](ClO_4)_2$	1070, 1121	1596	1269, 1286	3382, 3213
$[Mn(3\text{-}MeO\text{-}saltmen)(CH_3OH)(H_2O)](ClO_4)$	1058, 1080, 1099	1597	1258, 1305	3378, 3421
$[Mn^{III}(4\text{-}MeO\text{-}saltmen)(H_2O)_2](ClO_4).2H_2O$	1067, 1088, 1099	1599	1234, 1271	3001, 3211
$[Mn^{III}_2(5\text{-}MeO\text{-}saltmen)_2(H_2O)_2](ClO_4)_2$	1073, 1107	1603	1232, 1247, 1270	3211, 3348
$[Mn^{III}_2(5\text{-}Me\text{-}saltmen)_2(H_2O)_2](ClO_4)_2$	1066, 1097	1598	1250, 1286, 1328	3321, 3228
$[Mn^{III}(5\text{-}F\text{-}saltmen)(H_2O)_2](ClO_4)$	1051, 1091, 1140	1608	1253, 1282	3451
$[Mn^{III}_2(5\text{-}Cl\text{-}saltmen)_2(H_2O)_2](ClO_4)_2$	1059, 1080, 1117	1597	1258, 1305	3378, 3421
$[Mn^{III}_2(5\text{-}^tBu\text{-}saltmen)_2(H_2O)_2](ClO_4)_2$	1077, 1095	1613	1254, 1304	3460, 3297
$[Mn^{III}(4\text{-}HO\text{-}saltmen)(H_2O)_2](ClO_4)\cdot H_2O$	1059, 1126, 1137	1596	1201, 1237, 1264	3345, 3151
$[Mn^{III}(5\text{-}Cl\text{-}salmen)(H_2O)_2](ClO_4)$	1039, 1087	1617	1240, 1262, 1279	3299, 3471
$[Mn^{III}(5\text{-}MeO\text{-}salpen)(H_2O)_2](ClO_4)\cdot H_2O$	1031, 1062, 1110	1595	1234, 1272, 1278	3310, 3176
$[Mn^{III}_2(5\text{-}Me\text{-}salpen)_2(H_2O)_2](ClO_4)_2$	1071, 1129	1616	1230, 1274, 1294	3383, 3176
$[Mn^{III}(5\text{-}MeO\text{-}salen)(H_2O)_2](ClO_4)$	1034, 1076, 1100	1610	1244, 1275	3235, 3454

II.4.2.3. X-ray crystal structure

For all of the Mn^{III}-Schiff base compounds, X-ray crystallographic data were collected on the single crystal to determine firstly whether the right precursor has been synthesized and then if it crystallizes in the mononuclear or dinuclear form. Table II.5 and II.6 contain the X-ray crystallographic parameters of the mononuclear and the dinuclear Mn^{III}-Schiff base complexes respectively. Herein, the crystal structures are not described in great details as our present work does

not require such a detailed inspection into the crystal packing of the molecular precursors. From the crystal structure of these Mn^{III}-Schiff base complexes we basically look for the exact molecular formula and the nuclearity of the complexes, which is quantitatively very important to perform further synthesis of molecule-based magnets. Figure II.16 and figure II.17 display respectively the crystal structure of the mononuclear and the dinuclear Mn^{III}-Schiff base complexes.

Mn^{III}-Schiff base complexes crystallized in the mononuclear form:

[Mn^{III}(3-MeO-saltmen)(CH_3OH)(H_2O)](ClO_4): In this compound (figure II.16a), one of the axial positions of the Mn^{III} ion is occupied with a water molecule whereas the other axial position is satisfied with the oxygen atom coming from a methanol molecule.

[Mn^{III}(5-F-saltmen)(H_2O)$_2$](ClO_4): In this compound (figure II.16b), both axial positions of the Mn^{III} ion are coordinated with water molecules.

[Mn^{III}(4-MeO-saltmen)(H_2O)$_2$](ClO_4)·2H_2O: The Mn^{III} ion of this molecular precursor (figure II.16c) is also axially coordinated with two water molecules and the crystal also contains two molecules of water as the solvent of crystallization.

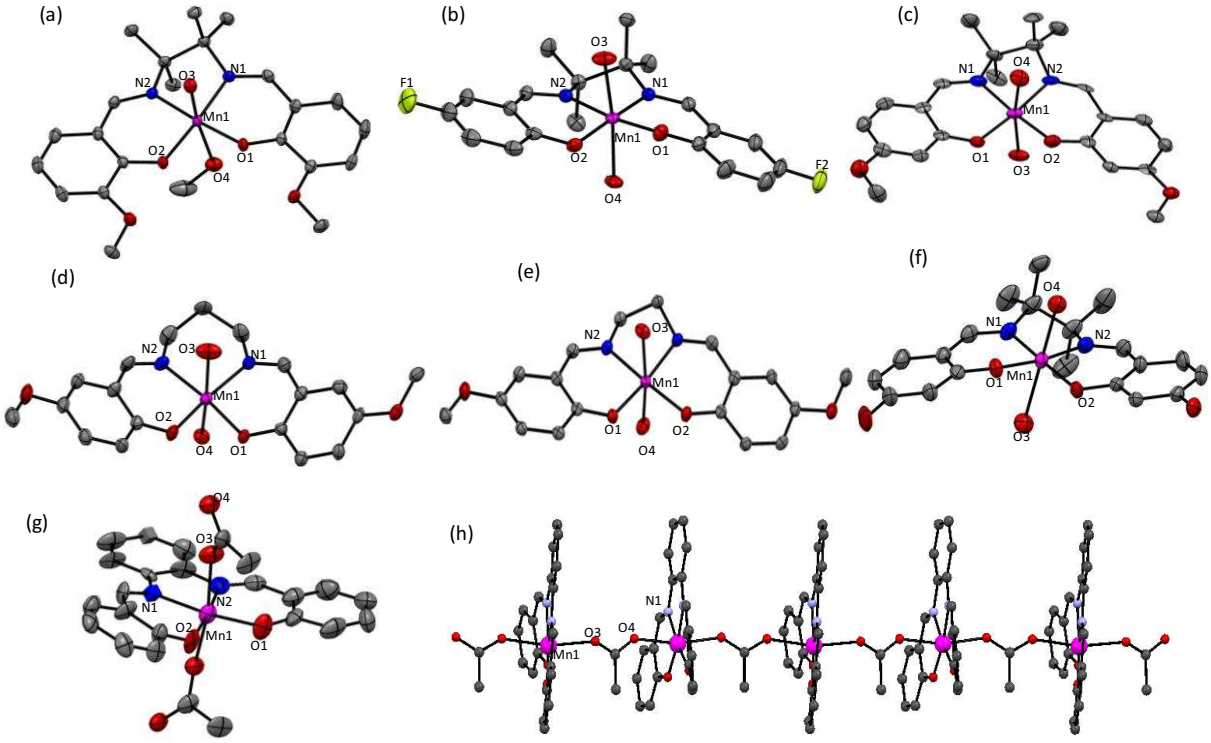

Figure II.16. ORTEP view of the crystal structures (50 % thermal probability) of the mononuclear Mn^{III}-Schiff base complexes where the magenta, red, grey and blue spheres represent the Mn, O, C and N atoms. The cocrystallizing water molecules, the ClO_4^- counter anions and the H atoms are not shown for clarity. (a) [Mn^{III}(3-MeO-saltmen)(CH_3OH)(H_2O)]$^+$; (b) [Mn^{III}(5-F-saltmen)(H_2O)$_2$]$^+$ (the pale green sphere represents the F atoms); (c) [Mn^{III}(4-MeO-saltmen)(H_2O)$_2$]$^+$; (d) [Mn^{III}(5-MeO-salpen)(H_2O)$_2$]$^+$; (e) [Mn^{III}(5-MeO-salen)(H_2O)$_2$]$^+$; (f) [Mn^{III}(4-HO-saltmen)(H_2O)$_2$]$^+$; (g) [Mn^{III}(salphen)(CH_3COO)$_2$]$^-$ and (h) the one dimensional view of [Mn^{III}(salphen)(CH_3COO)] in ball and stick model.

[Mn^{III}(5-MeO-salpen)(H$_2$O)$_2$](ClO$_4$)·H$_2$O: The axial coordination sites of the Mn^{III} ion are occupied with two water molecules (figure II.16d) and we can find one cocrystallizing water molecule in the unit cell.

[Mn^{III}(5-MeO-salen)(H$_2$O)$_2$](ClO$_4$): The Mn^{III} ion in this compound (figure II.16e) is axially coordinated with two water molecules.

[Mn^{III}(4-HO-saltmen)(H$_2$O)$_2$](ClO$_4$)·H$_2$O: In this compound (figure II.16f), the unit cell contains water molecules in the two axial positions of the Mn^{III} ion and also two molecules of cocrystallizing water.

[Mn^{III}(salphen)(CH$_3$COO)]: In this compound the acetate (CH_3COO^-) anion not only balances the charge of the $[Mn^{III}(salphen)]^+$ molecule but also act as a bridge between two $[Mn^{III}(salphen)]^+$ units to form a one dimensional coordination polymer (figure II.16h). The axial positions of the Mn^{III} ion are occupied by two acetate ions (figure II.16g).

Table II.5 Crystal data and structure refinement of mononuclear Mn^{III}-Schiff base complexes

Compounds	[Mn^{III}(3-MeO-saltmen)(CH$_3$OH)(H$_2$O)](ClO$_4$)	[Mn^{III}(5-F-saltmen)(H$_2$O)$_2$](ClO$_4$)	[Mn^{III}(4-MeO-saltmen)(H$_2$O)$_2$](ClO$_4$).2H$_2$O	[Mn^{III}(5-MeO-salpen)(H$_2$O)$_2$](ClO$_4$).H$_2$O	[Mn^{III}(5-MeO-salen)(H$_2$O)$_2$](ClO$_4$)	[Mn^{III}(4-HO-saltmen)(H$_2$O)$_2$](ClO$_4$).H$_2$O	[Mn^{III}(salphen)(CH$_3$COO)]
Sum formula	$C_{23}H_{32}ClMnN_2O_{10}$	$C_{20}H_{24}ClF_2MnN_2O_8$	$C_{22}H_{34}ClMnN_2O_{12}$	$C_{38}H_{50}Cl_2Mn_2N_4O_{22}$	$C_{18}H_{22}ClMnN_2O_{10}$	$C_{20}H_{26}ClMnN_2O_{11}$	$C_{22}H_{17}MnN_2O_4$
MW (g/mol)	586.90	548.8	608.96	1090.56	516.76	562.83	428.32
Temp. (K)	150(2)	120(2)	100(2)	120(2)	120(2)	120(2)	120(2)
Crystal System	Monoclinic	Monoclinic	Orthorhombic	Orthorhombic	Monoclinic	Monoclinic	Monoclinic
Space group	$P2_1/c$	C2/c	Pbca	$Pna2_1$	$P2_1/c$	$P2_1/c$	$P2_1/n$
a (Å)	8.508(1)	16.4697(15)	16.574(5)	7.699(5)	7.582(6)	7.027(5)	11.347(6)
b (Å)	26.107(1)	19.5925(19)	14.042(5)	22.913(5)	25.156(5)	14.894(5)	14.054(7)
c (Å)	11.389(1)	15.1282(13)	22.788(5)	25.395(5)	12.154(4)	23.388(5)	12.466(7)
α (°)	90	90	90	90	90	90	90
β (°)	93.82(1)	103.794(4)	90	90	98.45(4)	97.613(5)	115.419(15)
γ (°)	90	90	90	90	90	90	90
Volume (Å^3)	2524.1(8)	4740.8(8)	5304(3)	4480(3)	2511.1(9)	2426(2)	1795.5(17)
Z	4	8	8	4	4	4	4
Density(g.cm^{-3})	1.544	1.538	1.512	1.617	1.331	1.541	1.584
$\mu_{MoK\alpha}$ (mm^{-1})	0.689	0.733	0.663	0.773	0.673	0.716	0.769
F000	1224	2256	2504	2244	1215	1168	880
GooF	1.180	1.030	1.164	1.041	1.115	1.073	1.225
[a]R_1 ($I > 2.00\sigma(I)$)	0.0374	0.0532	0.0784	0.0426	0.0702	0.0784	0.1348
[b]wR_2	0.1324	0.1470	0.2322	0.1341	0.1506	0.2272	0.4100

[a]$R_1 = \Sigma ||F_0| - |F_C|| / \Sigma|F_0|$, [b]$wR_2 = [\Sigma w(F_0^2 - F_C^2)^2 / \Sigma w(F_0^2)^2]^{1/2}$, $w = 1/[\sigma^2 F_0^2 + (0.0313P)^2 + 1.5564P]$; where $P = (F_0^2 + 2F_C^2)/3$

Mn^{III}-Schiff base complexes crystallized in the dinuclear form:

In these dinuclear compounds, we found that the axially coordinated solvent molecules are water. The compounds *[Mn$^{III}_2$(saltmen)$_2$(H$_2$O)$_2$](ClO$_4$)$_2$* (figure II.17a), *[Mn$^{III}_2$(5-Cl-saltmen)$_2$(H$_2$O)$_2$](ClO$_4$)$_2$* (figure II.17b), *[Mn$^{III}_2$(5-Me-saltmen)$_2$(H$_2$O)$_2$](ClO$_4$)$_2$* (figure II.17c),

[Mn^{III}_2(5-MeO-saltmen)$_2$(H_2O)$_2$](ClO_4)$_2$ (figure II.17d), and *[Mn^{III}_2(5-Me-salpen)$_2$(H_2O)$_2$](ClO_4)$_2$* (figure II.17e) crystallized without any solvents of crystallization.

On the other hand, *[Mn^{III}_2(5-Cl-salmen)$_2$(H_2O)$_2$](ClO_4)$_2$·2H_2O* (figure II.17f) and *[Mn^{III}_2(5-^{t}Bu-saltmen)$_2$(H_2O)$_2$](ClO_4)$_2$·2H_2O* (figure II.17g) crystallized with two water molecules in the unit cell as solvents of crystallization.

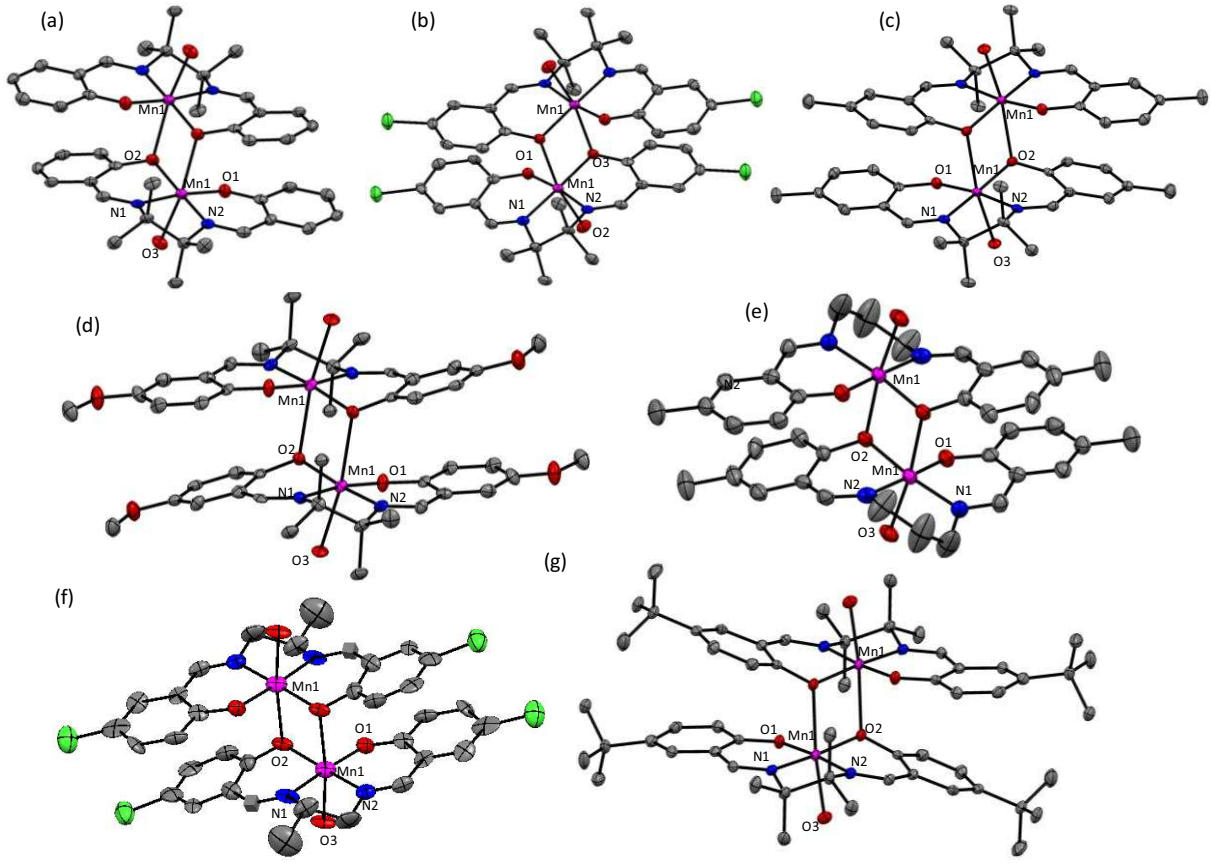

Figure II.17. ORTEP view of the crystal structures (50 % thermal probability) of the dinuclear Mn^{III}-Schiff base complexes where the magenta, green, red, grey and blue spheres represents the Mn, Cl, O, C and N atoms. The cocrystallizing water molecules, ClO_4^- counter anions and the H atoms are not shown for clarity. (a) $[Mn^{III}_2(saltmen)_2(H_2O)_2]^{2+}$; (b) $[Mn^{III}_2$(5-Cl-saltmen)$_2(H_2O)_2]^{2+}$; (c) $[Mn^{III}_2$(5-Me-saltmen)$_2(H_2O)_2]^{2+}$; (d) $[Mn^{III}_2$(5-MeO-saltmen)$_2(H_2O)_2]^{2+}$; (e) $[Mn^{III}_2$(5-Me-salpen)$_2(H_2O)_2]^{2+}$; (f) $[Mn^{III}_2$(5-Cl-salmen)$_2(H_2O)_2]^{2+}$; (g) $[Mn^{III}_2$(5-^{t}Bu-saltmen)$_2(H_2O)_2]^{2+}$.

Table II.6 Crystal data and structure refinement for dinuclear Mn^{III}-Schiff base complexes

Compounds	$[Mn^{III}_2(salmen)_2(H_2O)_2](ClO_4)_2$	$[Mn^{III}_2(5\text{-}Cl\ saltmen)_2(H_2O)_2](ClO_4)_2$	$[Mn^{III}_2(5\text{-}Cl\ salmen)_2(H_2O)_2](ClO_4)_2.2H_2O$	$[Mn^{III}_2(5\ ^tBu\text{-}saltmen)_2(H_2O)_2](ClO_4)_2.2H_2O$	$[Mn^{III}_2(5\ Me\text{-}saltmen)_2(H_2O)_2](ClO_4)_2$	$[Mn^{III}_2(5\ MeO\text{-}saltmen)_2(H_2O)_2](ClO_4)_2$	$[Mn^{III}_2(5\ Me\text{-}salpen)_2(H_2O)_2](ClO_4)_2$
Sum formula	$C_{40}H_{48}N_4O_{14}Cl_2Mn_2$	$C_{40}H_{44}N_4O_{14}Cl_6Mn_2$	$C_{34}H_{36}N_4O_{16}Cl_6Mn_2$	$C_{56}H_{80}N_4O_{16}Cl_6Mn_2$	$C_{44}H_{56}N_4O_{14}Cl_2Mn_2$	$C_{44}H_{56}N_4O_{18}Cl_2Mn_2$	$C_{38}H_{44}N_4O_{14}Cl_2Mn_2$
MW (g/mol)	989.62	1127.37	1075.22	1250.05	1042.05	1109.71	961.55
Temp. (K)	150(2)	120(2)	120(2)	120(2)	120(2)	120(2)	120(2)
Crystal System	Monoclinic	Orthorhombic	Monoclinic	Monoclinic	Monoclinic	Monoclinic	Monoclinic
Space group	$P2_1/a$	$P2_1/c$	$P2_1/c$	$P2_1/n$	$P2_1/c$	$P2_1/c$	$C2/c$
a (Å)	20.830(1)	7.3466(5)	7.125(5)	14.0612(16)	7.4105(15)	7.359(5)	19.264(2)
b (Å)	13.596(1)	15.4336(12)	20.955(5)	12.4690(12)	15.416(3)	16.370(5)	15.430(2)
c (Å)	7.526(1)	19.2928(15)	13.720(5)	18.702(2)	19.641(4)	19.641(5)	14.412(13)
α (°)	90	90	90	90	90	90	90
β (°)	89.818(8)	90	96.210(5)	111.806(4)	90.20(3)	93.310(5)	108.916(6)
γ (°)	90	90	90	90	90	90	90
Volume (Å^3)	2131.3(3)	2187.5(3)	2036.4(17)	3044.4(6)	2243.8(8)	2362.1(9)	4052.5(8)
Z	2	2	2	2	2	2	4
Density (g.cm^{-3})	1.542	1.712	1.753	1.364	1.548	1.560	1.576
$\mu_{MoK\alpha}$ (mm^{-1})	0.790	1.017	1.092	0.571	0.755	0.728	0.829
F000	1024	1152	1088	1320	1088	1152	1984
GooF	1.290	0.866	1.141	0.996	1.054	1.195	1.039
$^aR_1$ ($I > 2.00\sigma(I)$)	0.048	0.0367	0.1340	0.0446	0.0392	0.1383	0.0693
$^bwR_2$	0.138	0.1104	0.3126	0.1329	0.1270	0.3654	0.2288

$^aR_1 = \Sigma\ ||F_0| - |F_C||/\ \Sigma|F_0|$, $^bwR_2 = [\Sigma w(F_0^2 - F_C^2)^2/\Sigma w(F_0^2)^2]^{1/2}$, $w = 1/[\sigma^2F_0^2 + (0.0313P)^2 + 1.5564P]$; where $P = (F_0^2 + 2F_C^2)/3$

II.4.3. $[M(cyclam)]^{2+}$ complexes

Using cyclam (1,4,8,11-tetraazacyclotetradecane), *N, N′*-dimethylcyclam (1,8-dimethyl-1,4,8,11-tetraazacyclotetradecane) and the metal (Cu^{II} and Ni^{II}) perchlorate salts almost all of metal cyclam complexes were synthesized in one step.

II.4.3.1. Synthetic details of the M-cyclam complexes

$[Ni^{II}(cyclam)](ClO_4)_2$: Under constant stirring, Nickel(II) perchlorate hexahydrate ($Ni^{II}(ClO_4)_2.6H_2O$, 0.365 g, 1 mmol) was dissolved in 10 mL of absolute ethanol followed by drop wise addition of 5 mL of an absolute ethanol solution containing 200 mg (1 mmol) of cyclam ligand. Some yellow-orange precipitate formed immediately. The mixture was heated to 50 °C and stirring was continued for 1 hour. The reaction mixture was cooled to room temperature and the yellow-orange precipitate was collected by filtration and dried in air. The yield of the product was about 85 % The precipitate was crystallized from water by slow evaporation at room temperature and orange crystals of $[Ni^{II}(cyclam)](ClO_4)_2$ were collected by filtration.

$[Cu^{II}(cyclam)(ClO_4)_2]$: Under constant stirring, Copper(II) perchlorate hexahydrate ($Cu^{II}(ClO_4)_2.6H_2O$, 0.370 g, 1 mmol) was dissolved in 10 mL of absolute ethanol followed by drop wise addition of 5 mL of an absolute ethanol solution containing 200 mg (1 mmol) of cyclam ligand.

Some pink precipitate was formed immediately. The mixture was heated to 50° C and stirring was continued for 1 hour. The reaction mixture was cooled to room temperature and the pink precipitate was collected by filtration and dried in air. The yield of the product was about 85 %. The precipitate was crystallized from water by slow evaporation at room temperature and deep pink-violet crystals were collected by filtration.

[Cu^{II}(N, N´-dimethylcyclam)(ClO_4)$_2$]: Under constant stirring, Copper(II) perchlorate hexahydrate ($Cu^{II}(ClO_4)_2.6H_2O$, 0.370 g, 1 mmol) was dissolved in 10 mL of absolute ethanol followed by drop wise addition of 5 mL of an absolute ethanol solution containing 228 mg (1 mmol) of *N, N´*-dimethylcyclam ligand. Some pink precipitate formed immediately. The mixture was heated to 50° C and stirring was continued for 1 hour. The reaction mixture was cooled to room temperature and the violet precipitate was collected by filtration and dried in air. The yield of the product was about 90 %. The precipitate was crystallized from water by slow evaporation at room temperature.

II.4.3.2. Infrared spectroscopic characterization

Regarding the FT-IR spectroscopic analysis of all metal-cyclam compounds, the most important observation is the shift of the secondary amine (C-N) stretching band which is found at ~1206 cm^{-1} for free cyclam. After complex in with the Ni^{II} or Cu^{II} ions, the C-N stretching band shifts to lower energy and buried under the strong broad stretching bands coming from ClO_4^- counter anion of these metal ligand complexes. In these compounds the characteristic $\bar{\nu}_{Cl\text{-}O}$ stretching band from the perchlorate ion is found in the range of 1000-1100 cm^{-1}. Similar shifts of the N-H bond stretching frequencies are also noticed after formation of metal-cyclam complexes. In the free ligand, the sharp N-H stretching bands are found at ~3180 cm^{-1} and ~3262 cm^{-1} which overlap to give a broad band lying between those two wave numbers. [Ni^{II}(cyclam)](ClO_4)$_2$ shows the perchlorate stretching signals at 1019 cm^{-1} and 1080 cm^{-1} and the N-H stretching vibrations at 3204 cm^{-1}. [Cu^{II}(cyclam)(ClO_4)$_2$] shows the perchlorate stretching signals at 1061 cm^{-1} and 1091 cm^{-1} and the N-H stretching vibrations at 3241 cm^{-1}. [Cu^{II}(*N, N´*-dimethylcyclam)(ClO_4)$_2$] shows the perchlorate stretching signals 1055 cm^{-1} and 1099 cm^{-1} and the N-H stretching vibrations at 3235 cm^{-1}.

II.4.3.3. X-ray crystal structure

The X-ray crystallographic data on single crystals were collected for each of the three M-cyclam molecular precursors. The crystallographic parameters of the three M^{II}-cyclam complexes are tabulated in the table II.7.

Table II.7. Crystal data and structure refinement for the M-cyclam complexes

	$[Ni^{II}(cyclam)](ClO_4)_2$	$[Cu^{II}(cyclam)(ClO_4)_2]$	$[Cu^{II}(N,N'\text{-dimethylcyclam})(ClO_4)_2]$
Sum formula	$C_{10}H_{24}Cl_2NiN_4O_8$	$C_{10}H_{24}Cl_2CuN_4O_8$	$C_{12}H_{28}Cl_2CuN_4O_8$
Molecular weight (g/mol)	457.85	462.78	490.83
Temperature (K)	120(2)	120(2)	120(2)
Crystal System	Monoclinic	Triclinic	Orthorhombic
Space group	$P2_1/c$	P-1	Pnnm
a (Å)	9.6225(19)	7.943(5)	8.2215(16)
b (Å),	13.905(3)	8.214(5)	9.1210(18)
c (Å)	16.307(5)	3.394(2)	12.858(3)
α (°)	90	113.267(5)	90
β (°)	126.16(2)	116.283(5)	90
γ (°)	90	95.277(5)	90
Volume ($Å^3$)	1770.5(13)	427.(5)	964.2(3)
Z	4	1	2
Density ($g.cm^{-3}$)	1.727	1.800	1.593
$\mu_{MoK\alpha}$ (mm^{-1})	1.452	1.640	1.455
F000	952	239	454
GooF	1.126	0.579	3.338
$^aR_1$ ($I > 2.00\sigma(I)$)	0.1312	0.0421	0.1992
$^bwR_2$ (all reflections)	0.4008	0.1353	0.5747

$^aR_1 = \Sigma ||F_0| - |F_C|| / \Sigma|F_0|$, $^bwR_2 = [\Sigma w(F_0^2 - F_C^2)^2 / \Sigma w(F_0^2)^2]^{1/2}$, $w = 1/[\sigma^2 F_0^2 + (0.0313P)^2 + 1.5564P]$; where $P = (F_0^2 + 2F_C^2)/3$

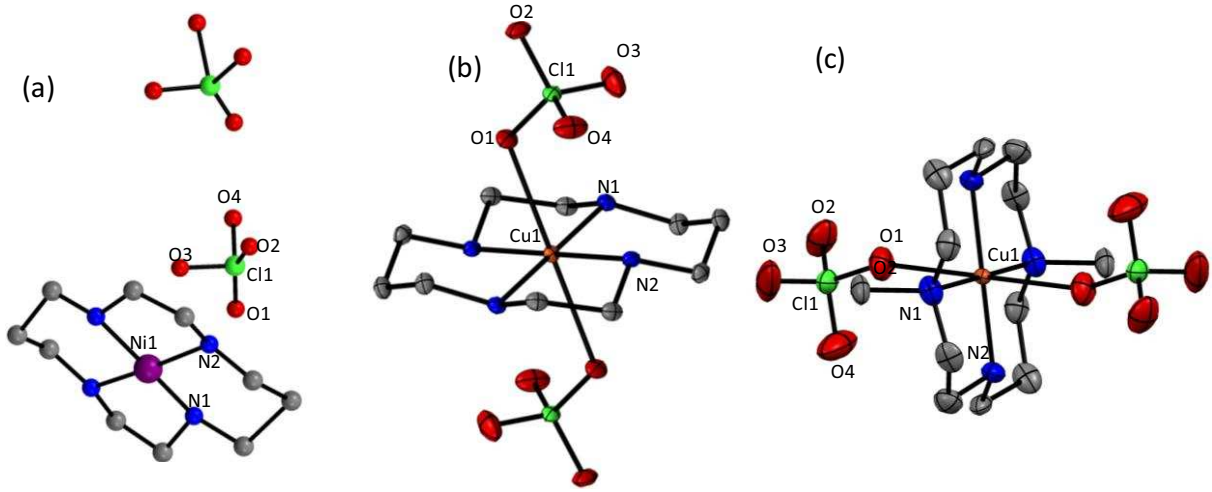

Figure II.18. M^{II}-cyclam complexes used in the thesis, the grey, blue, red, green, violet and the brown spheres are respectively C, N, O, Cl, Ni and Cu atoms. The H atoms are not shown for clarity. (a) Crystal structures of the $[Ni^{II}(cyclam)](ClO_4)_2$ in ball and stick model, due to a huge disorder the all atoms are refined isotropically. (b) and (c) ORTEP diagram (50% thermal ellipsoid) of the crystal structure of $[Cu^{II}(cyclam)(ClO_4)_2]$ (in b) and $[Cu^{II}(N, N'\text{-dimethylcyclam})(ClO_4)_2]$ (in c).

The Ni^{II} ion in *$[Ni^{II}(cyclam)](ClO_4)_2$* is in a square planar ligand environment (figure II.18a) and therefore resides in the cavity of the cyclam macromolecule. The four N atoms of the cyclam ligand satisfy the planar coordination sites of the Ni^{II} ion, while two ClO_4^- counter anions balance the charge of the $[Ni^{II}(cyclam)]^{2+}$ moiety. $[Cu^{II}(cyclam)\ (ClO_4)_2]$ and $[Cu^{II}(N, N'\text{-dimethylcyclam})(ClO_4)_2]$ have quite comparable crystal structures where the Cu^{II} ion is in a distorted octahedral environment. In the equatorial plane, the Cu^{II} ion is coordinated with four nitrogen atoms of the cyclam ligand, and the axial positions of the Cu^{II} ion are connected with the oxygen atoms of two ClO_4^- groups (figure II.18b

and II.18c). All the M^{II}-N (M = Ni, Cu) distances in the equatorial plane are between 2.0 and 2.05 Å. In both Cu^{II} complexes, the axial Cu-O bonds are very long compared to the equatorial Cu-N bond distances. These Cu-O bonds are 2.544(2) Å for $[Cu^{II}(cyclam)(ClO_4)_2]$ and 2.547(9) Å for $[Cu^{II}$(N, N′-dimethylcyclam)$(ClO_4)_2]$ which is an indication of a large Jahn-Teller effect on the Cu^{II} ion with tetragonal elongation.

II.4.4. $[M(LN_3O_2)]^{2+}$ complexes

We have synthesized two M-LN_3O_2 complexes, $[M^{II}(LN_3O_2)(H_2O)Cl]Cl$ (M = Fe and Mn), according to the literature method with few modifications using the chlorido salts of Fe^{II} and Mn^{II}, 2,6-diacetylpyridine and 3,6-dioxooctano-1,8-diamine.[17, 19]

II.4.4.1. Synthetic details of the M-LN_3O_2 complexes

$[Fe^{II}(LN_3O_2)(H_2O)Cl]Cl$: All the solvents were dried before the reaction. $FeCl_2.4H_2O$ (1 g, 5.1 mmol) was dissolved in 50 mL MeOH and combined with a 15 mL H_2O solution of $Na_2S_2O_4$ (438 mg), used as an anti-oxidant. Thereafter, 2,6-diacetylpyridine (0.82 g, 5.1 mmol) and 3,6-dioxooctano-1,8-diamine (0.82 g, 5.1 mmol) were successively added, giving a dark blue-violet solution. The mixture was refluxed for 16 hours. After cooling down the reaction medium, the volume was reduced to half under vacuum. The solution was left to crystallize in the dry box yielding dark blue-violet crystals (2.22 g, 94 %).

$[Mn^{II}(LN_3O_2)(H_2O)Cl]Cl$: A 50 mL methanol solution of 2,6-diacetylpyridine (0.82 g, 5 mmol) was added to a 25 mL MeOH solution of $MnCl_2 \cdot 4H_2O$ (0.98 g, 5 mmol). The mixture was kept at 50° C, and a solution of 3,6-dioxaoctano-1,8 diamine (0.74 g, 5 mmol) in methanol (25 mL) was added over 15 min with continuous stirring. The product was heated to reflux for 6 h, and then cooled to room temperature. The orange solution was filtered and the filtrate was kept for slow evaporation at room temperature. After 2 days large orange crystals were collected by filtration. The yield of the product was 90 % on the basis of the Mn^{II} salt used.

II.4.4.2. Infrared spectroscopic characterization

The infrared spectra of both $[M^{II}(LN_3O_2)(H_2O)Cl]Cl$ (M = Fe, Mn) complexes are quite comparable. The characteristic ether-type C-O stretching band is found at 1078 cm^{-1} for

$[Fe^{II}(LN_3O_2)(H_2O)Cl]Cl$, while that for the Mn^{II} analogue is at 1072 cm^{-1}. The sharp peak at 1635 cm^{-1} (for the Fe^{II} complex) and 1644 cm^{-1} (for the Mn^{II} complex) originate from the C=N stretching of the macrocyclic ligand. The C-H stretching vibrations of the macrocyclic LN_3O_2 ligand exhibit broad peaks in the 2880-2930 cm^{-1} range for both compounds. The O-H stretching of the water molecules exhibit broad peaks in the 3130-3400 cm^{-1} range.

II.4.4.3. X-ray crystal structure

The $[M^{II}(LN_3O_2)(H_2O)Cl]Cl$ (M = Fe, Mn) compounds crystallized with water molecules in the form $[Fe^{II}(LN_3O_2)(H_2O)Cl]Cl{\cdot}H_2O$ and $[Mn^{II}(LN_3O_2)(H_2O)Cl]Cl{\cdot}5H_2O$. The single crystal X-ray data are summarized in table II.8.

Table II.8. Crystal data and structure refinement for M-LN_3O_2 complexes

	$[Fe^{II}(LN_3O_2)(H_2O)Cl]Cl.H_2O$	$[Mn^{II}(LN_3O_2)(H_2O)Cl]Cl.5H_2O$
Sum formula	$FeC_{15}N_3O_4Cl_2H_{25}$	$MnC_{15}N_3O_8Cl_2H_{33}$
Molecular weight (g/mol)	438.13	509.28
Temperature (K)	150(2)	120(2)
Crystal System	Triclinic	Monoclinic
Space group	P-1	$P2_1/c$
a (Å), b (Å), c (Å)	7.0130(5), 10.2866(1), 14.3066(1)	11.228(5), 8.374(5), 26.653(5)
α (°), β (°), γ (°)	104.490(1), 98.975(1), 105.932(1)	90, 111.352(12), 90
Volume ($Å^3$)	1932.463	2334.0(18)
Z	2	4
Density ($g.cm^{-3}$)		1.446
$\mu_{MoK\alpha}$ (mm^{-1})		0.838
F000		1068
GooF		1.093
[a] R_1 ($I > 2.00\sigma(I)$)		0.0435
[b] wR_2 (all reflections)		0.1438

[a] $R_1 = \Sigma ||F_0| - |F_C|| / \Sigma |F_0|$, [b] $wR_2 = [\Sigma w(F_0^2 - F_C^2)^2 / \Sigma w(F_0^2)^2]^{1/2}$, $w = 1/[\sigma^2 F_0^2 + (0.0313P)^2 + 1.5564P]$; where $P = (F_0^2 + 2F_C^2)/3$

The Fe^{II} and Mn^{II} ions are in a heptacoordinated environment (figure II.19) and the crystals structure of both $[M^{II}(LN_3O_2)(H_2O)Cl]Cl$ molecules are very similar. The metal resides in the cavity of the macrocyclic LN_3O_2 where three nitrogen and two oxygen atoms from the LN_3O_2 ligand coordinate with equatorial positions of the metal ions. One of the axial positions of Fe^{II} and Mn^{II} is coordinated with one chlorido group and the other axial position is occupied by the oxygen atom of a water molecule. These coordinated chlorido and aqua groups are almost perpendicular to the M-LN_3O_2 plane, such that the Cl-Fe-O and Cl-Mn-O angles are 168.44(1)° and 171.40(5)° respectively. The Fe-N bonds are 2.181(0) Å, 2.113(7) Å and 2.141(5) Å; whereas the average Mn-N bonds are a little longer than the Fe^{II} analogue, 2.219(2) Å, 2.247(2) Å and 2.243(3) Å. The Fe-O bonds with the macrocyclic oxygen are 2.280(7) Å and 2.293(1) Å and those of the Mn^{II} analogue are 2.279(2) Å and 2.294(2) Å. The M-Cl bonds are 2.491(1) Å and 2.583(1) Å for Fe^{II} and Mn^{II} complexes respectively. The axial M-O distances with the water molecules are respectively 2.162(6) Å and 2.225(2) Å for the

Fe^{II} and Mn^{II} complexes. In both complexes, one anion chloride is present in the crystal structure to neutralize the charge of the $[M^{II}(LN_3O_2)(H_2O)Cl]^+$ moiety.

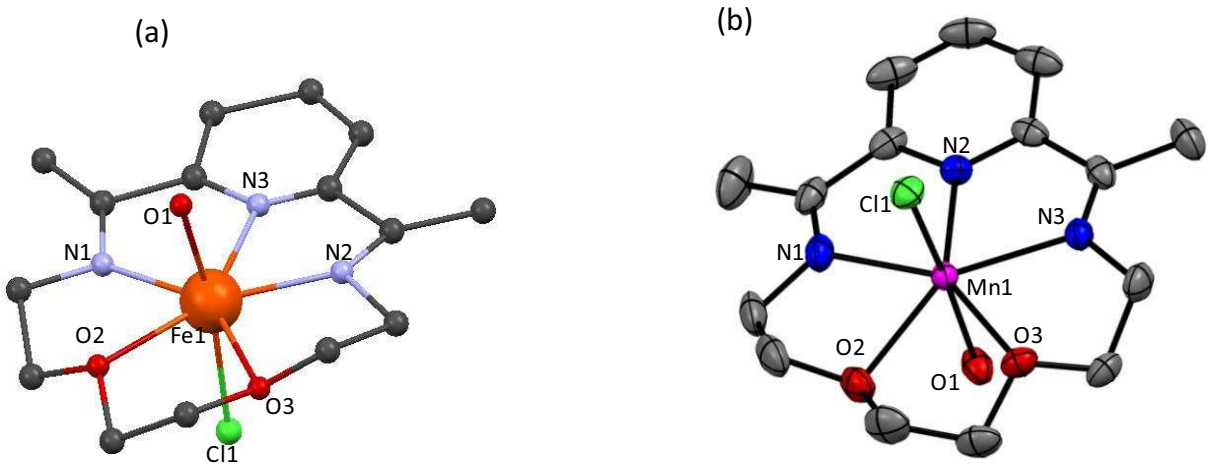

Figure II.19. (a) The molecular structure view of $[Fe^{II}(LN_3O_2)(H_2O)Cl]Cl{\cdot}H_2O$ in ball and stick, due to very poor crystal quality the atoms are refined isotropically and some crystallographic parameters are not given. (b) ORTEP type view of the molecular structure (50% thermal probability) of $[Mn^{II}(LN_3O_2)(H_2O)Cl]Cl{\cdot}5H_2O$. The grey, blue, red, green, orange (in a) and pink (in b) spheres are C, N, O, Cl, Fe and Mn atoms. The H atoms, solvent molecules (water) and chloride anions have been removed for clarity.

II.4.5. *Trans*-$(Bu_4N)_2[Re^{IV}Cl_4(CN)_2]{\cdot}2DMA$

The tetrabutylammonium salt of *trans*-$[Re^{IV}Cl_4(CN)_2]^{2-}$ has been synthesized according to the literature method using commercially available $Re^{V}Cl_5$[21a] and $Bu_4N(CN)$.

II.4.5.1. Synthetic details of *trans*-$(Bu_4N)_2[Re^{IV}Cl_4(CN)_2]{\cdot}2DMA$

In a dry box, 1 g of $Re^{V}Cl_5$ was dissolved in 20 mL of THF and kept closed. After 2 days green crystals of *cis*-$Re^{IV}Cl_4(THF)_2$ were obtained which were collected through filtration inside the dry box and dried over filter paper (the crystals are very sensitive to moisture). Crystallographic structural analysis of this compound shows the *cis* orientation of the two THF molecules coordinated with Re^{IV} through the oxygen atom. In a dry box, 0.243 g (~0.5 mmol) of *cis*-$Re^{IV}Cl_4(THF)_2$ and 0.593 g (~2 mmol) of $Bu_4N(CN)$ were each dissolved separately in 1 mL DMF each. The Re^{IV} solution was added in a the stirred solution of $Bu_4N(CN)$. The mixture was allowed to stir for 24 hours. The dark blue-violet solution was brought outside the dry box and about 30 mL of distilled water was added, resulting in immediate bluish grey precipitation. The precipitate was collected by filtration and

thoroughly washed with distilled water. The precipitate was dried for 2 hours in air and then dissolved in 1.5 mL of dimethylacetamide (DMA). Slow diffusion of diethyl ether vapor through the DMA solution gave pale blue rod-shaped crystals of *trans*-$(Bu_4N)_2[Re^{IV}Cl_4(CN)_2]\cdot 2DMA$ after one day. The crystals were collected by removing the solution and adding 10 mL of diethylether to the crystal immediately. The crystals were collected by filtration and then dried in air. The yield of *trans*-$(Bu_4N)_2[Re^{IV}Cl_4(CN)_2]\cdot 2DMA$ is 44% on the basis of the quantity of *cis*-$Re^{IV}Cl_4(THF)_2$ used.

II.4.5.2. Infrared spectroscopic characterization

The shift of the complexed cyanido stretching band ($\bar{\nu}_{C\equiv N}$) to higher wavenumbers compared to the free cyanido one of $Bu_4N(CN)$ (broad peak at 2078 cm^{-1}) is an indication of the formation of metal-cyanido bonds. In *trans*-$(Bu_4N)_2[Re^{IV}Cl_4(CN)_2]\cdot 2DMA$, the characteristic $\bar{\nu}_{C\equiv N}$ is found at 2125 cm^{-1}. The sharp peak at 1610 cm^{-1} comes from the stretching of C=O in the cocrystallized DMA molecule. The prominent peaks in the 2800-3000 cm^{-1} range is due to several aliphatic C-H stretching bands and therefore confirms the presence of Bu_4N groups in the compound.

II.4.5.3. X-ray crystal structure

X-ray crystallographic data on the single crystal were collected for *cis*-$Re^{IV}Cl_4(THF)_2$ and *trans*-$(Bu_4N)_2[Re^{IV}Cl_4(CN)_2]\cdot 2DMA$ and the crystallographic parameters are listed in table II.9.

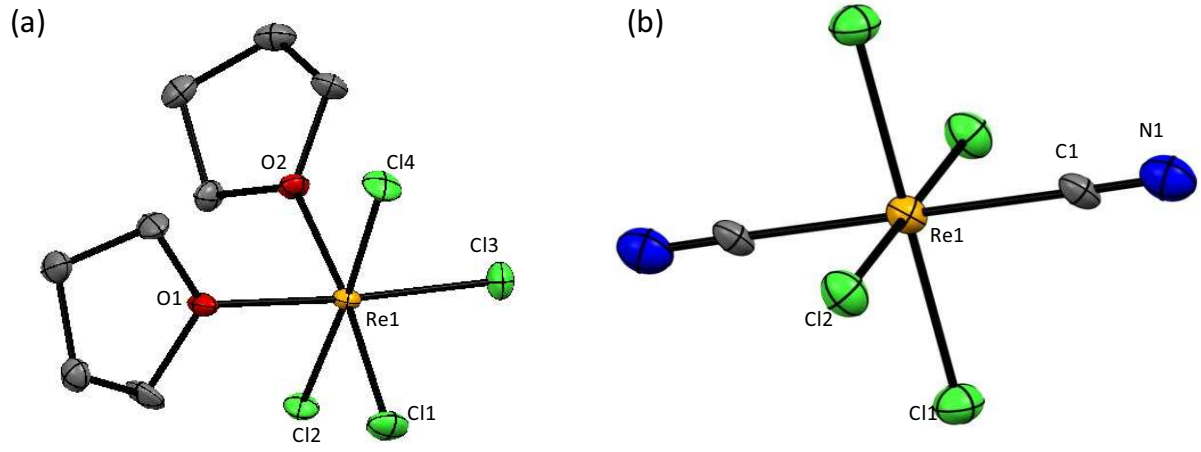

Figure II.20. ORTEP type view of the crystal structure (50 % thermal probability) of (a) *cis*-$Re^{IV}Cl_4(THF)_2$ and (b) *trans*-$(Bu_4N)_2[Re^{IV}Cl_4(CN)_2]\cdot 2DMA$. In both figures the grey, blue, red, green and the orange spheres represent respectively the C, N, O, Cl and Re atoms. The H atoms, solvent molecules (DMA) and counter cation Bu_4N^+ are not displayed for clarity.

Table II.9. Crystal data and structure refinement for the Re^{IV} complexes

	cis-$Re^{IV}Cl_4(THF)_2$	*trans*-$(Bu_4N)_2[Re^{IV}Cl_4(CN)_2]\cdot 2DMA$
Sum formula	$C_8H_{16}Cl_4O_2Re$	$C_{42}H_{90}Cl_4N_6O_2Re$
Molecular weight (g/mol)	472.22	1039.21
Temperature (K)	150(2)	139(2)
Crystal System	Orthorhombic	Triclinic
Space group	$P2_12_12_1$	P-1
a (Å), b (Å), c (Å)	7.7305(15), 12.670(3), 13.922(3)	10.5629(8), 11.9119(9), 12.1271(9)
α (°), β (°), γ(°)	90, 90, 90	64.183(1), 75.015(1), 82.151(1)
Volume ($Å^3$)	1363.6(5)	33.24(17)
Z	4	1
Density ($g.cm^{-3}$)	2.30	1.294
$\mu_{MoK\alpha}$ (mm^{-1})	9.674	2.151
F000	892	543
GooF	1.104	1.046
$^aR_1$ ($I > 2.00\sigma(I)$)	0.0396	0.0337
$^bwR_2$ (all reflections)	0.0985	0.0859

$^aR_1 = \Sigma ||F_0| - |F_C|| / \Sigma|F_0|$, $^bwR_2 = [\Sigma w(F_0^2 - F_C^2)^2 / \Sigma w(F_0^2)^2]^{1/2}$, $w = 1/[\sigma^2F_0^2 + (0.0313P)^2 + 1.5564P]$; where $P = (F_0^2 + 2F_C^2)/3$

Figure II.20 represents a molecular view of both of these Re^{IV} complexes. In these compounds, the Re^{IV} ion is in an octahedral crystal environment. The *cis*-$Re^{IV}Cl_4(THF)_2$ complex has four chlorido anions connected to the Re^{IV} center, balancing the charge of the metal ion. The two neutral THF molecules are connected to the Re^{IV} ion through their oxygen atoms in a *cis* conformation. The four Re-Cl bond distances in *cis*-$Re^{IV}Cl_4(THF)_2$ range between 2.295(2) Å and 2.334(2) Å and the two Re-O distances are 2.102(5) Å and 2.106(5) Å. In the structure of *trans*-$(Bu_4N)_2[Re^{IV}Cl_4(CN)_2]\cdot 2DMA$, the equatorial plane of the Re^{IV} ion contains four chlorido groups and the axial coordination sites are occupied by two carbon atoms of the cyanido group. The Re^{IV} atom resides on an inversion center and the C-Re-Cl and Cl-Re-Cl bond angles are close to 90°. In this compound the Re-C distance is 2.148(4) Å and the mean Re-Cl distance is 2.346(1) Å. Two Bu_4N^+ groups neutralise the charge of one $[Re^{IV}Cl_4(CN)_2]^{2-}$ moiety. In the unit cell of this compound, two molecules of DMA fill the void spaces in the crystal packing.

II.4.6. *Trans*-$Ru^{III}(CN)_2$-schiff base complexes

The two *trans*-$Ru^{III}(CN)_2$-schiff base complexes *trans*-$(PPh_4)[Ru^{III}(salen)(CN)_2]\cdot MeOH\cdot H_2O$ and *trans*-$(Bu_4N)[Ru^{III}(5\text{-Cl-saltmen})(CN)_2]$ were synthesized via a similar procedure. The Schiff base ligand H_2salen was synthesized using salicylaldehyde and ethylenediamine according to the synthetic method described in section II.4.1. The 5-Cl-saltmenH_2 ligand was synthesized similarly using 5-Cl-salicylaldehyde and 1,1,2,2-tetramethylethylenediamine (see section II.4.1). The $Ru^{III}Cl_3.nH_2O$, PPh_4Cl and Bu_4NCl precursors were obtained from authorized chemical providers.

II.4.6.1. Synthetic details of the *trans*-$Ru^{III}(CN)_2$-schiff base complexes

***Preparation of trans-$(PPh_4)[Ru^{III}(salen)(CN)_2].MeOH.H_2O$*:**

Preparation of $Ru^{II}(PPh_3)_3Cl_2$: A methanol solution of PPh_3 and $Ru^{III}Cl_3$ (6:1) was refluxed under nitrogen for about 10 hours, giving a red-brown crystalline precipitate of $Ru^{II}(PPh_3)_3Cl_2$. The precipitate was collected by filtration and washed with methanol and Et_2O and dried under vacuum (yield 90 % on basis of $Ru^{III}Cl_3$ starting material).

Preparation of $Ru^{III}(salen)(PPh_3)Cl$: H_2salen (0.068 g, 0.25 mmol) was dissolved in 10 mL of ethanol (slight warming at about 50° C was necessary) and excess triethylamime (0.4 g) was added. The solution was heated to boiling followed by the addition of 0.242 g (0.25 mmol) of $Ru^{II}(PPh_3)_3Cl_2$ as a solid. Air was drawn through the hot solution (or conversely, the mixture can be stirred in a vessel with a wide opening to increase air contact with the reaction mixture) until the solid dissolved completely forming a green solution, which was boiled for about 4 hours. Then it was cooled and filtered and the volume of the green filtrate was decreased to 2 mL. The solid was extracted with an excess of diethyl ether followed by washing with little amount of toluene to remove PPh_3. The green precipitate was washed with distilled water several times to remove NEt_3HCl and air dried (yield 75 % on the basis of $Ru^{II}(PPh_3)_3Cl_2$ used).

Preparation of trans-$(PPh_4)[Ru^{III}(salen)(CN)_2]\cdot MeOH\cdot H_2O$: Ru^{III}(salen)(PPh_3)Cl (0.2 g, 0.3 mmol) was dissolved in 15 mL of MeOH. Then KCN (0.065 g, 1 mmol) was added and the mixture was refluxed for 2 hours. The green solution was cooled and the volume was reduced under vacuum evaporation to dryness. 10 mL of distilled water was added to the green residue and then filtered. A 3 mL aqueous solution of 0.12 g (slightly more than 0.3 mmol) of PPh_4Cl was added to the deep green filtrate with constant stirring. A dark green precipitate formed immediately. The resulting solution was allowed to settle and then filtered. The precipitate was washed with water followed by Et_2O and dried in air. Yield of *trans*-$(PPh_4)[Ru^{III}(salen)(CN)_2]$ is 70 % on the basis of $Ru^{III}(salen)(PPh_3)Cl$ used for the synthesis. The compound was crystallized from slow evaporation of a MeOH-H_2O (5:1) solution and the crystals of *trans*-$(PPh_4)[Ru^{III}(salen)(CN)_2]\cdot MeOH\cdot H_2O$ were collected by filtration.

Preparation of trans-$(Bu_4N)[Ru^{III}(5\text{-}Cl\text{-}saltmen)(CN)_2]$:

Preparation of $Ru^{III}(5\text{-}Cl\text{-}saltmen)(PPh_3)Cl$: $Ru^{II}(PPh_3)_3Cl_2$ was prepared according to the method described above. 5-Cl-H_2saltmen (0.1 g, 0.25 mmol) was dissolved in 15 mL of EtOH by warming the solution and excess triethylamime (0.4 g) was added. Solid $Ru^{II}(PPh_3)_3Cl_2$ (0.242 g, 0.25 mmol) was added to the Schiff base ligand solution and the mixture was refluxed for 6 hours. The solution was filtered after cooling to room temperature and the volume was decreased to 2 mL. Ru^{III}(5-

Cl-saltmen)(PPh_3)Cl was separated as a green solid from the solution by adding diethyl ether and followed by washing with a little of water (yield 50 % on the basis of $Ru^{II}(PPh_3)_3Cl_2$ used).

Preparation of trans-(Bu_4N)[Ru^{III}(5-Cl-saltmen)$(CN)_2$]: Ru^{III}(5-Cl-saltmen)(PPh_3)Cl (0.156 g, 0.2 mmol) was dissolved in 10 mL of MeOH and 0.065 g (1 mmol) of KCN was added followed by reflux for 4 hours. The solution was cooled to room temperature and the volume reduced to dryness by vacuum evaporation. The residue was dissolved in 5 mL of water followed by addition of 0.07 g (a little more than 0.2 mmol) of solid Bu_4NCl. Some precipitate started to appear within few hours. The solution was kept overnight to settle the precipitate and then collected by filtration. The precipitate was washed with Et_2O and dried in air. Yield of *trans*-(Bu_4N)[Ru^{III}(5-Cl-saltmen)$(CN)_2$] was 40 % with respect to Ru^{III}(5-Cl-saltmen)(PPh_3)Cl used for the synthesis. The solid was dissolved in MeOH and crystallized by slow diffusion of diethyl ether through the solution.

II.4.6.2. Infrared spectroscopic characterization

The characteristic $\bar{\nu}_{C\equiv N}$ band in *trans*-(PPh_4)[Ru^{III}(salen)$(CN)_2$] is found at 2090 cm^{-1} whereas that for *trans*-(Bu_4N)[Ru^{III}(5-Cl-saltmen)$(CN)_2$] is at 2093 cm^{-1}. In *trans*-(PPh_4)[Ru^{III}(salen)$(CN)_2$], the sharp peak at 1608 cm^{-1} is characteristic of the imino C=N stretching from the salen ligand. The 5-Cl-saltmen ligand exhibits the sharp C=N stretching vibration at 1590 cm^{-1} in *trans*-(Bu_4N)[Ru^{III}(5-Cl-saltmen)$(CN)_2$]. In the complex *trans*-(Bu_4N)[Ru^{III}(5-Cl-saltmen)$(CN)_2$], the Bu_4N^+ counter cation displays the characteristic $\bar{\nu}_{C-H}$ stretching at 2871 cm^{-1} and 2960 cm^{-1}.

II.4.6.3. X-ray crystal structure

X-ray crystallographic data on the single crystals were collected for both *trans*-(PPh_4)[Ru^{III}(salen)$(CN)_2$]·MeOH·H_2O and *trans*-(Bu_4N)[Ru^{III}(5-Cl-saltmen)$(CN)_2$]. The crystallographic parameters are listed in the table II.10.

Both Ru^{III} molecular precursors crystallized in the P-1 space group. Figure II.21a and II.21b represent the molecular view of these Ru^{III} precursors. The Ru^{III} ion is in an octahedral environment where the equatorial plane of the Ru^{III} is occupied by two imine nitrogen atoms and two phenoxido oxygen atoms of the $salen^{2-}$ or 5-Cl-$saltmen^{2-}$ ligands. The two axial positions of the Ru^{III} ion are occupied with the C atoms of the cyanido groups. In the $[Ru^{III}(salen)(CN)_2]^-$ moiety, the Ru-N distances are 1.997(2) Å and 1.983(2) Å, the Ru-O bond lengths are 2.008(2) Å and 2.025(2) Å and the axial Ru-C distances are 2.080(3) Å and 2.066(3) Å. In case of the $[Ru^{III}$(5-Cl-saltmen)$(CN)_2]^-$

moiety, the Ru-N distances are 2.001(3) Å and 2.017(3)Å, the Ru-O distances are 2.022(2) Å and 2.026(2) Å and the axial Ru-C bonds are 2.081(4) Å and 2.088(4) Å. The Ru-C-N angles are 178.3(3)°/175.3(3)° and 174.1(3)°/175.5(3)° for $[Ru^{III}(salen)(CN)_2]^-$ and $[Ru^{III}(5\text{-Cl-saltmen})(CN)_2]^-$ respectively. The PPh_4^+ and the Bu_4N^+ cations neutralize the charge of Ru^{III}-Schiff base moieties the in these molecular precursors. In case of *trans*-$(PPh_4)[Ru^{III}(salen)(CN)_2]$, one water and one methanol molecule cocrystallized in each unit cell; whereas the other Ru^{III} precursor crystallized without any cocrystallizing solvent.

Table II.10. Crystal data and structure refinement *trans*-$Ru^{III}(CN)_2$-schiff base complexes

	trans-$(PPh_4)[Ru^{III}(salen)(CN)_2]\cdot MeOH\cdot H_2O$	*trans*-$(Bu_4N)[Ru^{III}(5\text{-Cl-saltmen})(CN)_2]$
Sum formula	$C_{43}H_{40}N_4O_4PRu$	$C_{38}H_{56}Cl_2N_5O_2Ru$
Molecular weight (g/mol)	808.83	786.85
Temperature (K)	150(2)	120(2)
Crystal System	Triclinic	Triclinic
Space group	P-1	P-1
a (Å), b (Å), c (Å)	10.206(2), 12.589(3), 15.747(4)	13.605(3), 15.880(3), 19.030(4)
α (°), β (°), γ (°)	109.82(9), 92.70(7), 96.21(1)	91.451(11), 104.593(20), 93.15(1)
Volume ($Å^3$)	1884.599(5)	3969.5(14)
Z	2	4
Density ($g.cm^{-3}$)	1.420	1.317
$\mu_{MoK\alpha}$ (mm^{-1})	0.507	0.567
F000	828	1652
GooF	1.102	0.995
[a]R_1 ($I > 2.00\sigma(I)$)	0.0556	0.0464
[b]wR_2 (all reflections)	0.1536	0.1170

[a]$R_1 = \Sigma\ ||F_0| - |F_C||/\ \Sigma|F_0|$, [b]$wR_2 = [\Sigma w(F_0^2 - F_C^2)^2/\Sigma w(F_0^2)^2]^{1/2}$, $w = 1/[\sigma^2F_0^2 + (0.0313P)^2 + 1.5564P]$; where $P = (F_0^2 + 2F_C^2)/3$

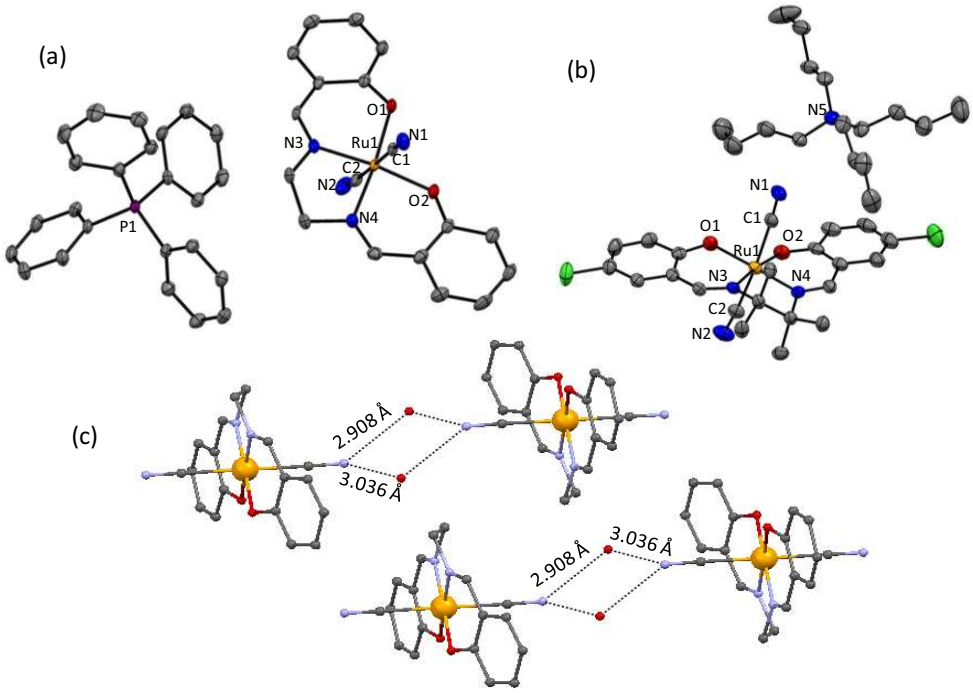

Figure II.21. ORTEP type view of the crystal structure (50 % probability) of (a) *trans*-$(PPh_4)[Ru^{III}(salen)(CN)_2]\cdot MeOH\cdot H_2O$ and (b) *trans*-$(Bu_4N)[Ru^{III}(5\text{-Cl-saltmen})(CN)_2]$. The orange, grey, blue and red spheres respectively represent the Ru, C, N and O atoms. The violet (in a) and the green (in b) sphere correspond to P and Cl atoms respectively. The H atoms and solvent molecules are omitted for clarity. (c) The H bonding interaction between the pair like $[Ru^{III}(salen)(CN)_2]$ units.

Interestingly, in the crystal packing of *trans*-$(PPh_4)[Ru^{III}(salen)(CN)_2]\cdot MeOH\cdot H_2O$, one can find two $[Ru^{III}(salen)(CN)_2]^-$ units associated through hydrogen bonding short contacts involving the cyanido nitrogen atoms and two water molecules . This supramolecular interaction ($d_{N...O}$ *ca*. 2.908-3.036 Å, figure II.21c) is likely the key reason for the weak ferromagnetic interaction between the two Ru^{III} ions of the pairs (in section II.3.2.3).

II.5. Conclusions and perspectives

In this chapter, we have discussed the qualitative and quantitative characterization of all the molecular precursors used to synthesize the molecule-based magnetic materials. We mentioned earlier in several times that our main focus of this research is to synthesize the low dimensional cyanido bridged heterometallic magnetic materials with the help of coordination chemistry. Therefore, in one hand, we have selected the 3*d* transition metal based precursors like $[Mn^{III}(SB)(solvent)_2]^+$ or $[Mn^{III}{}_2(SB)_2(solvent)_2]^{2+}$, $[Ni^{II}/Cu^{II}(cyclam)]^{2+}$ and $[Fe^{II}/Mn^{II}(LN_3O_2)]^{2+}$, each of which has the available two axial positions to coordinate with the nitrogen atom of the cyanido ligand. On the other hand, we focused on *trans*-$[Ru^{III}(salen)(CN)_2]^-$ (4*d* metal ion) and *trans*-$[Re^{IV}Cl_4(CN)_2]^{2-}$ (5*d* metal ion) precursors which can coordinated with maximum two metal ions via cyanido bridging. Thus our selection of precursors is able to restrict the dimension of the final product from bimetallic compound to one dimensional coordination network.

In order to characterize the molecular precursor we used the tools of Infrared spectroscopy and single crystal X-ray diffraction. Unfortunately, all the crystal structures of these precursors are not very good in quality, but they are good enough to determine their coordination environments with the ligands and the molecular formula as well. Both parameters (coordination geometry around the metal center and the molecular weight) are very important for their further use in design and qualitative synthesis of heterometallic complexes.

In this chapter, we have also mentioned many literature examples using these precursors. These examples help us and the reader to understand the magnetic properties and various coordination capabilities of these molecular precursors. Due to the significant uniaxial anisotropy, the Mn^{III}-Schiff base complexes are widely used in the field of molecule-based magnetic materials. The hepta-coordinated Fe^{II}/Mn^{II}-LN_3O_2 complexes are also well known for their higher anisotropic contribution due to their coordination geometry. Besides, the Ru^{III}-based (4*d* metal) and Re^{IV}-based (5*d*) building blocks can contribute also to the magnetic anisotropy of the system originated from the more diffused higher *d*-orbitals.

This present chapter contains the precursors used in the present research work. Due to the limited time of our research, we had to choose a few suitable building blocks and then further proceed to the synthesis of magnetic materials. But one can synthesize several other precursors which may serve the same purpose of finding new low dimensional magnetic materials. For example, numerous building blocks can be synthesized simply varying the Schiff base ligands on the $[Mn^{III}(SB)(solvent)_2]^+$ and *trans*-$[Ru^{III}(salen)(CN)_2]^-$ complexes, and this variation would significantly affect the magnetic properties and coordination mode of the compounds. Moreover, several other $M^{II}/^{III}$-LN_3O_2 type complexes could be tried with different transition metal ions. In the following chapters (Chapter III, IV and V), we will describe the synthesis of many new cyanido based heterometallic magnetic materials using the molecular precursors described in this chapter II.

II.6. References

[1] (a) H. Miyasaka, R. Clérac, T. Ishii, H. –C. Chang, S. Kitagawa, M. Yamashita, *J. Chem. Soc. Dalton Trans*, **2002**, 1528. (b) Thèse "*Systematic Studies on Ferromagnetism and Magnetization Relaxation Dynamics in Dimeric Mn(III) Tetradentate Schiff-Base Complexes*" C. Kachi, Department of Chemistry Graduate School of Science Tokyo Metropolitan University, **2006**. (c) H. Miyasaka, A. Saitoh, S. Abe, *Coord. Chem. Rev*., **2007**, 251, 2622.

[2] (a) H. Miyasaka, A. Saitoh, M. Yamashita, R. Clérac, *Dalton Trans*., **2008,** 2422. (b) T. T. Tidwell*, Angew. Chem. Int. Ed.*, **2008**, 47, 1016.

[3] (a) H. Miyasaka, R. Clérac, W. Wernsdorfer, L. Lecren, C. Bonhomme, K.-i. Sugiura, M. Yamashita, *Angew. Chem. Int. Ed.*, **2004**, 43, 2801. (b) Q. Wu, Y.-G. Li, Y.-H. Wang, R. Clérac, Y. Lu, E.-B. Wang, *Chem. Commun.*, **2009**, 5743.

[4] (a) F. Neese, *J. Am. Chem. Soc*., **2006**, 128, 10213. (b) S. Mitra, *Prog. Inorg. Chem*., **1977**, 22, 309. (c) B. Figgis, *Trans. Faraday Soc*., **1960**, 56, 1554.

[5] (a) B. J. Kennedy, K. S. Murray, *Inorg. Chem*., **1985**, 24, 1552. (b) P. Garge, R. Chikate, S. Padhye, J.-M. Savariault, P. Loth, J.-P. Tuchagues, *Inorg. Chem*., **1990**, 29, 3315. (c) R. C. Reem, E. I. Solomon, *J. Am. Chem. Soc*., **1987**, 109, 1216.

[6] (a) R. Clérac, H. Miyasaka, M. Yamashita, C. Coulon, *J. Am. Chem. Soc*., **2002**, 124, 12837. (b) H. Miyasaka, R. Clérac, K. Mizushima, K.–I. Sugiura, M. Yamashita, W. Wernsdorfer, C. Coulon, *Inorg. Chem*., **2003**, 42, 8203. (c) H. Miyasaka, T. Nezu, K. Sugimoto, K. Sugiura, M. Yamashita, R. Clérac, *Inorg. Chem*., **2004**, 43, 5486. (d) H. Miyasaka, T. Nezu, K. Sugimoto, K. Sugiura, M. Yamashita, R. Clérac, *Chem. Eur. J*., **2005**, 11, 1592.

[7] M. Ferbinteanu, H. Miyasaka, W.Wernsdorfer, K. Nakata, K. Sugiura, M. Yamashita, C. Coulon, R. Clérac, *J. Am. Chem. Soc*., **2005**, 127, 3090.

[8] H. Miyasaka, T. Madanbashi, A. Saitoh, N. Motokawa, R. Ishikawa, M. Yamashita, S. Bahr, W. Wernsdorfer, R. Clérac. *Chem. Eur. J.*, **2012**, 18, 13, 3942.

[9] (a) P. Przychodzen, K. Lewinski, M. Balanda, R. Pelka, M. Rams, T.Wasiutynski, C. Guyard-Duhayon, B. Sieklucka, *Inorg. Chem*. **2004**, 43, 2967. (b) S.-F. Si, J.-K.Tang, Z.-Q. Liu, D.-Z. Liao, Z.-H. Jiang, S.-P.Yan, P. Cheng*, Inorg. Chem. Commun.*, **2003**, 6, 1109. (c) X. Shen, B. Li, J. Zou, H. Hu, Z. Xu, *J. Mol. Struct*., **2003**, 657, 325. (d) J. H. Yoo, J. H. Lim, H.C. Kim, C. S. Hong, *Inorg. Chem.*, **2006,** 45, 9613. (e) C. Kachi-Terajima, H. Miyasaka, A. Saitoh, N. Shirakawa, M. Yamashita, R. Clérac, *Inorg. Chem.*, **2007**, 46, 5861. (f) H. Miyasaka, N. Matsumoto, H. Okawa, N. Re, E. Gallo, C. Floriani, *J. Am. Chem. Soc.*, **1996**, 118, 981. (g) H. Miyasaka, T. Nezu, K. Sugimoto, K. Sugiura, M. Yamashita, R. Clérac, *Inorg. Chem.*, **2004**, 43, 5486. (h) Z. H. Ni, H. Z. Kou, L. F. Zhang, C. Ge, A. L. Cui, R. J.Wang, Y. Li, O. Sato, *Angew. Chem. Int. Ed*., **2005**, 44, 7742. (i) H. Miyasaka, H. Ieda, N. Matsumoto, N. Re, R. Crescenzi, C. Floriani, *Inorg. Chem*., **1998**, 37, 255. (j) Y. Kim, S.-M. Park, W. Nam, S.-J. Kim, *Chem. Commun.*, **2001**, 4, 1470. (k) Y. Kim, S.-M. Park, S.-J. Kim, *Inorg. Chem. Commun*., **2002**, 5, 592. (l) H. Zhou, J. Wang, H. S. Wang, Y. L. Xu, X. J. Song, Y. Song, X. Z. You, *Inorg. Chem*., **2011**, 50, 6868.

[10] (a) H. Miyasaka, H. Ieda, N. Matsumoto, N. Re, R. Crescenzi, C. Floriani, *Inorg. Chem*.,**1998**, 37, 255. (b) K. J. Cho, D. W. Ryu, H. Y. Kwak, J. W. Lee, W. R. Lee, K. S. Lim, E. K. Koh, Y. W. Kwon, C. S. Hong, *Chem. Commun.*, **2012**, 48, 7404.

[11] B. Bosnich, M. L. Tobe, G. A. Webb, *Inorg. Chem*., **1965**, 4, 1109.

[12] J. A. Duimstra, C. L. Stern, T. J. Meade, *Polyhedron*, **2006**, 25, 2705.

[13] W. F. Yeung, P. H. Lau, T. C. Lau, H. Y. Wei, H. L. Sun, S. Gao, Z. D. Chen, W. T. Wong, *Inorg. Chem*., **2005**, 44, 6579.

[14] H. Oshio, H. Okamoto, T. Kikuchi, T. Ito, *Inorg. Chem*., **1997**, 36, 3201.

[15] O. Jeannin, R. Clérac, T. Cauchy, M. Fourmigué, *Inorg. Chem.*, **2008**, 47, 10656.

[16] Y. S. You, D. Kim, Y. Do, S. J. Oh, C. S. Hong, *Inorg. Chem*., **2004**, 43, 22, 6899.

[17] T. S. Venkatakrishnan, S. Sahoo, N. Bréfuel, C. Duhayon, C. Paulsen, A. L. Barra, S. Ramasesha, J. P. Sutter, *J. Am. Chem. Soc*., **2010**, 132, 6047.

[18] (a) D. Zhang, H. Wang, Y. Chen, Z.-H. Ni, L. Tian, J. Jiang, *Inorg. Chem*., **2009**, 48, 12, 5488. (b) B. Drahos, J. Kotek, P. Hermann, I. Lukes, E. Toth, *Inorg. Chem*., **2010**, 49, 3224.

[19] Y. Z. Zhang, B.-W. Wang, O. Sato, S. Gao, *Chem. Commun*., **2010**, 46, 6959.

[20] F. Bonadio, M.-C. Senna, J. Ensling, A. Sieber, A. Neels, H. Stoeckli-Evans, S. Decurtins, *Inorg. Chem*., **2005**, 44, 969.

[21] (a) T. D Harris, M. V. Bennett, R. Clérac, J. R. Long, *J. Am. Chem. Soc*., **2010**, 132, 3980. (b) T. D. Harris, C. Coulon, R. Clérac, J. R. Long, *J. Am. Chem. Soc*., **2011**, 133, 123. (c) X. Feng, J. Liu, T. D. Harris, S. Hill, J. R. Long, *J. Am. Chem. Soc.*, **2012**, 134, 7521. (d) T. D. Harris, H. S. Soo, C. J. Chang, J. R. Long, *Inorg. Chim. Acta.*, **2011**, 369, 82.

[22] (a) W. H. Leung, C. M. Che, *Inorg. Chem*., **1989**, 28, 4619. (b) J. A. Duimstra, C. L. Stern, T. J. Meade, *Polyhedron*, **2006**, 25, 2705.

[23] J. H. Yoon, H. S. Yoo, H. C. Kim, S. W. Yoon, B. J. Suh, C. S. Hong, *Inorg. Chem*., **2009**, 48, 816.

[24] (a) R. Sayre, *J. Am. Chem. Soc*., **1955**, 77, 6689. (b) C.-M. Che, K.-Y. Wong, H.-W. Lam, K.-F. Chin, Z.-Y. Zhou, T. C. W. Mak, *J. Chem. Soc. Dalton Trans*., **1993**, 857.

CHAPTER III

Re^{IV}-Mn^{III}-Schiff base systems

III.1. Introduction

This chapter describes details of new compounds obtained from reactions between Mn^{III}-Schiff base complexes[1] and *trans*-$(Bu_4N)_2[Re^{IV}Cl_4(CN)_2]\cdot 2DMA$[2,10-11] precursors. The synthesis and properties of these molecular precursors have been already discussed in chapter II. The reactions between them resulted in different kinds of bimetallic compounds with different nuclearity, including one dimensional compounds. All the reactions were performed at ambient temperature using organic solvents such as MeOH, MeCN, $MeNO_2$ etc and occasionally water. Notably, we found that the type of resulting compound significantly depends on the Mn^{III}-Schiff base analogue used for the synthesis. We will discuss the synthesis and crystal structures of all of the newly obtained compounds throughout this chapter along with an explicit discussion of their magnetic properties.

III.2. Re^{IV}-Mn^{III} molecular systems

The synthesized Re^{IV}-Mn^{III}-Schiff base systems which are not one dimensional according to their X-ray crystallographic structure are here categorized as zero dimensional molecular systems. These zero dimensional systems are further categorized according to the coordination mode of the precursors and nuclearity of the product. Therefore we have three different classes of compounds in the zero dimensional family, (i) the non-coordinated Re^{IV}/Mn^{III} salts, (ii) the trinuclear complexes and (iii) a hexanuclear systems.

III.2.1. Non-coordinated Re^{IV}/Mn^{III} salts

Not all of the Mn^{III}-Schiff base precursors were found to coordinate with the Re^{IV} ion through the cyanido bridge. In organic solvent/water media the nitrogen atom of the cyanido ligand of the *trans*-$[Re^{IV}Cl_4(CN)_2]^{2-}$ building block competes with the solvent molecules to fill the coordination sphere of the Mn^{III} ion. In the present case of the non-coordinated Re^{IV}/Mn^{III} systems, the solvent molecules win over the cyanido ligand to coordinate the Mn^{III} ion in its axial positions. Consequently, the *trans*-$[Re^{IV}Cl_4(CN)_2]^{2-}$ moiety acts as a counter anion to the Mn^{III} complex and also helps to develop the crystal structure via hydrogen bonding interactions between the nitrogen atom of the cyanido ligand and solvent molecules. In the present research work, we synthesized three of such non-coordinated Re^{IV}/Mn^{III} salts type systems. Due to the absence of direct coordination between the Mn^{III} and Re^{IV} ions, the magnetic properties of these compounds are not strongly influenced by Mn^{III}-Re^{IV}

magnetic exchange, but are rather guided by the sum of the magnetic properties of the Mn^{III} and Re^{IV} precursors.

III.2.1.1. Synthesis

a) ***$[Mn^{III}(3\text{-}MeO\text{-}saltmen)(H_2O)_2]_2[Re^{IV}Cl_4(CN)_2]\cdot 2MeCN$*** (**1**): $[Mn^{III}$(3-MeO-saltmen)$(CH_3OH)(H_2O)](ClO_4)$ (0.0117 g, 0.02 mmol) was dissolved in 2 mL of MeCN and poured into a thin glass tube of 1.5 cm diameter and 2 mL of pure MeCN was carefully layered over it. A 1.5 mL MeCN solution of $(Bu_4N)_2[Re^{IV}Cl_4(CN)_2]\cdot 2DMA$ (0.0103 g, 0.01 mmol) was very carefully poured as a layer over the pure solvent to avoid fast mixing of the reactants. Then the tube sealed with parafilm to avoid evaporation. After one week, brown block-shaped crystals were found at the bottom of the tube. The yield of the product was *ca.* 70 % on the basis of the Mn^{III}-Schiff base precursor used. Elemental analysis calculated (%) for $C_{50}H_{62}Cl_4Mn_2N_8O_{12}Re$ (M = 1404.96 g/mol): C 42.74, H 4.45, N 7.98; and experimentally found (%) as C 42.64, H 4.40, N 7.89; IR (KBr): $\bar{\nu}$ = 2126 (C≡N stretch), 1596 (C=N stretch) cm^{-1}.

b) ***$[Mn^{III}(5\text{-}^tBu\text{-}saltmen)(H_2O)]_2[Re^{IV}Cl_4(CN)_2]\cdot 2CH_3CH(OH)CH_3$*** (**2**): $[Mn^{III}{}_2$(5-^{t}Bu-saltmen)$_2(H_2O)_2](ClO_4)_2\cdot 2H_2O$ (0.0125 g, 0.01 mmol) was dissolved in 3 mL of isopropyl alcohol $[CH_3CH(OH)CH_3]$ and 1 mL MeOH solution of $(Bu_4N)_2[Re^{IV}Cl_4(CN)_2]\cdot 2DMA$ (0.0103 g 0.01 mmol) was added drop wise. The solution slowly evaporated at room temperature by covering the vial opening with parafilm and making few small holes in it. After two days, brown block-shaped crystals were found in the bottom of the vial and separated by filtration. The yield of the product was *ca.* 60 % on the basis of the Mn^{III}-Schiff base precursor. Elemental analysis calculated (%) for $C_{64}H_{96}Cl_4Mn_2N_6O_8Re$ (M = 1515.37 g/mol): C 50.73, H 6.39, N 5.55; and experimentally found (%) as C 50.68, H 6.44, N 5.58; IR (KBr): $\bar{\nu}$ = 2126 (C≡N stretch), 1609 (C=N stretch) cm^{-1}.

c) ***$[Mn^{III}(5\text{-}MeO\text{-}salen)(MeOH)_2]_2[Re^{IV}Cl_4(CN)_2]$*** (**3**): $[Mn^{III}$(5-MeO-salen)$(H_2O)_2](ClO_4)$ (0.0103 g, 0.02 mmol) was dissolved in 3 mL of MeOH and 1 mL MeCN solution of $(Bu_4N)_2[Re^{IV}Cl_4(CN)_2]\cdot 2DMA$ (0.0103 g, 0.01 mmol) was added drop wise. The solution slowly evaporated at room temperature by covering the vial opening with parafilm and making few small holes in it with a needle. After one day, large needle-shaped brown crystals were found in the bottom of the vial and separated through filtration. The yield of the product was *ca.* 80 % on the basis of the Mn^{III}-Schiff base precursor. Elemental analysis calculated (%) for $C_{42}H_{52}Cl_4Mn_2N_6O_{12}Re$ (M = 1270.79 g/mol): C 39.70, H 4.12, N 6.61; and experimentally found (%) as C 39.74, H 4.16, N 6.57; IR (KBr): $\bar{\nu}$ = 2125 (C≡N stretch), 1608 (C=N stretch) cm^{-1}.

Interestingly the stretching vibration of the cyanido group $\bar{\nu}_{CN}$ in the infrared spectra of these compounds was found at almost same wavenumber as for the Re^{IV} precursor.[2] This similarity emphasizes that the cyanido groups are not coordinated to the Mn^{III} ion, after compound formation.

III.2.1.2. X-ray crystal structure

The single crystal X-ray crystallographic data of **1-3** are summarized in table III.1. The figure III.1 show their crystal structures.

Table III.1. Crystal data and structure refinement of **1, 2** and **3.**

	1	**2**	**3**
Sum formula	$C_{50}H_{62}Cl_4Mn_2N_8O_{12}Re$	$C_{64}H_{96}Cl_4Mn_2N_6O_8Re$	$C_{42}H_{52}Cl_4Mn_2N_6O_{12}Re$
Molecular weight (g/mol)	1404.96	1515.37	1270.79
Temperature (K)	150(2)	100(2)	100(2)
Crystal System	Triclinic	Monoclinic	Triclinic
Space group	P-1	C2/c	P-1
a (Å)	10.301(2)	29.622(11)	9.961(5)
b (Å)	12.300(3)	15.617(6)	10.575(5)
c (Å)	12.502(3)	21.495(8)	13.620(5)
α (°)	76.53(3)	90	84.755(5)
β (°)	76.54(3)	131.489(1)	69.502(5)
γ (°)	71.88(3)	90	63.735(5)
Volume ($Å^3$)	1441.9(6)	7448.6(5)	1201.7(9)
Z	1	4	1
Density ($g.cm^{-3}$)	1.613	1.351	1.756
$\mu_{MoK\alpha}$ (mm^{-1})	2.775	2.149	3.318
F000	703	3116	635
GooF	1.193	1.099	1.086
[a]R_1 ($I > 2.00\sigma(I)$)	0.0290	0.0464	0.0398
[b]wR_2 (all reflections)	0.1139	0.1629	0.1036

[a]$R_1 = \Sigma ||F_0| - |F_C|| / \Sigma |F_0|$, [b]$wR_2 = [\Sigma w(F_0^2 - F_C^2)^2 / \Sigma w(F_0^2)^2]^{1/2}$, $w = 1/[\sigma^2 F_0^2 + (0.0313P)^2 + 1.5564P]$; where $P = (F_0^2 + 2F_C^2)/3$

Compounds **1** and **3** crystallized in the triclinic crystal system and P-1 space group, while the crystal structure of **2** is monoclinic with a C2/c space group. In unit cell, the Mn^{III} and the Re^{IV} building blocks are in a 2:1 ratio. In compounds **1** and **3**, the Mn^{III}-Schiff base units are mononuclear. In **1**, the axial positions of the Mn^{III} ion are occupied by water molecules, while in **3** the Mn^{III} ion is axially coordinated by MeOH molecules. In compound **2**, the Mn^{III}-Schiff base complexes crystallized as an out of plane dinuclear complex, where one axial position of Mn^{III} ion is occupied by the phenoxido oxygen originating from the other Mn^{III} moiety and the remaining axial coordination site is fulfilled by water molecule.

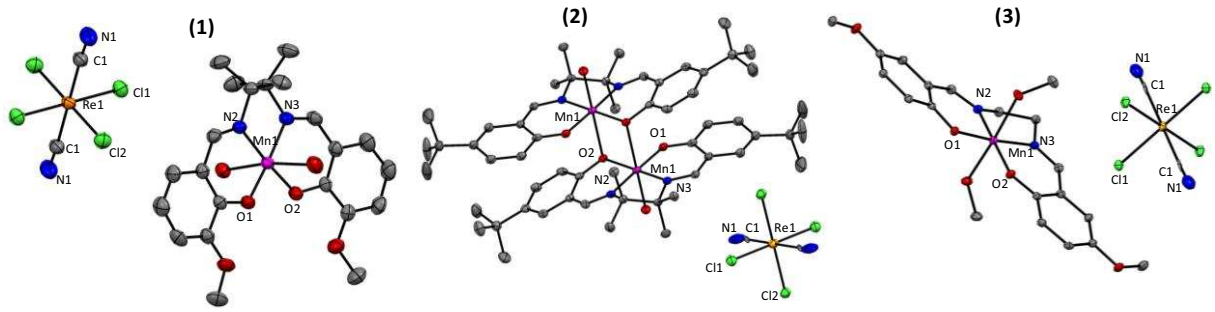

Figure III.1. ORTEP diagrams (50 % thermal probability) of compound **1-3**. The Re, Mn, C, O, N and Cl atoms are shown in orange, magenta, grey, red, blue and green respectively. The hydrogen atoms and solvent molecules have been omitted for clarity.

For **1** and **2**, acetonitrile and isopropyl alcohol molecules are present respectively in the crystal packing and display a variety of hydrogen bonding interactions, which are important in building the crystal structure. Quite similar to **3**, in compound **1** we observed a pair-like arrangement of two $[Mn^{III}(3\text{-MeO-saltmen})(H_2O)_2]^+$ moieties through hydrogen bonding interactions between one of the water molecules (axially coordinated to Mn^{III}) and (i) the oxido of 3-methoxy group (*ca.* $d_{O\ldots O}$ = 2.90 Å) and (ii) the phenoxido (*ca.* $d_{O\ldots O}$ = 2.95 Å) groups of the nearest Mn^{III}-Schiff base moiety (figure III.2a). The other water molecule has an H-bonding interaction with the nitrogen atoms of the acetonitrile molecule (*ca.* $d_{O\ldots N}$ = 2.90 Å) and of the *trans*-$[Re^{IV}Cl_4(CN)_2]^{2-}$ moiety (*ca.* $d_{O\ldots N}$ = 2.79 Å).

In the crystal structure of **2**, the dinuclear $[Mn^{III}(5\text{-}^t\text{Bu-saltmen})(H_2O)]_2^{2+}$ units have a Mn-O^*_{phen} distance of 2.454(3) Å that results in a Mn-Mn distance of 3.335 Å. Each of the axial water molecules is in an hydrogen bonding interaction with two oxygen atoms belonging to two isopropanol molecules (*ca.* $d_{O\ldots O}$ = 2.76-2.83 Å), while these –OH groups of the isopropanol also form H-bonding short contacts with the cyanido nitrogen of the *trans*-$[Re^{IV}Cl_4(CN)_2]^{2-}$ unit (*ca.* $d_{O\ldots N}$ = 2.87 Å) (figure III.2b).

In the crystal structure of **3**, there are no interstitial solvent molecules. In **3**, two of the $[Mn^{III}(5\text{-MeO-salen})(MeOH)_2]^+$ units are associated by significant hydrogen bonding interactions (*ca.* $d_{O\ldots O}$ = 2.72 Å) between the axial MeOH for each Mn^{III}-Schiff base moiety and the phenoxido oxygen of a neighboring Mn^{III}-Schiff base complex. The other axial MeOH molecule has a hydrogen bond short contact with the cyanido nitrogen (*ca.* $d_{O\ldots N}$ = 2.78 Å) from the *trans*-$[Re^{IV}Cl_4(CN)_2]^{2-}$ unit (figure III.2c).

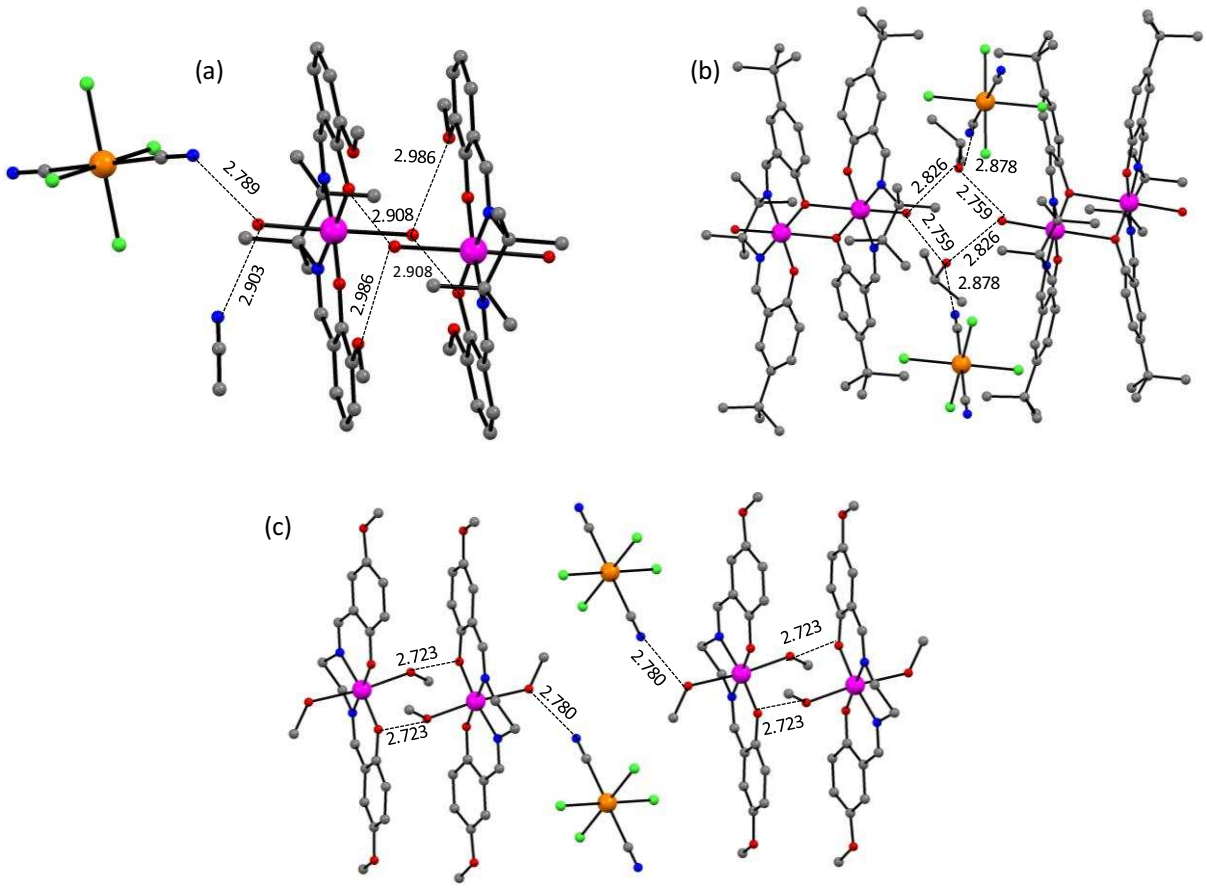

Figure III.2. Representation of **1** (a), **2** (b) and **3** (c) along with their hydrogen bonding short contacts through solvent molecules and the cyanido moiety. All distances are given in Å.

III.2.1.3. Magnetic properties

The magnetic susceptibility of compounds **1-3** as a function of temperature at an applied *dc* field of 1000 Oe is plotted as χT vs. T (figure III.3). As we have seen in the crystal structures, compounds **1** and **3** are comparable; likewise, their thermal behavior of χT are is also quite comparable. The high temperature values of χT are 8 cm^3K/mol at 290 K for **1**, 7.9 cm^3K/mol at 270 K for **2** and 7.7 cm^3K/mol at 270 K for **3**. Considering the g values as $g_{Re} = 1.7$[2] and $g_{Mn} = 2$[3d], the theoretical value of χT is about 7.2 cm^3K/mol at room temperature for all the Re^{IV}/Mn^{III} salt compounds, comparable to the experimental values. With the decrease of temperature, the χT of all these compounds remains almost unchanged until around 90 K for **1**, 85 K for **2** and 130 K for **3**, but further lowering of temperature results a decrease of χT for **1** and **3**, reaching minimum values of 1.2 and 0.9 cm^3K/mol at 1.8 K. In case of **2** χT starts to increase below 85 K and reaches a maximum value of 11.4 at 1.8 K.

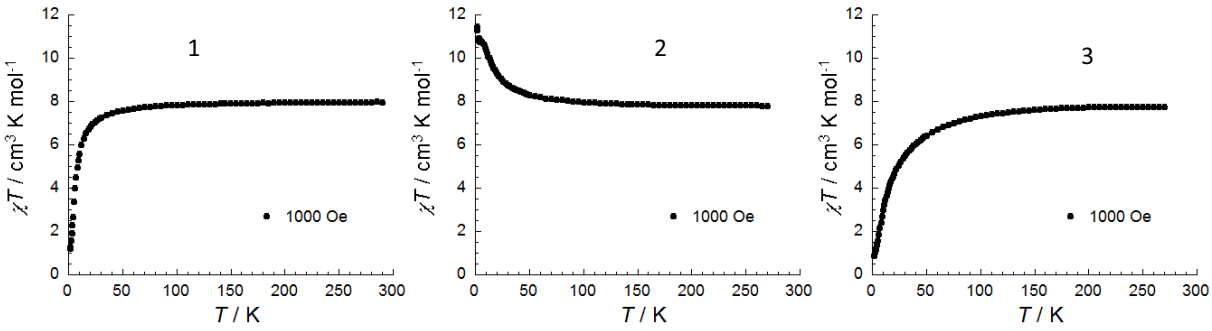

Figure III.3. The temperature dependence of the molar χT product at 1000 Oe between 290-1.8 K for **1, 2** and **3**.

Although none of the compounds have Mn^{III}-Re^{IV} bonding interactions mediated by cyanido bridges, the temperature dependence of the χT product clearly demonstrates dominating ferromagnetic interactions in **2** and antiferromagnetic interactions in **1** and **3**. In **2**, the Mn^{III}-Schiff base complex moiety crystallized in the dinuclear form. From previous studies,[1a] the two Mn^{III} are known to be coupled ferromagnetically. This and the consideration that the Re^{IV} centers are quite far from the Mn^{III}-dinuclear units, suggests that the increase of χT in **2** at low temperature originates from the ferromagnetic interaction between the two Mn^{III} ions of the dinuclear complex. In **1** and **3**, the mononuclear Mn^{III}-Schiff base units closely interact with each other as with well as the $[Re^{IV}Cl_4(CN)_2]$ moieties through hydrogen bonding interactions. These interactions lead to an overall antiferromagnetic coupling between the magnetic centers which leads to the significant decrease of the χT of **1** and **3** at lower temperature. The crystal structure of **3** possesses no solvent molecules and thus the magnetic Re^{IV} and Mn^{III} centers are closer compared to in **1**. Thus the drop in χT begins at a higher temperature in **3** (below 130 K) than in **1** (below 90 K).

In order to further investigate the interactions between the magnetic units, the magnetization (M) of **1-3** was measured as a function of applied magnetic field (H) between 1.83 and 8 K (figure III.4).

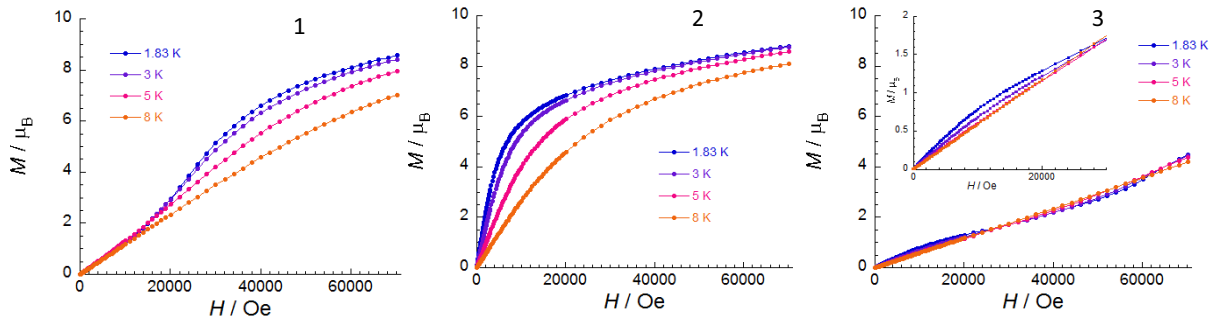

Figure III.4. The field dependence of magnetization for **1-3** between 1.83 and 8 K.

The nature of the M vs. H curves of **2** resembles that of a paramagnetic substance, which clearly indicates the absence of significant antiferromagnetic interactions in the system. The

magnetization curves of **1** exhibit an inflection point around 20000 Oe which further emphasizes the presence of antiferromagnetic interactions in the compound. In **3**, the stronger antiferromagnetic interactions are also highlighted by the spape of the magnetization curves, which indicates the characteristic field of the system is very high (H^* > 7 T).

III.2.2. Trinuclear Re^{IV}-Mn^{III} molecular systems

These trinuclear systems are composed of molecules having one *trans*-$[Re^{IV}Cl_4(CN)_2]^{2-}$ moiety connected to two Mn^{III}-Schiff base units through the nitrogen end of the cyanido and thus forming a neutral Mn^{III}-Re^{IV}-Mn^{III} complex. The cyanido group occupies one axial position of the Mn^{III}-Schiff base moiety and the other axial position is satisfied by a solvent molecule. As the molecule is neutral no counter anion or cation was observed in the crystal structure. Three trinuclear systems derived from the Mn^{III}-Schiff base complexes $[Mn^{III}(5\text{-MeO-salpen})(H_2O)_2](ClO_4)\cdot H_2O$, $[Mn^{III}(salphen)(CH_3COO)]$ and $[Mn^{III}_2(5\text{-Cl-salmen})_2(H_2O)_2](ClO_4)_2\cdot 2H_2O$, have been synthesized. In the crystal structure of these all three compounds, supramolecular interactions through hydrogen bonding is a common but very important parameter to build the crystal structures. The magnetic properties of the trinuclear compounds are quite comparable to one another, involving Re^{IV}-Mn^{III} antiferromagnetic interactions and three dimensional ordered antiferromagnetic state with a metamagnetic behavior.

III.2.2.1. Synthesis

a) ***$[Mn^{III}(5\text{-MeO-salpn})(H_2O)]_2[Re^{IV}Cl_4(CN)_2]$*** (**4**): $[Mn^{III}(5\text{-MeO-salpen})(H_2O)_2](ClO_4)\cdot H_2O$ (0.0109 g, 0.02 mmol) was dissolved in 2 mL of MeCN and poured into a thin glass tube of 1.5 cm diameter and 2 mL volume of pure MeCN was carefully layered over it. A 1.5 mL MeCN solution of $(Bu_4N)_2[Re^{IV}Cl_4(CN)_2]\cdot 2DMA$ (0.0103 g, 0.01 mmol) was very carefully poured as a layer over the pure solvent to avoid fast mixing of the reactants. The tube was sealed with parafilm to avoid evaporation. After three days, brown needle-shaped crystals were found on the walls of the tube. The yield of the product was *ca.* 80 % on the basis of the Mn^{III}-Schiff base precursor. Elemental analysis calculated (%) for $C_{40}H_{44}Cl_4Mn_2N_6O_{10}Re$ (M = 1206.70 g/mol): C 39.81, H 3.68, N 6.96; and experimentally found (%) as C 39.77, H 3.69, N 6.98; IR (KBr): $\bar{\nu}$ = 2137 (C≡N stretch), 1604 (C=N stretch) cm^{-1}.

b) ***$[Mn^{III}(salphen)(MeOH)]_2[Re^{IV}Cl_4(CN)_2]$*** (**5**): $[Mn^{III}(salphen)(CH_3COO)]$ (0.0085 g, 0.02 mmol) was dissolved in 3 mL of MeOH and an 1 mL MeOH solution of

$(Bu_4N)_2[Re^{IV}Cl_4(CN)_2]\cdot 2DMA$ (0.0103 g, 0.01 mmol) was added drop wise. The solution slowly evaporated at room temperature by covering the vial opening with parafilm and making a small hole in it with a needle. The next day, brown block-shaped crystals appeared at the bottom of the vial and were separated by filtration. The yield of the product was *ca.* 80 % on the basis of the Mn^{III}-Schiff base precursor. Elemental analysis calculated (%) for $C_{44}H_{36}Cl_4Mn_2N_6O_6Re$ (M = 1182.68 g/mol): C 44.68, H 3.07, N 7.11; and experimentally found (%) as C 44.72, H 3.11, N 7.08; IR (KBr): $\bar{\nu}$= 2140 (C≡N stretch), 1610 (C=N stretch) cm^{-1}.

c) ***$[Mn^{III}(5\text{-}Cl\text{-}salmen)]_2[Re^{IV}Cl_4(CN)_2]\cdot 0.5MeCN\cdot 0.5MeOH\cdot H_2O$*** (**6**): $[Mn^{III}_2(5\text{-}Cl\text{-}salmen)_2(H_2O)_2](ClO_4)_2\cdot 2H_2O$ (0.0108 g, 0.01 mmol) was dissolved in 3 mL of MeOH and an 1 mL MeCN solution of $(Bu_4N)_2[Re^{IV}Cl_4(CN)_2]\cdot 2DMA$ (0.0103 g, 0.01 mmol) was added drop wise followed by the addition of 0.5 mL of water. The solution slowly evaporated at room temperature by covering the vial opening with parafilm and making a small hole in it with a needle. After two days, very small brown crystals appeared at the bottom and the wall of the vial and were separated by filtration. The yield of the product was *ca.* 60 % on the basis of the Mn^{III}-Schiff base precursor used. Elemental analysis calculated (%) for $C_{78}H_{86}Cl_{16}Mn_4N_{14}O_{18}Re_2$ (M = 2666.97 g/mol): C 35.13, H 3.25, N 7.35; and experimentally found (%) as C 35.10, H 3.27, N 7.31; IR (KBr): $\bar{\nu}$ = 2142 (C≡N stretch), 1610 (C=N stretch) cm^{-1}.

III.2.2.2. X-ray crystal structure

Crystallographic data for the three trinuclear Mn^{III}-Re^{IV}-Mn^{III} compounds (**4-6**) are summarized in table III.2.

Table III.2. Crystal data and structure refinement of **4**, **5** and **6**.

	4	**5**	**6**
Sum formula	$C_{40}H_{44}Cl_4Mn_2N_6O_{10}Re$	$C_{44}H_{36}Cl_4Mn_2N_6O_6Re$	$C_{78}H_{86}Cl_{16}Mn_4N_{14}O_{18}Re_2$
Molecular weight (g/mol)	1206.70	1182.68	2666.97
Temperature (K)	150(2)	120(2)	150(2)
Crystal System	Orthorhombic	Triclinic	Triclinic
Space group	Pcnb	P-1	P-1
a (Å)	13.6602 (4)	10.875(2)	13.4138(10)
b (Å)	15.3323(3)	10.939(2)	14.8083(9)
c (Å)	21.2610(3)	11.607(2)	15.2379(9)
α (°)	90	120.44(3)	89.796(3)
β (°)	90	115.38(3)	70.871(4)
γ (°)	90	106.15(3)	75.648(4)
Volume ($Å^3$)	4453.0(2)	1103.8(4)	2760.8(3)
Z	4	1	1
Density ($g.cm^{-3}$)	1.800	1.776	1.604
$\mu_{MoK\alpha}$ (mm^{-1})	3.574	3.598	3.077
F000	2380	581	1318
GooF	0.995	1.105	1.032
[a]R_1 ($I > 2.00\sigma(I)$)	0.0369	0.0430	0.0711
[b]wR_2 (all reflections)	0.0956	0.1579	0.2234

[a]$R_1 = \Sigma ||F_0| - |F_C|| / \Sigma |F_0|$, [b]$wR_2 = [\Sigma w(F_0^2 - F_C^2)^2 / \Sigma w(F_0^2)^2]^{1/2}$, $w = 1/[\sigma^2 F_0^2 + (0.0313P)^2 + 1.5564P]$; where $P = (F_0^2 + 2F_C^2)/3$

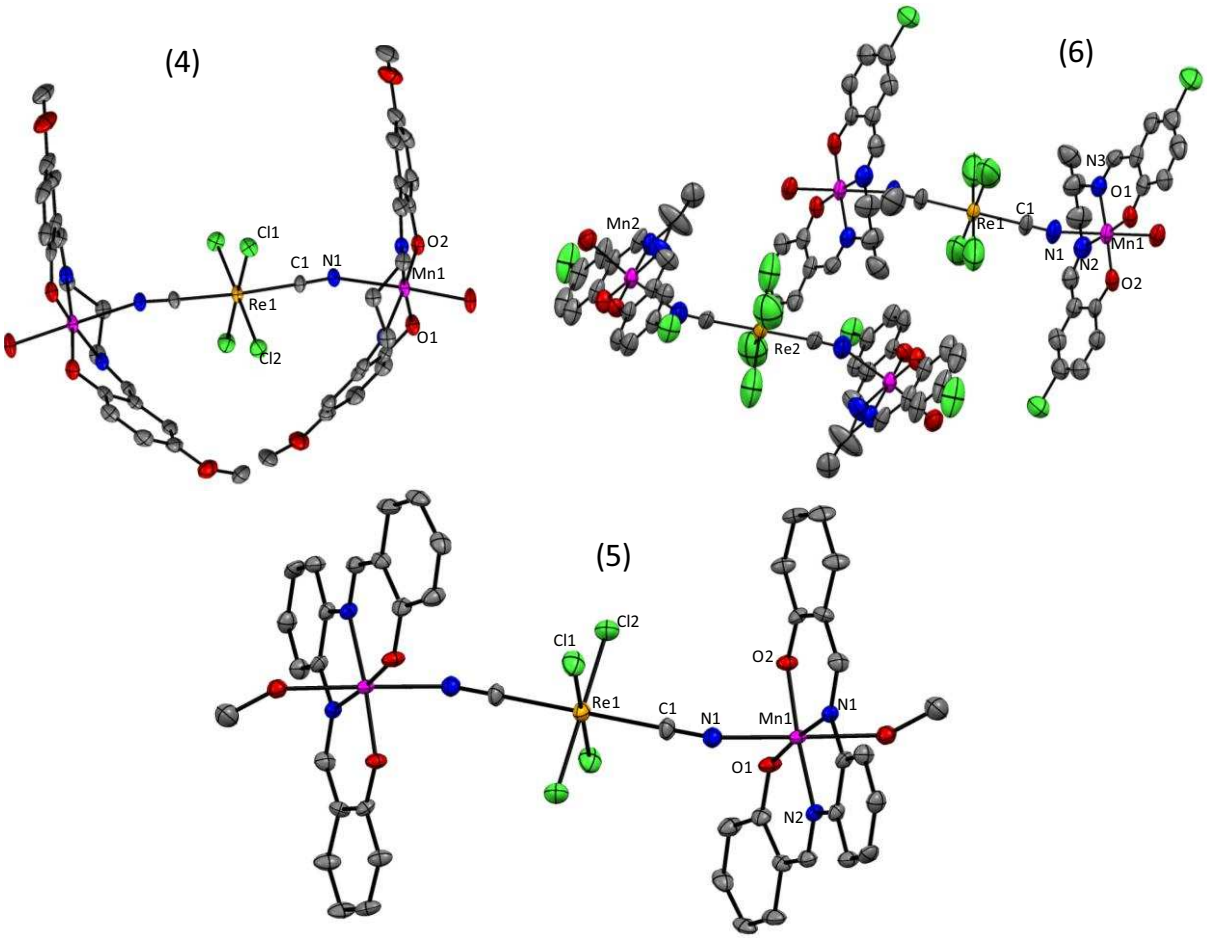

Figure III.5. ORTEP diagrams (50 % thermal probability) of compound **4-6.** The Re, Mn, C, O, N and Cl atoms are shown in orange, magenta, grey, red, blue and green respectively. The H atoms and solvent molecules (for **6**) have been omitted for clarity.

Compound **5** and **6** crystallized in the triclinic crystal system in the P-1 space group, whereas the compound **4** belongs to the orthorhombic Pcnb space group. For all trinuclear complexes both Re^{IV} and Mn^{III} ions are in an octahedral environment; the equatorial plane of Re^{IV} is occupied by four chloride, while two cyanido groups are axially coordinated through the C atoms (figure III.5). The Mn^{III} ion resides in the plane of the Schiff base ligand. Its equatorial coordination sites are occupied by nitrogen and oxygen atoms belonging to the Schiff base ligands. For all these compounds, the cyanido groups from the *trans*-$[Re^{IV}Cl_4(CN)_2]^{2-}$ moiety are connected to one axial position of each of the two Mn^{III} ions through the nitrogen atom. The remaining axial coordination sites of Mn^{III} ions are filled by solvent molecules (figure III.5), water for compounds **4** and **6**, and MeOH for **5**. In the crystal structure of **4** and **5,** there are no non-coordinated solvent molecules, but in case of **6** many non-coordinated solvent molecules (i.e. MeOH, MeCN and H_2O) occupy the void spaces in the crystal packing.

In the crystal structure of **4**, the Mn-N-C angle is 152.2(4)° and this deviation from linearity provides the molecule a twist along the Mn^{III}-Re^{IV}-Mn^{III} axis (figure III.6a) with respect to the Re

centre. This molecule possesses the *mmm* crystallographic point group symmetry where one of the glided planes passes through the $ReCl_4$ plane (this glided plane is parallel to the *ac* plane in the crystal structure). The molecules are closely packed if viewed along the *a* axis with supramolecular H-bonding interactions between the axially coordinated water molecules and phenoxido oxygen atoms coming from the Schiff base of the nearest trinuclear neighbor (*ca.* $d_{O...O}$ = 2.81-2.99 Å, figure III.6b). The π-stacking interactions between the aromatic rings of two successive trinuclear units with an average distance of 3.43 Å is another driving force keeping the molecules in close contact in **4** (figure III.6b). A view of the molecular packing of compound **4** in the *bc* plane is given in figure III.6c.

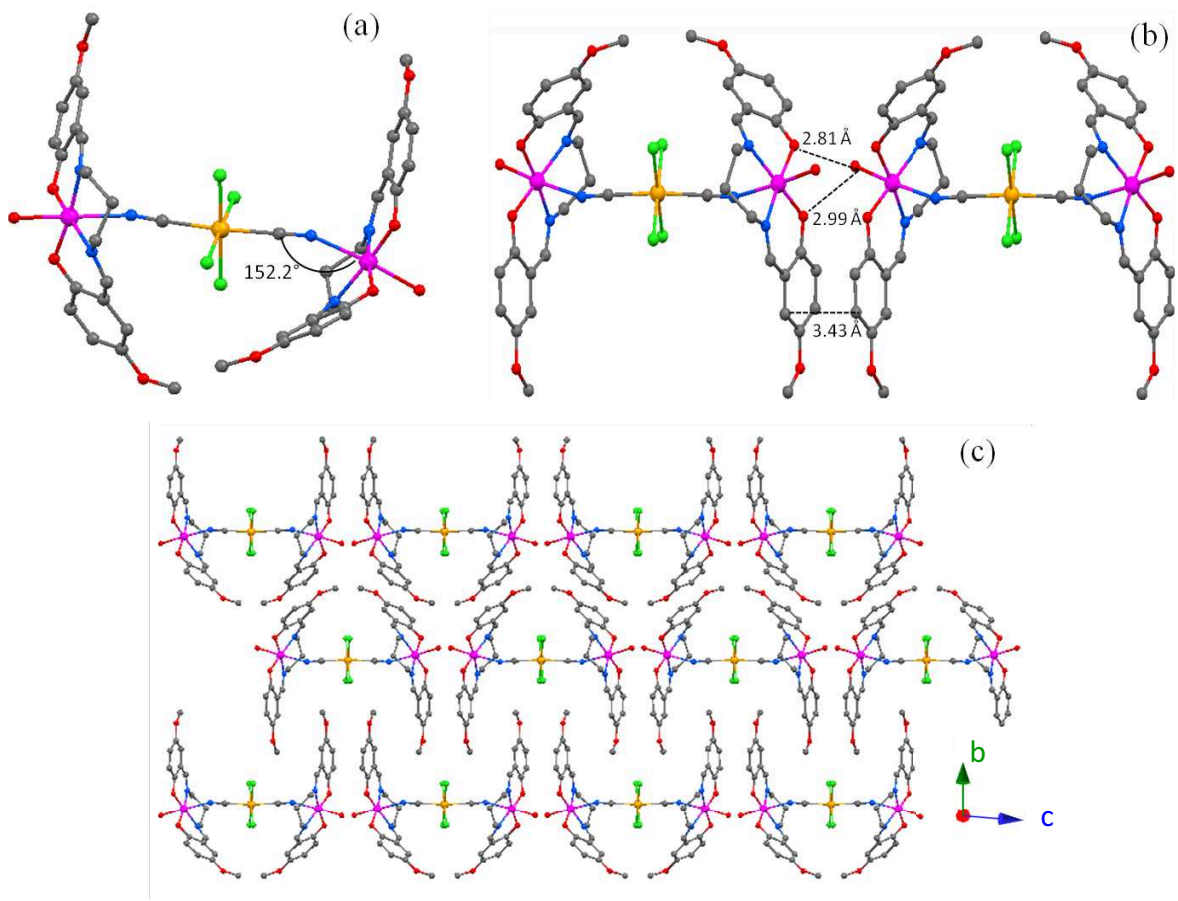

Figure II.6. Different views of **4**; the Re, Mn, C, O, N and Cl atoms are shown in orange, pink, grey, red, blue and green color respectively. The hydrogen atoms have been omitted for clarity. (a) Single molecule showing the Mn-N-C angle. (b) Hydrogen bonding interactions and π-stacking interactions between two successive trimers along the c axis and (c) Molecular packing in the *bc* plane.

In **5,** the Mn-N-C angle is 146.8(6)° and results in the bent pattern of the molecule along the Mn^{III}-Re^{IV}-Mn^{III} axis (figure III.7a) on both sides of the $ReCl_4$ plane. The Re^{IV} ion in **5** sits on an inversion center. The molecules of **5** are closely packed inside the crystal structure via supramolecular interactions similar to **4**. The oxygen atom from the axial MeOH molecule experiences H-bonding close contacts with the phenoxo oxygen of the salphen ligand of the nearest trinuclear neighbor (*ca.*

$d_{O...O}$ = 2.73 Å, figure III.7b). The π-stacking interactions (3.41Å) between the aromatic rings are another source of supramolecular interactions between the trinuclear units leading to closer packing inside the crystal without any solvent of crystallization (figure III.7b).

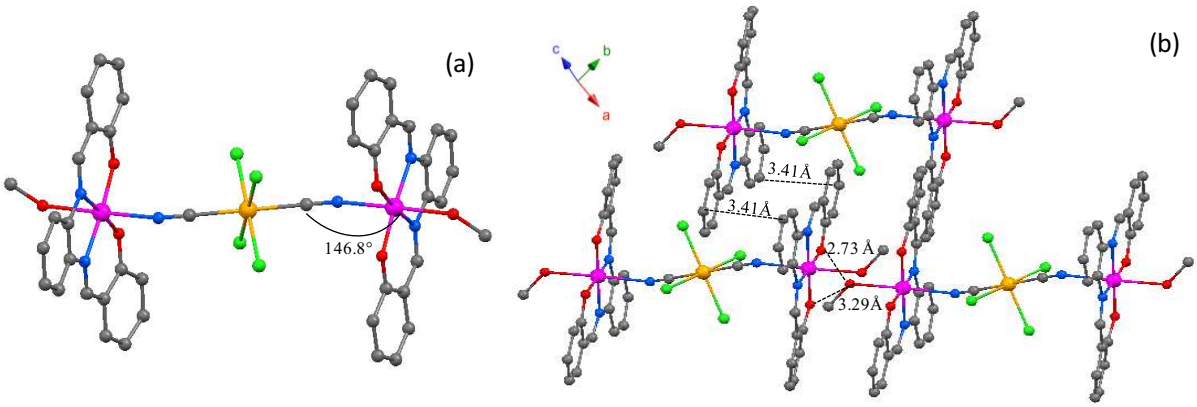

Figure II.7. Different views of **5**; the Re, Mn, C, O, N and Cl atoms are shown in orange, pink, grey, red, blue and green color respectively. The hydrogen atoms have been omitted for clarity. (a) Single molecule showing the Mn-N-C angle. (b) Hydrogen bonding interactions and π-stacking interactions between two neighboring molecules.

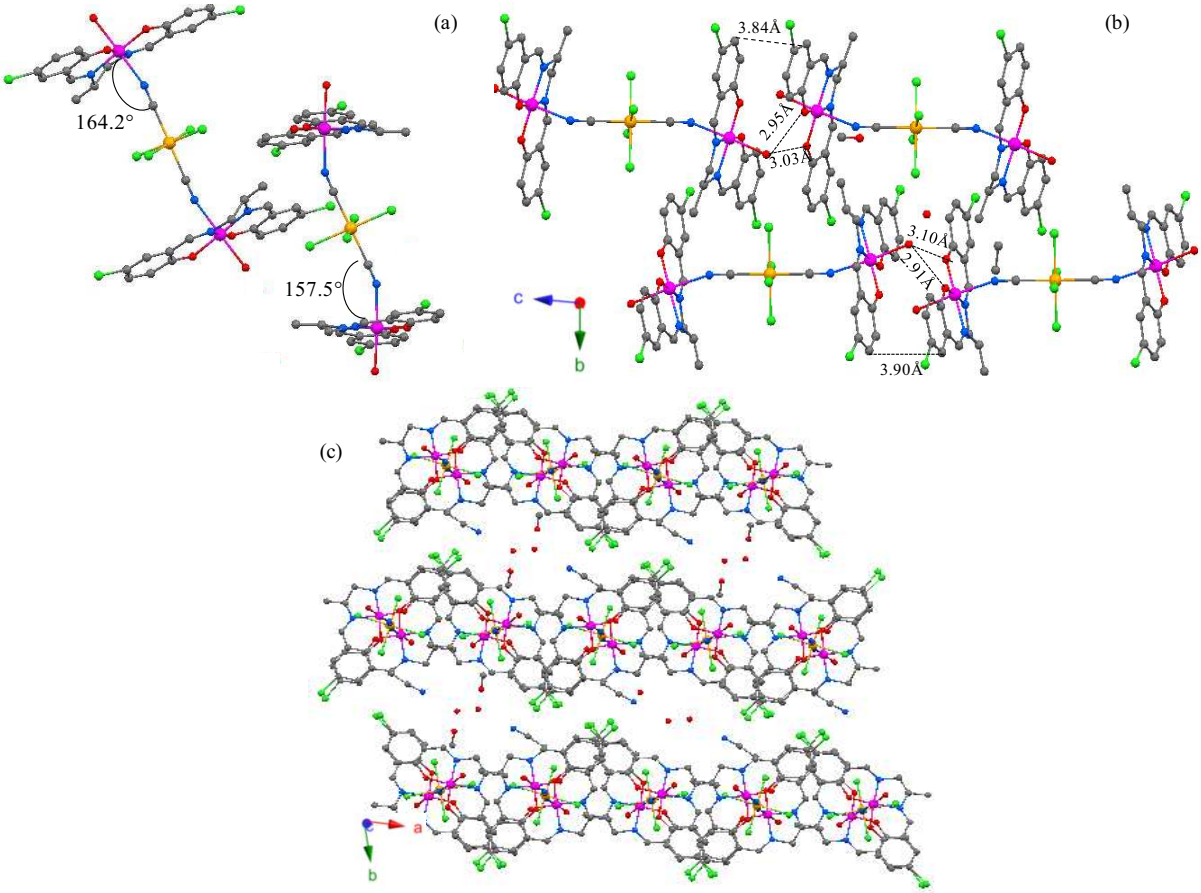

Figure III.8. Different views of **6**; the Re, Mn, C, O, N and Cl atoms are shown in orange, pink, grey, red, blue and green color respectively. The hydrogen atoms have been omitted for clarity. (a) Two independent molecules showing Mn-N-C angles and relative mutual orientation. (c) Hydrogen bonding interactions and π-stacking interactions between two successive trinuclear complexes. (c) Molecular packing view in the *ab* plane.

The crystal structure of **6** is quite different from the other trinuclear molecular systems. One can find two kinds of Mn^{III}-Re^{IV}-Mn^{III} complexes in **6** which differ in their orientation in the crystal structure and their geometry (angles and distances) (figure III.8a). In each Mn^{III}-Re^{IV}-Mn^{III} molecule in **6,** the Re^{IV} ion is on the inversion center. The Mn-N-C angles are respectively 164.2(7)° and 157.5(10)° in these two molecules, more linear along the Mn^{III}-Re^{IV}-Mn^{III} axis compared to **4** and **5**. The axially coordinated water molecules for both independent molecules in **6** exhibit hydrogen bonding interactions with the phenoxido oxygen coming from the nearest similar type molecule (*ca.* $d_{O...O}$ = 2.95-3.03 Å for one molecule and $d_{O...O}$ = 2.91-3.10 for the other molecule) which are displayed in figure III.8b. Although these H-bonding short contacts in **6** are found to be weaker (due to longer distance) than those in **4** and **5**, they are significant enough to orient all the molecular axes (Mn-Re-Mn axis) along the *c* direction. Moreover, the π-stacking interactions between the aromatic rings in **6** are not strong like compound **4** and **5**, but the weak presence of these interactions (average distance of 3.84-3.90 Å) might be an additional force to keep the molecules closely packed (figure III.8b). If one looks at the crystal structure of **6** along the *c* direction in the *ab* plane, the layer by layer packing of the molecules are observed where the solvent molecules (MeCN, MeOH and water) occupy the voids between two successive layers (figure III.8c).

III.2.2.3. Magnetic properties

All trinuclear compounds exhibit quite comparable magnetic properties. The magnetic susceptibility was measured for **4-6** in the temperature range between 280 and 1.8 K using a 1000 Oe *dc* magnetic field. In figure III.9, the temperature dependence of the χT product is shown for compound **4-6**. The χT values for **4**, **5** and **6** are 7.3 cm^3K/mol at 270 K, 6.8 cm^3K/mol at 280 K and 7.4 cm^3K/mol at 280 K respectively whereas the theoretical curie constant value is about 7.2 cm^3K/mol (for g_{Re} = 1.6[2] and g_{Mn} = 2[3d]). These χT values decrease with decreasing temperature and at 1.82 K they reach 0.7, 0.6 and 1.1 cm^3K/mol respectively for **4**, **5**, and **6**.

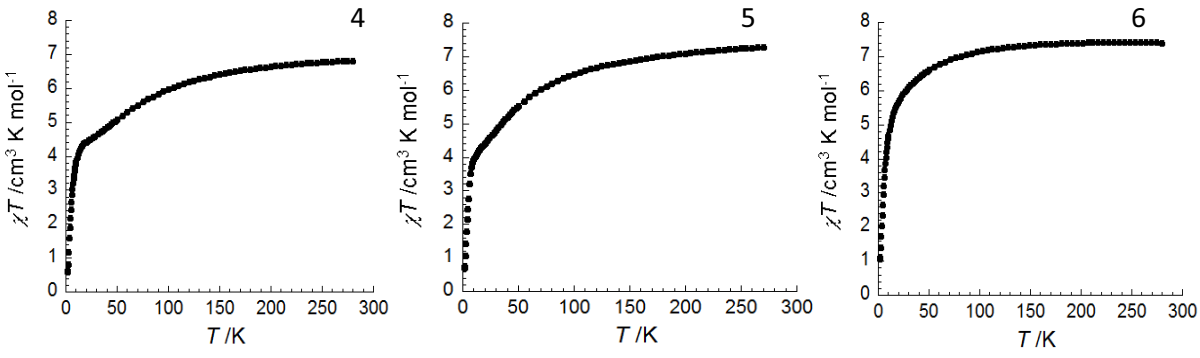

Figure III.9. The temperature dependence of the molar χT product at 1000 Oe between 280-1.8 K for **4-6**.

The decrease in the χT values with the lowering of temperature is an indication of dominating antiferromagnetic interaction between Mn^{III} and Re^{IV} metal ions through the cyanido bridge. To probe this interaction, the magnetic susceptibility data for these compounds were analysed using a trinuclear Mn^{III}-Re^{IV}-Mn^{III} model based on the Heisenberg Hamiltonian with isotropic spins:

$$\boldsymbol{H = -2J\,(S_{Mn}.S_{Re} + S_{Re}.S_{Mn})} \qquad \textbf{Eq.III.1}$$

where S_{Mn} = 2 , S_{Re} = 3/2, and J is the Mn^{III}-Re^{IV} magnetic interaction (figure III.10). Using this trinuclear model in the Van Vleck equation,[3] the expression of the magnetic susceptibility, χ, becomes:

$$\chi_{\text{trinuclear}} = \frac{Ng_{av}^2\mu_B^2}{4k_BT}\left[\frac{A}{B}\right] \qquad \textbf{Eq.III.2}$$

where, g_{av} is the average Landé factor corresponding to individual Mn^{III} and Re^{IV} ions;

A = 286 + 165[*exp*(-3*x*) + *exp*(-11*x*)]+ 84[*exp*(-6*x*) + *exp*(-12*x*)+ e*xp*(-20*x*)] + 35[*exp*(-9*x*) + *exp*(-13*x*) + *exp*(-19x) + *exp*(-27*x*)] + 10[*exp*(-12*x*) + *exp*(-14*x*) + *exp*(-18*x*) + *exp*(-24*x*)] + [*exp*(-17*x*) + *exp*(-21*x*)]

and

B = 6 + 5[*exp*(-3*x*) + *exp*(-11*x*)] + 4[*exp*(-6*x*) + *exp*(-12*x*) + *exp*(-20*x*)] + 3[*exp*(-9*x*) + *exp*(-13*x*) + *exp*(-19*x*) + *exp*(-27*x*)] + 2[*exp*(-12*x*) + *exp*(-14*x*) + *exp*(-18*x*) + *exp*(-24*x*)] + [*exp*(-17*x*) + *exp*(-21*x*)]

with $x = J/k_BT$. This trinuclear model nicely corresponds to the experimental data above 30 K for **4-6** (the red solid line in figure III.10) and yields g_{av} = 1.98(3), g_{av} = 1.90(2) and g_{av} = 1.97(2) and the J/k_B = - 4.66(3) K, -5.36(7) K and -1.89(2) K respectively. The lower value of g_{av} in these systems is due to the low g_{Re} of the anisotropic $[Re^{IV}Cl_4(CN)^2]^{2-}$ moiety.[2] The antiferromagnetic nature of the Re^{IV}-Mn^{III} magnetic interaction implies a spin ground state of S_T = 5/2 for the Mn^{III}-Re^{IV}-Mn^{III} trinuclear unit.

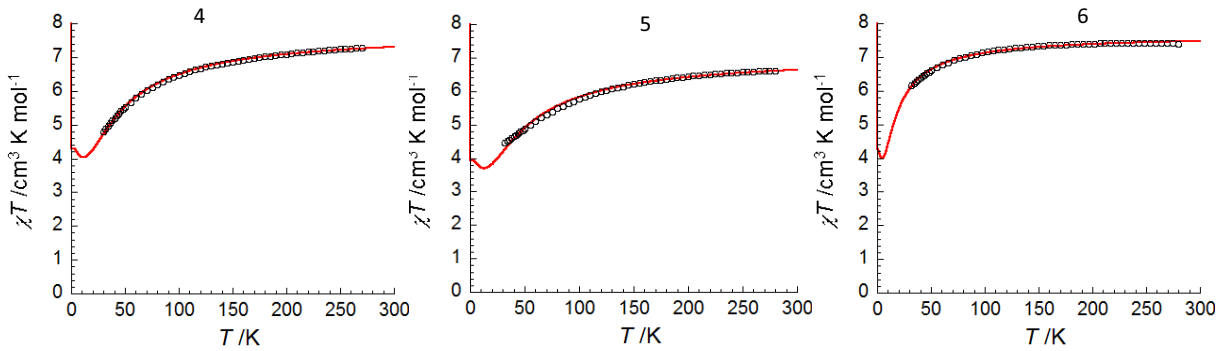

Figure III.10.The fit of the temperature dependence of the molar χT product at 1000 Oe for the Mn^{III}-Re^{IV}-Mn^{III} trinuclear systems, **4-6,** on the basis of Heisenberg Hamiltonian $\boldsymbol{H = -2J\,(S_{Mn}.S_{Re} + S_{Re}.S_{Mn})}$. The black hollow circles correspond to the experimental data and the red solid line is the fit of the experimental data.

The rapid decrease of χT product at low temperature is an indication of the magnetic anisotropy and/or additional antiferromagnetic interactions between the closely packed trinuclear units inside the crystal structure. The hydrogen bonding interactions and the π-stacking interactions are the obvious source of these intermolecular antiferromagnetic interactions in compounds **4-6**. In order to probe the low temperature region of magnetic susceptibility below 30 K with further estimation of inter-trimer antiferromagnetic interaction (J'), a mean field approximation was applied to the magnetic susceptibility data of the trinuclear molecules ($\chi_{trinuclear}$) according to the following equation:

$$\chi T = \chi_{trinuclear} T/(1 - czJ'\chi_{trinuclear}) \qquad \textbf{Eq.III.3}$$

where $c = 2/Ng^2\mu_B^2$ and z indicates the number of neighbors of each trinuclear unit. Unfortunately, the extended mean field treatment does not provide a significant improvement to the fit of the experimental susceptibility data suggesting that magnetic anisotropy is probably also relevant at low temperature. Therefore we have studied the low temperature magnetic behavior of **4-6** extensively with further experiments.

In order to investigate the inter-complexes antiferromagnetic interactions, variable temperature magnetic susceptibility measurements were performed on **4-6** under multiple applied *dc* fields, which were varied until the data reached a plateau at the higher value of applied *dc* field (figure III.11). The field dependence of the magnetic susceptibility is an indication of the presence of a magnetic phase transition in each of the systems. In **4**, the χ value begins to reach a plateau above 1.7 T whereas in **5** and **6** the magnetic susceptibility reaches the plateau above 2.2 T and 2 T respectively. This magnetic phase transition was further supported by the measurement of the magnetization as a function of field at multiple temperatures between 1.81 and 10 K (figure III.12). All of the magnetization curves possess a temperature-dependent inflection point, corresponding to the maximum value of χ (*viz. dM/dH*) (figure III.13) at a characteristic field (H_C) at different temperatures. The *dM/dH* vs. *H* plots (figure III.13) help to extract the temperature dependent H_C values at the maximum susceptibility.

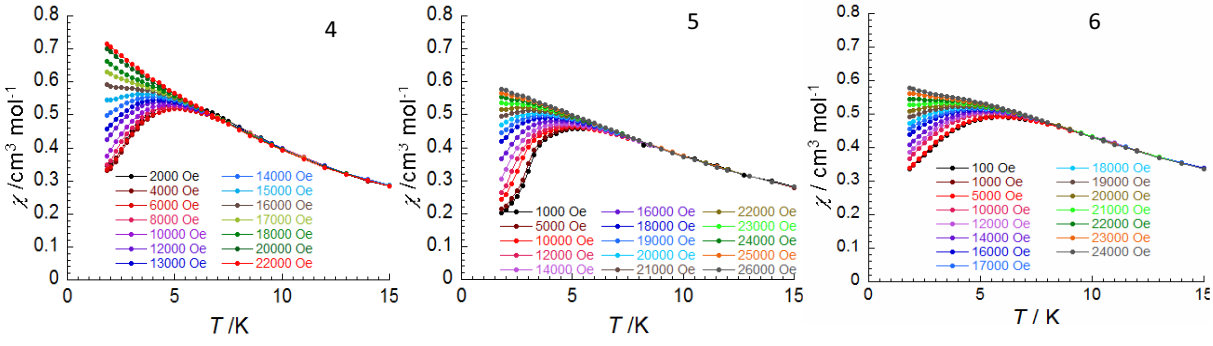

Figure III.11. The temperature dependence of the magnetic susceptibility of **4-6** at multiple applied *dc* field.

The *M* vs. *H* curves of **6** (figure III.12) do not saturates at the high *dc* field (7 T) which indicates the population of the excited spin states higher than $S_T = 5/2$. From the fit of the χT vs. *T* data of **6,** the Re^{IV}-Mn^{III} antiferromagnetic interaction $J/k_B = -1.89(2)$ K is clearly weaker than **4** and **5**, and thus the population of the excited spin states *S* = 7/2, 9/2 … is easier as shown by the higher magnetization values reach at 7 T (figure III.12).

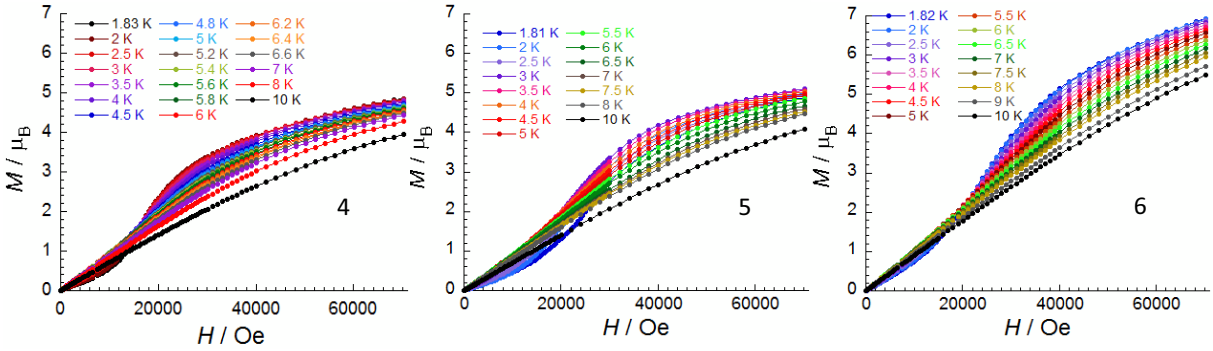

Figure III.12. The field dependence of the magnetization of **4-6** at multiple temperatures between 1.81 and 10 K.

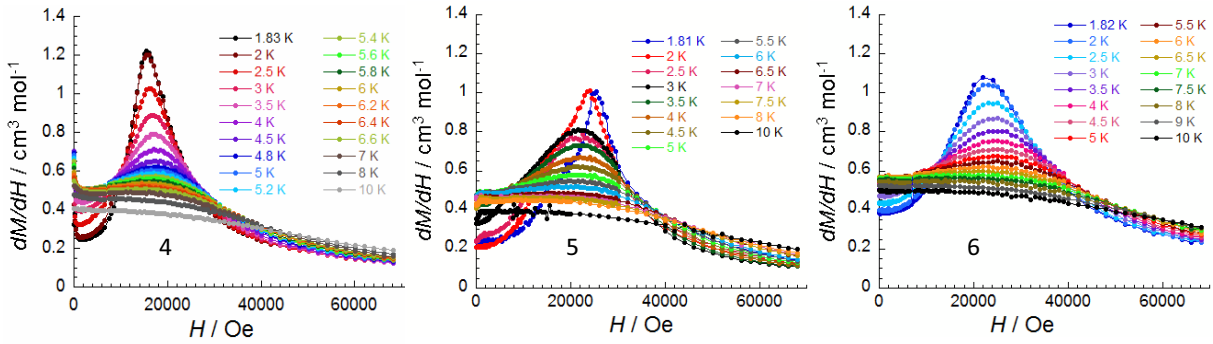

Figure III.13. Plot of derivative of magnetization for **4-6**, χ (*viz. dM/dH*), as a function of field at multiple temperatures to investigate characteristic field H_C at the maximum susceptibility.

Extracting the maximum susceptibilities found in the χ vs. *T* and *dM/dH* vs. *H* curves, we constructed an *H* vs. *T* phase diagram (figure III.14) for each compounds. These phase diagrams are characteristic of an ordered antiferromagnet displaying metamagnetic behavior. The temperature dependent H_C line corresponds to the transition line between the antiferromagnetic phase to the paramagnetic phase. Therefore, the higher is the H_C, the stronger are the intermolecular antiferromagnetic interactions. From the phase diagram, the Néel temperature (T_N) was found to be *ca.* 5 K, 3.4 K and 4.5 K for **4**, **5** and **6** respectively and the respective critical fields (H_C (0 K)) are *ca.* 16000 Oe, 23000 Oe and 24000 Oe. These relatively high values of the critical field in all these compounds arise from the close packing of the molecules inside the crystal structure. Therefore, due to these significant intermolecular antiferromagnetic interactions the discrete molecule does not exhibit any SMM-like properties. While *ac* susceptibility measurements of **4-6** were systematically

performed, the absence of out-of-phase *ac* signals above 1.8 K confirmed the absence of slow relaxation of the magnetization in these trinuclear compounds.

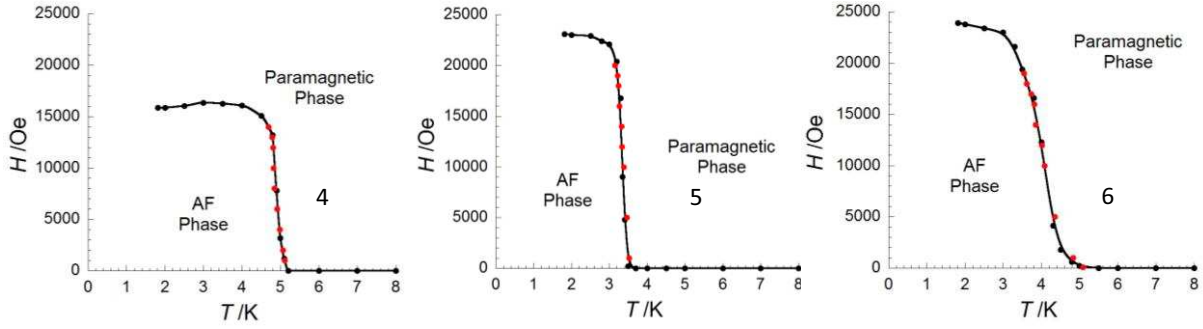

Figure III.14. Magnetic phase diagram (*T, H*) of **4-6** constructed from variable temperature (red circles) and variable field (black circles) magnetic susceptibility data (extracted from figure III.11 and III.13).

From the H_C, the inter-trinuclear antiferromagnetic interactions zJ'/k_B for **4**, **5** and **6** are respectively calculated as -0.40 K, -0.59 K and -0.63 K from equalizing the Zeeman and the exchange energies: $g\mu_B H_C(0\ \text{K})S_T = 2|zJ'|S_T^2$. Using these zJ'/k_B values, the calculated Néel temperature (T_N^{cal}) of these systems are near 2.3 K, 3.4 K and 3.7 K for **4**, **5** and **6** from the mean field relation: $T_N = 2|zJ'|S_T(S_T+1)/3k_B$. The comparable values of the theoretical and experimental Néel temperature indicates the intermolecular antiferromagnetic interactions of all these trinuclear systems can be compensated with the applied field H_C.

III.2.3. A hexanuclear Re^{IV}-Mn^{III} system

An interesting hexanuclear Re^{IV}-Mn^{III} compound was synthesized where one dinuclear Mn^{III}-Schiff base unit is connected to two *trans*-$[Re^{IV}Cl_4(CN)_2]$ moieties through the cyanido bridge, which are each furthermore connected to another Mn^{III}-Schiff base fragment. Thus as we will see, a Mn^{III}-Re^{IV}-Mn^{III}-Mn^{III}-Re^{IV}-Mn^{III} hexanuclear neutral molecule is formed which may also be categorized as a ferromagnetically interacting pair of trinuclear Mn^{III}-Re^{IV}-Mn^{III} units. A detailed discussion about this unique molecule is presented here.

2.3.1. Synthesis of $[Mn^{III}(saltmen)]_2[Re^{IV}Cl_4(CN)_2]_2[Mn^{III}(saltmen)(H_2O)]_2 \cdot 2MeCN$ (7)

$[Mn^{III}(saltmen)(H_2O)]_2(ClO_4)_2$ (0.0098 g, 0.01 mmol) was dissolved in 2 mL of acetonitrile followed by a slow drop wise addition of a 2 mL acetonitrile solution of $(Bu_4N)_2[Re^{IV}Cl_4(CN)_2]\cdot 2DMA$ (0.0103 g, 0.01 mmol). Both solutions were allowed to mix together through mutual diffusion for 10 minutes without stirring. Afterwards, diethyl ether vapor was allowed to diffuse into the solvent mixture inside a closed vial for five days. The brown crystals were collected through filtration and air dried. The yield was about 60 % on the basis of the Mn^{III} precursor. Elemental analysis calcd (%) for $C_{88}H_{98}Cl_8Mn_4N_{14}O_{10}Re_2$ (M = 2387.59 g/mol): C 44.27, H 4.14, N 8.21; and experimentally found (%) as C 44.35, H 4.22, N 8.28; IR: $\bar{\nu}$ = 2142 (C≡N stretch) 1599 (C=N stretch) cm^{-1}.

III.2.3.2. X-ray crystal structure

Crystallographic data for **7** are summarized in table III.3.

This bimetallic hexanuclear linear compound (figure III.15a, table III.3) crystallized in the triclinic P-1 space group. The Re^{IV} and Mn^{III} metal centers are in an octahedral environment where each Re^{IV} equatorial plane is occupied by four chlorido ligands and each Mn^{III} ion is equatorially coordinated with the two imino nitrogen atoms and the two oxido atoms of the phenoxido group of the Schiff base ligand. The axial positions of the Re^{IV} ion are connected with the carbon atoms of the cyanido ligands. In the center of the hexanuclear complex, there are two Mn^{III} ions mutually connected through two phenoxido oxygen atoms as previously observed in dinuclear Mn^{III}-Schiff base complexes.[1b] The middle of this Mn^{III}-dinuclear core is located an inversion center. The remaining

axial positions of the central [Mn_2] core are connected with one nitrogen of the cyanido ligand of *trans*-[$Re^{IV}Cl_4(CN)_2]^{2-}$. The nitrogen end of the remaining cyanido ligand is connected with another Mn^{III}-Schiff base moiety, forming a linear Mn^{III}-Re^{IV}-Mn^{III}_2-Re^{IV}-Mn^{III} complex. Both ends of this hexanuclear segment are completed by two water molecules which fulfill the axial coordination sites of the outer Mn^{III} ions. Therefore the molecule can be considered as a pair of trinuclear Mn^{III}-Re^{IV}-Mn^{III} moieties, an intermediate compound between the Re^{IV}-Mn^{III} trimers (section III.2.2) and a true one dimensional compound (section III.3). The Mn-Mn distance of the central dinuclear Mn^{III}-Schiff base moiety is about 3.39 Å with a Mn-O*$_{Phen}$ distance of 2.450(2) Å. The Mn-N-C angle belonging to the inner dinuclear Mn^{III}-core is 160.1(2)° and that belonging to the outer Mn^{III} core is 173.9(2)°. Thus the neutral molecule is quite linear with respect to the axis along the metal centers. In the crystal structure of **7**, the molecules are closely packed *via* hydrogen bonding and π-stacking interactions (figure III.15b). The water molecules axially coordinated to the outer Mn^{III} ions form hydrogen bonds (*ca.* $d_{O\cdots O}$ = 2.72-2.86 Å) with the phenoxido oxygen atoms of the outer Mn^{III}-Schiff base ligands of neighboring molecules (figures III.15b). Due to these interactions, the hexanuclear molecules are stacked in one direction along the Mn^{III}-Re^{IV}-Mn^{III}_2-Re^{IV}-Mn^{III} axis. Moreover, a weak π-stacking interaction of the aromatic rings (3.3 -3.9 Å) of neighboring molecules significantly contributes to the molecular packing. This additional weak interaction forces the molecules to orient in the same fashion in the crystal structure. Therefore the molecular axes (the axis along the metal centers) of all the molecules in the crystal structure of **7** are parallel. The acetonitrile molecules help to fill the void spaces in the crystal packing.

Table III.3. Crystal data and structure refinement of **7**

Sum formula	$C_{88}H_{98}Cl_8Mn_4N_{14}O_{10}Re_2$
Molecular weight (g/mol)	2387.59
Temperature (K)	100(2)
Crystal System	Triclinic
Space group	P-1
a (Å), b (Å), c (Å)	11.929(5), 12.896(5), 16.888(5)
α (°), β (°), γ (°)	80.607(5), 82.169(5), 66.448(5)
Volume (Å^3)	2342.4(15)
Z	1
Density (g.cm^{-3})	1.693
$\mu_{MoK\alpha}$ (mm^{-1})	3.389
F000	1190
GooF	0.984
[a]R_1 ($I > 2.00\sigma(I)$)	0.0436
[b]wR_2 (all reflections)	0.0885

[a]$R_1 = \Sigma ||F_0| - |F_C|| / \Sigma|F_0|$, [b]$wR_2 = [\Sigma w(F_0^2 - F_C^2)^2 / \Sigma w(F_0^2)^2]^{1/2}$, $w = 1/[\sigma^2 F_0^2 + (0.0313P)^2 + 1.5564P]$; where $P = (F_0^2 + 2F_C^2)/3$

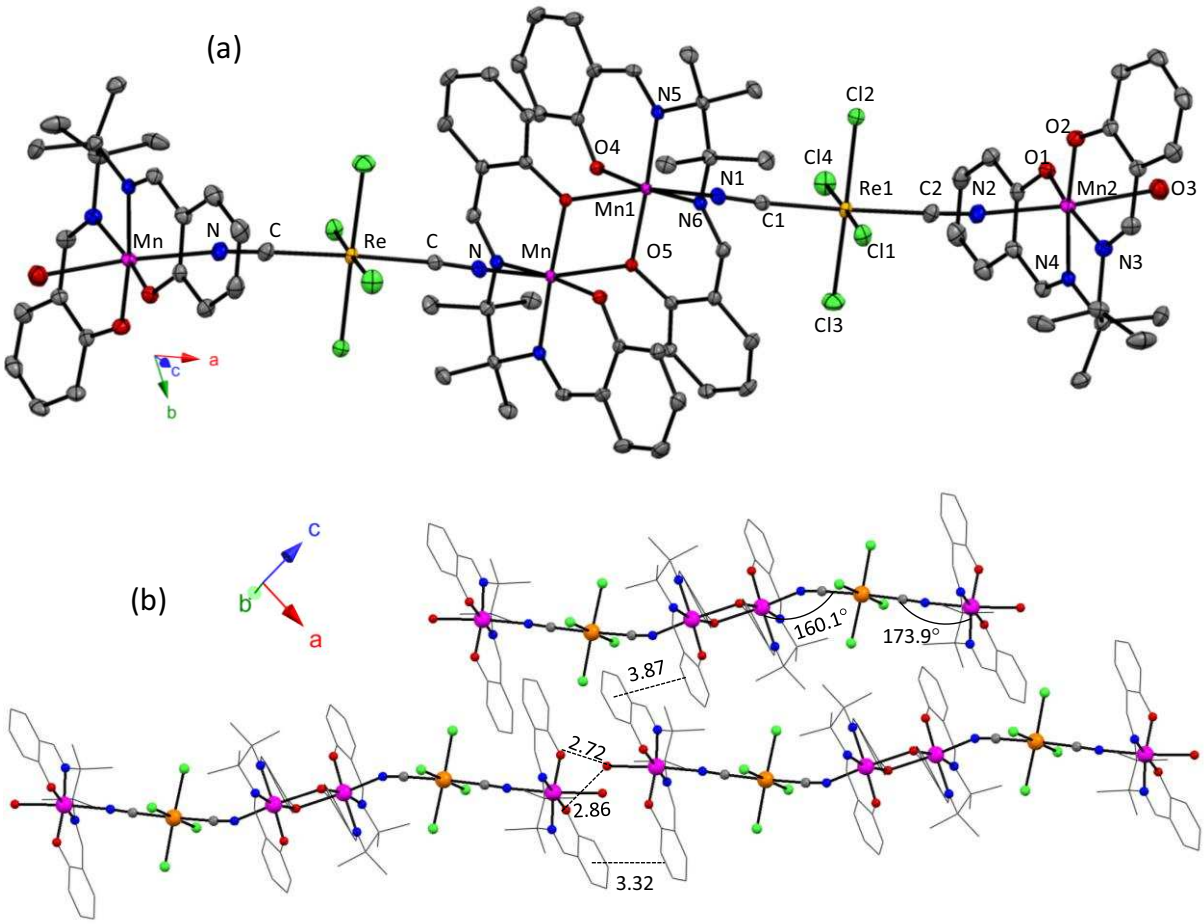

Figure III.15. (a) ORTEP views of **7** (50 % probability), the Re, Mn, C, O, N and Cl atoms are shown in orange, magenta, grey, red, blue and green sphere respectively. The hydrogen atoms and solvent molecules are omitted for clarity. (b) The different Mn-N-C angles are displayed along with the hydrogen bonding interactions and π-stacking interactions between the neighboring molecules (all distances are in Å).

III.2.3.3. Magnetic Properties

The temperature dependence of the magnetic susceptibility was measured on a polycrystalline sample of **7** at 1000 Oe *dc* field and the χT product was plotted as a function of temperature (figure III.16a).

At 270 K; χT was found to be 14.0 cm^3K/mol, very close to the theoretical χT = 14.4 cm^3K/mol (for g_{Re} = 1.6[2] and g_{Mn} = 2[3d]). On lowering the temperature, χT slowly decreased to reach 10.7 cm^3K/mol at 26 K followed by a rapid increase to 24.8 cm^3K/mol at 4.7 K. This temperature-dependent decrease of the magnetic susceptibility above 26 K indicates a governing antiferromagnetic interaction (J) between the Re^{IV} and Mn^{III} metal centers as observed in the trinuclear complexes (section III.2.2). At temperatures below 26 K, ferromagnetic exchange (J') between the two Mn^{III} ions of the dinuclear Mn^{III}-Schiff base moiety are observed. Therefore this compound behaves like a pair of

Mn^{III}-Re^{IV}-Mn^{III} trinuclear units interacting ferromagnetically. Below 4.7 K, the sharp decrease of the χT product is observed and at 1.81 K it reaches 6 cm^3K/mol, indicating the presence of additional inter-molecular antiferromagnetic interaction and/or magnetic anisotropy.

In order to quantify the magnetic exchange between Mn^{III} and Re^{IV}, the magnetic susceptibility data was initially treated with a trinuclear Mn^{III}-Re^{IV}-Mn^{III} model, neglecting J', based on the Heisenberg Hamiltonian with the isotropic spins: $\boldsymbol{H = -2J\ (S_{Mn}.S_{Re} + S_{Re}.S_{Mn})}$. With this trinuclear model, the expression of χ is given by **Eq. III.2** used previously in section III.2.2.3 to describe the magnetic properties of Re^{IV}-Mn^{III} trinuclear complexes. This model nicely corresponds to the experimental data above 64 K and yields J/k_B = -4.1(2) K and g_{av} = 1.92(1). The dotted red line in figure III.16b corresponds to the fit of the experimental magnetic susceptibility data with this simple trinuclear Heisenberg model.

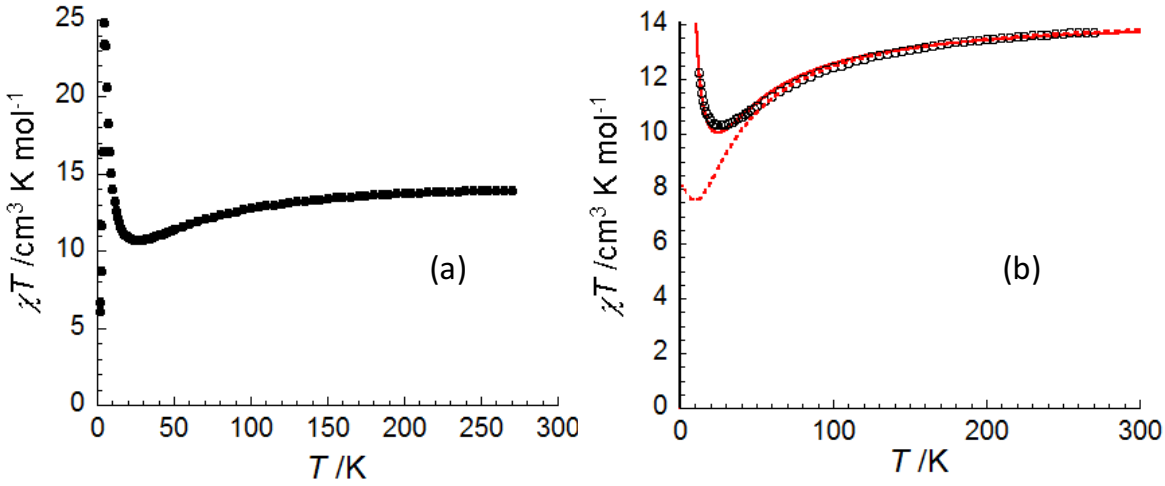

Figure III.16. (a) The temperature dependence of the molar χT product at 1000 Oe between 280-1.8 K for **7**. (b) Fit of the temperature dependence of the molar χT product at 1000 Oe for **7**, where the hollow black circles correspond to the experimental data, the dotted red line exhibits the fit of χT above 64 K with trinuclear Mn^{III}-Re^{IV}-Mn^{III} model and the solid red line is the extended fit of the experimental data down to 11 K with the help of mean field approximation.

To further roughly estimate the inter-trinuclear ferromagnetic interaction (J') present between the central core Mn^{III} ions, the above trinuclear model was modified treating J' in frame of the mean field approximation. This model fits well the experimental data above 11 K (given by the solid red line in figure III.16b) and provides g_{av} = 1.90(5), J/k_B = -5.6(7) K and zJ'/k_B = + 0.91(3) K.

The decrease of χT below 4.7 K suggests the presence of additional interactions between the hexanuclear complexes in **7** at low temperature. The close packing of the molecules as a result of inter-molecular hydrogen bonding and π-stacking interactions is the obvious source of their intermolecular antiferromagnetic interactions. For a detailed investigation of the low temperature magnetic properties, magnetic susceptibility measurements were performed below 10 K at multiple applied *dc* fields (figure III.17a). The χ vs. T curve collected at 100 Oe displayed a significant

susceptibility increase at low temperature, below 5 K (inset of figure III.17a). Such behavior of χ vs. T indicates the spontaneous magnetization present in the system, implying the canting of two magnetic sublattices in an ordered phase. With the increase of the applied *dc* field, the low temperature χ values decreases (figure III.17a) confirming the magnetic phase transition. The canted antiferromagnetic phase was verified by the alternating current (*ac*) magnetization measurements (magnetic susceptibilities χ' (in-phase) and χ'' (out-of-phase), figure III.17b) of **7** between 1.8 - 10 K and 1 – 1500 Hz, with zero *dc* field ($H_{dc} = 0$). The χ'' signal exhibits a strong frequency dependent response at 4.5 K (inset of figure III.17b) typical of an ordered phase with a spontaneous magnetization like a canted AF phase.

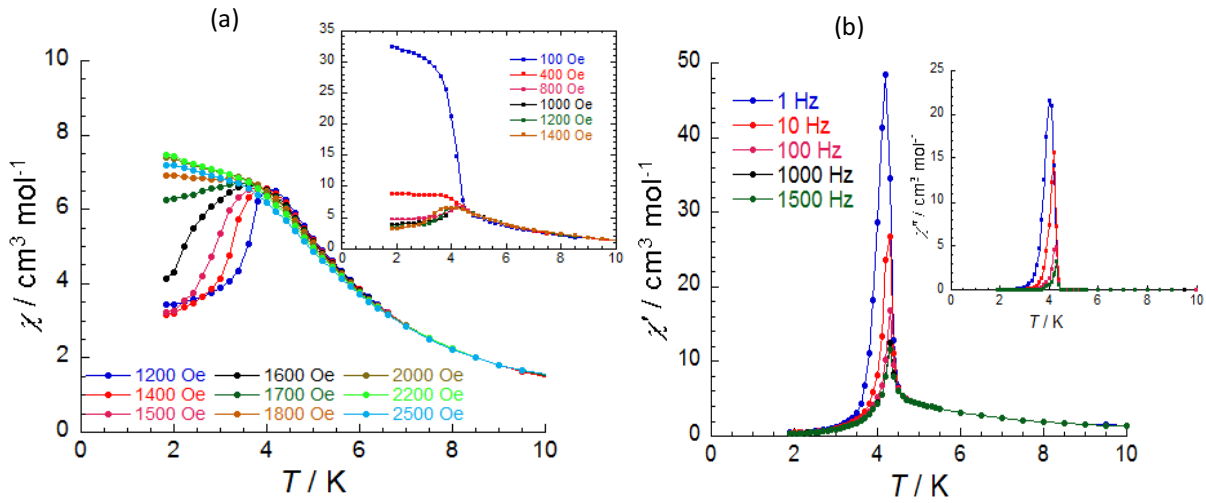

Figure III.17. (a) The temperature dependence of the magnetic susceptibility of **7** at multiple applied *dc* field; Inset: the same χ vs. T data collected at low field. (b) The temperature dependence of the χ' (in-phase) and χ''(out-of-phase) part of the *ac* magnetic susceptibility of **7** at $H_{dc} = 0$ Oe at different frequencies between 1 Hz and 1500 Hz.

In order to further estimate the low temperature magnetic properties of **7**, different temperature M vs. H data were collected with sweep rate of 180 Oe/min at different temperatures (figure III.18a and b). A small magnetic hysteresis behavior is observed at 1.88 K (figure III.18a) which is present until 5 K (figure III.18b). The *"S"* shape of the magnetization curves at zero field (figure III.18b) further emphasize the spontaneous magnetization in **7**. At 1.88 K, the remnant magnetization of **7** is $M_R = 0.6\ \mu_B$ (inset of figure III.18a). Therefore at low temperature (in the magnetically ordered phase), the equilibrium canting angle, α, is estimated as 13.8° from the relation $sin(\alpha/2) = 2M_R/M_{sat}$, where, $M_{sat} \approx 10\ \mu_B$ is the magnetization at saturation. We, in asymmetric part of the hexanuclear unit of **7**, have previously seen the presence of two different Mn-N-C angles are 160.1(2)° and 173.9(2)°, i.e. the difference is 13.8°. Therefore, the compatibility of α with the difference of Mn-N-C angles suggests this geometrical characteristic as the possible source of the canting between two magnetic sublattices.

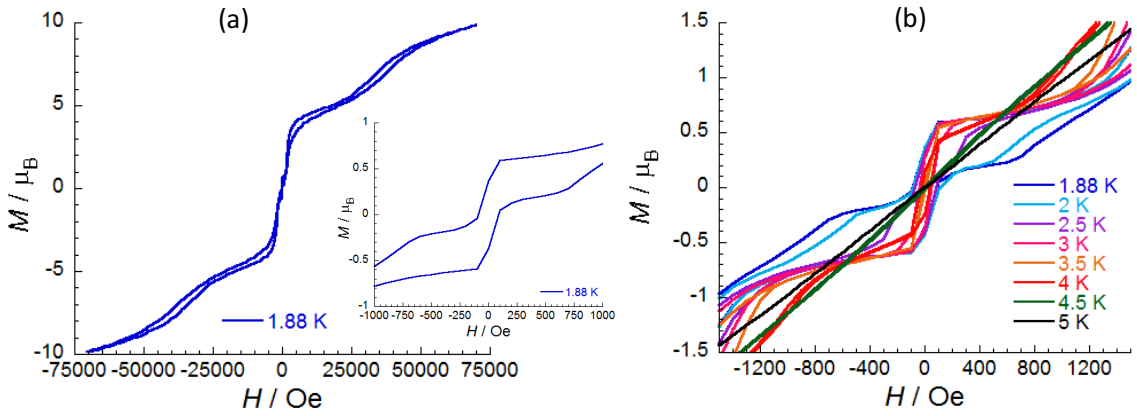

Figure III.18. The magnetic hysteresis M = f(H) plots of **7** with the field sweep rate of 180 Oe/min (a) at 1.88 K measured between -7 T and 7 T; Inset: the expanded view of the main plot between -0.1 T and 0.1 T showing the remnant magnetization M_R = 0.6 μ_B; (b) below 5 K (only the part between -0.14 T and 0.14 T has been displayed in the figure for better visibility of the "*S*" shape of the magnetization curves at zero field).

Above 1000 Oe, the strong field dependence of χ vs. T plot reveals a magnetic phase transition, i.e, from the canted antiferromagnetic ground state to the paramagnetic phase. This magnetic phase transition was further explored through the measurement of the magnetization as a function of field at multiple temperatures between 1.82 and 10 K (figure III.19a). Each magnetization curve below 5 K possesses an inflection point, corresponding to the maximum value of χ (*viz. dM/dH*) at a critical field (H_C) (inset of figure III.19a). Thus the canted antiferromagnetic to paramagnetic phase transition of **7** was detected below 2000 Oe. Therefore the H vs. T phase diagram has been built for **7** (figure III.19c) extracting the temperature dependence of the critical H_C field from the maximum of the χ vs. T (figure III.17a) and *dM/dH* vs. H (figure III.19b) curves. It reveals the H_C(0 K) = 1670 Oe and the T_N is near 5 K.

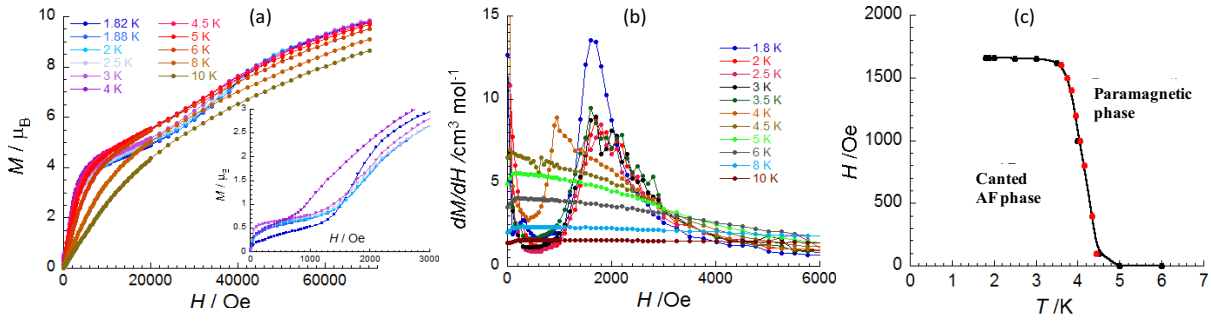

Figure III.19. (a) The field dependence of magnetization of **7** at multiple temperatures between 1.82 and 10 K; Inset: the expanded view of the low temperature M vs. H curves. (b) Plot of derivative of the magnetization for **7**, χ (*viz. dM/dH*), as a function of field (below 6000 Oe) at multiple temperatures to find out characteristic field H_C at the maximum susceptibility. (c) Magnetic phase diagram (*T, H*) of **7** constructed from the maximum found in χ vs. T (red circles) and *dM/dH* vs. H (black circles) data.

From H_C extrapolated at 0 K H_C(0 K) of 7 the antiferromagnetic interactions zJ_{perp}/k_B between the hexanuclear units is calculated as -0.021 K from the relation $g\mu_B H_C(0\ K)S_T = 2|zJ_{perp}|S_T^2$, where, g

= 1.9 and S_T = 5 (considering the ferromagnetic interaction within the [Mn^{III}_2] core dimer and the Re^{IV}-Mn^{III} antiferromagnetic interaction, the spin ground state (S_T) of the hexanuclear Mn^{III}-Re^{IV}-Mn^{III}_2-Re^{IV}-Mn^{III} unit is 5). Using this value of zJ_{perp}/k_B, the calculated Néel temperature (T_N^{cal}) of **7** is 0.42 K from the mean field relation $T_N = 2|zJ_{perp}|S_T(S_T+1)/3k_B$. This value is significantly smaller than the experimentally determined one (5 K) (figure III.19c). This discrepancy suggests a presence of stronger antiferromagnetic interaction in **7** other than zJ_{perp}/k_B.

In the crystal structure of **7**, we have observed two kinds of supramolecular interactions for the close packing of the molecules (i) the strong H-bonding interaction (*ca.* $d_{O\cdots O}$ = 2.72-2.86 Å) via axial water molecules (coordinated to Mn^{III} ions), causing a pseudo one dimensional arrangement of the Mn^{III}-Re^{IV}-Mn^{III}_2-Re^{IV}-Mn^{III} units (along the a + c direction, figure III.15 (b), figure III.20); and (ii) weak π-stacking interaction of the aromatic rings (3.3 -3.9 Å) in the perpendicular direction of the supramolecular unidimensional arrangement. Both supramolecular interactions contribute to the total antiferromagnetic interactions between the hexanuclear units, while the former (H-bonding) is much stronger than the later one (π-stacking). Therefore, applying the H_C(0 K), the system (compound **7**) can overcome the weaker interactions (zJ_{perp}/k_B) (see figure III.20) and induce the transition from the canted antiferromagnetic phase to the paramagnetic state, but this field is not enough to compensate the stronger interaction (zJ_{1D}/k_B) present between the hexanuclear units (in the direction of pseudo one dimensional arrangement, figure III.20).

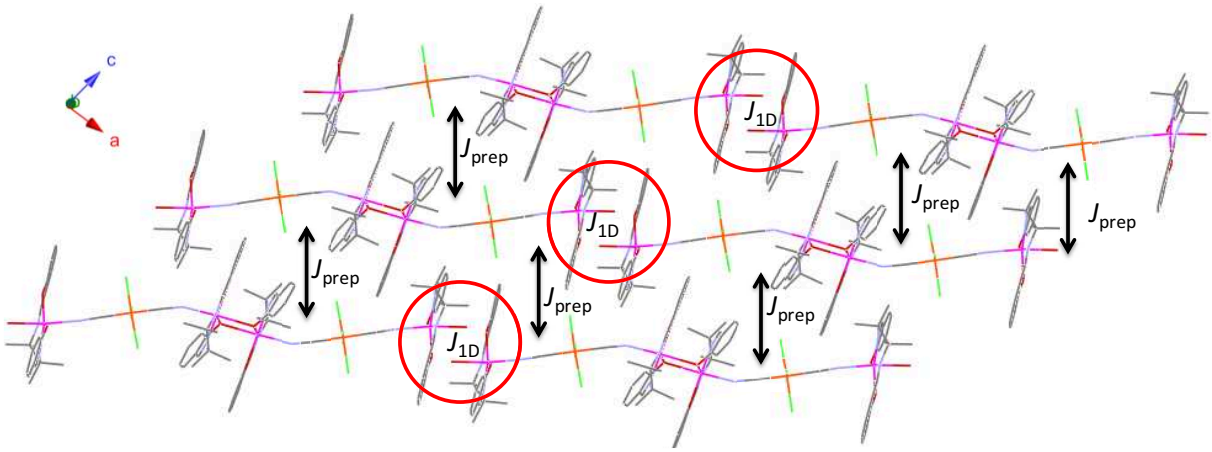

Figure III.20. (a) Highlight of the source of zJ_{perp}/k_B (with black arrows) and zJ_{1D}/k_B (with red circles) interactions in the crystal packing of **7**.

At significantly higher values of applied *dc* field (near 35000 Oe) one more inflection point is found in the *M* vs. *H* curves (figure III.21a). Therefore the *dM/dH* vs. *H* curves exhibit a maxima near the characteristic field *H** = 35000 Oe (figure III.21b). For comparison this *H** values for different temperature are also plotted in the phase diagram (figure III.21c) and found almost independent of temperature. Using *H** = 3.5 T the zJ_{1D}/k_B can be determined as -0.46 K from equalizing the Zeeman and exchange energies: $g\mu_B H^* S_T = 2|zJ_{1D}|S_T^2$.

Averaging the two kinds of antiferromagnetic interactions, zJ_{perp}/k_B and zJ_{1D}/k_B the overall antiferromagnetic interaction, zJ_{av}/k_B, between the hexanuclear units (where, $2zJ_{av}= zJ_{perp} + zJ_{1D}$) is determined as 0.24 K. Using this zJ_{av}/k_B value into the relation: $T_N = 2|zJ_{av}|S_T(S_T+1)/3k_B$, the Néel temperature of **7** can be calculated as 4.8 K, which is nicely comparable to the experimental T_N of 5 K, figure III.19c) of **7**. This compatibility of Néel temperatures suggests that the antiferromagnetic interaction between the hexanuclear moieties in the pseudo one dimensional direction (a + c) is compensated at the field 3.5 T.

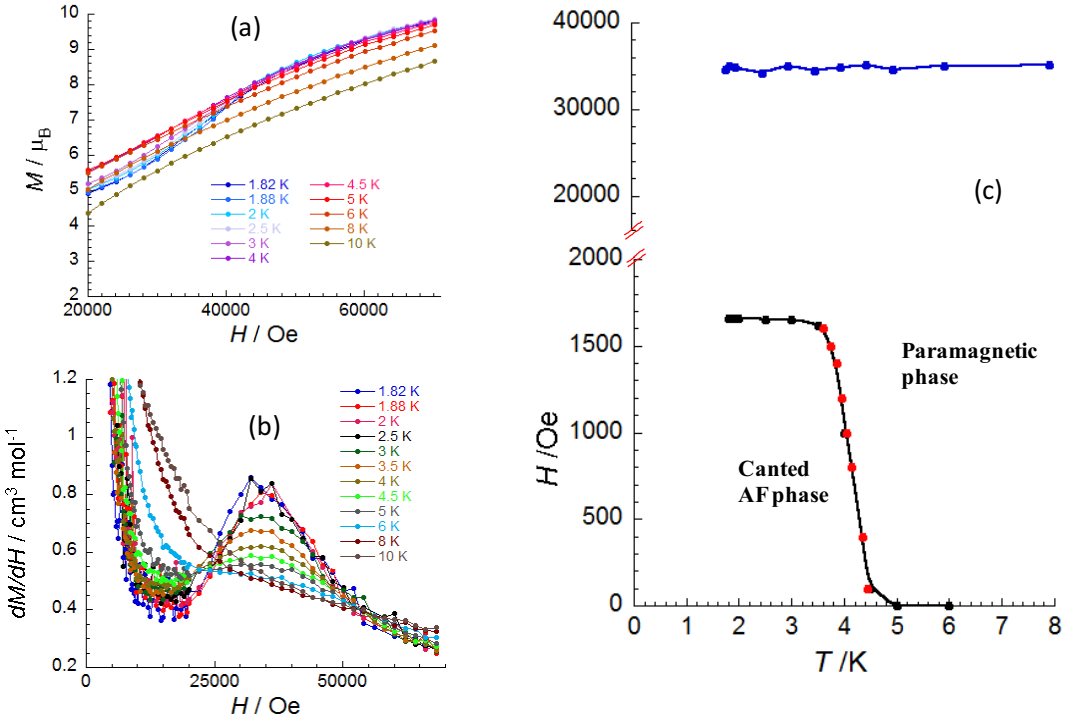

Figure III.21. (a) *M* vs. *H* plots. of **7** at multiple temperatures between 1.82 and 10 K expanding the view between 2 and 7 T (b) *dM/dH* vs. *H* plots at multiple temperatures displaying a maxima near 35000 Oe (*H**). (c) H vs. T plot including the blue dots representing the temperature dependence of *H**.

III.3. One dimensional Re^{IV}-Mn^{III} systems

The reaction between some of the Mn^{III}-Schiff base precursors and *trans*-$(Bu_4N)_2[Re^{IV}Cl_4(CN)_2]\cdot 2DMA$ provided a series of five new one dimensional Mn^{III}–Re^{IV} heterometallic systems with the general molecular formula: ***$[Mn^{III}_2(SB)_2Re^{IV}Cl_4(CN)_2]\cdot nCH_3CN$*** (**8-12**) ($SB^{2-}$ = Schiff base^{2-}, n = 0 to 3 acetonitrile molecules) wherein two Mn^{III} ions and one Re^{IV} ion are alternatively arranged in each chain. As might be expected from the magnetic behavior of the hexanuclear compound **7** (section III.2.3.3) the variable temperature *dc* magnetic susceptibility measurements of these compounds indicated the presence of dominating intra-chain antiferromagnetic

exchange interactions between the cyanido bridged Mn^{III} (S = 2, $t_{2g}^3e_g^1$) and Re^{IV} (S = 3/2, t_{2g}^3) ions, whereas the magnetic interaction within the dinuclear Mn^{III} units are known to be ferromagnetic.[1] All these compounds display three dimensional order due to significant inter-chain antiferromagnetic interactions. We also probed the dynamic properties of these compounds, which manifest pronounced evidence of slow relaxation of magnetization, especially for **8** and **9**. The synthetic, crystallographic and the magnetic discussion of compounds **8-12** will be presented here.

III.3.1. Synthesis

a) ***$[Mn^{III}(5\text{-Me-saltmen})]_2[Re^{IV}Cl_4(CN)_2]\cdot 3MeCN$*** (**8**): $[Mn^{III}(5\text{-Me-saltmen})(H_2O)]_2(ClO_4)_2$ (0.0104 g, 0.01 mmol) and $(Bu_4N)_2[Re^{IV}Cl_4(CN)_2]\cdot 2DMA$ (0.0103 g, 0.01 mmol) were separately dissolved in 2 mL of acetonitrile. The solution of Mn^{III} was poured into a thin tube of 1.5 cm diameter and then layered with 2 mL of pure acetonitrile. Over the pure solvent the $(Bu_4N)_2[Re^{IV}Cl_4(CN)_2]\cdot 2DMA$ solution was very carefully layered to avoid fast mixing of the reactants. The tube was then hermetically sealed with parafilm to avoid evaporation. After 2 days, brown needle-shaped crystals were found at the bottom and wall of the tube. The crystals were collected through filtration and air dried. The yield of the product was about 85 % on the basis of the Mn^{III} precursor; elemental analysis calcd (%) for $C_{52}H_{61}Cl_4Mn_2N_9O_4Re$ (M = 1313.98 g/mol): C 47.53, H 4.68, N 9.59; and experimentally found (%) as C 47.28, H 4.75, N 9.50; IR (KBr): $\bar{\nu}$ = 2141(C≡N stretch) 1596 (C=N stretch) cm^{-1}.

b) ***$[Mn^{III}(saltmen)]_2[Re^{IV}Cl_4(CN)_2]$*** (**9**)**:** $[Mn^{III}(saltmen)(H_2O)]_2(ClO_4)_2$ (0.0098 g, 0.01 mmol) was dissolved in 2 mL of methanol followed by slow drop wise addition of a methanol solution (2 mL) of $(Bu_4N)_2[Re^{IV}Cl_4(CN)_2]\cdot 2DMA$ (0.0103 g, 0.01 mmol) and kept for slow evaporation after addition of distilled water (0.5 mL). Dark brown block-shaped crystals were collected after 5 days by filtration with a 60 % yield on the basis of the Mn^{III} starting material; elemental analysis calcd (%) for $C_{42}H_{44}Cl_4Mn_2N_6O_4Re$ (M = 1134.75 g/mol): C 44.46, H 3.91, N 7.41; and experimentally found (%) as C 44.28, H 3.98, N 7.48; IR (KBr): $\bar{\nu}$ = 2137 (C≡N stretch) 1600 (C=N stretch) cm^{-1}.

c) ***$[Mn^{III}(5\text{-F-saltmen})]_2[Re^{IV}Cl_4(CN)_2]$*** (**10**): $[Mn^{III}(5\text{-F-saltmen})(H_2O)_2](ClO_4)$ (0.0110 g, 0.02 mmol) was dissolved in 2 mL of acetonitrile followed by slow drop wise addition of an acetonitrile solution (2 mL) of $(Bu_4N)_2[Re^{IV}Cl_4(CN)_2]\cdot 2DMA$ (0.0103 g, 0.01 mmol) and the mixture was allowed to slowly evaporate in air. Brown crystalline plates were collected after 1 day by filtration. The yield of the product was 80 % on the basis of the Mn^{III}-Schiff base precursor; elemental analysis calcd (%) for $C_{42}H_{40}Cl_4F_4Mn_2N_6O_4Re$ (M = 1206.69 g/mol): C 41.80, H 3.34, N 6.96; and experimentally found (%) as C 41.68, H 3.51, N 7.01; IR (KBr): $\bar{\nu}$ = 2143 (C≡N stretch) 1609 (C=N stretch) cm^{-1}.

d) ***$[Mn^{III}$(5-MeO-saltmen)$]_2[Re^{IV}Cl_4(CN)_2]$·2MeCN*** **(11):** This compound was synthesized similarly to **8** using $[Mn^{III}(5\text{-MeO-saltmen})(H_2O)]_2(ClO_4)_2$ (0.0111 g, 0.01 mmol) and $(Bu_4N)_2[Re^{IV}Cl_4(CN)_2]$·2DMA (0.0103 g, 0.01 mmol) resulting in small needle-like brown crystals in 90 % yield on the basis of the Mn^{III}-Schiff base starting material. The crystals were collected through filtration after 3 days and air dried. Elemental analysis calcd (%) for $C_{50}H_{58}Cl_4Mn_2N_8O_8Re$ (M = 1336.98 g/mol): C 44.92, H 4.37, N 8.38; and experimentally found (%) as C 44.98, H 4.51, N 8.71; IR (KBr): $\bar{\nu}$ = 2133 (C≡N stretch) 1598 (C=N stretch) cm^{-1}.

e) ***$[Mn^{III}$(5-Me-salpen)$]_2[Re^{IV}Cl_4(CN)_2]$·2MeCN*** **(12):** This compound was synthesized similarly to **8** using $[Mn^{III}(5\text{-Me-salpen})(H_2O)]_2(ClO_4)_2$ (0.0097 g, 0.01 mmol) and $(Bu_4N)_2[Re^{IV}Cl_4(CN)_2]$·2DMA (0.0103 g, 0.01 mmol) resulting in block-shaped crystals on the wall of the tube after 7 days with a yield of 70 % on the basis of the Mn^{III}-Schiff base starting material. The crystals were collected through filtration and air dried. Elemental analysis calcd (%) for $C_{44}H_{46}Cl_4Mn_2N_8O_4Re$ (M = 1188.77 g/mol): C 44.45, H 3.90, N 9.43; and experimentally found (%) as C 44.28, H 4.01, N 9.70; IR (KBr): $\bar{\nu}$ = 2137 (C≡N stretch) 1599 (C=N stretch) cm^{-1}.

III.3.2. X-ray crystal structure

Crystallographic data for the five one dimensional Mn^{III}-Re^{IV} compounds (**8-12**) are summarized in table III.4.

Table III.4. Crystal data and structure refinement of compound **8-12**.

	8	**9**	**10**	**11**	**12**
Sum formula	$C_{52}H_{61}Cl_4Mn_2N_9O_4Re$	$C_{42}H_{44}Cl_4Mn_2N_6O_4Re$	$C_{42}H_{40}Cl_4F_4Mn_2N_6O_4Re$	$C_{50}H_{58}Cl_4Mn_2N_8O_8Re$	$C_{44}H_{46}Cl_4Mn_2N_8O_4Re$
Molecular weight ($g.mol^{-1}$)	1313.98	1134.75	1206.69	1336.93	1188.77
Temperature (K)	150(2)	120(2)	120(2)	150(2)	120(2)
Crystal System	monoclinic	monoclinic	triclinic	triclinic	triclinic
Space group	$P2_1/c$	$P2_1/c$	P-1	P-1	P-1
a (Å)	11.5321(3)	12.173(2)	8.230(5)	8.527(17)	10.009(3)
b (Å)	17.4522(5)	13.066(3)	11.929(5)	13.189(3)	10.533(4)
c (Å)	14.0824(4)	13.883(3)	12.646(5)	13.996(3)	12.260(5)
α (°)	90	90	103.906(5)	104.99(3)	68.769(2)
β (°)	93.209(2)	99.19(3)	105.637(5)	107.35(3)	75.436(2)
γ (°)	90	90	104.289(5)	105.17(3)	81.799(2)
Volume ($Å^3$)	2829.79(14)	2179.9(8)	1101.7(9)	1349.7(7)	1164.10(8)
Z	2	2	1	1	1
Density ($g.cm^{-3}$)	1.542	1.745	1.819	1.645	1.696
$\mu_{MoK\alpha}$ (mm^{-1})	2.813	3.658	3.614	2.951	3.408
F000	1322	1126	595	671	591
GooF	1.025	1.048	1.071	1.028	1.043
[a]R_1 ($I > 2.00\sigma(I)$)	0.0328	0.0327	0.0186	0.0380	0.0278
[b]wR_2 (all reflections)	0.0807	0.1240	0.0420	0.0985	0.0589

[a]$R_1 = \Sigma ||F_0| - |F_C|| / \Sigma|F_0|$, [b]$wR_2 = [\Sigma w(F_0^2 - F_C^2)^2 / \Sigma w(F_0^2)^2]^{1/2}$, $w = 1/[\sigma^2F_0^2 + (0.0313P)^2 + 1.5564P]$; where $P = (F_0^2 + 2F_C^2)/3$

In the crystal structures of **8-12** (figure III.22) both the Mn^{III} and Re^{IV} ions are in an octahedral environment. Each Re^{IV} ion of the *trans*-$[Re^{IV}Cl_4(CN)_2]^{2-}$ unit is connected to the axial coordination site of two Mn^{III} through the nitrogen atoms of both cyanido ligands. The equatorial plane of Re^{IV} contains four chlorido groups (Re-Cl_{av} ≈ 2.332(2) Å) and the carbon of the cyanido groups is axially connected to the Re^{IV} ions (Re-C_{av} bonds range between 2.115(2) Å for **10** to 2.136(4) Å for **11**). The equatorial positions of the hexa-coordinated Mn^{III} ion are occupied by the oxygen and nitrogen atoms originating from the Schiff base ligands (Mn-N_{av} ≈ 1.98 Å, Mn-O_{av} ≈ 1.88 Å), while the remaining axial position of each manganese atom is coordinated with one of the phenoxido oxygen atoms from a neighboring Mn^{III}-Schiff base unit as previously seen in **7** (section III.2.3.2) and in related materials.[1a,6,8] Thus, inside the crystal structure there are one dimensional chain like polymers. The Mn^{III}-Re^{IV}-Mn^{III} fragment acts as the elementary unit connected through phenoxido oxygen atoms to form a one dimensional chain. The Re^{IV} center lies on an inversion center resulting in only one type of Mn^{III} and Re^{IV} sites in **8-12**. The phenoxido oxygen which links the two manganese atoms is slightly out of the equatorial plane of the parent Mn^{III}-Schiff base complex. Thus the angles between Mn-O*-Mn are *ca.* 100° for **8-12** and the Mn-O* distance ranges from 2.32 to 2.74 Å, resulting in Mn-Mn distances between 3.26 and 3.55 Å. The coordination spheres of the manganese ion are therefore strongly distorted due to their out-of-plane dinuclear arrangement. The Mn^{III}-N-C angles in each compound are nonlinear (ranging from 152.4(2)° to 155.0(3)°) which provides slight zigzag pattern to the chain. In table III.5, the Mn-O* and Mn-Mn* distances are summarized for compound **8** to **12** along with the Mn-N-C and Mn-O*-Mn angles.

Table III.5. Some significant bond distances and angles of compound **8** to **12**

	Mn-O* (Å)	Mn-Mn* (Å)	Mn-N-C (°)	Mn-O*-Mn (°)
8	2.737(2)	3.552	155.0(3)	98.8(9)
9	2.587(4)	3.442	150.0(5)	99.2(2)
10	2.450(2)	3.344	154.9(2)	99.7(7)
11	2.708(3)	3.563	157.2(4)	100.0(1)
12	2.320(2)	3.264	152.4(2)	99.89(8)

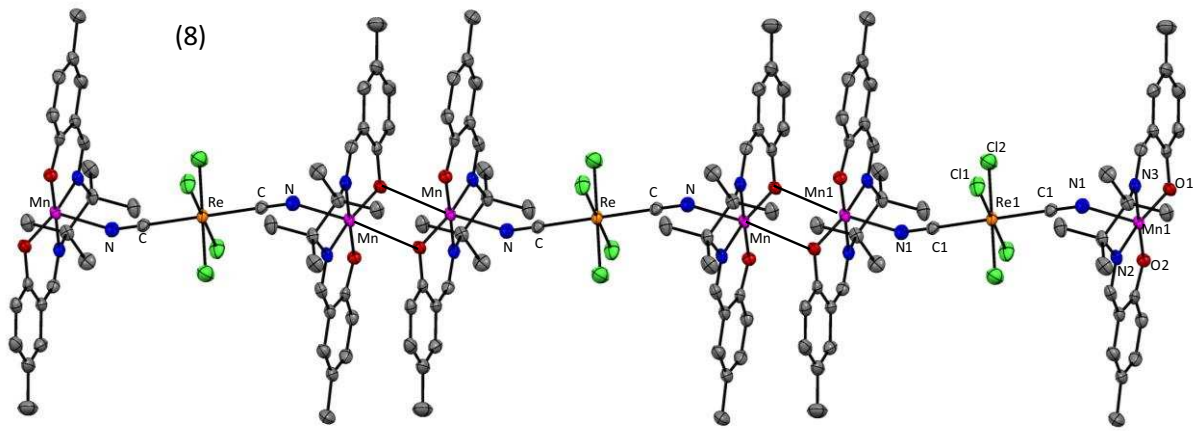

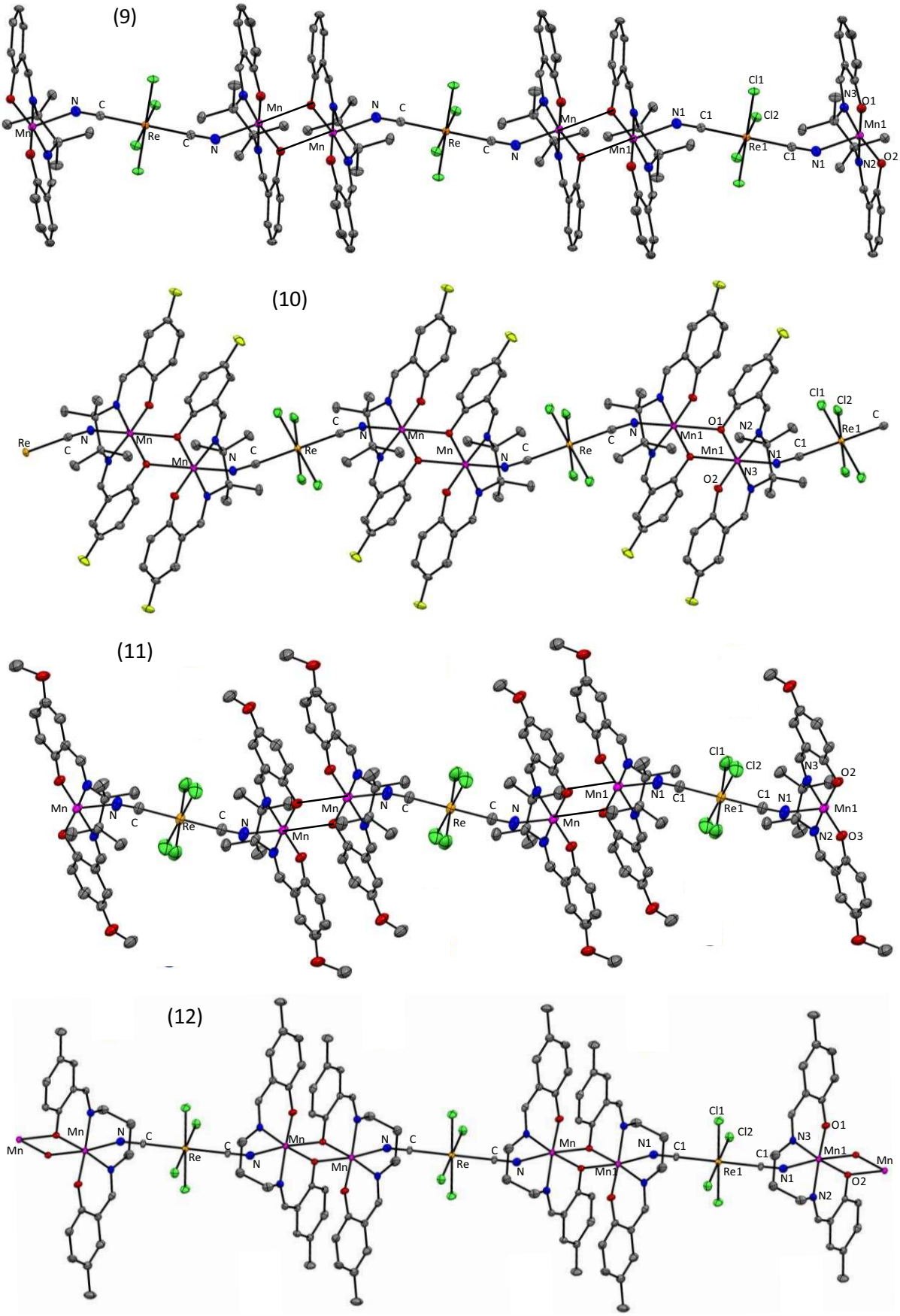

Figure III.22. ORTEP view of the (50% thermal probability) one dimensional structure of **8-12**, the Re, Mn, C, O, N, Cl and F atoms are shown in orange, magenta, grey, red, blue, green and pale green color respectively. The hydrogen atoms and solvent molecules are omitted for better clarity.

Compounds **8** and **9** crystallize in the monoclinic $P2_1/c$ space group; whereas the rest of the three complexes (**10-12**) are isostructural with respect to their crystal system (triclinic) and space group (P-1). For **8** and **9**, we observe two kinds of chain orientation in the crystal packing. If we view these two one dimensional chains (figure III.23a and III.23b) along their crystallographic *c* axes, the presence of two different kinds of chains (chain A and chain B in figure III.23) in the crystal structure becomes more visible. Each chain in **8** has four first neighboring chains (two of the same kind and two of different kinds); the average distance between the nearest metal centers of the same kinds of chain (between chain A-A or B-B) is about 11.5 Å for and for the different kinds of chain (between chain A-B) is about 8.7 Å (figure III.23a). In the compound **9,** the nearest four neighbors are different kinds of chains (for 'A' kind chain, the nearest neighbors are 'B'; and for 'B' kind of chain they are 'A') with a 9 Å average distance between the nearest metal centers (figure III.23b).

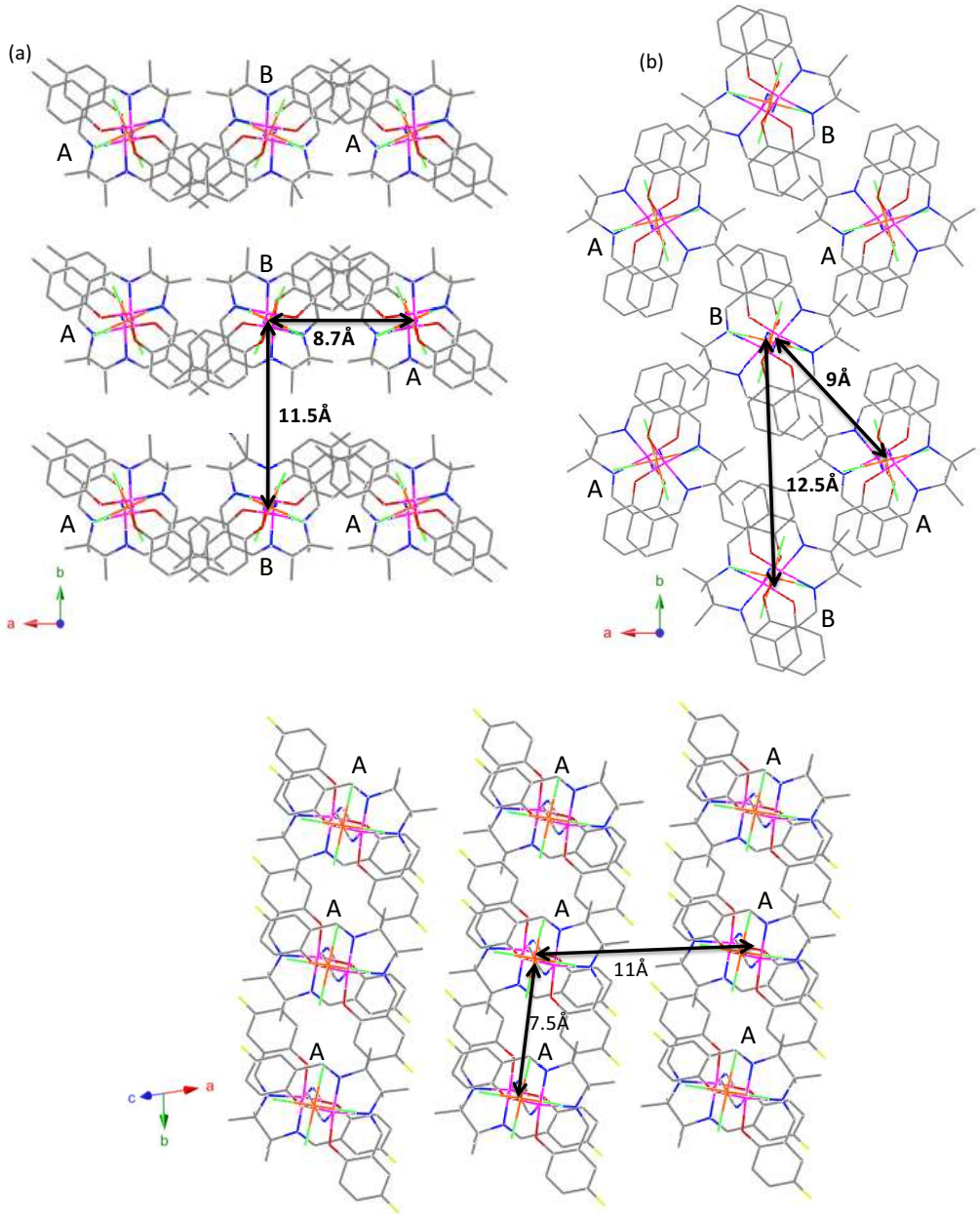

Figure III.23. View of the chains along the *c* axis to see their mutual orientations and distances for **8** (a) and **9** (b). (c) View of the chains in **10**, that are identically oriented but the mutual distances are different.

In contrast, for **10-12** all the chains possess a similar orientation inside the crystal packing and each chain is also surrounded by four neighboring chains (figure III.23c). In the crystal structure of **10**, the two second neighbor chains are on average 7.5 Å away and two farther neighbor chains are 11.5 Å distant from each chain with respect to the metal centers; these distances are 8 Å and 12 Å for **11** and 8 Å and 11.5 Å for **12**. In the case of **8**, **11** and **12**, acetonitrile molecules fill the vacant spaces between the distant chains inside the crystal packing but the remaining two compounds crystallize without any solvent molecules. For all these one dimensional compounds, although the Mn-N-C axes are not linear, the Jahn-Teller axes of the dinuclear Mn^{III} units (N-Mn^{III}-O*), are parallel to one another within a chain. Therefore in the crystals of **10-12** all the Jahn-Teller axes are oriented in the same direction. On the other hand, the Jahn-Teller axes of the Mn^{III} ions belonging to two different kinds of chains have a 25° angle between them (figure III.24) in **8** and a 41° angle for **9**. This inter-chain angle of the magnetic easy axis in chains **8** and **9** provides a strong impact on their magnetic properties (see below).

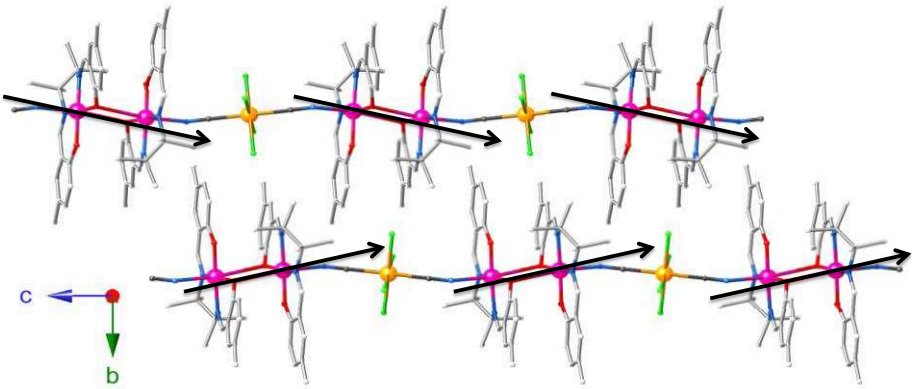

Figure III.24. View emphasizing the presence and the orientation (at *ca.* 25° based on the Mn-O Jahn Teller axes of the Mn^{III} site) of the two different chains present in the crystal structure of **8**, whereas the same topology is seen for **9** with an angle of 41°.

III.3.3. Magnetic properties

***Static magnetic properties**:*

Variable temperature magnetic susceptibility measurements were performed on **8-12** to probe the intra-chain magnetic exchange interactions and the magnetic ground state. In agreement with the structural characterizations that shows similar crystal structures for **8** and **9**, the magnetic properties for **8** and **9** in one hand and **10-12** on the other hand are very comparable.

For **8** and **9**, the temperature dependence of the χT product collected in a 1000 Oe *dc* magnetic field is shown in figure III.25. The χT value is 6.9 cm^3K/mol and 7.0 cm^3K/mol at 280 K for **8** and **9** respectively, which is in good agreement with the expected Curie constant of 7.2 cm^3K/mol (for g_{Re} = 1.65[2] and g_{Mn} = 2[3d]). The χT product decreases gradually with decreasing temperature for both compounds and reaches a minimum value χT = 5.4 cm^3K/mol at 40 K for **8** and χT = 5.1 cm^3K/mol at 36 K for **9**. A further decrease of the temperature results in a sharp increase of χT up to 13.5 cm^3K/mol at 7.4 K for **8** and to 17.5 cm^3K/mol at 3.8 K for **9**. Further lowering of the temperature causes a rapid drop in χT which at 1.8 K reaches 2.2 cm^3K/mol and 5.0 cm^3K/mol for **8** and **9** respectively.

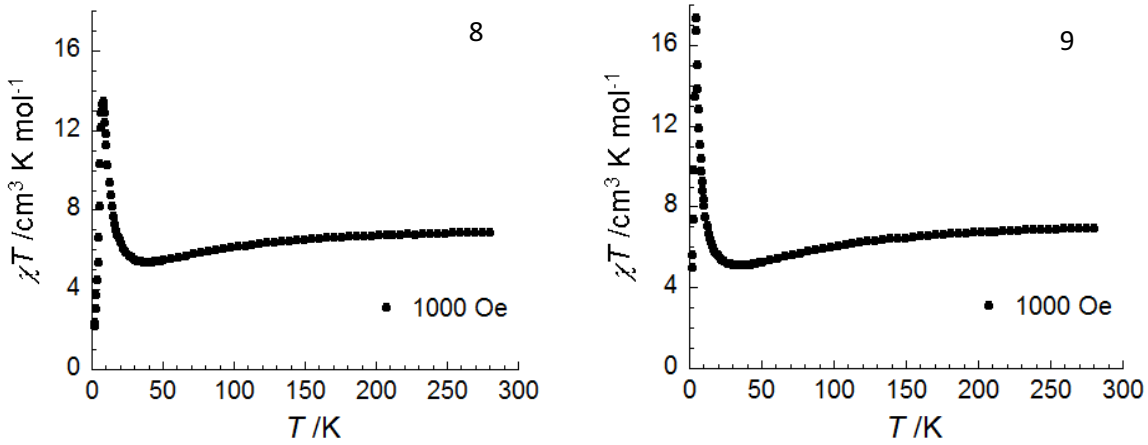

Figure III.25. The plot of the temperature dependence of the χT product at 1000 Oe for chain **8** and **9**.

In case of **10-12**, the temperature dependence of the χT product was collected in the same conditions, at 1000 Oe between 1.8 and 300 K (figure III.26). For **10**, **11** and **12** the respective values of the room temperature χT are 7.0 cm^3K/mol at 270 K, 7.2 cm^3K/mol at 280 K and 7.7 cm^3K/mol at 300 K in good agreement with the expected Curie constant (7.2 cm^3K/mol). The χT products decrease with decreasing temperature to reach 6.1, 5.2, and 4.8 cm^3K/mol at 34, 19 and 22 K for **10**, **11** and **12** respectively. With a further lowering of the temperature, χT values for these compounds increase but to a much lower extent than that of **8** and **9**, respectively reaching 8.3, 5.5 and 4.9 cm^3K/mol at 8.7, 8.9 and 10.0 K. Thereafter, a further decrease in temperature causes a sharp decrease of χT to 0.41, 0.49 and 1.18 cm^3K/mol at 1.8 K for **10**, **11** and **12** respectively.

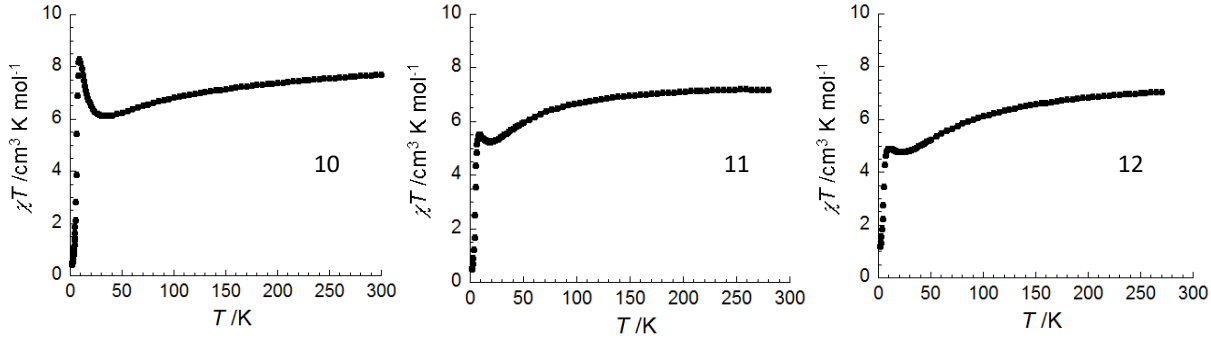

Figure III.26. The plot of the temperature dependence of the χT products at 1000 Oe for chain **10**, **11** and **12**.

From the experimental data, the temperature dependence of the magnetic susceptibility of all of the chain compounds was found to be qualitatively comparable. The magnetic interaction in the dinuclear building block of Mn^{III} is known to be ferromagnetic and comparatively small in magnitude (below +3 K);[1,4a,6-8] therefore the observed temperature-dependent decrease of χT at higher temperatures indicates the presence of dominating antiferromagnetic interaction (J) between neighboring Mn^{III} and Re^{IV} centers within the chain through the cyanido bridge. After χT reaches its minimum, the Mn-Mn ferromagnetic interaction (J') is detected, resulting in an increase in χT to a maximum value. As the temperature was further lowered, the rapid decrease of χT results from additional interchain antiferromagnetic interactions or/and magnetic anisotropy.

Based on these results, compounds **8-12** can be deduced as a magnetic point of view as a one dimensional assembly of trinuclear (Mn^{III}-Re^{IV}-Mn^{III}) units, having relatively strong Re^{IV}-Mn^{III} antiferromagnetic interactions (J) and weak ferromagnetic interactions (J') along the chain. The magnetic susceptibility data was thus initially analysed with a trinuclear Mn^{III}-Re^{IV}-Mn^{III} model, neglecting the weak J' and only considering the antiferromagnetic J exchange, based on the following Heisenberg Hamiltonian with isotropic spins, $\boldsymbol{H = -2J\,(S_{Mn}.S_{Re} + S_{Re}.S_{Mn})}$, where $S_{Mn} = 2$ and $S_{Re} = 3/2$. The expression of magnetic susceptibility χ is thus given by **Eq.III.2**, like for the trinuclear complexes, where g is the average Landé factor for Mn^{III} (g_{Mn}) and Re^{IV} (g_{Re}). This trinuclear model nicely corresponds to the experimental data above 60 K (indicated as a dotted red line in figures III.27 and figure III.28) for all the compounds, implying that the spin ground state of the Mn^{III}-Re^{IV}-Mn^{III} unit is $S_T = 5/2$ and yielding the g_{av} values between 1.91 and 1.96 and antiferromagnetic interaction (J) between -2.3 and -5.3 K (see table III.6).

Table III.6. The g_{av}, J and J' values found from the fit of χT vs. T data of **8-12** with the Heisenberg trinuclear model and mean field approximation.

compounds	Trinuclear model		Trinuclear + mean field model		
	g_{av}	J/k_B (K)	g_{av}	J/k_B (K)	J'/k_B (K)
8	1.93(1)	- 4.4(5)	2.12(5)	- 10.8(6)	+ 0.50(5)
9	1.95(2)	- 5.3(3)	2.13(5)	- 10.9(5)	+ 0.33(5)
10	1.91(3)	- 2.3(4)	1.90(6)	- 5.7(5)	+ 0.78(5)
11	1.95(3)	- 2.9(2)	1.95(6)	- 4.4(5)	+ 0.33(5)
12	1.96(2)	- 5.3(3)	1.90(6)	- 6.5(5)	+ 0.38(5)

In order to fit the experimental data down to lower temperature, we next considered the inter-trinuclear ferromagnetic interaction (J') along the chain, treated in the mean field approximation. The expression of the magnetic susceptibility becomes, $\boldsymbol{\chi = \chi_{trinuclear}/(1- czJ'\chi_{trinuclear})}$ (**Eq.III.3**), where c = $2/Ng^2\mu_B^2$ and z indicates the number of neighbors for each trinuclear unit (here z = 2). This mean field approach significantly improved the fit of the experimental susceptibility data (see solid red line in figure III.27 and III.28) for **8** and **9**. In the case of **8**, the experimental data agree well with this mean field model above 9 K, yielding $g_{av} = 2.12(5)$, $J/k_B = -10.8(6)$ K and $J'/k_B = + 0.50(5)$ K. Likewise, for

9 the experimental data are also well fitted by this approach above 6 K and yields g_{av} = 2.13(5), J/k_B = -10.9(5) K and J'/k_B = +0.33(5) K.

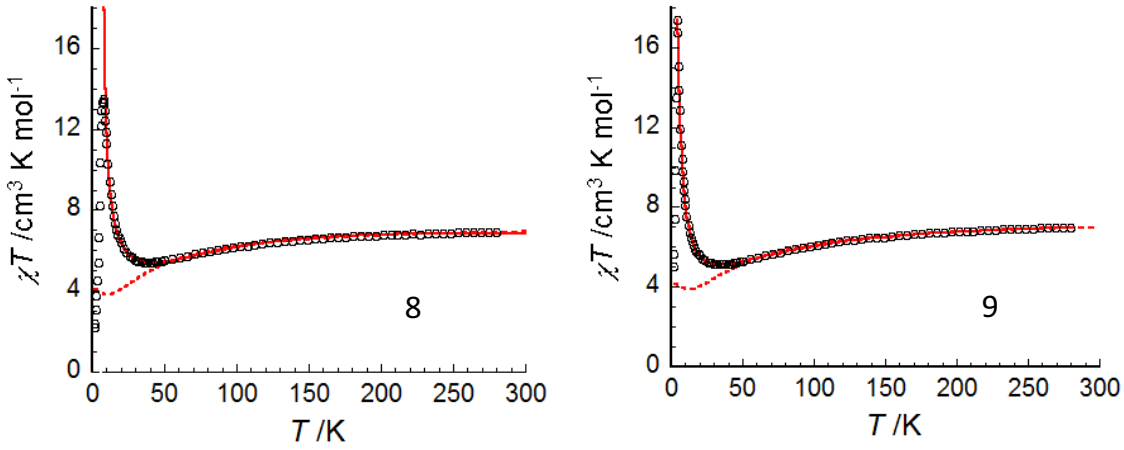

Figure III.27. Temperature dependence of the molar χT product at 1000 Oe for **8** and **9**, where the hollow black circles correspond to the experimental data, the dotted red line is the fit of χT above 60 K with the trinuclear Mn^{III}-Re^{IV}-Mn^{III} model and the solid red line is the fit of the experimental data using the mean field approximation modified over trinuclear model.

The experimental values of the susceptibility for **10-12** revealed that the increase in χT at low temperatures is less marked than that in **8** and **9**. As a result, the mean field model gave a poorer fit to the experimental data for **10-12** (figure III.28) compared to **8-9**. This model corresponds to the experimental susceptibility data above 19 K, 12 K and 18 K for **10**, **11** and **12** respectively, yielding g_{av} = 1.90(6), J/k_B = -5.7(5) K and J'/k_B = +0.78(5) K for **10**, g_{av} = 1.95(6), J/k_B = -4.4(5) K and J'/k_B = +0.33(5) K for **11**, and g_{av} = 1.90(6), J/k_B = -6.5(5) K and J'/k_B = +0.38(5) K for **12**. All of the values of g_{av}, J and J' of **8-12** found from the fit of the magnetic susceptibility with trinuclear model and mean field approximation are tabulated in table III.6.

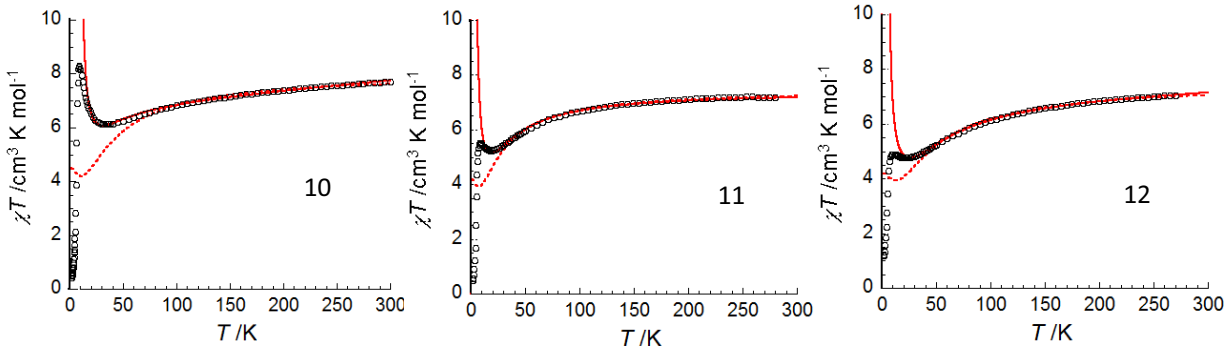

Figure III.28. Temperature dependence of the molar χT product at 1000 Oe for **10-12**, where the hollow black circles correspond to the experimental data, the dotted red line is the fit of χT above 60 K with trinuclear Mn^{III}-Re^{IV}-Mn^{III} model and the solid red line is the fit of the experimental data using the mean field approximation-modified trinuclear model.

In order to further investigate the low temperature properties of these systems and the extent of the one dimensional magnetic correlation along the chain axis, the temperature dependence of the

zero *dc* field magnetic susceptibility (χ') of **8-12** were collected with an *ac* field of 3 Oe oscillating at 100 Hz. The experimental data were analyzed as $\chi'T$ vs. $1/T$ in a semilog plot in order to emphasize a possible exponential increase of the correlation length expected for anisotropic, Ising like 1D systems.[4a] In the case of **8**, this plot revealed the exponential increase of $\chi'T$ according to the equation $\boldsymbol{\chi T/C = exp(\Delta_\xi/k_B T)}$ above 10 K, where C is the effective Curie constant and Δ_ξ the energy to create domain walls. We see the $\ln(\chi'T)$ vs. $1/T$ plot is linear between 10-25 K which further emphasizes the one dimensional correlation and the Ising-like magnetic anisotropy [4a] in **8**.

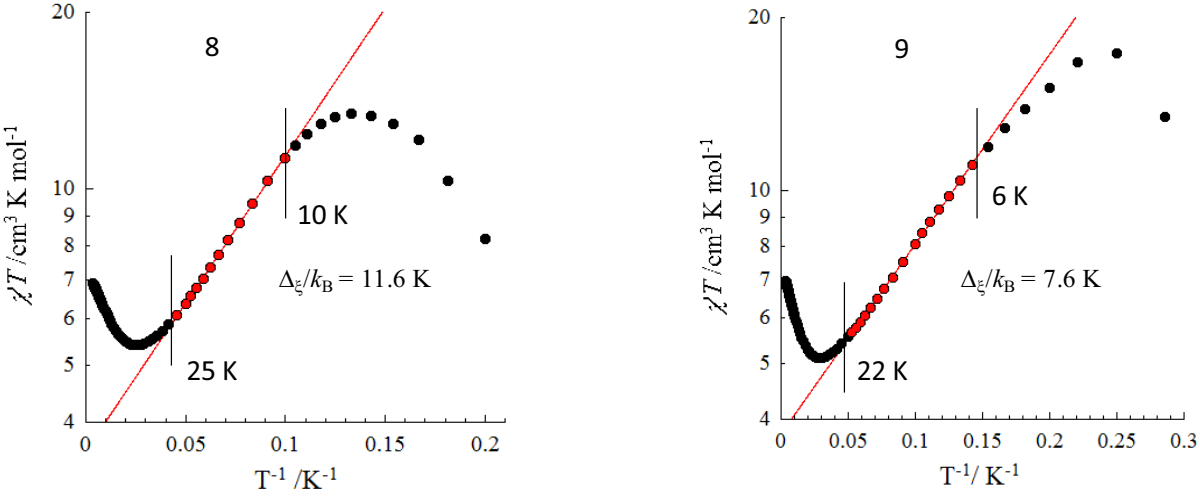

Figure III.29. Plot of $\chi'T$ vs $1/T$ for **8** and **9** where the y axis is in logarithmic scale, and χ' is the molar magnetic susceptibility collected without an applied *dc* field but in an *ac* field of 3 Oe oscillating at 100 Hz. The solid red line corresponds to the fit of the linear portion of the experimental data (solid red dots) between 10-25 K for **8** and between 6-22 K for **9**, with the equation $\boldsymbol{\chi T/C = exp(\Delta_\xi/k_B T)}$. The solid black circles represent the experimental data.

From the best fit of the linear region (solid red straight line in figure III.29) of the experimental data, Δ_ξ/k_B , the energy gap to create the domain walls was found to be 11.6 K and C = 3.57 cm^{3}K/mol for **8**. In the Ising limit, the inter-trinuclear interactions calculated from the domain wall energy ($\Delta_\xi = 4J'S_T^2$) is about J'/k_B = + 0.46 K, in good agreement with the ferromagnetic exchange deduced earlier through the mean field approximation-modified Mn^{III}-Re^{IV}-Mn^{III} model (table III.6). This $\chi'T$ product reaches a maximum below 10 K and decreases with decreasing temperature, indicating either the obvious presence of finite size effects where the magnetic correlation is limited by crystalline defects and/or a 3D antiferromagnetic ground state of the system. Similarly the $\ln(\chi'T)$ vs $1/T$ plot for **9** (figure III.29) is linear between 6 and 22 K. The fit of the linear region with the equation $\boldsymbol{\chi T/C = exp(\Delta_\xi/k_B T)}$ yields Δ_ξ/k_B = 7.6 K and C = 3.77 cm^{3}K/mol. From this, one obtains J'/k_B = + 0.31 K, in good agreement with the previous fit of the magnetic susceptibility at 1000 Oe (figure III.27 and the text). The crystalline defects or/and 3D antiferromagnetic ground state in **9** also results in the decrease of $\chi'T$ below 6 K.

As above, the temperature-dependent zero *dc* field magnetic susceptibility product ($\chi'T$) of **10** was plotted against $1/T$. As displayed in figure III.30, the lower slope of the linear region of the experimental data between 11 K and 20 K demonstrate the comparably poorer one dimensional magnetic correlation in **10** with an energy gap of Δ_ξ/k_B = 5.0 K. We have already seen that the Mn^{III}-Re^{IV} magnetic exchange (J/k_B = -5.7(5) K) in **10** is weaker than that of **8** and **9**, which is probably the reason behind the weaker Δ_ξ value. In the case of compounds **11** and **12**, the $\chi'T$ vs $1/T$ plot exhibits even poorer one dimensional behavior. Therefore, from the comparison of **8-12**, only the chains in **8** and **9** can be considered a one dimensional system from a magnetic point of view, whereas the rest of the chain compounds are one dimensional only from a crystallographic point of view.

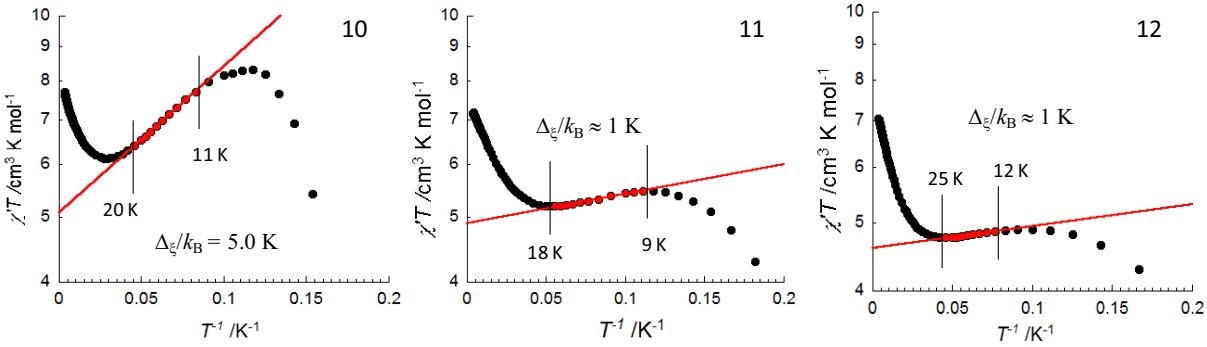

Figure III.30. Plot of $\chi'T$ vs $1/T$ for **10-12** where the y axis is logarithmic and $\chi'T$ is the molar magnetic susceptibility collected without applied *dc* field but in a *ac* field of 3 Oe oscillating at 100 Hz. The solid red straight line corresponds to the fit of the linear portion of experimental data between 11-20 K for **10**, 9-18 K for **11**, 12-25 K for **12**, (solid red dots in the experimental data) with the equation $\boldsymbol{\chi T/C = exp(\Delta_\xi/k_B T)}$. The solid black circles represent experimental data.

In all of the above compounds, we observe a sharp decline of χT product or $\chi'T$ at low temperatures. Therefore, variable temperature magnetic susceptibility measurements were performed under multiple applied *dc* fields. Compounds **8-12** show a significant field dependence of the susceptibility, thus suggesting the presence of a magnetic phase transition from the paramagnetic to an antiferromagnetic phase. The phase transition phenomenon is further emphasized by the magnetization measurements as a function of applied field at multiple temperatures. For all compounds, these measurements exhibit a temperature dependent inflection point in the magnetization curves corresponding to the maximum value of χ (*viz. dM/dH*) at a critical field (H_C). Extracting the maximum susceptibilities found in the χ vs. T and *dM/dH* vs. H curves, we constructed an H vs. T phase diagram for each of the compounds **8-12**, all indicating metamagnet type behavior with specific T_N and H_C values.

For **8**, the $\chi(T)$ data were collected at different applied *dc* fields between 100 Oe and 4500 Oe until the susceptibility value reached saturation in the low temperature region below 4 K (shown in figure III.31a). With the applied *dc* magnetic fields between 100 Oe to 2800 Oe, the susceptibility values reach a maximum around 6 K, and above 3000 Oe the susceptibility starts to plateau. In these

data we observe that at 100 Oe the χ value was 0.2 cm^3/mol at 1.8 K, but this value gradually increased to 1.4 cm^3/mol (at 1.8 K) with an applied field of 600 Oe. This behavior suggests the presence of residual magnetization in the antiferromagnetic phase and this phenomenon is emphasized with the magnetic hysteresis behavior of **8** (figure III.31b). Thus we antiferromagnetic phase of **8** considered a canted antiferromagnetic phase. The *M* vs. *H* hysteresis loops for **8** are systematically detected below 6.2 K (figure III.31b) with coercive fields up to 2100 Oe at 180 Oe/min and a remnant magnetization of $M_R = 0.19\ \mu_B$ at 1.8 K (inset of figure III.31b). Thus, **8** is a magnet below 6.2 K, which can only be induced by a canting of two magnetic sublattices in the ordered phase. This behavior is supported by the two kinds of chain orientation (figure III.23a and III.24) present in the crystal packing of **8**. In the canted antiferromagnetic phase, the equilibrium canting angle, α, between the two magnetic sublattices in **8** is estimated at 8° from the remnant magnetization (as $sin(\alpha/2) = 2M_R/M_{sat}$, $M_{sat} \approx 5.3\ \mu_B$ being the magnetization at saturation with $g = 2.12$).

The *M* vs. *H* data for this compound was collected between 1.8 and 15 K (figure III.31c) and therefore inflection points corresponding to H_C were extracted from the *dM/dH* vs. *H* plot below 6 K (figure III.31d). Subsequently, the H_C vs. *T* phase diagram for **8** was constructed (figure III.31e) from the maxima of the experimental χ vs. *T* and *dM/dH* vs. *H* curves. This obtained phase diagram is characteristic for an antiferromagnet or canted antiferromagnet displaying a metamagnetic behavior with a Néel temperature $T_N \approx 6.2$ K. The $H_C(T)$ line in the phase diagram corresponds to an antiferromagnet to paramagnet phase transition that happens in presence of an applied field. If this H_C line is extrapolated to the absolute zero temperature, the critical field H_C (0 K) of **8** is found about 2600 Oe.

Considering the experimental 1D correlation length shown in the figure III.29 (from the χ' vs. $1/T$ fit collected at 0 *dc* field) the theoretical T_N for the quasi-1D model can be estimated. On the basis of the experimental phase diagram shown in figure III.31e, the metamagnetic critical field (transition line between the canted antiferromagnetic and the paramagnetic phases) extrapolated at 0 K can be estimated at *ca*. 2600 Oe. This field is the magnetic field necessary to overcome the inter-chain interactions, J_{perp}. Therefore it can be easily deduced equalizing the interaction and the Zeeman energies: $2z|J_{perp}|S_T^2/k_B = g\mu_B H_C S_T/k_B = 0.92$ K and thus $zJ_{perp}/k_B = -0.074$ K, where $J_{perp}/k_B = -18$ mK for $z = 4$ (because each chain has four neighbours). Considering a one-dimension model of anisotropic S_T spins in the Ising limit ($|D/J| > 4/3$), the normalized susceptibility obeys the following relation: $\chi'_{1D}/C_{eff} = (1/T)\ exp(\Delta_\xi/k_B T)$ where C_{eff} is the Curie constant of this model and Δ_ξ is the energy to create domain walls along the chain (figure III.31f). For **8**, $C_{eff} = 3.57$ cm^3K/mol and $\Delta_\xi/k_B = 11.6$ K. The interchain magnetic interaction can be introduced in this model using the mean-field approximation and thus the resulting staggered magnetic susceptibility can be written: $\chi_{AF} = \chi'_{1D}/(1 - 2z|J_{perp}|S_T^2\chi'_{1D}/C_{eff}k_B)$. The critical temperature of this model is obtained for the divergence of this susceptibility and thus for $2z|J_{perp}|S_T^2\chi'_{1D}/C_{eff}k_B = 1$ (see figure III.31f). This relation can be used to

estimate the theoretical transition temperature of the present system considering the interchain interaction energy, $2z|J_{perp}|S_T^2/k_B$ = 0.92 K, deduced from the metamagnetic critical field and the one-dimensional model used to fit the experimental data between 25 and 10 K: $\chi'_{1D} = (C_{eff}/T)\ exp(\Delta_\xi/k_BT)$ (red line in figure III.29 and III.31f; with C_{eff} = 3.57 cm^3K/mol and Δ_ξ/k_B = 11.6 K). Graphically as shown in figure III.31f, the critical temperature is obtained when $\chi'_{1D}/C_{eff} = k_B/(2z|J_{perp}|S_T^2)$ = 1.09 K^{-1} and thus the critical temperature of the system is estimated at 6.15 K in excellent agreement with the experimental value of 6.2 K.

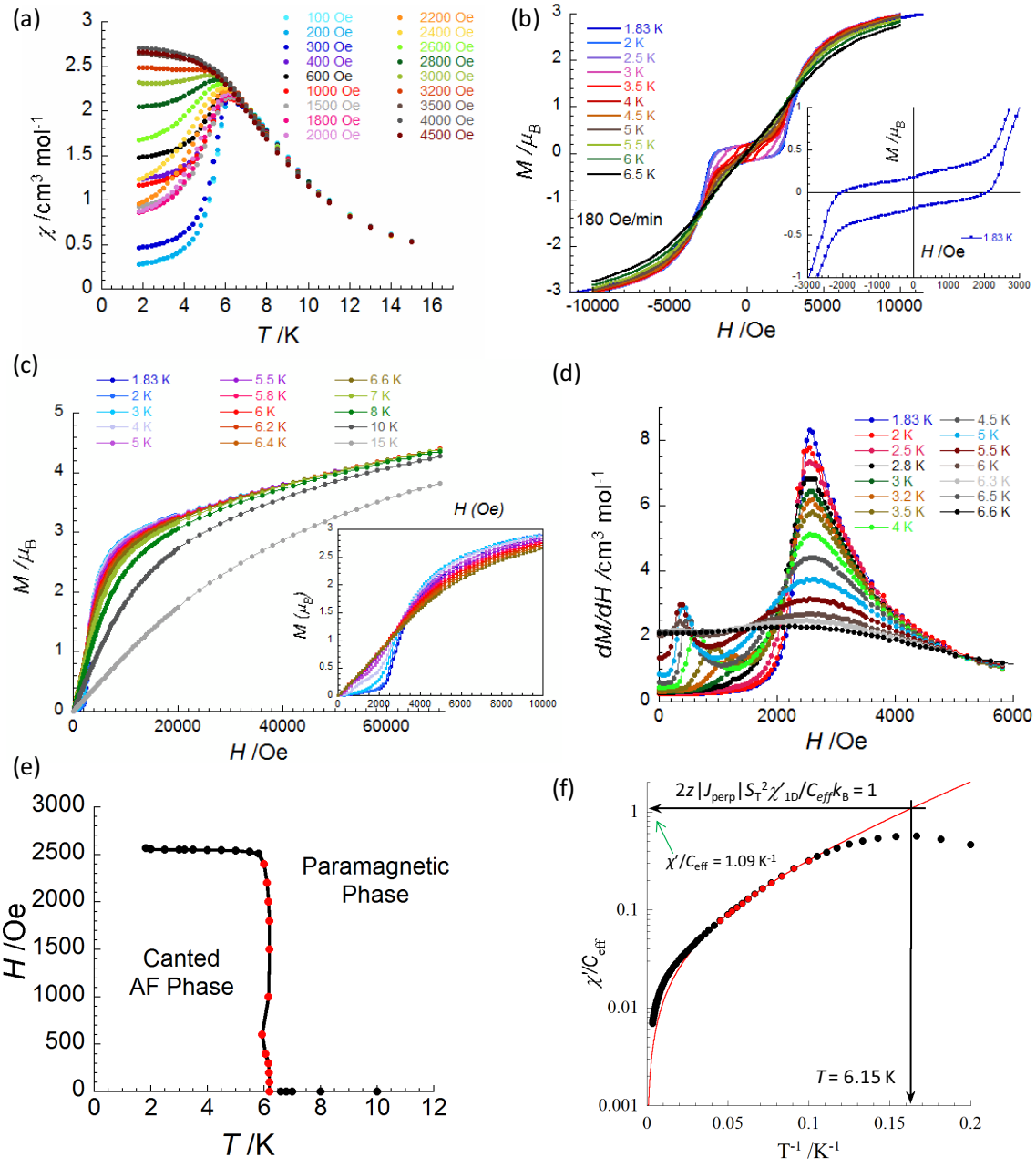

Figure III.31.low temperature magnetic properties for 8 (a) $\chi(T)$ plots at different *dc* fields. (b) The magnetic hysteresis M = f(H) plots with the field sweep rate of 180 Oe/min below 6 K; Inset: the expanded view of the main figure at 1.83 K. (c) M vs. H plots at multiple temperatures; Inset: Expanded view of the data at low field up to 6.6 K. (d) dM/dH (= χ), as a function of field at multiple temperatures (the second maxima below 2100 Oe coming from hysteresis behavior). (e) Magnetic phase diagram (T, H) constructed from the maxima of plots (a) and (d), giving T_N = 6.2 K and H_C(0 K) ≈ 2600 Oe. (f) The χ'/C_{eff} is plotted against 1/T with black circles, where the solid red line is the fit with the one dimensional Ising model.

Similarly for **9** the $\chi(T)$ data were collected between 50 to 2400 Oe at different *dc* fields (figure III.32a). With applied *dc* magnetic fields between 50 Oe and 1900 Oe, above 500 Oe the susceptibility values reach a maximum around 4.5 K, and above 2000 Oe the susceptibility starts to plateau. As shown in the inset of the figure III.3.11a at applied *dc* fields (below 400 Oe) the susceptibility is very high indicating a spontaneous magnetization of the system corresponding to a transition to a canted antiferromagnetic phase as in **8**. It should be mentioned here, that we have observed two different orientations of the chains in the crystal structure of **9** (figure III.23b) as a source of uncompensated sub-lattices of the canted antiferromagnetic phase. Therefore M vs H hysteresis data of **9** were collected with a field sweep rate of 180 Oe/min (figure III.32b). This sweeping of the magnetic field between -7 T to 7 T at 1.83 K for **9** demonstrates significant hysteresis in the magnetization with a coercive field 1000 Oe and a remnant magnetization of 0.437 μ_B (inset of the figure III.32b). This magnetic hysteresis behavior of **9** is preserved upto 4.5 K. The equilibrium canting angle, α, between the two magnetic sublattices in **9** is estimated as 19° from the relation $sin(\alpha/2) = 2M_R/M_{sat}$ ($M_{sat} \approx 5.3\ \mu_B$ being the magnetization at saturation with $g = 2.13$).

The M vs. H data for **9** were collected between 1.81 and 10 K at different temperatures (figure III.32c) which showed the sigmoid shape as an indication of magnetic phase transition. The H_C values at different temperatures were extracted from the maxima of the dM/dH vs. H (figure III.32d) curves below 4.5 K and thus the H_C vs. T phase diagram was constructed for **9** (figure III.32e). From the phase diagram, the Néel temperature was found to be 4.4 K and the H_C (0 K) to be 1700 Oe.

From the phase diagram, inter-chain antiferromagnetic interaction, J_{perp}/k_B = -12 mK using the relation $2z|J_{perp}|S_T^2/k_B = g\mu_B H_C S_T/k_B = 0.61$ K for **9** with $g_{av} = 2.13$, $S_T = 5/2$ and $H_C = 0.17$ T. Similar to **8**, the χ'/C_{eff} was plotted against $1/T$ (figure III.32f). Considering a one-dimension model of anisotropic S_T spins in the Ising limit ($|D/J| > 4/3$), the χ'/C_{eff} ratio follows the relation $\chi'_{1D}/C_{eff} = (1/T)\ exp(\Delta_\xi/k_B T)$ where C_{eff} = 3.77 cm^3K/mol and Δ_ξ/k_B= 7.6 K (figure III.29). Now, introducing the interchain magnetic interaction in this model with the mean-field approximation staggered magnetic susceptibility becomes: $\chi_{AF} = \chi'_{1D}/(1 - 2z|J_{perp}|S_T^2\chi'_{1D}/C_{eff}k_B)$. Therefore critical temperature of this model is obtained (for the divergence of this susceptibility at $2z|J_{perp}|S_T^2\chi'_{1D}/C_{eff}k_B = 1$),as 4.08 K (figure III.32f), which is quite comparable with the Néel temperature of **9** obtained from its phase diagram.

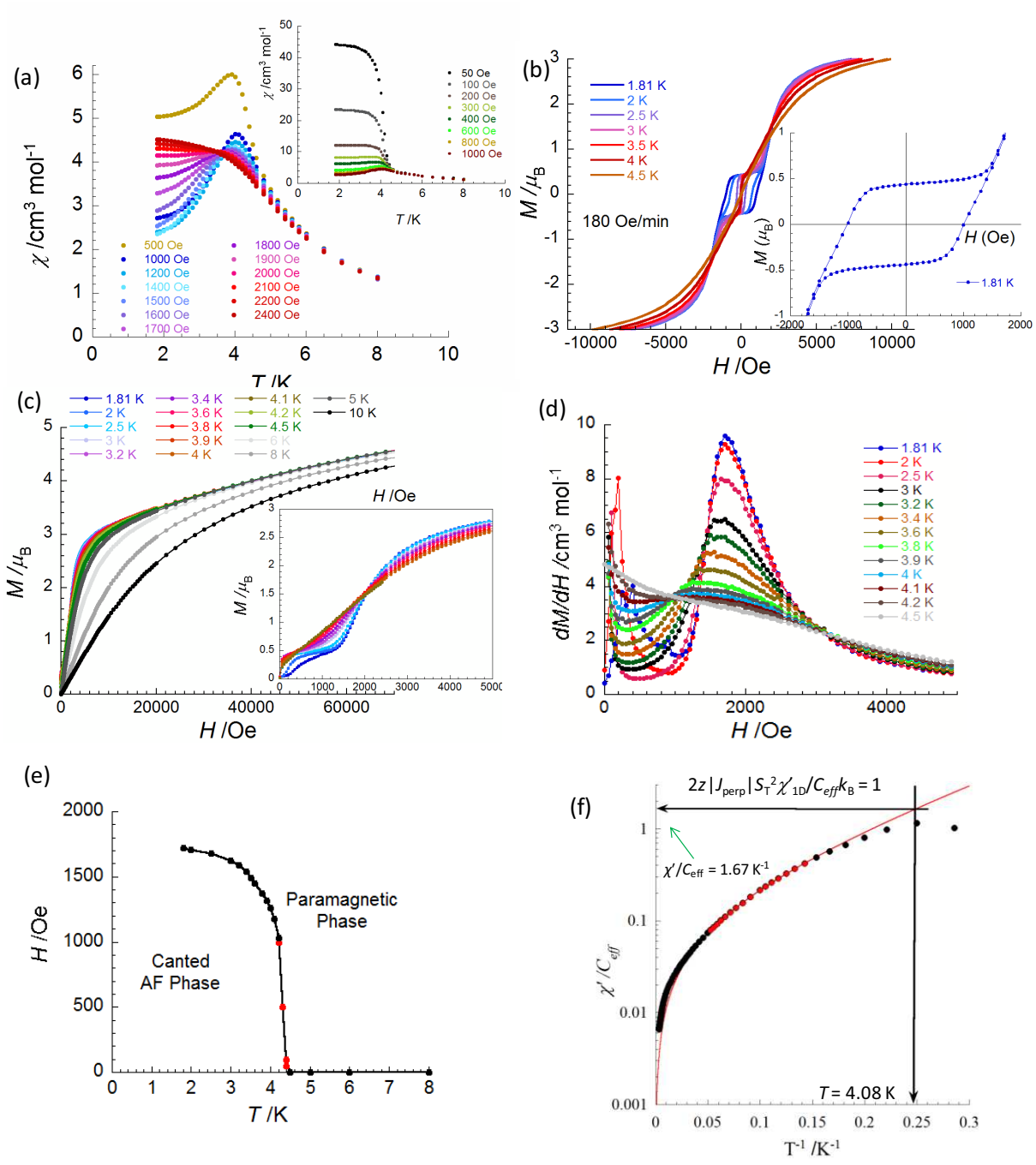

Figure III.32. Low temperature magnetic properties for **9** (a) Plot of $\chi(T)$ at different applied *dc* fields. (b) The magnetic hysteresis $M = f(H)$ plots with the field sweep rate of 180 Oe/min below 4.5 K; Inset: the expanded view of the main figure at 1.81 K. (c) The plot of M vs. H at multiple temperatures; Inset: Expanded view of the data at low field up to 4.5 K. (d) Plot of dM/dH (= χ) as a function of field at multiple temperatures (the second maxima below 1000 Oe coming from hysteresis behavior). (e) Magnetic phase diagram (T, H) constructed from the maxima of plots (a) and (d), giving T_N = 4.4 K and H_C(0 K) ≈ 1700 Oe. (f) The χ'/C_{eff} is plotted against $1/T$ with black circles, where the solid red line is the fit with the one dimensional Ising model.

Measurements of $\chi(T)$ at different fields and M vs. H at different temperatures for **10** were performed between 1000-12000 Oe and 1.84-10 K respectively as shown in figure III.33a and III.33b, followed by the dM/dH curves in figure III.33c. The χ vs. T plots exhibits field dependent maxima

between 1000 and 9500 Oe near 7.5 K and above 10000 Oe χ starts to plateau. From these measurements the (T, H) phase diagram was built for **10** (figure III.33d), providing T_N = 8 K and H_C(0 K) = 9300 Oe. This critical field extracts the interchain interaction of **10** is determined as zJ_{perp}/k_B = -0.232 K, which is off course much higher than that of **8** and **9**. From the fit of the $\chi'T$ vs. $1/T$ of **10** we have already found that the Δ_ξ is low in that system. Similar to **8** and **9,** from the χ'_{1D}/C_{eff} vs $1/T$ plots (figure III.33e) of **10**, the theoretical Néel temperature is 6.45 K when $\chi'_{1D}/C_{eff} = 1/(2z|J_{perp}|S_T^2) = 0.35$. This temperature is quite different from the T_N (= 8 K) found from its phase diagram. This discrepancy occurs due to lesser one dimensional magnetic behavior in **10** compared to **8** or **9**.

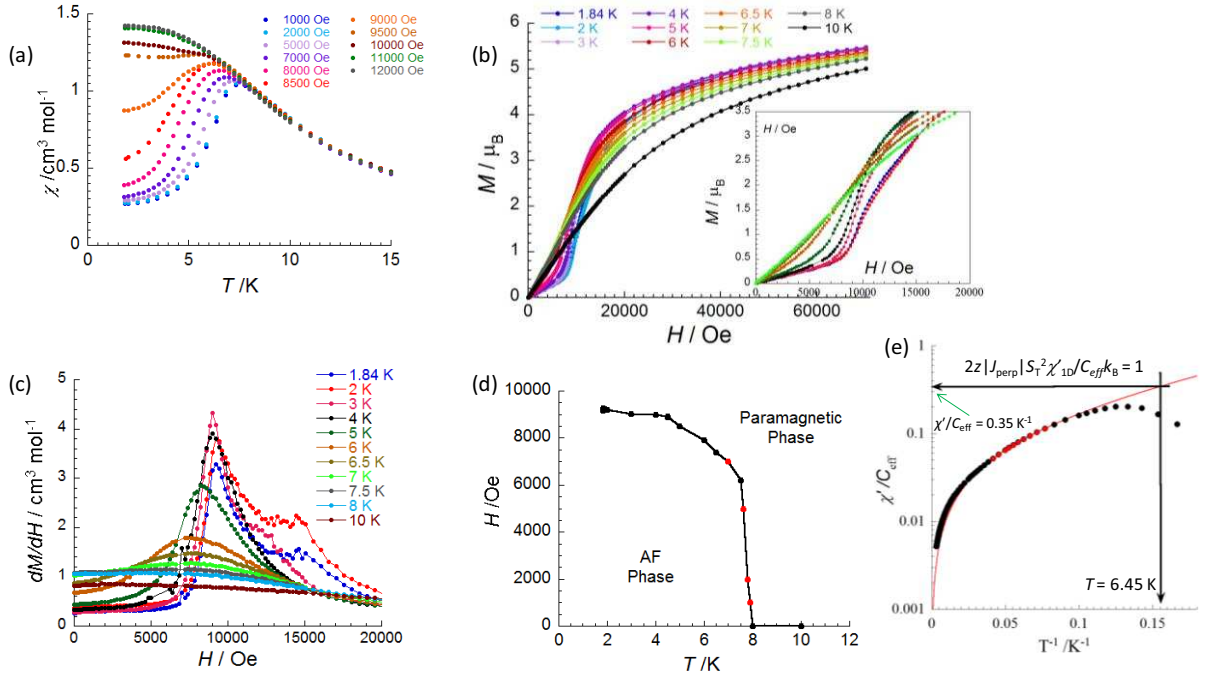

Figure III.33. Low temperature magnetic properties for **10**. (a) Plot of $\chi(T)$ at different applied *dc* fields. (b) Plot of M vs. H at multiple temperatures; Inset: Expanded view of the data at low field up to 7.5 K (c) Plot of dM/dH (= χ) as a function of field at multiple temperatures. (d) Magnetic phase diagram (T, H) constructed from maxima of plot (a) and (c) giving T_N = 8 K and H_C(0 K) = 9300 Oe. (e) The χ'/C_{eff} is plotted against $1/T$ with black circles, where the solid red line is the fit with the one dimensional Ising model.

In the case of **11**, the $\chi(T)$ data were collected between 100-12000 Oe (figure III.34a) and the susceptibility exhibited field dependent maxima around 6 K below 9500 Oe; above 9500 Oe it started to become saturated at low temperature. Then the M vs. H data were collected between 1.82-10 K (figure III.34b), followed by the creation of the dM/dH plot exhibited in figure III.34c. For **11**, T_N = 6.5 K and H_C(0 K) = 8300 Oe are obtained from the (T, H) phase diagram (figure III.34d). Therefore an inter-chain antiferromagnetic interaction zJ_{perp}/k_B = -0.216 K is calculated equalizing the Zeeman and exchange energies: $g\mu_B H_C(0\text{ K})S_T = 2|zJ_{perp}|S_T^2$.

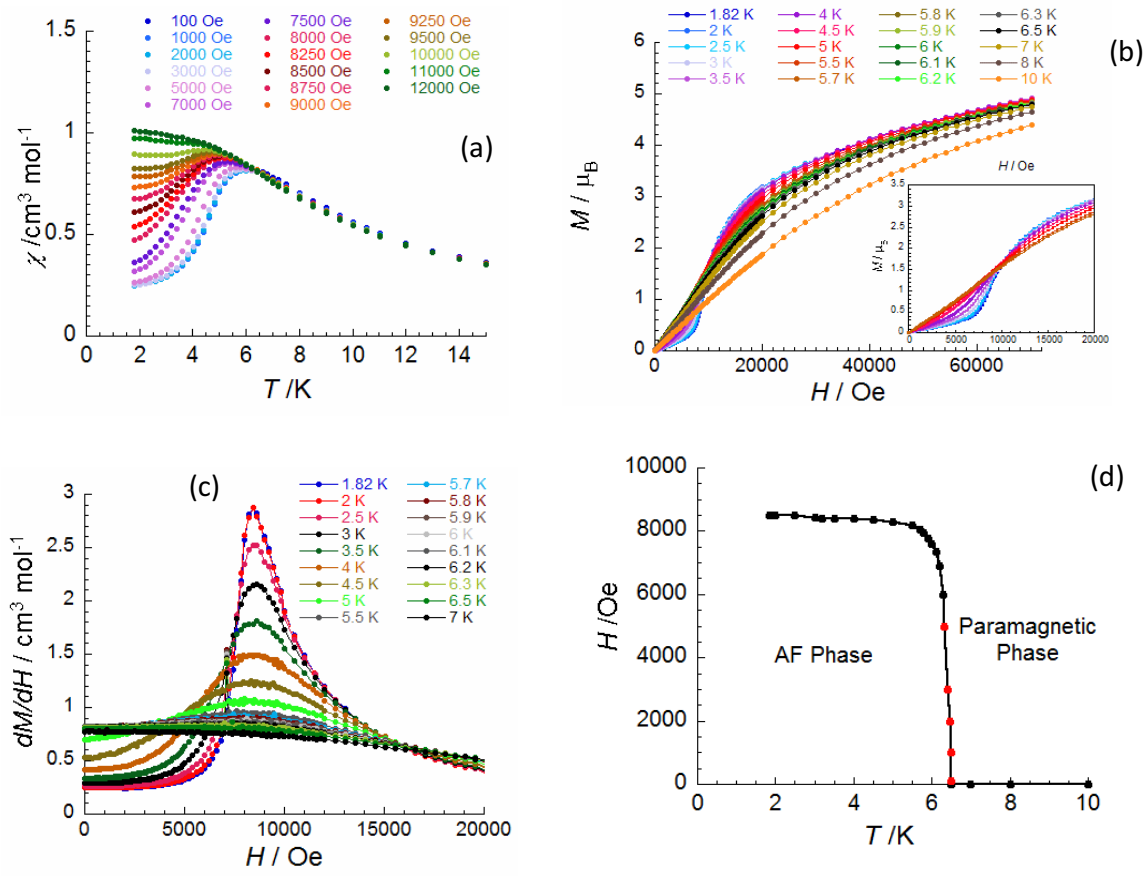

Figure III.34. Low temperature magnetic properties for **11**. (a) Plot of $\chi(T)$ at different applied *dc* fields. (b) M vs. H plots at multiple temperatures; Inset: Expanded view of the data at low field up to 6 K. (c) Plot of dM/dH (= χ) as a function of field at multiple temperatures. (d) Magnetic phase diagram (T, H) constructed from variable the maxima of plot (a) and (c) giving T_N =6.5 K and H_C(0 K) = 8300 Oe.

For **12** the $\chi(T)$ data were collected between 100 and 10000 Oe and the field dependent maxima are found around 6 K below 7500 Oe; at lower temperature it reaches saturation (figure III.35a). M vs. H data were collected between 1.82-15 K (figure III.35b) followed by the creation of the dM/dH plot (figure III.35c). The (T, H) phase diagram of **12** (figure III.35d) extracts the parameters T_N = 5.8 K and H_C(0 K) = 6200 Oe. Using this H_C(0 K), the inter-chain antiferromagnetic interaction is found about zJ_{perp}/k_B = -0.18 K, by equalizing the Zeeman and exchange energies with the relation: $g\mu_B H_C(0\ K)S_T = 2|zJ_{perp}|S_T^2$.

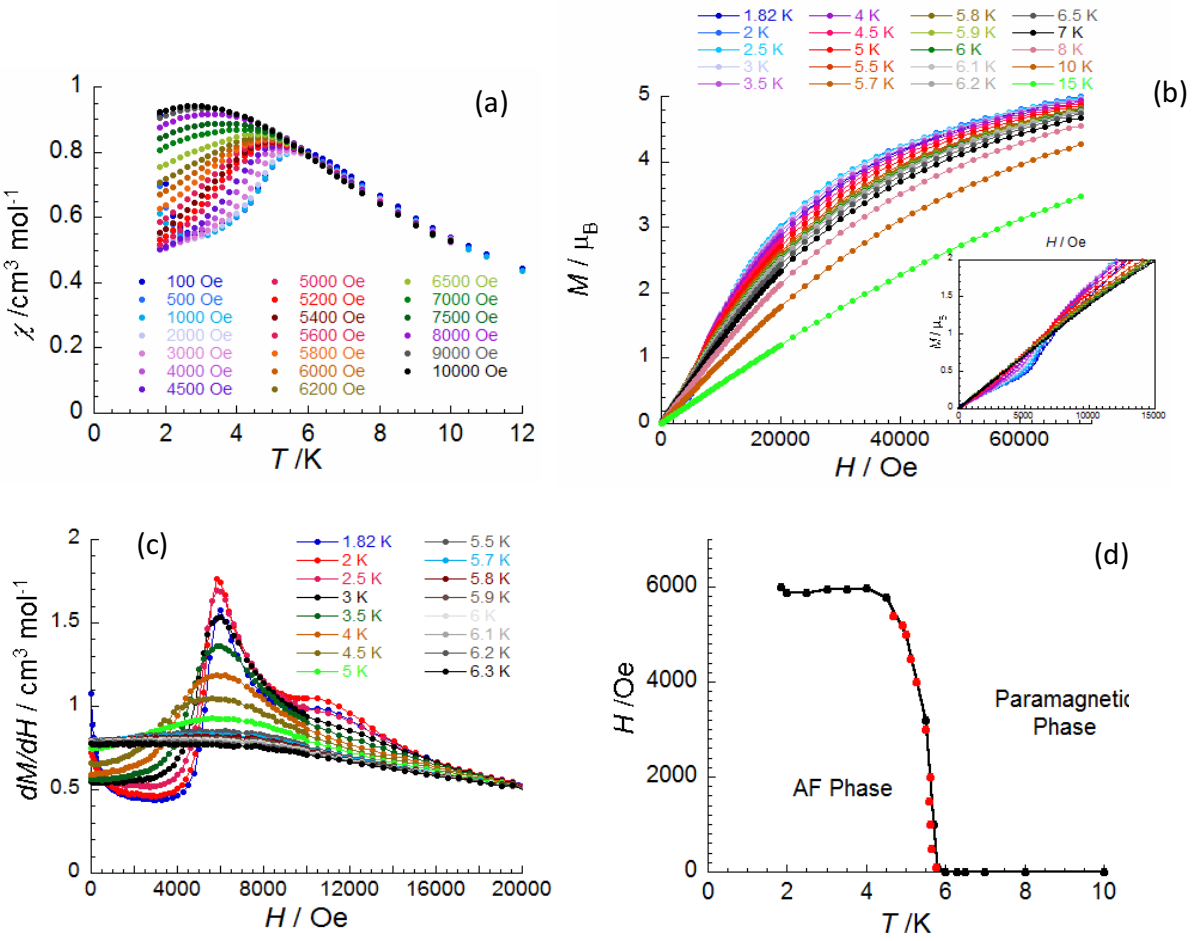

Figure III.35. Low temperature magnetic properties for **12**. (a) Plot of $\chi(T)$ at different applied *dc* fields. (b) M vs. H plots at multiple temperatures; Inset: Expanded view of the data at low field up to 7 K. (c) Plot of dM/dH (= χ) as a function of field at multiple temperatures. (d) Magnetic phase diagram (T, H) constructed from the maxima of plot (a) and (c) giving T_N = 5.8 K and H_C(0 K) = 6200 Oe.

On the other hand, in order to compare the theoretical T_N of **11** and **12** with the experimental one, we have applied an mean field approach at very low field $\chi(T)$ considering the inter-chain antiferromagnetic interactions (J_{perp}). This J_{perp} is determined from the H_C (0 K) of the corresponding phase diagrams of **11** and **12** (figure III.34d and figure III.35d). As **11** and **12** are not one dimensional on a magnetic point of view, we may consider these systems as three dimensional arrangements of spin S_T = 5/2 (schematically shown in figure III.36) where each unit has two equivalent neighbors in each of the three directions. Along the crystallographic chain direction of the compound, the S_T = 5/2 unit experiences a ferromagnetic interaction (J') with two neighbors and in the other directions, it experiences an antiferromagnetic interaction (J_{perp}) with the other four neighbors. Now at zero field, if the system gains the thermal energy equivalent to the H_C of the system, it will overcome the all J_{perp} interactions to form a paramagnetic state. The zJ_{perp}/k_B for **11** and **12** have been already calculated as -0.216 K and -0.18 K respectively. If the J_F and J_{AF} are the total ferromagnetic and antiferromagnetic interactions between two successive S_T =5/2 units then we can define $J_F = 2z|J'/k_B|S_T^2$ and $J_{AF} = 2z|J_{perp}/k_B|S_T^2$ respectively where the z is the number of neighbor for each S_T = 5/2 moiety.

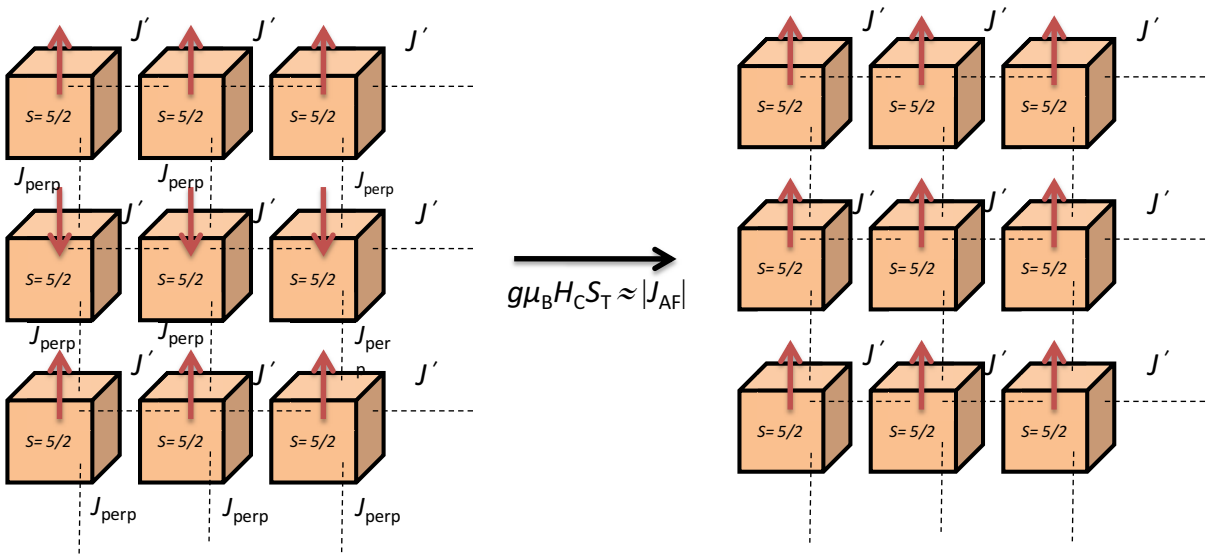

Figure III.36. The schematic view of the three dimensional arrangement of S_T = 5/2 units in the chain **11** and **12** displaying only one plane (only a two dimensional view is given for better visibility).

When we perform the mean field approximation over the magnetic susceptibility in a system having two different kinds of magnetic exchange interactions (J_F and J_{AF} in the present case), according to the Curie-Weiss law, the Weiss constant, θ of the system is the difference between the two types of exchange interaction i.e., $\theta = J_F - |J_{AF}|$.[12] So, in order to investigate θ of **11** and **12**, the very low *dc* field $1/\chi$ (at $H << H_C$) is plotted as a function of T (figure III.37a and III.37b) followed by the linear fit of the experimental data at higher temperature i.e., in the paramagnetic region. As these plots have been constructed at low applied *dc* magnetic field, the influence of the field over the amplitude of magnetic exchange is ignored. From the fit, θ is found to be about 1.0 K and 1.3 K for **11** and **12** respectively. Considering that J_{AF} = 2.7 and 2 K respectively for chain **11** and **12** (zJ_{perp}/k_B = -0.216 K and -0.18 K respectively), the J_F becomes about 3.7 K for **11** and 3.3 K for **12**. From these J_F/k_B values we can extract also the respective J'/k_B = + 0.15 K and + 0.13 K for **11** and **12**. Although the one dimensional magnetic correlation in **10** is higher than in **11** and **12**, we have tried to apply the mean field approach to this system as well. Therefore $1/\chi$ at 1000 Oe plotted against T (see figure III.37c) gives θ = 3 K leading to J_F = 5.9 K and J'/k_B = + 0.24 K with the value J_{AF} = 2.9 K (zJ_{perp}/k_B = -0.232 K).

Moreover, in such systems where two types of magnetic exchange interactions are present (J_F and J_{AF} in the presently discussed systems), staggered magnetization is generated in the system, which implies the Néel temperature of such systems is the numerical sum of the two kinds of interaction, i.e., $T_N = J_F + |J_{AF}|$. We have already determined the magnitude of J_F, thus with this relation T_N (mean field) of **10**, **11** and **12** were calculated as 8.8, 6.4 and 5.3 K, which are quite comparable with the T_N found in the respective phase diagrams (figure III.33d, III.34d and III.35d). In case of **10** the J_F/J_{AF} ratio is higher than the other two chains which indicates an increase of the 1D character of the system in comparison to **11** and **12**. This ratio is not enough high to show significant disagreement with the

mean field treatment. In the chain **8** and **9,** this mean field approach is not performed due to the presence of a much stronger one dimensional character of the magnetic properties.

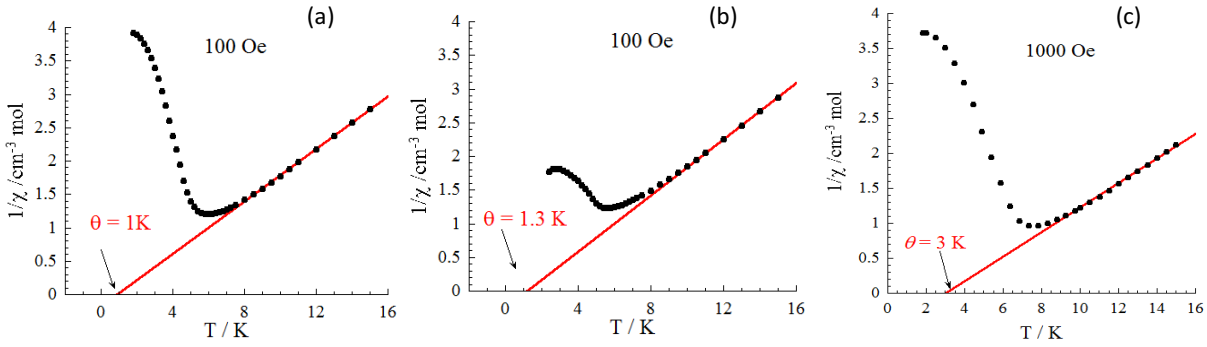

Figure III.37. The plot of the temperature dependent $1/\chi$ at weak applied *dc* field and the linear fit of the high temperature paramagnetic region (solid red line) to find out the θ; (a) for chain **11** at 100 Oe, (b) for chain **12** at 100 Oe and (c) for chain **10** at 1000 Oe.

The static magnetic properties of **8-12** establish that, similar to the crystal structures, **8** and **9** possess comparable magnetic properties such as greater Ising –like one dimensional magnetic correlation, magnetic hysteresis, a canted antiferromagnetic phase at low temperatures with a lower magnitude of inter-chain coupling. On the other hand, **11** and **12** are comparable with more three dimensional magnetic correlations and a metamagnet type behavior with a higher amplitude of the inter-chain antiferromagnetic interactions. Compound **10** falls between these two categories with a modulated 1D character. Indeed, the close packing of the chains in the crystal structure without solvent molecules results in the highest interchain interaction, but the intrachain ferromagnetic interaction is almost twice as in **11** and **12**.

***Dynamic magnetic properties**:*

To probe the dynamics of **8-12** we have further performed alternating (*ac*) current magnetization measurements between 1.8-15 K and 1-1500 Hz. Compounds **8** and **9** exhibited significant slow dynamics of the magnetization observed by *ac* magnetic measurements whereas in **10-12** the slow dynamics of the magnetization is detected, but much more difficult to study in these antiferromagnetic systems with strong interchain interactions.

In the compound **8**, under zero *dc* field, the imaginary component χ'' exhibits weak signals around 6.2 K (figure III.38), close to the previously found Néel temperature (6.2 K) as expected at the paramagnetic/canted AF phase transition. Below 4 K a strongly frequency dependent relaxation mode of **8** is observed along with the real part of the *ac* susceptibility, χ' (insets of figure III.38). The relaxation time (τ) of **8** is deduced as a function of the temperature ($\tau(T) = 1/(2\pi\nu)$) from the maximum of $\chi''(\nu)$ curves at different temperatures. From the semi log plot of τ vs. $1/T$ (figure III.40,

right) in 0 Oe the associated relaxation time of this latter mode was deduced below 3.2 K and was found to follow the Arrhenius law: $\tau(T) = \tau_0 \exp(\Delta_\tau/k_BT)$, with Δ_τ/k_B = 36.4 K and $\tau_0 = 9\times10\text{-}^{10}$ s (where τ_0 is the pre-exponential constant and Δ_τ is the energy needed to reverse the magnetization).

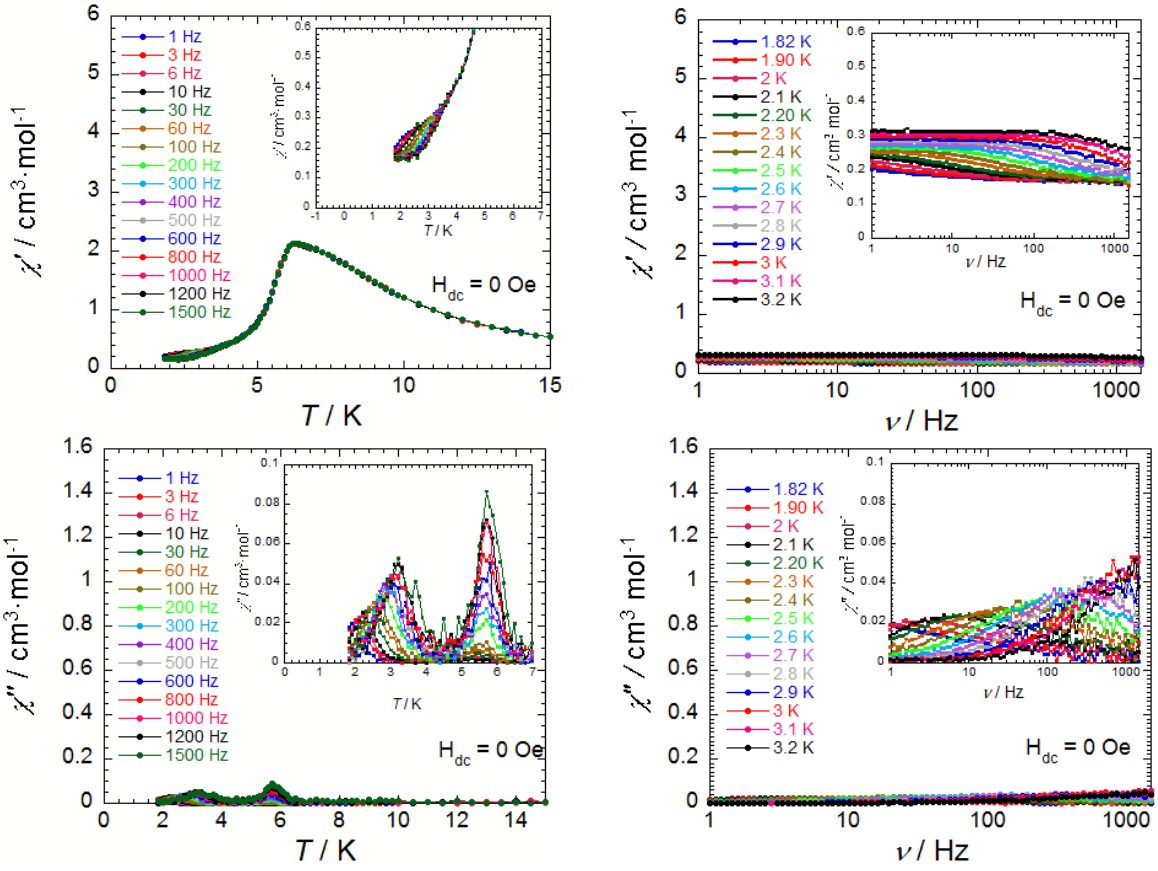

Figure III.38. Temperature and frequency dependence of the χ' (in-phase) and χ''(out-of-phase) part of the *ac* magnetic susceptibility of **8** at H_{dc} = 0 Oe.

Therefore, we carried out measurements to clarify the frequency dependence of χ' and χ''at multiple applied *dc* fields between 0-4000 Oe at 3 K (figure III.39). The frequencies corresponding to the maximum values of χ'' in each applied *dc* field are plotted and show a minimum at 2400 Oe (figure III.39). As already reported in 3D AF order phases of SCMs,[5,9] the application of a *dc*-field slow down the observed dynamics (e.g. at 3 K, from 767 Hz at 0 Oe to 61 Hz at 2400 Oe). This variation confirms that **8** relaxes most slowly at 2400 Oe (at 3 K), which implies the system requires a critical field around 2400 Oe to overcome its own intrinsic internal field. Expectedly, this critical field is consistent with the critical field we identified from the phase diagram at 3 K (near 2500 Oe), near the canted AF/paramagnetic transition line.

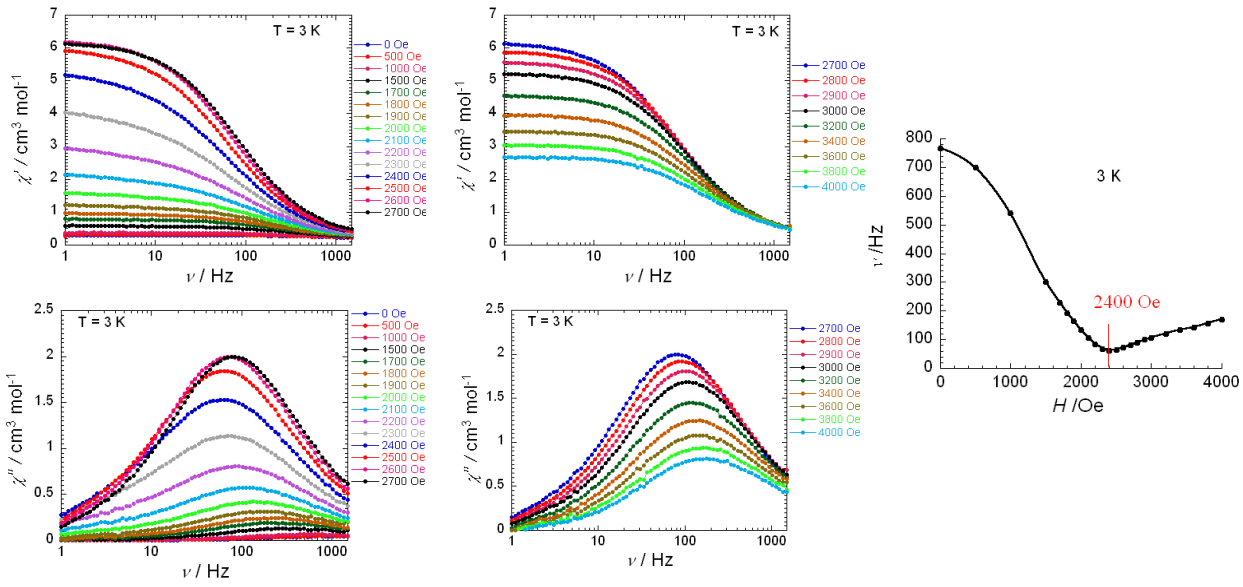

Figure III.39. (left) Frequency dependence of the χ' and χ'' part of the *ac* magnetic susceptibility of **8** at different values of applied *dc* field at 3 K. (right) ν = f(H) for maximum *ac* magnetic susceptibility at 3 K , the minima at 2400 Oe corresponds to the critical field of the system to overcome the inter-chain antiferromagnetic order.

Thereafter we continued the *ac* magnetic susceptibility measurements of **8** as a function of temperature and frequency in an applied *dc* field of 2400 Oe, which demonstrate a significant frequency dependence of the magnetization below 5 K with a decrease of χ' and the appearance of χ'' signals (figure III.40, left). This phenomenon is directly correlated with the blocking of the magnetization when the thermal energy is not sufficient to allow the magnetization to follow the *ac* field at a given frequency, inducing a freezing of magnetization below the so called blocking temperature (T_B). The relaxation time (τ) of **8** is deduced as a function of T ($\tau(T) = 1/(2\pi\nu)$) from the maximum of $\chi''(\nu)$ curves at different temperatures(figure III.40). In **8**, $\tau(T)$ follows two thermally activated regimes above and below 2.6 K with $\Delta_{\tau 1}/k_B$ = 48.6 K (τ_0 = 2.3×10-10 s) and $\Delta_{\tau 2}/k_B$ = 36.6 K (τ_0 = 2.2×10-^{8} s) respectively. Remarkably, $\Delta_{\tau 2}$ energy barrier remains almost equal in Δ_ξ determined in the absence of an applied field (red line in figure III.40, right) which implies that the applied magnetic field has no effect on the finite regime size. As expected for a SCM, the difference between these two energy barriers, 12 K, agrees well with the experimental Δ_ξ (11.6 K) and thus the intrachain interactions. In the SCM, this spin reversal energy (Δ_τ) is the sum of correlation energy (Δ_ξ) and anisotropy energy (Δ_A) where $\Delta_{\tau 1} = \Delta_\xi + \Delta_A$ for the finite regime and $\Delta_{\tau 2} = 2\Delta_\xi + \Delta_A$ for the infinite regime.[4a] All these relations give us an anisotropy energy (Δ_A) of about 25 K; therefore, the anisotropy parameter D/k_B (defined by $H = DS_{T,z}^2$) of the system is about -4.1 K ($\Delta_A = (S_T^2\text{-}1/4)|D|$ for half integer spin) considering the S_T = 5/2 spin ground state for the Mn^{III}-Re^{IV}-Mn^{III} unit. Based on the crossover temperature, T^* = 2.6 K, and Δ_ξ/k_B = 11.6 K, the average number of chain units ($n \approx 2\xi \approx exp(\Delta_\xi/k_B T^*)$) is estimated at 87 in this compound ($L \approx$ 120 nm, similar to related SCMs). [7,8]

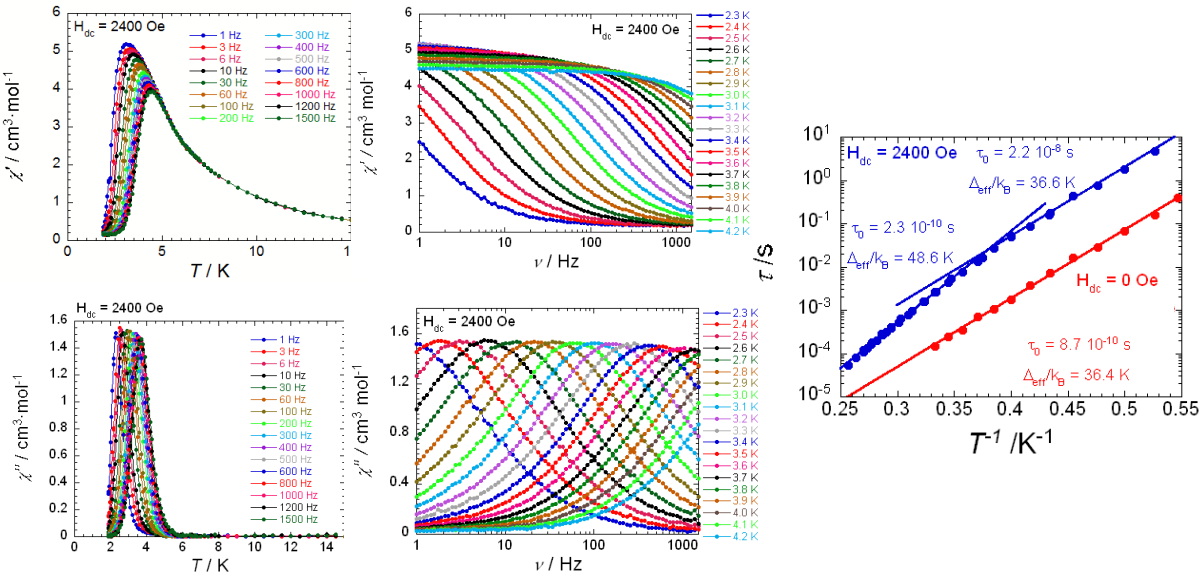

Figure III.40. (left) Temperature and frequency dependence of χ' (in-phase) and χ'' (out-of-phase) part of the *ac* magnetic susceptibility of **8** at H_{dc} = 2400 Oe, (right) Thermal variation of τ of **8**, solid lines are the best fits to the Arrhenius laws $\tau(T) = \tau_0 \exp(\Delta_\tau/k_B T)$.

For **9**, χ' and χ'' were measured at H_{dc} = 0 Oe (figure III.41), and they showed a very significantly frequency dependent peak near 4.5 K, that is, at the Néel temperature of the system supporting the paramagnetic/canted antiferromagnetic phase transition. It is worth noting that no lower temperature ac signal has been detected. Therefore, the frequency dependence of χ' and $\chi''$was evaluated at multiple applied *dc* fields between 0-2600 Oe at 2 K (figure III.42). The frequencies corresponding to the maximum values of χ'' in each applied *dc* field are plotted, giving a minimum at 1700 Oe (figure III.42, right). This implies that **9** requires a field around 1700 Oe (at 2 K) to overcome its own intrinsic internal field and therefore relaxes slowly at 2 K in presence of a 1700 Oe field. Expectedly, this field is comparable to the H_C (= 1700 Oe) determined in the phase diagram of **9** at 2 K. Therefore the dynamics of the system was investigated in the presence of an applied *dc* field of 1700 Oe and χ' and χ'' exhibited a strong temperature and frequency dependence below 4 K, with a decrease of χ' and the increase of χ'' (see figure III.43). Such slow dynamics of the system implies SCM like properties for **9** as observed in **8** and in related ordered systems.[5]

Furthermore the relaxation time (τ) of **9** was deduced as a function of T ($\tau(T) = 1/(2\pi\nu)$) from the maximum of χ'' (ν) curves at different temperatures. The semi log plot of τ vs. $1/T$ (figure III.44, right) at a 1700 Oe *dc* field clearly manifests the thermally activated behavior of **9** through the linear fit of the experimental data, giving an energy barrier Δ_τ/k_B = 32.4 K along with $\tau_0 = 3.4 \times 10^{-10}$ s. Considering Δ_τ as the energy of the finite size regime the Δ_A/k_B of **9** becomes 24.8 K with Δ_ξ/k_B = 7.6 K and the anisotropy of the system $D/k_B \approx$ -4.1 K, comparable in magnitude with the values found for **8** and related systems.[4,5,8,9]

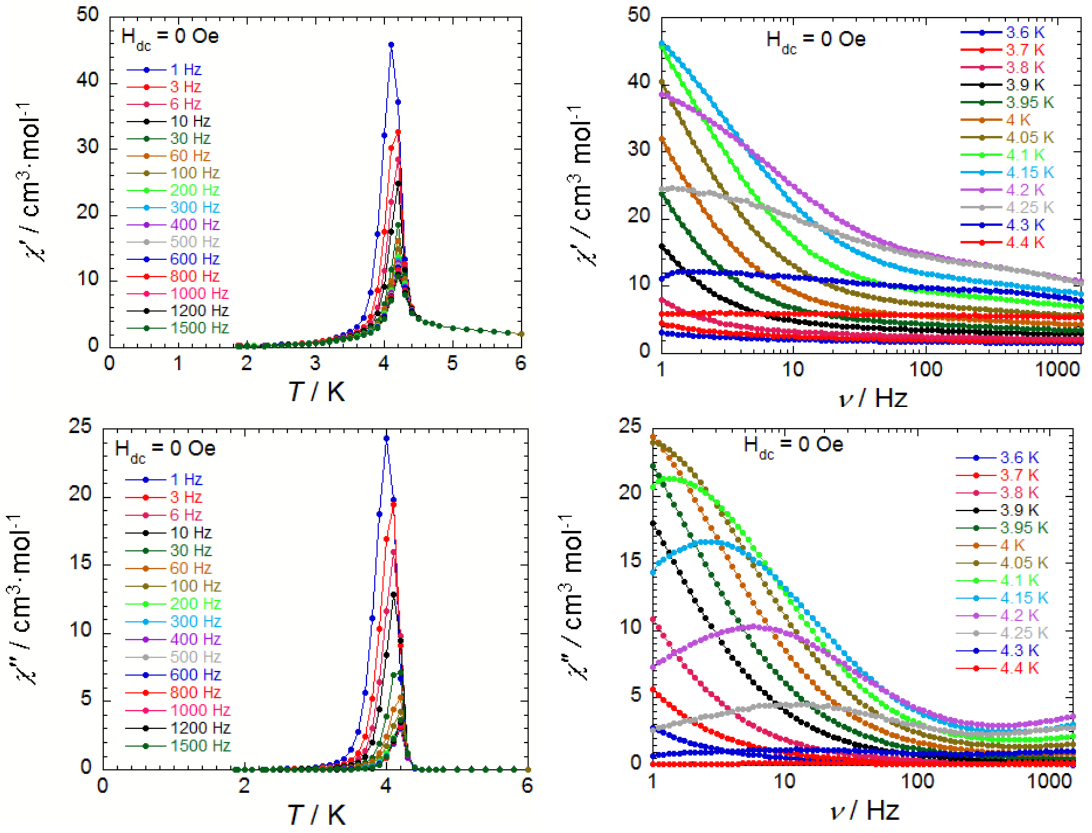

Figure III.42. Temperature and frequency dependence of χ' (in-phase) and χ''(out-of-phase) part of the *ac* magnetic susceptibility of chain **9** at H_{dc} = 0 Oe.

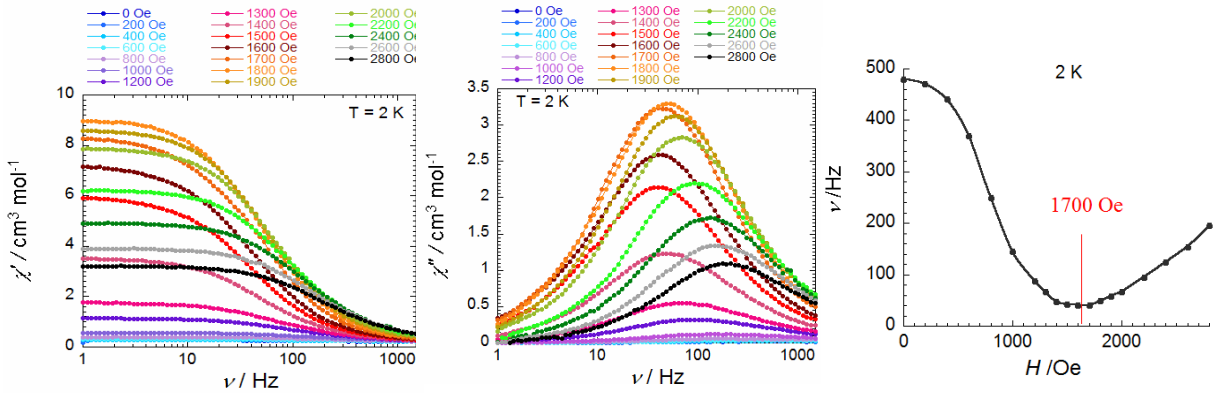

Figure III.43. (left) Frequency dependence of χ' and χ'' part of the *ac* magnetic susceptibility of **9** at different values of applied *dc* field at 2 K; (right) ν = f(H) for maximum *ac* magnetic susceptibility at 2 K, the minima at 1700 Oe corresponds to the field of the system necessary to overcome the inter-chain antiferromagnetic interaction.

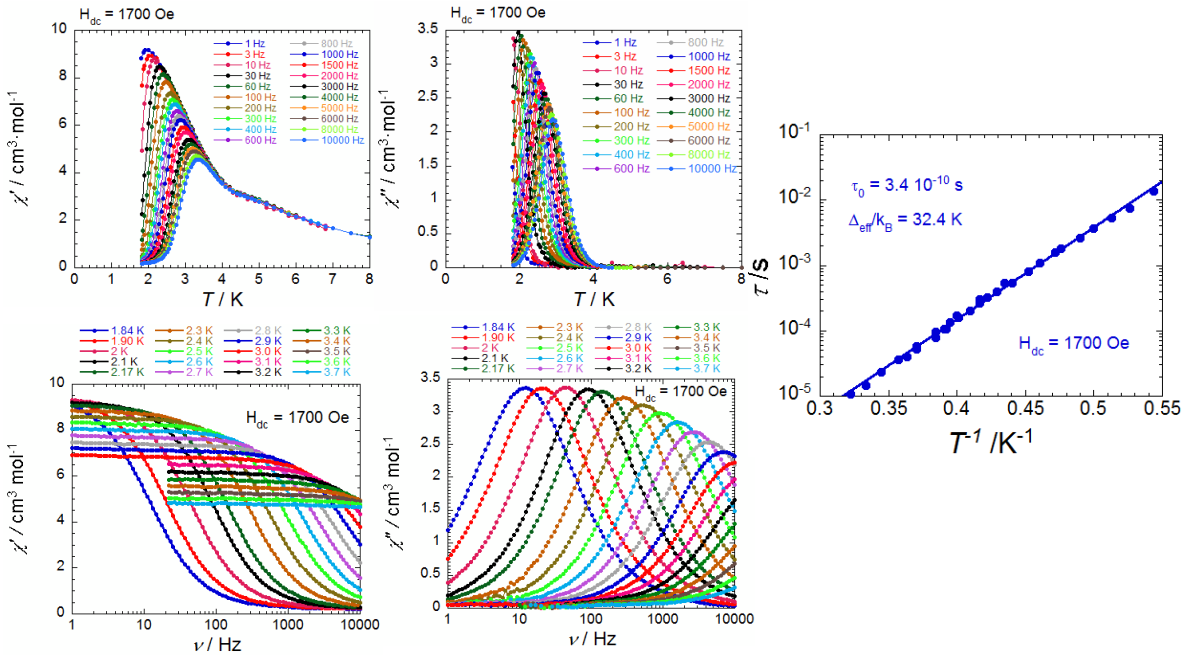

Figure III.44. (left) Temperature and frequency dependence of χ' (in-phase) and χ'' (out-of-phase) part of the *ac* magnetic susceptibility of **9** at H_{dc} = 1700 Oe, (right) Thermal variation of τ of **9** described by an Arrhenius law $\tau(T) = \tau_0 \exp(\Delta_\tau/k_B T)$ (solid line).

In the case of **12**, χ' and χ'' were measured at H_{dc} = 0 Oe (figure III.45) and displayed a very weak temperature and frequency dependence below 2.5 K.

$\chi'(\nu)$ and $\chi''(\nu)$ were measured at multiple applied *dc* magnetic fields at 1.85 K (figure III.46, left). The variation of ν_{max} (maxima of the $\chi''(\nu)$ curves at 1.85 K in different fields) with the applied *dc* field shows the slowest rate of magnetic relaxation of **12** at 5800 Oe (figure III.46, right). Therefore this is the field necessary to overcome the antiferromagnetic order of the system, which is quite comparable to the critical field identified from its phase diagram. Thereafter χ' and χ'' of **12** were measured both as a function of T and ν at different frequencies and temperatures, respectively, in presence of H_{dc} = 5800 Oe (figure III.47, left). These measurements revealed the notable appearance of χ'', which is evidence of slow relaxation of the magnetization at H_{dc} = 5800 Oe. The thermal behavior of τ of **12** at 5800 Oe with the help of the Arrhénius law: $\tau(T) = \tau_0 \exp(\Delta_\tau/k_B T)$, determines Δ_τ/k_B = 24 K and $\tau_0 = 1 \times 10^{-9}$ s (figure III.47, right).

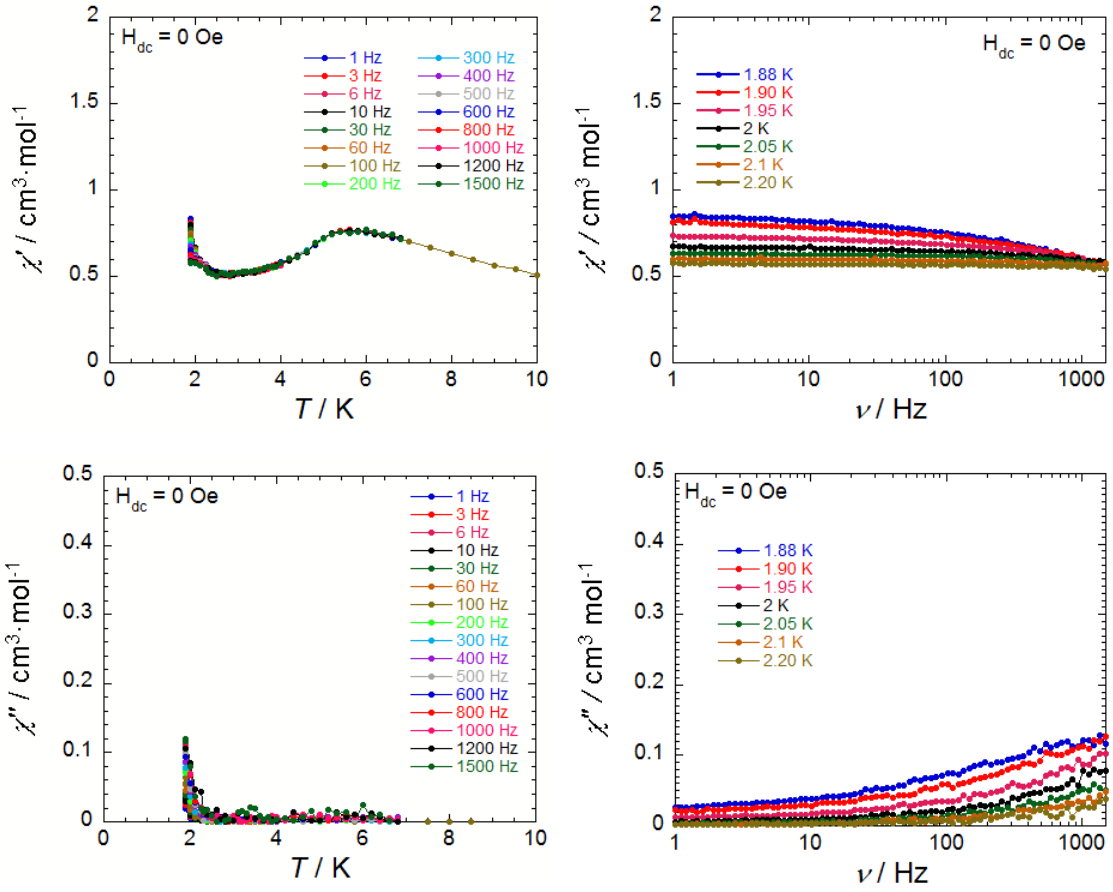

Figure III.45. Temperature and frequency dependence of the χ' (in-phase) and χ''(out-of-phase) part of the *ac* magnetic susceptibility of **12** at H_{dc} = 0 Oe.

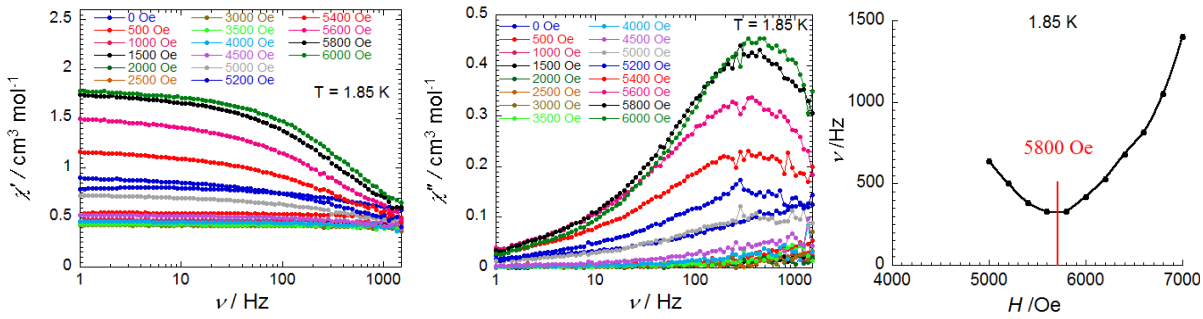

Figure III.46. (left) Frequency dependence of the χ' and χ'' part of the *ac* magnetic susceptibility of **12** at different values of applied *dc* field at 1.85 K; (right) ν = f(H) for maximum *ac* magnetic susceptibility at 1.85 K, the minima at 5800 Oe corresponds to the field of the system to overcome the inter-chain antiferromagnetic order.

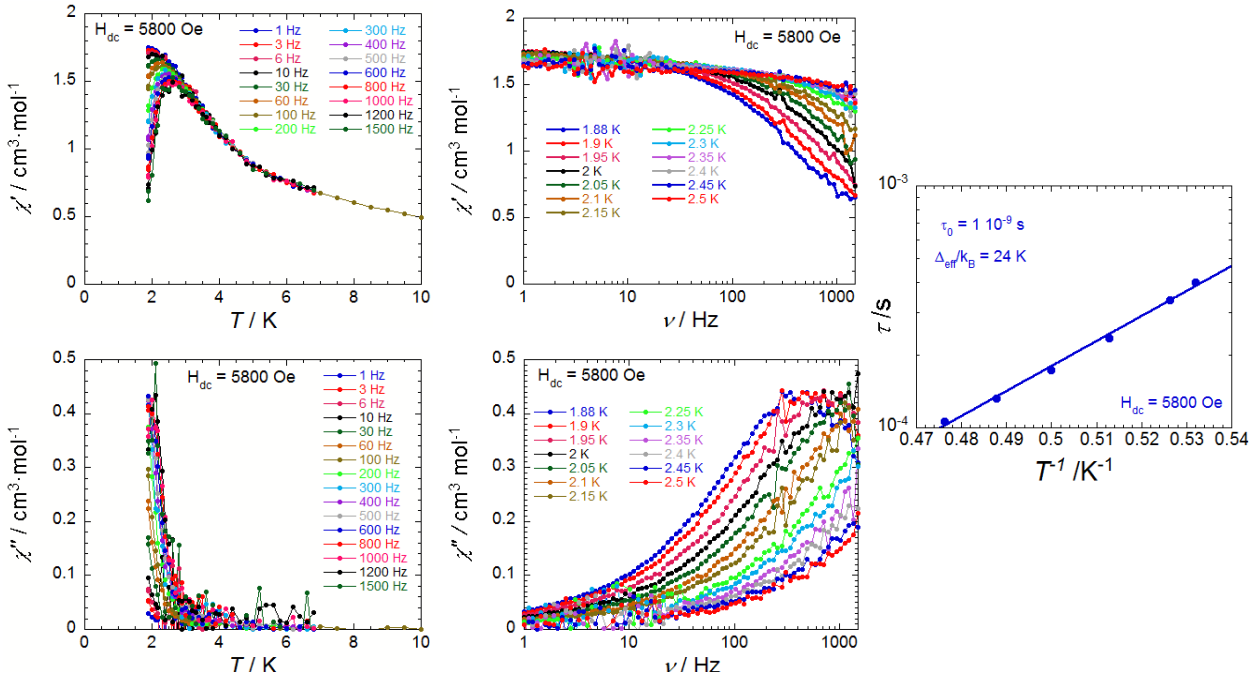

Figure III.47. (left) Temperature and frequency dependence of the χ' (in-phase) and χ'' (out-of-phase) part of the *ac* magnetic susceptibility of **12** at H_{dc} = 5800 Oe, (right) Thermal variation of τ of **12,** solid lines are the best fits to the Arrhenius law $\tau(T) = \tau_0 \exp(\Delta_\tau/k_B T)$.

χ' and χ'' signals of **10** and **11** have a comparatively weak response to the *ac* magnetic field. In the case of **10** at H_{dc} = 0 Oe the susceptibility has no significant temperature dependence at an *ac* frequency of 100 Hz (figure III.48a and III.48b). The field dependence of χ' and χ'' display a transition near 9200 Oe (figure III.48c and III.48d) at 1.9 K which is comparable to the critical field found from the phase diagram of **10**. Therefore the temperature dependence of χ' and χ'' of **10** was measured at an applied *dc* field of 9200 Oe at multiple frequencies (figure III.48e and III.48f), demonstrating the appearance of a weak and noisy χ'' signal. Moreover the frequency dependence of $\chi''(T)$ (figure III.48f) does not exhibit a maximum above 1.8 K (due to the limitations in the experiment, we are not able to measure below 1.8 K). The dynamic behavior of **10** in an *ac* magnetic field implies the lack of slow magnetic relaxation properties above 1.8 K due to strong interchain interactions (compared to **8**, **9** and **12**).

In the absence of an applied magnetic field, $\chi'(T)$ and $\chi''(T)$ signals of **11** did not show the presence of slow dynamics at 10 Hz or 1000 Hz (figure III.49a and III.49b). Therefore, in order to determine the characteristic field of the system, the frequency dependence of the susceptibilities were determined at different applied *dc* magnetic fields at 1.8 K (figure III.49c and III.49d), which exhibited the slowest relaxation of magnetization at 8500 Oe. This field is consistent with the H_C (8300 Oe) found in the phase diagram made from the early *dc* magnetic measurements. With the aim of further investigating the dynamic magnetic properties of **11** $\chi'(\nu)$ and $\chi''(\nu)$ values of the system were measured at different temperatures with an applied *dc* magnetic field of 8500 Oe (figure III.49e

and III.49f). The nature of the frequency dependence of the susceptibilities is evidence of a slow relaxation property present in **11** at 8500 Oe, but the experimental data are not enough (due to the limitation of experimental frequency range we cannot go above 1500 Hz) to determine the relaxation time. The lack of magnetic relaxation phenomena above in **10** and **11** is likely due to stronger antiferromagnetic interactions.

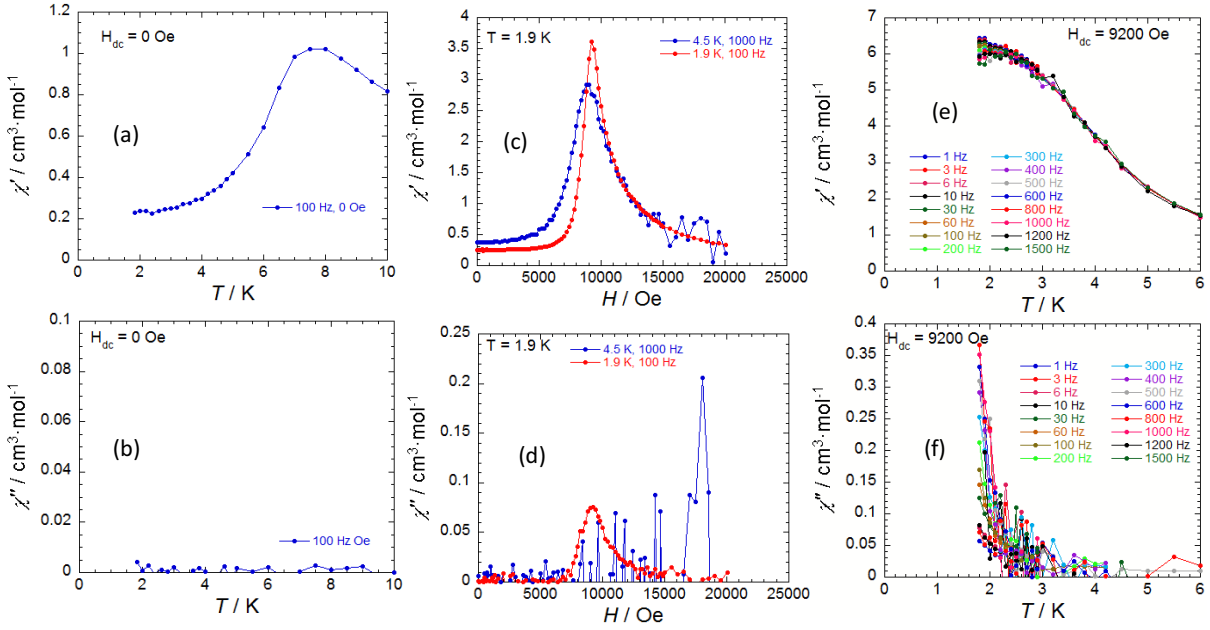

Figure III.48. The different types of *ac* magnetic measurements of **10**; (a) $\chi'(T)$ at 100 Hz in absence of *dc* magnetic field; (b) $\chi''(T)$ at 100 Hz in absence of *dc* magnetic field; (c) $\chi'(H)$ at 1.9 K and 100 Hz (plot in red); (d) $\chi''(H)$ at 1.9 K (plot in red); (e) $\chi'(T)$ at different frequencies at the H_{dc} = 9200 Oe; (f) $\chi''(T)$ at different frequencies at the H_{dc} = 9200 Oe.

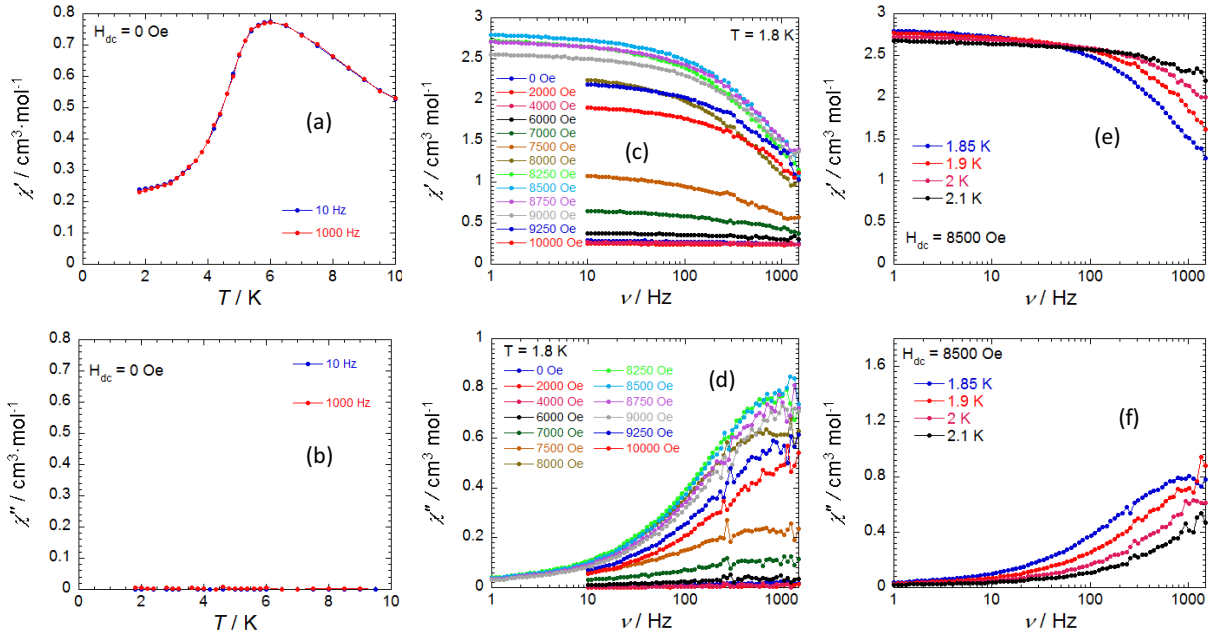

Figure III.49. The different types of *ac* magnetic measurements for **11**; (a) $\chi'(T)$ at 10 Hz and 1000 Hz in the absence of a *dc* magnetic field ; (b) $\chi''(T)$ at 10 Hz and 1000 Hz in the absence of a *dc* magnetic field; (c) $\chi'(\nu)$ at 1.8 K in different *dc* fields; (d) $\chi'(\nu)$ at 1.8 K in different *dc* fields; (e) $\chi'(\nu)$ at different temperatures at H_{dc} = 8500 Oe; (f) $\chi''(\nu)$ at different temperatures at H_{dc} = 8500 Oe.

III.4. Conclusions and perspectives

Throughout this chapter, the reader can find a step wise approach towards one dimensional systems, starting from the formation of the co-crystallized complexes, and their study from both chemical and magnetic points of view. Although the co-crystallized compounds did not display very interesting magnetic behavior, their susceptibilities and magnetization demonstrates the significant impact of intermolecular antiferromagnetic interactions on their properties. Only compound **2** displayed a less presence of intermolecular antiferromagnetic interactions, as the Mn^{III} and Re^{IV} were quite far from each other in the crystal structure. In compounds **1** and **3** different types of intermolecular antiferromagnetic interactions lead to the decrease of the magnetic susceptibilities with decreasing temperature.

The trinuclear Mn^{III}-Re^{IV}-Mn^{III} systems **4-6** give the properties of the $S_T = 5/2$ repeating units of the hexanuclear compound **7** and the one dimensional compounds, **8-12**, from both a structural and magnetic point of view. The hexanuclear compound **7** is a dimer of the trinuclear unit, whereas the chain compounds **8-12** consist of the infinite repetition of these Mn^{III}-Re^{IV}-Mn^{III} units in one dimension. These trinuclear Mn^{III}-Re^{IV}-Mn^{III} systems **4-6** helped us to understand and estimate the Re^{IV}-Mn^{III} antiferromagnetic interaction from the fit of the experimental susceptibility data with the proper model (Eq. III.1 and Eq. III.2). We have observed that the Re^{IV}-Mn^{III} antiferromagnetic interactions (from -1.9 to -5.4 K) are stronger than the Mn^{III}-Mn^{III} ferromagnetic interactions (< + 1 K) in the hexanuclear species **7** and the chain compounds **8-12**. Therefore we have extensively used the trinuclear Mn^{III}-Re^{IV}-Mn^{III} model (Eq. III.1 and Eq. III.2) to probe the experimental magnetic susceptibility data of compound **7-12**, and the weaker Mn^{III}-Mn^{III} interactions are estimated with the mean field approximation applied over the trinuclear Mn^{III}-Re^{IV}-Mn^{III} model.

Compounds **8** and **9** exhibited significant slow magnetic relaxation under the application of *dc* fields of 2400 Oe and 1700 Oe respectively, which allow the systems to overcome the inter-chain antiferromagnetic interactions (as these critical fields decouple the antiferromagnetically interacted chains). It demonstrates that the individual one dimensional coordination network in **8** and **9** possesses Single Chain Magnet properties as the origin of their magnet-like behaviors. Actually in all the coordinated Re^{IV}-Mn^{III} systems, we have observed the presence of intermolecular (for compounds **4**-**7**) or inter-chain (for compounds **8-12**) antiferromagnetic interactions followed by the presence of a paramagnetic to an antiferromagnetic (or canted antiferromagnetic) phase transition.

From the magnetic properties of all these Re^{IV}-Mn^{III} compounds, we can conclude that the antiferromagnetic or canted antiferromagnetic order of these systems can only be avoided if we can separate the molecules / chains far from each other in the crystal structure, in order to minimize the intermolecular or inter-chain antiferromagnetic coupling. With this goal in mind, we have varied the

reaction solvent and the Mn^{III}-Schiff base ligand substitutents. We tried to crystallize the compounds using larger organic solvents, or changing both the nature and position of the substituent on the Schiff base ligands. But as the reaction between the Re^{IV} and the Mn^{III} molecular precursors were found to be rapid, the use of bigger solvent molecules like isopropanol, benzonitile, nitromethane etc. results in the precipitation of the compound without being able to obtain single crystals. Another problem with using the bigger organic solvent molecules is the limitation of solubility of both molecular precursors. Moreover, although we have tried to change the substituent on the Schiff-base ligands, we could not try all the possibilities during the time limits of this research work. In any case, these efforts led us to obtain four more Re^{IV}-Mn^{III} systems (compounds **23**-**27**) that are described in the Annex of this manuscript. These compounds consist of three one dimensional systems with the molecular formula $[Mn^{III}(5\text{-Me-saltmen})]_2[Re^{IV}Cl_4(CN)_2]\cdot 3MeNO_2$ and $[Mn^{III}(5\text{-X-saltmen})]_2[Re^{IV}Cl_4(CN)_2]$ (X = Cl and Br), one trinuclear system $[Mn^{III}(4\text{-MeO-saltmen})(H_2O)]_2[Re^{IV}Cl_4(CN)_2]$ and one non-coordinated system $[\{Mn^{III}(5\text{-}^{t}Bu\text{-saltmen})(H_2O)\}_2]_2[Re^{IV}Cl_4(CN)_2](ClO_4)_2\cdot 4H_2O$. The preliminary structural and magnetic characterization of those compounds has been only partially performed as shown in the Annex at the section I.

III.5. References

[1] (a) H. Miyasaka, R. Clérac, W. Wernsdorfer, L. Lecren, C. Bonhomme, K. Sugiura, M. Yamashita, *Angew. Chem., Int. Ed.* **2004**, 43, 2801. (b) H. Miyasaka, R. Clérac, T. Ishii, H. Chang, S. Kitagawa, M. Yamashita, *J. Chem. Soc.*, *Dalton Trans.*, **2002**, 1528.

[2] T. D. Harris, M. V. Bennett, R. Clérac, J. R. Long, *J. Am. Chem. Soc*., **2010**, 132, 3980.

[3] (a) J. H. Van Vleck, *The Theory of Electric and Magnetic Susceptibilities,* Oxford university Press, Oxford, **1965**; (b) C. J. O'Connor, *Prog . Inorg. Chem*., **1982**, 29, 203. (c) B. E. Myers, L. Berger, S. Friedberg, *J. Appl. Phys.*, **1969**, 40, 1149. (d) R. L. Carlin. *In Magnetochemistry*. Springer-Verlag, New York, **1986**.

[4] (a) C. Coulon, H. Miyasaka, R. Clérac, *Struct. Bond.*, **2006**, 122, 163-206. (b) R. J. Glauber, *J. Math. Phys*., **1963**, 4, 294.

[5] C. Coulon, R. Clérac, W. Wernsdorfer, T. Colin, H. Miyasaka, *Phys. Rev. Lett.* **2009,** 102, 167204(1-4).

[6] R. Clérac, H. Miyasaka, M. Yamashita, C. Coulon, *J. Am. Chem.Soc.*, **2002**, 124, 12837.

[7] C. Coulon, R. Clérac, L. Lecren, W. Wernsdorfer, H. Miyasaka, *Phys. Rev. B,* **2004**, 69, 132408.

[8] M. Ferbinteanu, H. Miyasaka, W. Wernsdorfer, K. Nakata, K. Sugiura, M. Yamashita, C. Coulon, R. Clérac, *J. Am. Chem. Soc.*, **2005**, 127, 3090.

[9] H. Miyasaka, K. Takayama, A. Saitoh, S. Furukawa, M. Yamashita, R. Clérac, *Chem. Eur. J.*, **2010**, 16, 3656.

[10] (a) T. D. Harris, C. Coulon, R. Clérac, J. R. Long, *J. Am. Chem. Soc*., **2011**, 133, 123. (b) T. D. Harris, H. S. Soo, C. J. Chang, J. R. Long, *Inorg. Chim. Acta.*, **2011**, 369, 82.

[11] X. Feng, J. Liu, T. D. Harris, S. Hill, J. R. Long, *J. Am. Chem. Soc.*, **2012**, 134, 7521.

[12] (a) C. Kittel, *Introduction To Solid State Physics*, *7th Ed*., John Wiley & Sons, Inc., New York, **1996**. (b) A. Herpin, *Théorie du magnétism*, Eds CEA,**1968**.

CHAPTER IV

Re^{IV}-M(macrocycle) one dimensional systems

IV.1. Introduction

In this chapter, we will discuss one dimensional $[Re^{IV}Cl_4(CN)_2]$-M^{II}(macrocycle) systems (M = Ni, Cu, Fe, Mn) where the Re^{IV} and the M^{II} ions are organized alternatively in these chain compounds. The synthesis and characterization of all the molecular precursors to obtain these one dimensional compounds have been discussed in chapter II of this thesis.[1, 3-5] Three new one-dimensional cyanido-bridged heterometallic $Re^{IV}Ni^{II}$ and $Re^{IV}Cu^{II}$ systems were synthesized using Ni^{II}/Cu^{II}(cyclam)-type compounds and extensively characterized both structurally and magnetically. The other two chains are $Re^{IV}Fe^{II}$ and $Re^{IV}Mn^{II}$ heterometallic systems obtained from reactions between $[M^{II}(LN_3O_2)(H_2O)Cl]Cl$ (M = Fe, Mn) [4, 5, 11] and *trans*-$(Bu_4N)_2[Re^{IV}Cl_4(CN)_2]\cdot 2DMA$.[1, 2, 12]

IV.2. Re^{IV}-M^{II}(cyclam) based chains

In order to explore these bimetallic 3*d*-5*d* systems, we will here discuss one dimensional systems where the $[Re^{IV}Cl_4(CN)_2]^{2-}$ unit is linked to 3*d* transition metal macrocycles $[M^{II}(cyclam)]^{2+}$ (M = Ni, Cu, and cyclam = 1,4,8,11-tetraazacyclotetradecane) and $[Cu^{II}$(*N, N'*-dimethylcyclam)$]^{2+}$ (*N, N'*-dimethylcyclam = 1,8-dimethyl-1,4,8,11-tetraazacyclotetradecane). We have already seen that the *trans*-$[Re^{IV}Cl_4(CN)_2]^{2-}$ can form magnetically interesting chains with 3*d* transition metal ions (Mn^{II}, Fe^{II}, Co^{II}, Ni^{II}).[1] The magnetic exchange through the cyanido bridge between Re^{IV}-Ni^{II} or Re^{IV}-Cu^{II} ions was found to be ferromagnetic.[1, 2] Notably in the Re^{IV}-Cu^{II} case[2], the ferromagnetic interaction between the two different metal ions is significant of the order of +40 K when equatorial Cu^{II} coordination is involved. The synthesis, single crystal X-ray and magnetic characterization of these three cyanido-bridged heterometallic Re^{IV}-Ni^{II} and Re^{IV}-Cu^{II} chain compounds are described below.

IV.2.1. Synthesis

IV.2.1.1. $[Ni^{II}(cyclam)][Re^{IV}Cl_4(CN)_2]\cdot H_2O$ (14)

$[Ni^{II}(cyclam)](ClO_4)_2$ (0.0046 g, 0.01 mmol) was dissolved in 2 mL of water, placed in a 1.5 cm diameter tube and layered with 2 mL of pure acetonitrile. Over the pure solvent an acetonitrile solution of *trans*-$(Bu_4N)_2[Re^{IV}Cl_4(CN)_2]\cdot 2DMA$ (10 mg, 0.0099 mmol) was layered very carefully. The tube was then closed with parafilm to avoid evaporation. After 2 days, brown plate crystals suitable for single-crystal X-ray diffraction were found at the bottom and walls of the tube. The crystals were collected through filtration and dried in air. The yield was *ca.* 60 % based on the Ni^{II}

starting material. Elemental analysis calcd (%) for $C_{12}H_{26}Cl_4N_6NiORe$ (M = 657.10 g/mol): C 21.91, H 3.96, N 12.78; found (%) C 21.85, H 4.03, N 12.65; IR (KBr): $\bar{\nu}$ = 2141 (C≡N), 1296 (C–N) cm^{-1}.

IV.2.1.2. $[Cu^{II}(cyclam)][Re^{IV}Cl_4(CN)_2]\cdot H_2O$ (15)

$[Cu^{II}(cyclam)](ClO_4)_2$ (0.0046 g, 0.0099 mmol) was dissolved in 2 mL of nitromethane, placed in a 1.5 cm diameter tube and layered with 2 mL of pure nitromethane. A nitromethane solution of of *trans*-$(Bu_4N)_2[Re^{IV}Cl_4(CN)_2]\cdot 2DMA$ (10 mg, 0.0099 mmol) was layered very carefully on the top of the pure solvent layer. The tube was then closed with parafilm to avoid evaporation. After 2 days, red crystalline plates suitable for single-crystal X-ray diffraction were found at the bottom and walls of the tube. The crystals were collected through filtration and dried in air. The yield was *ca.* 70 % based on the Cu^{II} precursor. Elemental analysis calcd (%) for $C_{12}H_{26}Cl_4N_6CuORe$ (M = 661.93 g/mol): C 21.75, H 3.93, N 12.69; found (%) C 21.70, H 4.02, N 12.59; IR (KBr): $\bar{\nu}$ = 2132 (C≡N), 1280 (C–N) cm^{-1}.

This compound **15** can also be synthesized using acetonitrile instead of nitromethane. But if the compound **15** is allowed to stay a long time (more than one month) in the acetonitrile solution, the axial coordination site of $[Cu^{II}(cyclam)]^{2+}$ is substituted by the N atom of the acetonitrile molecule and thus a cocrystallized compound $[Cu^{II}(cyclam)(CH_3CN)_2][Re^{IV}Cl_4(CN)_2]$ (**15a**) is formed. The single crystal X-ray crystallographic characterization of this compound is given in section IV.2.2.

IV.2.1.3. $[Cu^{II}$(N, N′-dimethylcyclam)$][Re^{IV}Cl_4(CN)_2]$ (16)

This red-colored crystalline compound was synthesized following the same procedure as for compound **15** using 2 mL of a nitromethane solution of $[Cu^{II}$(*N, N'*-dimethylcyclam)$(ClO_4)_2]$ (0.0049 g 0.010 mmol). The yield was *ca.* 60 % based on the Cu^{II} precursor. Elemental analysis calcd (%) for $C_{14}H_{28}Cl_4N_6CuRe$ (M = 671.96 g/mol): C 25.00, H 4.17, N 12.50; found (%) C 25.09, H 4.28, N 12.46; IR: $\bar{\nu}$ = 2130 (C≡N), 1364, 1391 (C–N) cm^{-1}.

IV.2.2. X-ray crystal structure

Single crystal X-ray data were collected at 100 K for **14** and **15,** at 82 K for **16** and at 120 K for **15a.** Table IV.1 contains the summary of the crystallographic and structure refinement parameters

for all the compounds. Compounds **14-16** crystallized in the monoclinic C2/c space group and display very comparable crystal structures. Indeed, **14** and **15** are isostructural while **16** is only differentiated by the absence of the lattice water molecules. The cocrystallized compound **15a** also crystallizes in the same space group, although the cell parameters are quite different compared to those of **14**, **15** and **16**. The structures of compounds **14-16** consist of one-dimensional chains (figures IV.1) composed of alternating $[Re^{IV}Cl_4(CN)_2]^{2-}$ and $[M^{II}(cyclam)]^{2+}$ (M = Ni in **14**, Cu in **15**) or $[Cu^{II}(N, N'$-dimethylcyclam$)]^{2+}$ (in **16**) units.

Table IV.1. Crystal data and structure refinement for compounds **14- 16** and **15a**.

	14	**15**	**16**	**15a**
Formula	$C_{12}H_{26}Cl_4N_6NiORe$	$C_{12}H_{26}Cl_4N_6CuORe$	$C_{14}H_{28}Cl_4N_6CuRe$	$C_{16}H_{30}Cl_4N_8CuRe$
MW (g/mol)	657.10	661.93	671.96	726.04
***T* (K)**	100(2)	100(2)	82(2)	120(2)
Crystal System	Monoclinic	Monoclinic	Monoclinic	Monoclinic
Space group	C2/c	C2/c	C2/c	C2/c
***a* (Å)**	18.9716(19)	19.3757(12)	19.4944(9)	10.699(2)
***b* (Å)**	7.7040(8)	7.7226(5)	7.5209(3)	14.944(3)
***c* (Å)**	16.538(3)	16.3870(10)	17.3197(8)	15.668(3)
***β* (°)**	121.474(3)	122.861(2)	121.289(4)	93.96(3)
Volume (Å^3)	2061.6(4)	2059.7(2)	2170.01(17)	2499.1(8)
Z	4	4	4	4
***D* (g.cm^{-3})**	2.117	2.135	2.057	1.930
$\mu_{MoK\alpha}$ (mm^{-1})	7.312	7.437	7.058	6.138
F_{000}	1276	1280	1304	1416
GooF	1.133	1.043	1.109	1.146
[a]R_1 ($I > 2\ \sigma(I)$)	0.0186	0.0235	0.0495	0.0393
[b]wR_2 (all)	0.0466	0.0533	0.0988	0.1323

[a]$R_1 = \Sigma\ ||F_0| - |F_C||/\ \Sigma|F_0|$, [b]$wR_2 = [\Sigma w(F_0^2 - F_C^2)^2/\Sigma w(F_0^2)^2]^{1/2}$, $w = 1/[\sigma^2F_0^2 + (0.0313P)^2 + 1.5564P]$; where $P = (F_0^2 + 2F_C^2)/3$

In these one-dimensional systems, the cyanido groups of the $[Re^{IV}Cl_4(CN)_2]^{2-}$ unit bridge the 3*d* metal ions via the nitrogen donor sites. In compound **16**, the nitrogen and carbon atoms of the cyanido bridge were modeled as disordered over two positions with relative occupancies of 0.7 and 0.3. In the major part, the cyanido bridge is essentially perpendicular to the $ReCl_4$ plane, (Cl1-Re1-C1A = 94.1(3)° and Cl2-Re1-C1A = 92.1(3)°). The displacement of C1 and N1 in the minor part generates a second bridge position, which is distorted relative to the Re-Cl axes (Cl1-Re1-C1B = 101.8(6)° and Cl2-Re1-C1B = 98.2(6)°). The angles between these two cyanido bridges in **16** are about 20° (figure IV.1c). Disorder on the cyclam ring around the nitrogen atom bearing the methyl group was also modeled with the same relative occupancies. This disorder projects the minor methyl group towards the opposite face of the cyclam. To simplify the comparison between the compounds, the following discussion will mainly be concerned to the major part of compound **16**.

Each metal ion in **14-16** resides on an inversion center and adopts an octahedral coordination geometry. Carbon atoms from the cyanido groups are coordinated to the Re^{IV} axial sites with similar Re-C bond distances (2.126(3) Å in **14**, 2.131(2) Å in **15** and 2.124(8) Å in **16**), and quite linear Re-C-N angles (170.7(2)° for **14,** 174.6(9)° in **16** and 174.1(2)° in **15**). The equatorial plane of Re^{IV} is

occupied by four chlorido ligands (Re-Cl: 2.322(2) to 2.3562(5) Å) that are almost perfectly perpendicular to the C-Re-C axis (C-Re-Cl obtuse angles: 90.41(7) in **14** to 94.1(3)° in **16**) with Cl-Re-Cl angles close to 90° (obtuse angles between 90.80(2)° in **15** and 92.0(1)° in **16**). These geometric parameters are nearly identical to those observed for the *trans*-$(Bu_4N)_2[Re^{IV}Cl_4(CN)_2]\cdot 2DMA$ or in the related systems made with this Re^{IV} precursor[1, 2].

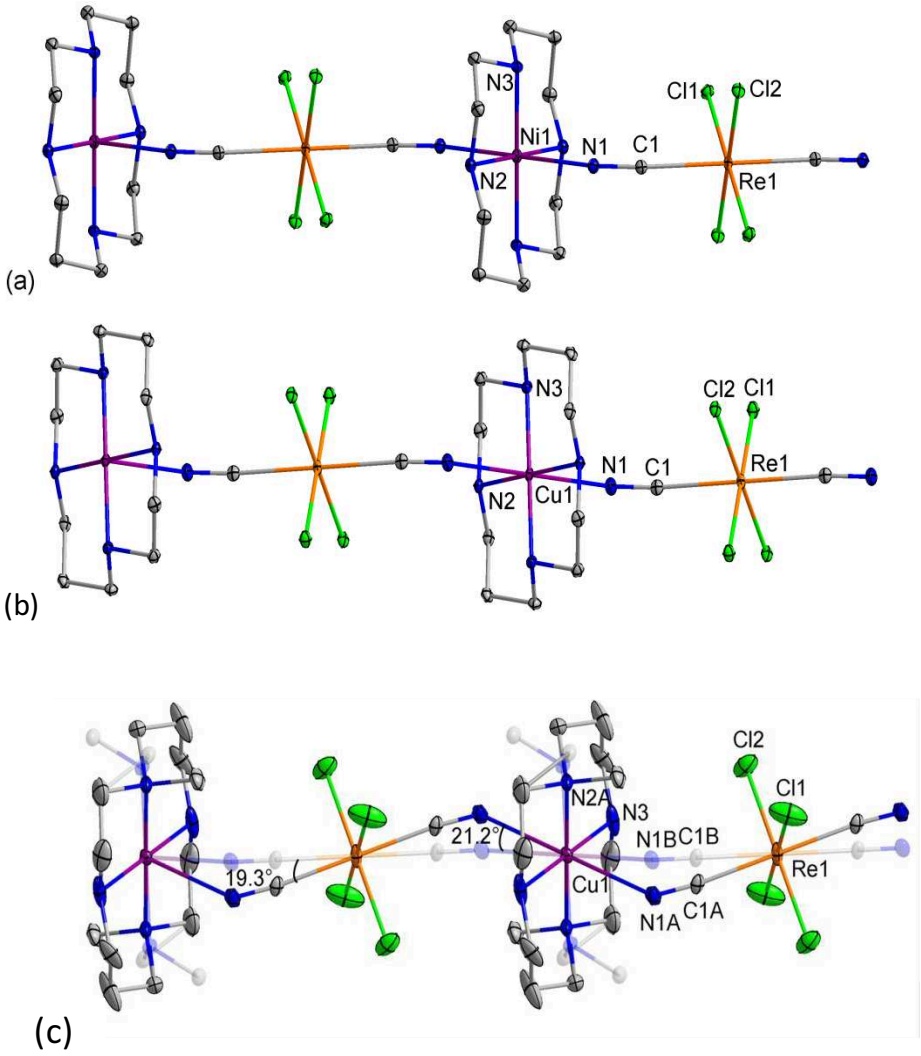

Figure IV.1. ORTEP type view of the crystal structures emphasizing the one-dimensional arrangement of **14** (a), **15** (b) and **16** (c) with selected atom-labeling schemes and thermal ellipsoids at 30% probability. The orange, green, blue, gray and violet ellipsoids correspond to Re, Cl, N, C and Ni/Cu atoms, respectively. Hydrogen atoms are omitted for clarity. The disorder of the cyanido groups and cyclam ligands is highlighted in **16** (in c) with shaded atoms corresponding to the minor part (*ca.* 30%) of the disordered atoms

The Ni^{II} and Cu^{II} metal ions possess an axially elongated octahedral coordination sphere with four nitrogen atoms belonging to the neutral cyclam ligand occupying the equatorial positions (Ni-N: 2.073(2), 2.080(2) Å in **14**, Cu-N: 2.021(2) Å, 2.041(2) Å in **15** and 2.079(9), 2.005(6) Å in **16**). It is worth noting that the Cu-N bond distances are significantly longer for the N atoms bearing hydrogen atoms (2.079(9) Å) than with those bearing methyl groups (2.005(6) Å) in **16**. The distortion of the 3*d*

metal ion octahedral geometry is clearly seen in the axial positions, which are occupied by the N atoms of the cyanido groups, with Ni-N and Cu-N bond distances reaching 2.129(2) Å in **14** and 2.531(9) Å in **16** (2.482(2) Å in **15**), respectively. We clearly find that axial elongation is more significant in Cu^{II} than in Ni^{II}. The M-N-C angles deviate notably from linearity with Ni-N-C and Cu-N-C angles of 148.5(2)° (in **14**) and 132.1(2)°/130.9(8)° (in **15**/**16**), respectively. Due to this nonlinearity, the individual chains adopt a mild zig-zag pattern along their axis of propagation.

In **14** and **15**, water molecules fill the vacant space inside the crystal packing between chains, while in **16**, the methyl groups of the macrocycle ligand play this role. Therefore, these three compounds experience very similar packing of the chains. In the crystal structures, the individual chains are parallel to the (*ab*) plane, forming layers of chains, which stack to form the crystal. The chain axes originating from two successive layers are tilted with an angle of *ca* 51° for **14** and **15**, and about 55° for **16** with respect to each other (figure IV.2a).

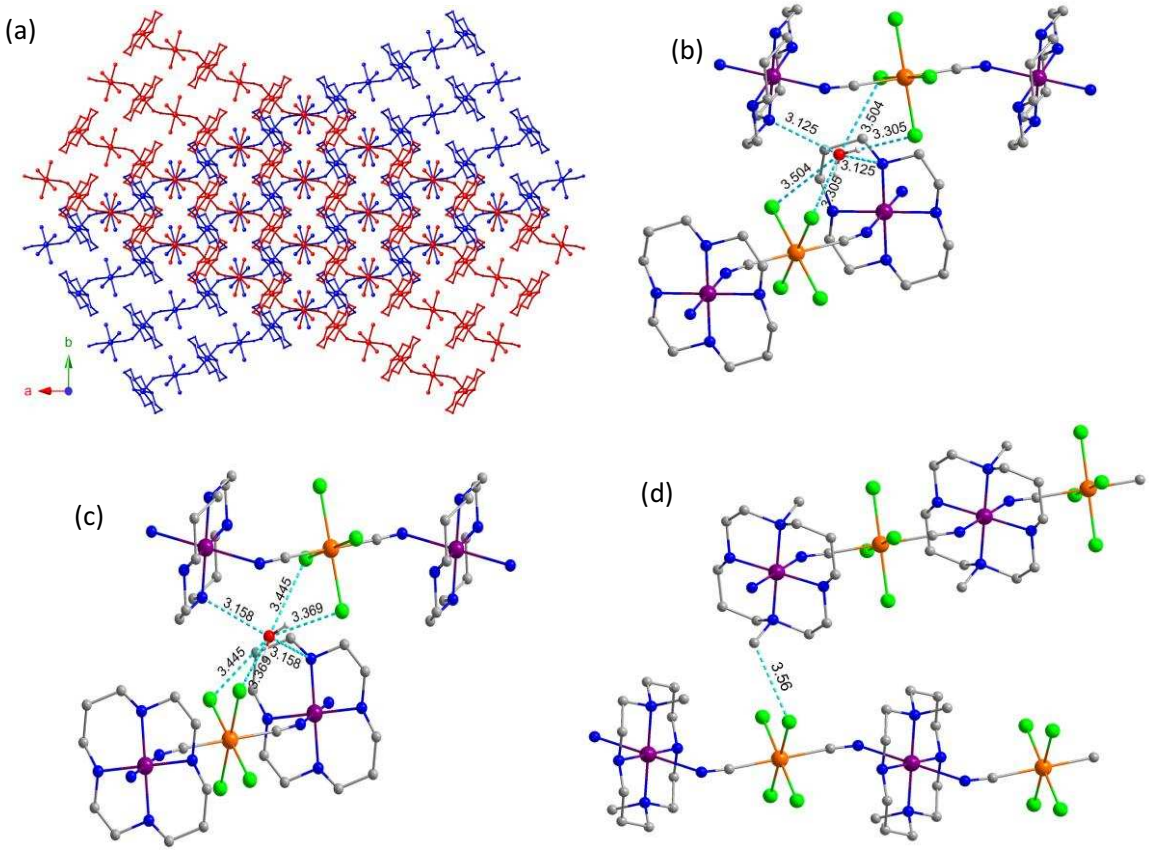

Figure IV.2. (a) Crystal packing perpendicular to the *c* axis for **14** illustrating the organization of two consecutive chain layers parallel to the (*ab*) plane, shown in red and blue. For visual clarity, each layer is represented in a different color. Hydrogen atoms and water molecules are omitted for clarity. (b) Hydrogen bonding pattern observed in **14** with a water molecule connecting the chain layers. (c) Hydrogen bonding pattern observed in **15** with a water molecule connecting the chain layers. (d) Short Cl…C contact observed in **16** between the chain layers.

In **14** and **15**, the water molecules are weakly hydrogen bonded to four chlorido ligands belonging to two Re^{IV} sites of neighboring chains in two different layers (figure IV.2b and IV.2c) with an average distance $d_{O\cdots Cl}$ of *ca.* 3.41 Å. Additionally, these water molecules also act as hydrogen bond acceptors with two N-H groups of the cyclam ligands ($d_{N\cdots O}$ = 3.13 - 3.16 Å). Similarly, for compound **16**, close contacts between the chloride atoms and the methyl groups of the cyclam ($d_{C\cdots Cl}$ = 3.56 Å) are observed (figure IV.2d).

The Cu^{II} center of the cocrystallized compound $[Cu^{II}(cyclam)(CH_3CN)_2][Re^{IV}Cl_4(CN)_2]$ (**15a**) (figure IV.3a) is also in an octahedral ligand environment. The equatorial plane of the Cu^{II} ion in the $[Cu^{II}(cyclam)(CH_3CN)_2]^{2+}$ is occupied by four N atoms having equatorial Cu^{II}-N distances of 2.034(6) Å and 2.019(6) Å. The two axial positions of the Cu^{II} ion are connected with the two N atoms coming from two acetonitrile molecules with a Cu^{II}-N distance of 2.546(6) Å. The $[Re^{IV}Cl_4(CN)_2]^{2-}$ moiety acts as the counter anion and compensate the change of the Cu^{II} complex. Both cyanido nitrogen atoms of the $[Re^{IV}Cl_4(CN)_2]^{2-}$ moiety experience weak hydrogen bonding contacts with an N-H group of the cyclam ligand of two different Cu^{II} moieties ($d_{N\cdots O}$ = 3.03 - 3.31 Å) as displayed in figure IV.3b.

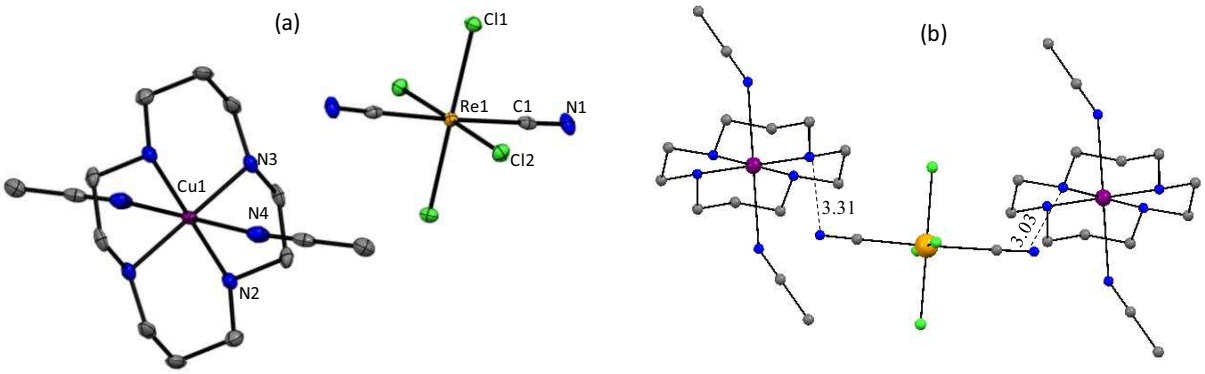

Figure IV.3. (a) ORTEP type view of the crystal structure of cocrystallizing compound **15a** with thermal ellipsoids at 50% probability. The orange, green, blue, gray and violet ellipsoids correspond to Re, Cl, N, C and Cu atoms, respectively. Hydrogen atoms are omitted for clarity. (b) The hydrogen bonding short contacts in **15a** between the cyanido nitrogen atoms and the N-H of the cyclam ligand.

IV.2.3. Magnetic properties

The *ac* and *dc* susceptibility measurements were performed on a polycrystalline sample of the three one-dimensional compounds **14-16** to probe their magnetic properties. The magnetic properties of **15a** were not measured because the X-ray crystal structure confirms the absence of close Re^{IV}-Cu^{II} interactions.

The temperature dependence of the χT products collected in a *dc* magnetic field of 1000 Oe are shown in figure IV.4 for **14**, **15**, and **16**, along with the *trans*-$(Bu_4N)_2[ReCl_4(CN)_2]\cdot 2DMA$ precursor for comparison. At 270 K, the χT value is 2.7, 1.9 and 1.8 cm^3 K mol^{-1} for **14**, **15** and **16**, respectively, in good agreement with the expected Curie constants of 2.6, 1.8 and 1.8 cm^3 K mol^{-1} considering respective *g* factors of 2.2, 2.2 and 1.7 for isolated Ni^{II} ($S = 1$), Cu^{II} ($S = ½$) and Re^{IV} ($S = 3/2$) [1] spin carriers. The temperature dependence of the χT product for the three compounds is quite different. For the Ni^{II} analogue **14**, upon lowering the temperature, χT decreases first down to 2.41 cm^3 K mol^{-1} at 19.5 K, then increases to 2.48 cm^3 K mol^{-1} at 9.2 K before finally decreasing abruptly down to 0.35 cm^3 K mol^{-1} at 1.8 K. For **15**, χT increases first up to 2.03 cm^3 K mol^{-1} at *ca.* 31 K indicating a dominant intrachain ferromagnetic interaction as already observed in a related cyanido-bridged Re^{IV}/Cu^{II} system.[2] At lower temperatures, χT decreases slightly to 1.97 cm^3 K mol^{-1} around 7 K and finally decreases abruptly down to 0.17 cm^3 K mol^{-1} at 1.8 K. For **16**, χT noticeably decreases to 1.13 cm^3 K mol^{-1} at about 7.8 K, then increases up to 4.06 cm^3 K mol^{-1} at 3.9 K and lastly decreases down to 2.29 cm^3 K mol^{-1} at 1.8 K.

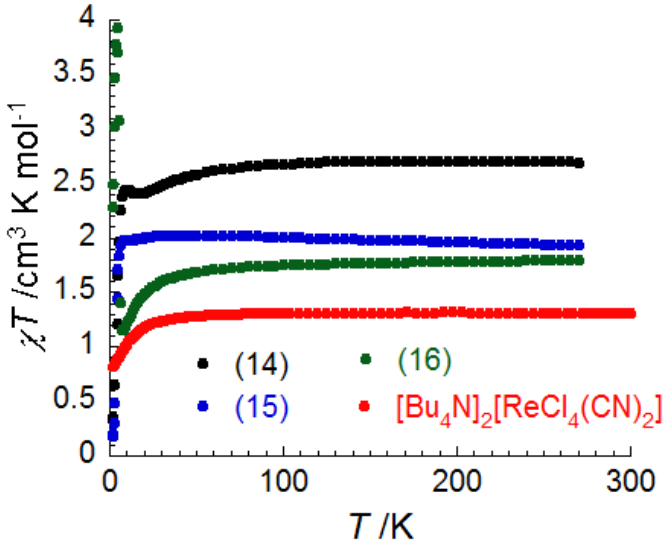

Figure IV.4. Temperature dependence of the χT products collected in an applied *dc* field of 1000 Oe for **14**, **15**, **16** and the *trans*-$(Bu_4N)_2[Re^{IV}Cl_4(CN)_2]\cdot 2DMA$ precursor.

Due to the intrinsic magnetic properties of the $[Re^{IV}Cl_4(CN)_2]^{2-}$ precursor, it is not straightforward to assign the nature of the intrachain magnetic interactions in **14** and **16**. As shown previously, [1,2] the decrease of the χT product upon lowering the temperature for the Re^{IV} precursor (figure IV.4) is essentially due to its magnetic anisotropy. This thermal behavior is superimposed onto the effect of the intrachain interactions and thus no simple one-dimensional magnetic model can be applied to evaluate these exchange couplings. Nevertheless, the ferromagnetic nature of the intrachain interaction in **15** is clearly established by the increase of the χT product between 270 and 31 K. This is also confirmed by the magnetization at value 1.8 K and 7 T that reaches 2.73 μ_B (figure IV.5b), in

agreement with a ferromagnetic arrangement of the spins along the chain (expected magnetization values at 7 T and 1.8 K for the Re^{IV} precursor: 1.5 μ_B[1] and the Cu^{II} moiety with g = 2.2: 1.1 μ_B). For **14** and **16**, the same conclusion concerning the nature of the intrachain interactions can be drawn based on the *M vs*. *H* data (figure IV.5a and IV.5c). At 1.8 K and 7 T, the magnetizations of **14** and **16** reach 2.8 μ_B and 1.9 μ_B, respectively, which are only compatible with ferromagnetic intrachain interactions. If the intrachain interactions are antiferromagnetic in nature, it would lead to small magnetization values around 0.7 μ_B for **14** (expected magnetization value for the Ni^{II} moiety with g = 2.2 at 7 T and 1.8 K: 2.2 μ_B) and 0.4 μ_B for **15** and **16** at 7 T. For **14** and **16**, it seems that the 3*d*/5*d* ferromagnetic interactions through the cyanido bridge are weaker than in **15** and thus they do not compensate or overcome the effect of the Re^{IV} magnetic anisotropy leading to a decrease of the χT product upon lowering the temperature (figure IV.4). The low temperature (below 10 K) variations of magnetic susceptibility (χ) have been measured at multiple *dc* fields (figure IV.6).

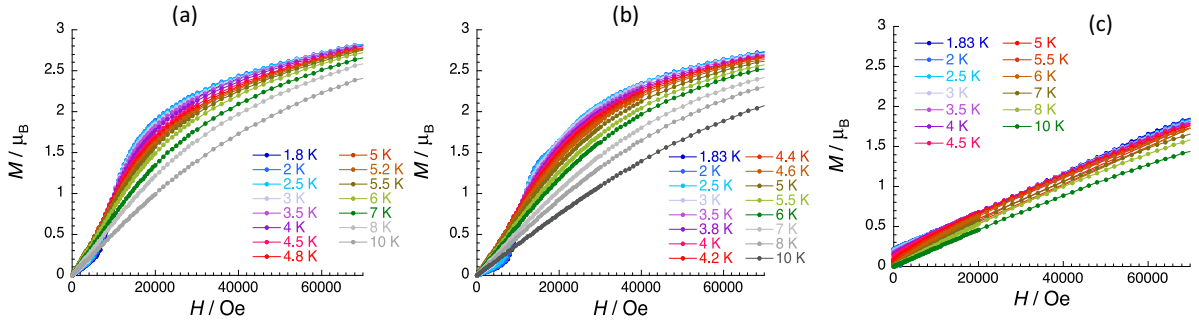

Figure IV.5. *M* vs. *H* plot for a polycrystalline sample of **14** (a), **15** (b) and **16** (c) between 1.8 and 10 K.

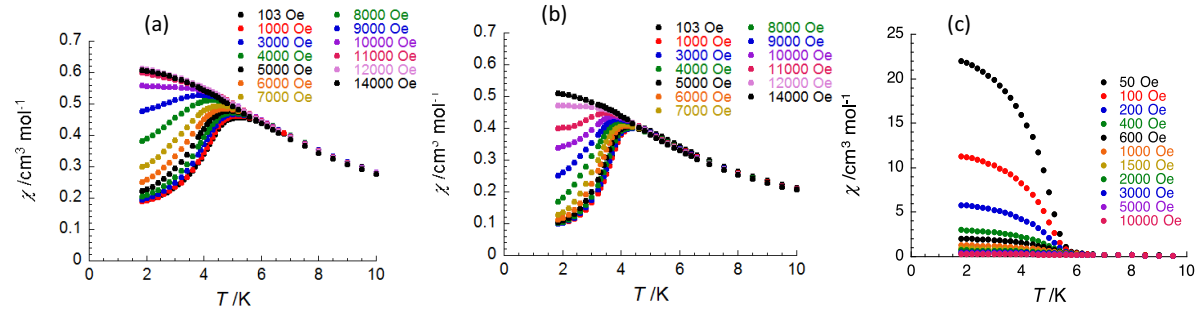

Figure IV.6. Plots of χ *vs. T* at different *dc* fields up to 1.4 T between 1.83 and 10 K for a polycrystalline sample for of **14** (a), **15** (b) and **16** (c).

The *M* vs. *H* data measured below 10 K (figure IV.5) for the three compounds also reveal their respective magnetic ground state. **14** and **15** display very similar low temperature magnetic properties with typical "S" shaped magnetization curves (i.e. with an inflection point at H_C) at 1.8 K. This feature reveals the presence of antiferromagnetic interactions between chains compensated by the applied magnetic field at H_C = 9400 Oe and 9340 Oe for **14** and **15**, respectively. This characteristic field has been followed as a function of temperature (using combined *M* vs. *H* and χ vs. *T* data and taking the

maximum of the d*M*/d*H* vs. *H* and χ vs. *T* plots; figure IV.5a-b, IV.6a-b and IV.7a-b) in order to build the corresponding (*T*, *H*) magnetic phase diagram (figure IV.7c). These results demonstrate the presence of a three-dimensional antiferromagnetic order in both **14** and **15** with T_N = 4.5 K and 4.1 K, respectively. Heat capacity (C_p) measurements of **14** and **15** (figure IV.8a-b) further confirm the presence of magnetic phase transitions as evidenced by marked C_p peaks observed at the Néel temperatures. The topology of the phase diagram shown in figure IV.7c for **14** and **15** is characteristic of metamagnetic behavior with only an antiferromagnetic to paramagnetic transition line that is certainly induced by the magnetic anisotropy brought by the Re^{IV} metal ions. This strong magnetic anisotropy is also revealed by the high-field magnetization of these compounds, which does not saturate even at 1.8 K and 7 T.

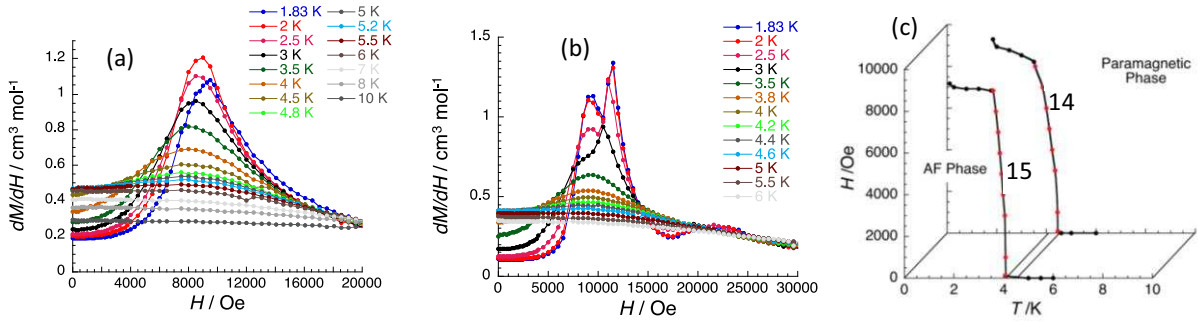

Figure IV.7. (a) *dM/dH* vs. *H* plots for a polycrystalline sample of **14** (a)and **15** (b) between 1.8 and 10 K. (c) *H* vs. *T* magnetic phase diagram for **14** and **15**. The black and red dots are respectively the experimental points deduced from the *M vs. H* and χ *vs. T* data. The solid black line is a guide for the eye.

In order to estimate the average interchain interactions, z*J'*, between the effective spins (S_{eff} = 5/2 for **14** and S_{eff} = 2 for **15**) of the Re^{IV}-M^{II} chains, the following expression was used [6,7]:

$$g_{av}\mu_B H_C^0 S_{eff} = 2|zJ'|S_{eff}^2 \qquad \textbf{Eq.IV.1}$$

where g_{av} is the average *g* factor of the Re^{IV}-M^{II} (M = Ni^{II} and Cu^{II}) unit along the chain (g_{av} = 1.95) and H_C^0 is the critical field extrapolated at 0 K (9500 Oe for **14** and 9400 Oe for **15**). z*J'*/k_B is thus estimated at -0.25 and -0.31 K for **14** and **15**, which confirms the existence of significant interchain interactions responsible for the antiferromagnetic phase transition. From z*J'*, the theoretical Néel temperature (T_N) for a three-dimensional network of magnetic interactions treated in the mean field approximation can be estimated at 1.5 K and 1.2 K for **14** and **15**, respectively, using the following well-known relation: $T_N = 2|zJ'|S_{eff}(S_{eff}+1)/3k_B$. The marked underestimation of the experimental T_N by this mean-field approach demonstrates the low-dimensional nature of the materials and thus the presence of much stronger intrachain interactions than interchain interactions.

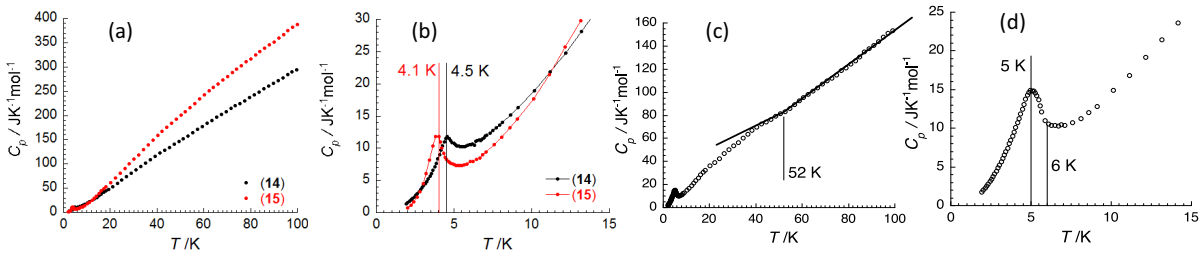

Figure IV.8. (a) Temperature dependence of the heat capacity C_p of **14** and **15** between 1.9 and 100 K. (b) Temperature dependence of the heat capacity C_p between 1.9 and 15 K (right) for a polycrystalline sample of **14** and **15** at a zero external field during the cooling process. (c) Temperature dependence of the heat capacity C_p of **16** between 1.9 and 100 K; (d) Temperature dependence of the heat capacity C_p between 1.9 and 15 K for a polycrystalline sample of **16** at a zero external magnetic field during the cooling process.

The magnetic ground state of **16** is different from the two first compounds **14** and **15**. The *M* vs. *H* data measured below 10 K reveal the presence of a hysteresis effect with a coercive field of 1700 Oe at 1.8 K (at about 180 Oe/min, figure IV.9a). An *M* vs. *H* hysteresis loop is observed up to 5.5 K. At higher field, the magnetization increases almost linearly up to 7 T and reaches 1.9 μ_B at 1.83 K (figures IV.9a and IV.5c). This magnetic behavior and the strong increase of the susceptibility at low fields below 6 K (figure IV.6c) is the typical signature of a canted antiferromagnetic ground state.

The small spontaneous magnetization resulting from the non-compensation of the two sublattices in the canted antiferromagnetic phase (M = 0.22 μ_B at 1.83 K) has been deduced from the *M vs. H* data and plots after normalization, M/M_{sat}, as a function of temperature. As shown in figure IV.9c (top part, blue solid line), the M/M_{sat} vs. T data compare almost perfectly with the temperature variation of the Ising order parameter (m) in the mean field approximation (that is, the solution of the self-consistent equation $m = \tanh(mT_C/T)$).[8,9] This theoretical and experimental agreement confirms the correlation between the T dependence of M/M_{sat} and the magnetic phase transition with T_C = 4.9 K. Between 4.9 K and 6 K, fluctuation effects above the magnetic phase transition are observed in the M/M_{sat} vs. T data (figure IV.9c). The presence of short-range order in this temperature range is also seen by *ac* susceptibility measurements. While no out-of-phase component (χ'') of the *ac* susceptibility was observed for **14** and **15**, as expected for an antiferromagnetic ground state, compound **16** exhibits a marked *ac* response around T_C with a succession of two peaks on both χ' and χ'' components (figure IV.9b and the bottom part of figure IV.9c). The comparison of the M/M_{sat} vs. T and χ'' vs. T data as done in figure IV.9c help to easily assign the first χ'' maximum to a pre-transitional effect while the second peak at 4.9 K is clearly the signature of the magnetic transition. Heat capacity (C_p) measurements (figure IV.8d) confirm the presence of both the magnetic phase transition at *ca.* 5 K and the pre-transitional effects between 5 and 6 K, as evidenced by the broad shape of the observed C_p peak.

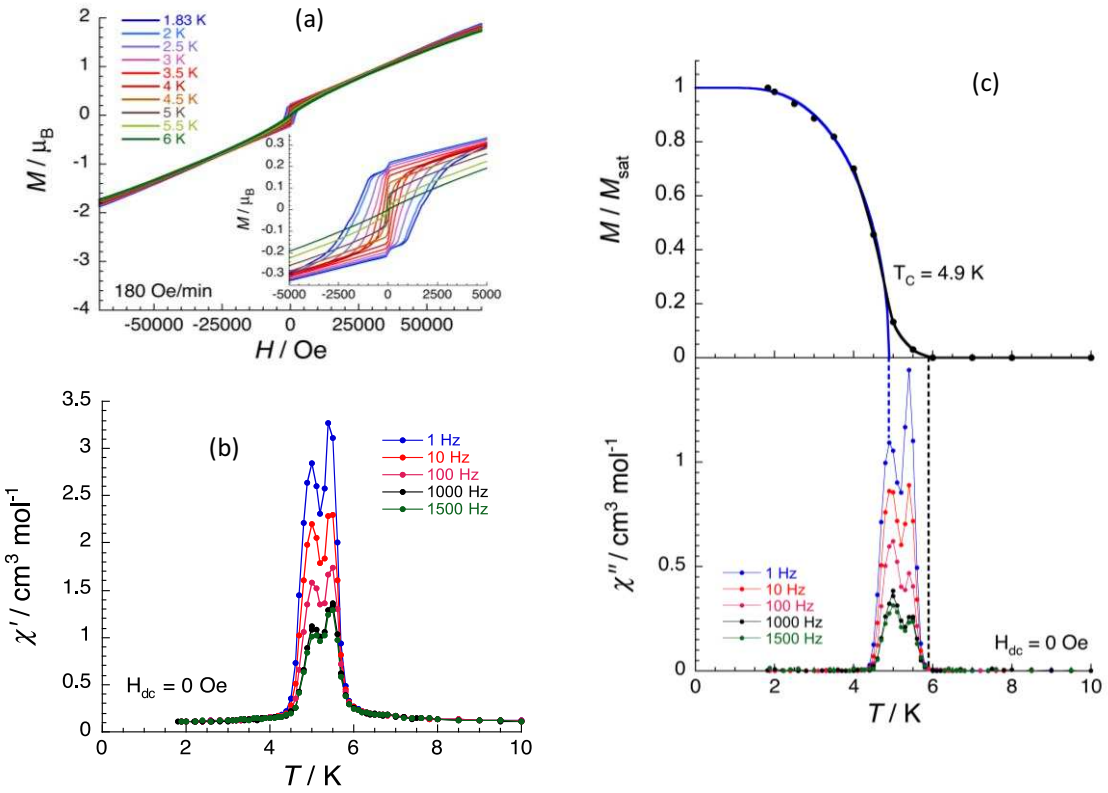

Figure IV.9. (a) Field dependence of the magnetization for a polycrystalline sample of **16** between 1.83 and 6 K with sweep-rates of 180 Oe/min. Inset: Expanded view of the main figure between -0.5 and 0.5 T emphasizing the *M* vs. *H* hysteresis. Solid lines are guides for the eye. (b) The real (χ') part of the ac susceptibility in zero *dc* field at different *ac* frequencies for a polycrystalline sample for **16**. Solid lines are guides for the eye. (c) **Top part:** Temperature dependence of the normalized spontaneous magnetization for a polycrystalline sample of **16** between 1.8 and 10 K deduced from the *M* vs. *H* data shown in (a). The solid blue line is the theoretical spontaneous magnetization in the frame of the incompressible Ising model in the mean field approximation with T_C = 4.9 K [8, 9]. Solid black line is a guide for the eye. **Bottom part**: Temperature dependence of the out-of-phase component of the *ac* susceptibility (χ'') between 1.8 and 10 K at different *ac* frequencies, under zero *dc* field and with a 3 Oe *ac* field modulation. Solid lines are guides for the eye.

Therefore the obvious question is raised regarding the magnetic properties of these three compounds: why do **14** and **15** display an antiferromagnetic ground state and **16** a canted antiferromagnetic ground state while they have almost the same crystal structures? In **14** and **15**, the layers of chains shown by different colors in figure IV.2a are likely sheets of antiferromagnetically coupled chains that are themselves antiferromagnetically coupled in the third direction to lead to a three-dimensional antiferromagnetic order. Therefore the tilt angle of *ca.* 51-55° between chains of neighboring layers does not prevent the antiferromagnetic order and thus is not responsible for the canted antiferromagnetic order seen in **16** as well. The key difference between **16** with respect to **14** and **15** is the presence of a disorder along the chains (figure IV.1c) with two different orientations of the anisotropic $[Re^{IV}Cl_4(CN)_2]^{2-}$ moiety along the chains. The angle between these two orientations is about 20° (noted α, see figure IV.1c). Quite remarkably, an angle of around 18° between the two uncompensated sublattices of the canted antiferromagnetic phase is deduced from the spontaneous

magnetization ($\sin(\alpha/2) = 2M/M_{HF}$, with M = 0.22 μ_B at 1.83 K and M_{HF} = 2.8 μ_B being the magnetization expected at high field after saturation). This result strongly supports the hypothesis that the origin of the canted antiferromagnetic phase in **16** is found in the one-dimensional arrangement itself. As a consequence, it seems very likely that an order-disorder structural phase transition occurs between 82 K (lowest temperature of the crystal structure collection) and T_C (4.9 K) in order to stabilize a well-ordered magnetic state. This hypothesis is also supported by heat capacity measurements (figure IV.8c) that display a broad feature at *ca.* 52 K that could be the signature of this phase transition. Unfortunately, in the time frame of this work, we did not manage to obtain from our collaborators a crystal structure below 52 K to confirm this hypothesis.

IV.3. Re^{IV}-$M^{II}(LN_3O_2)$ Systems

In $[M^{II}(DMF)_4][Re^{IV}Cl_4(CN)_2]$ (where M = Fe, Mn) SCM systems, the $Re^{IV}Fe^{II}$ and the $Re^{IV}Mn^{II}$ interactions were found to be ferromagnetic and antiferromagnetic respectively.[1] Herein, we have designed and studied similar $[M^{II}(LN_3O_2)][Re^{IV}Cl_4(CN)_2]$ compounds (M = Fe, Mn) to investigate the effect of the anisotropy of the $[M^{II}(LN_3O_2)]^{2+}$ moiety on the magnetic properties of these one dimensional $Re^{IV}Fe^{II}$ and $Re^{IV}Mn^{II}$ systems.

IV.3.1. Synthesis

IV.3.1.1. $[Fe^{II}(LN_3O_2)][Re^{IV}Cl_4(CN)_2]$ (17)

$[Fe^{II}(LN_3O_2)(H_2O)Cl]Cl$ (0.0042 g, 0.01 mmol) was dissolved in 1 mL of water, placed in a 1.5 cm diameter tube and layered with 3 mL of pure acetonitrile. Over the pure solvent a 2 mL acetonitrile solution of of *trans*-$(Bu_4N)_2[Re^{IV}Cl_4(CN)_2]\cdot 2DMA$ (0.0103 g, 0.01 mmol) was layered very carefully. The tube was then closed with parafilm to avoid evaporation. After one week, blue crystals suitable for single-crystal X-ray diffraction were found at the bottom and walls of the tube. The crystals were collected through filtration and dried in air. The yield was *ca.* 40 % based on the Fe^{II} starting material. Elemental analysis calcd (%) for $C_{17}H_{21}Cl_4N_5O_2FeRe$ (M = 711.24 g/mol): C 28.71, H 2.98, N 9.85; found (%) C 28.80, H 3.03, N 9.65; IR (KBr): $\bar{\nu}$ = 2141 (C≡N), 1296 (C–N) cm^{-1}.

IV.3.1.2. $[Mn^{II}(LN_3O_2)][Re^{IV}Cl_4(CN)_2]$ (18)

$[Mn^{II}(LN_3O_2)(H_2O)Cl]Cl{\cdot}5H_2O$ (0.0051 g, 0.01 mmol) was dissolved in 1 mL of water, placed in a 1.5 cm diameter tube and layered with 3 mL of pure acetonitrile. Over the pure solvent, a 2 mL acetonitrile solution of of *trans*-$(Bu_4N)_2[Re^{IV}Cl_4(CN)_2]{\cdot}2DMA$ (10.3 mg, 0.01 mmol) was layered very carefully. The tube was then closed with parafilm to avoid evaporation. After one week, yellow crystals suitable for single-crystal X-ray diffraction were found at the walls of the tube. The crystals were collected through filtration and dried in air. The yield was *ca.* 40 % based on the Mn^{II} starting material. Elemental analysis calcd (%) for $C_{17}H_{21}Cl_4N_5O_2MnRe$ (M = 710.34 g/mol): C 28.74, H 2.98, N 9.86; found (%) C 28.80, H 3.05, N 9.69; IR (KBr): $\bar{}$ = 2137 (C≡N), 1296 (C–N) cm^{-1}.

IV.3.2. X-ray crystal structure

Table IV.2 contains the summary of the single crystal X-ray diffraction and structure refinement parameters for **17** and **18**.

Table IV.2. Crystal data and structure refinement for compounds **17** and **18**.

	17	**18**
Formula	$C_{170}H_{210}Cl_{40}N_{50}O_{20}Fe_{10}Re_{10}$	$C_{170}H_{210}Cl_{40}N_{50}O_{20}Mn_{10}Re_{10}$
MW (g/mol)	7112.47	7103.37
***T* (K)**	120(2)	120(2)
Crystal System	Monoclinic	Monoclinic
Space group	C2/c	C2/c
***a* (Å)**	46.649(9)	46.269(2)
***b* (Å)**	13.102(3)	13.144(3)
***c* (Å)**	18.659(4)	18.937(4)
***β* (°)**	91.38(3)	91.67(3)
Volume ($Å^3$)	11423(4)	11534(3)
Z	2	2
***D* ($g.cm^{-3}$)**	2.068	1.045
$\mu_{MoK\alpha}$ (mm^{-1})	6.421	6.278
F_{000}	6860	6840
GooF	1.054	1.104
[a] R_1 ($I > 2\ \sigma(I)$)	0.0511	0.0498
[b] wR_2 (all)	0.1660	0.1622

[a] $R1 = \Sigma\ ||F_0| - |F_C||/\ \Sigma|F_0|$, [b] $wR_2 = [\Sigma w(F_0^2 - F_C^2)^2/\Sigma w(F_0^2)^2]^{1/2}$, $w = 1/[\sigma^2F_0^2 + (0.0313P)^2 + 1.5564P]$; where $P = (F_0^2 + 2F_C^2)/3$

Both compounds are composed of an alternative arrangement of $[M^{II}(LN_3O_2)]^{2+}$ (M = Fe and Mn) and $[Re^{IV}Cl_4(CN)_2]^{2-}$ moieties and thus form one dimensional compounds having an isostructural crystal structure (figure IV.10). One can find three different Re^{IV} crystallographic sites and three different metal (Fe^{II}, Mn^{II}) ions in these chain compounds.

Both compounds crystallized in the C2/c space group. As it is typical in these types of compounds, the equatorial plane of $[Re^{IV}Cl_4(CN)_2]^{2-}$ is occupied with four chloride atoms which are

almost mutually perpendicular, with Re^{IV}-Cl distances ranging between 2.31 Å and 2.36 Å. The axial positions of the Re^{IV} ion are occupied by the carbon atom of the cyanido group and the Re^{IV}-C-N angles are quite close to linearity (ranging between 173.3(7)° and 176.7(7)° for **17** and between 174.2(7)° and 176.5(7)° for **18**). The Fe^{II} or the Mn^{II} ions of the $[M^{II}(LN_3O_2)]^{2+}$ fragment has heptacoordinate geometry where the five equatorial coordination positions are occupied with three N and two O atoms of the LN_3O_2 ligand. The neutral cyclic LN_3O_2 ligand has a nearly planar geometry around the Fe^{II}/Mn^{II} centers. The equatorial Fe^{II}-N distances in **17** are found between 2.110(7) Å and 2.204(8) Å, the equatorial Mn^{II}-N distances in **18** are between 2.183(8) Å and 2.257(8) Å. The equatorial Fe^{II}-O distances are between 2.287(7) Å and 2.304(6) Å and for **18** the equatorial Mn^{II}-O distances range between 2.282(6) Å and 2.298(6) Å. The remaining two axial positions of the Fe^{II}/Mn^{II} complexes are coordinated to N atoms coming from the cyanido group of the $[Re^{IV}Cl_4(CN)_2]^{2-}$ moiety. These axial Fe^{II}-N distances are found between 2.125(8) Å and 2.155(7) Å in **17**, whereas in **18** the axial Mn^{II}-N bonds range from 2.229(8) Å to 2.254(6) Å. In the compound **17**, the Fe^{II}-N-C angles are found between 152.7(7)° and 158.8(7)° whereas the Mn^{II}-N-C distances fall between 148.4(7)° and 156.4(7)° in **18**. The deviations of the M^{II}-N-C angle from linearity give a zigzag pattern to the one dimensional view of both compounds, although **17** is slightly more linear than **18**. In both compounds a center of inversion is found at the middle of the $\{[M^{II}(LN_3O_2)][Re^{IV}Cl_4(CN)_2]\}_5$ fragment (on the Re3 and Re1 sites respectively for **17** and **18**, see figure IV.10) which makes half of this $\{[M^{II}(LN_3O_2)][Re^{IV}Cl_4(CN)_2]\}_5$ the asymmetric unit. This structural criterion implies that all the $[M^{II}(LN_3O_2)][Re^{IV}Cl_4(CN)_2]$ units in a $\{[M^{II}(LN_3O_2)][Re^{IV}Cl_4(CN)_2]\}_{2.5}$ fragment are not identical on the basis of bond distances and angles.

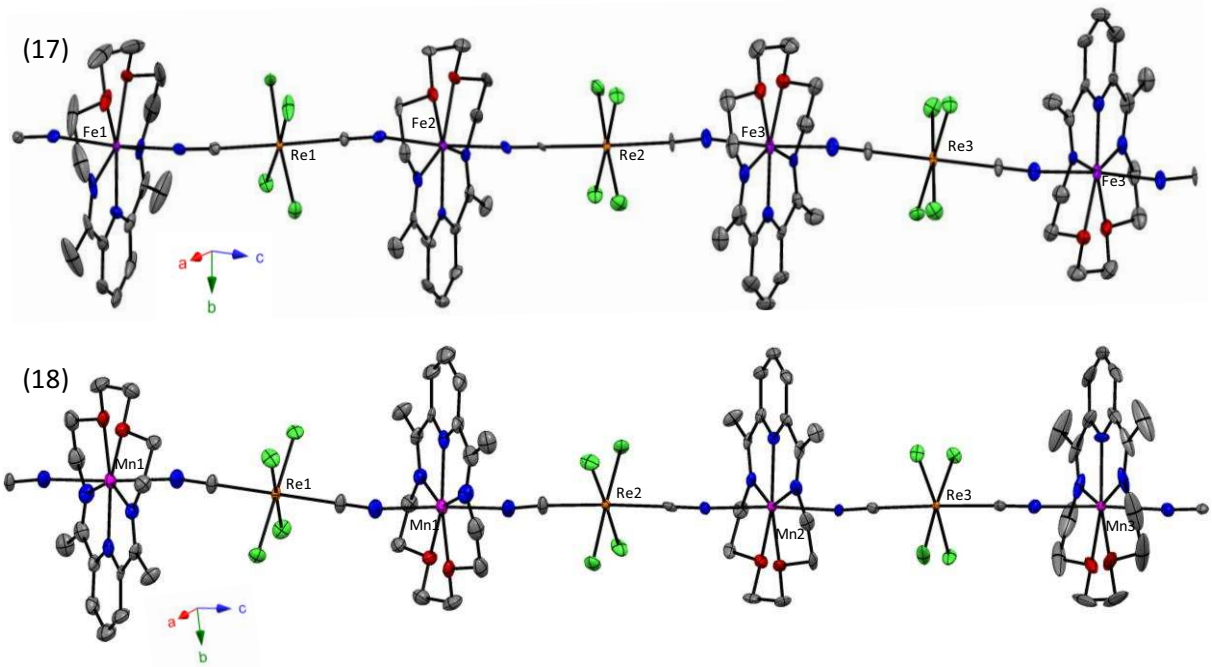

Figure IV.10. ORTEP type view of fragment of the one dimensional system **17** and **18** compounds; thermal ellipsoids are shown at 50 % probability. The C, N, O, Cl, Fe (in **17**), Mn (in **18**), and Re atoms are represented in grey, blue, red, green, violet (in **17**), magenta (in **18**) and orange. Hydrogen atoms are omitted for clarity.

IV.3.3. Magnetic properties

The magnetic properties of **17** were measured on a polycrystalline sample. Due to time limitations of this work, we did not measure the magnetic properties of **18**.

The temperature dependence of the magnetic susceptibility (plotted as χT vs T) of **17** was measured between 290-1.8 K in a 1000 Oe *dc* applied field (figure IV.11a). The χT value is 4.8 cm^3 K mol^{-1} at 290 K where the calculated Curie constant χT should be 4.3 cm^3 K mol^{-1} for this species (for a 1:1 Fe^{II} (S_{Fe} = 2): Re^{IV} (S_{Re} = 3/2) system having g_{Fe} = 2 and g_{Re} = 1.67[1]). With decrease of the temperature, the χT product gradually increases to 9.13 cm^3 K mol^{-1} at 13 K, followed by a sudden decrease to 2.21 cm^3 K mol^{-1} at 1.8 K. This increase of the magnetic susceptibility with the decrease of temperature indicates dominant ferromagnetic interaction between Fe^{II} and Re^{IV} magnetic centers. Furthermore, the low temperature decrease of χT suggests presence of interchain antiferromagnetic interaction. In order to probe the magnetic interaction between the magnetic sites, the χT *vs.* T data were modeled with the following spin Hamiltonian of alternating Heisenberg classical spins S_{Re} = 3/2 and S_{Fe} = 2,[10]

$$H = -2J\sum_{i=1}^{n}(S_{Re_i}S_{Fe_i} + S_{Fe_i}S_{Re_{i+1}}) \qquad \textbf{Eq IV.2}$$

Using this Heisenberg Hamiltonian the expression of χ becomes,

$$\chi = \frac{N\mu_B^2}{6k_BT}\left[(M_{Re}+M_{Fe})^2\frac{1+P}{1-P} + (M_{Re}-M_{Fe})^2\frac{1-P}{1+P}\right] \qquad \textbf{Eq.IV.3}$$

where,

$M_{Re} = g_{av}\sqrt{S_{Re}(S_{Re}+1)}$, and $M_{Fe} = g_{av}\sqrt{S_{Fe}(S_{Fe}+1)}$

and

$$P = \coth\left[\frac{2J\sqrt{S_{Re}(S_{Re}+1)S_{Fe}(S_{Fe}+1)}}{k_BT}\right] - \left[\frac{k_BT}{2J\sqrt{S_{Re}(S_{Re}+1)S_{Fe}(S_{Fe}+1)}}\right]$$

where g_{av} is the average g factor of the Re^{IV}-Fe^{II} unit along the chain and J is the ferromagnetic exchange parameters between Re^{IV} and Fe^{II}. This chain model corresponds well to the experimental data above 15 K and yields the parameters g_{av} = 2.03(1) and J/k_B = + 3.01(1) K.

In the experimental plot of χT vs. T (figure IV.11a) at low temperatures (below 13 K) the decrease of χT suggests the presence of interchain antiferromagnetic interaction. To investigate the

magnetic properties in this low temperature domain, the magnetization *M* was measured as a function of applied field at multiple temperatures between 1.83 K and 12 K (figure IV.11b). At 1.83 K, the *M* vs. *H* curve (inset of figure IV.11b) exhibits a sigmoidal shape with an inflection point near 8000 Oe, which suggest a paramagnetic to antiferromagnetic phase transition at 1.83 K. The '*S*' shape of the magnetization curves was observed up to 8 K, giving the temperature dependent of this characteristic field. In order to quantify this field at different temperatures the *dM*/*dH* vs. *H* plots (figure IV.12a) were calculated from data derived from the *M* vs. *H* plots (figure IV.11b).

The maximum in the *dM*/*dH* vs. *H* plots (figure IV.12a) indicates the maximum values of the magnetic susceptibility χ (= *dM*/*dH*) at different temperatures. To further support the presence of a phase transition in **17**, variable temperature magnetic susceptibility measurements were performed below 12 K at multiple applied *dc* fields (figure IV.12b). Consequently a (*T*, *H*) phase diagram was built for **17** (figure IV.12c) using the maximum susceptibilities found in the χ vs. *T* and *dM*/*dH* vs. *H* curves. From the phase diagram we find T_N is near 8 K and $H_C(0\ K) = 7500$ Oe, through extrapolation of the $H_C(T)$ line to the absolute zero temperature. The topology of this phase diagram is typical of a metamagnetic behavior.

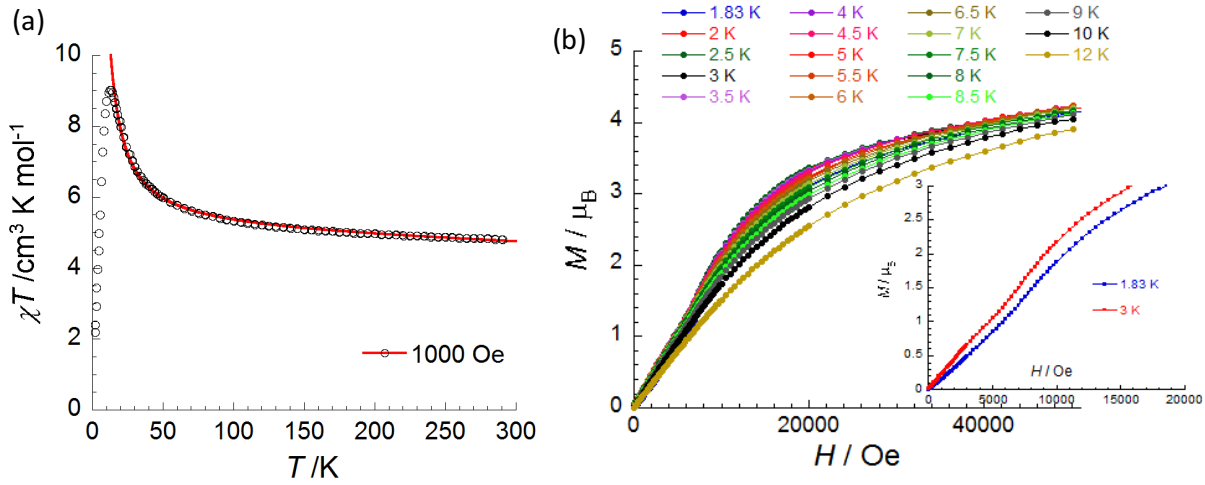

Figure IV.11. (a) The temperature dependence of the molar χT product at 1000 Oe between 280-1.8 K for **17** where the solid red line corresponds to the fit of molar χT product with Eq.IV.3. (b) The field dependence of the magnetization of **17** at multiple temperatures between 1.83 K and 12 K, inset: the expanded view of the *M*(*H*) curves at 1.83 K and 2 K exhibiting the sigmoidal shape.

The *M* vs. *H* data with a field sweep rate of 180 Oe/min below the Néel temperature ($T_N \approx 8$ K) reveals a hysteresis behavior for **17** (figure IV.13a). At 1.85 K, the remnant magnetization is about $M_r = 0.127\ \mu_B$ with a coercive field of 485 Oe. This suggests the presence of a spontaneous magnetization in the system in its antiferromagnetic phase. From the structural description of **17**, we have observed that the $\{[Fe^{II}(LN_3O_2)][Re^{IV}Cl_4(CN)_2]\}_{2.5}$ unit is the asymmetric repeating unit of the chain. Inside this asymmetric unit, we find the cyanido bridged N-Fe^{II}-N axes in the different

$[Fe^{II}(LN_3O_2)(NC)_2]$ portions are tilted towards one another; this is also observed in the C-Re^{IV}-C axes in this asymmetric unit. The small angles between different N-Fe^{II}-N axes result in a slight canting between the spins (or magnetic moments) along the chain direction. This canting is probably the origin of the magnetic hysteresis in **17** with a small coercive field. As expected, this hysteresis behavior is observed until the phase transition at 8 K. Therefore the three dimensionally oriented phase of the system is a canted antiferromagnetic phase. The coercive field is plotted as a function of temperature in figure IV.13b.

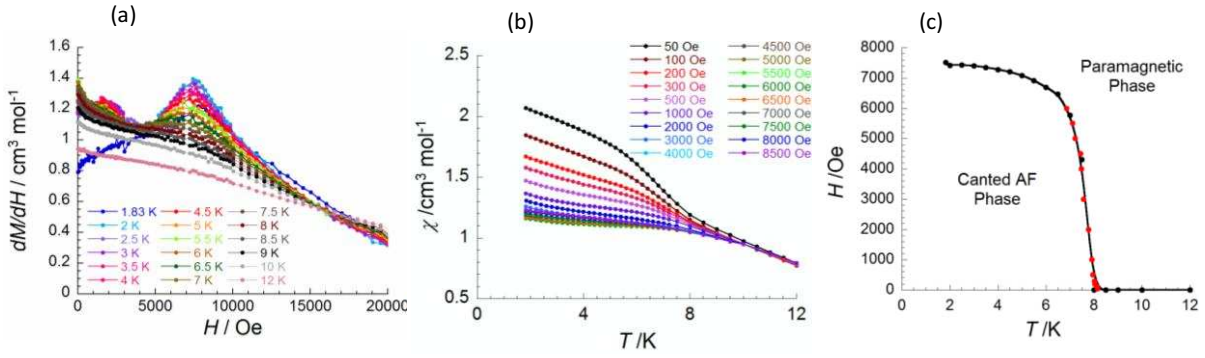

Figure IV.12. (a) Plot of the derivative of the magnetization for **17**, χ (*viz. dM/dH*), as a function of field at multiple temperatures to determine H_C at the maximum susceptibility. (b) The temperature dependence of the magnetic susceptibility of **17** at multiple applied *dc* fields. (c) Magnetic (*T*, *H*) phase diagram of **17** constructed from the maximum values of magnetic susceptibility (χ) from the χ vs. *T* (red circles) and *dM/dH* vs. *H* (black circles) data.

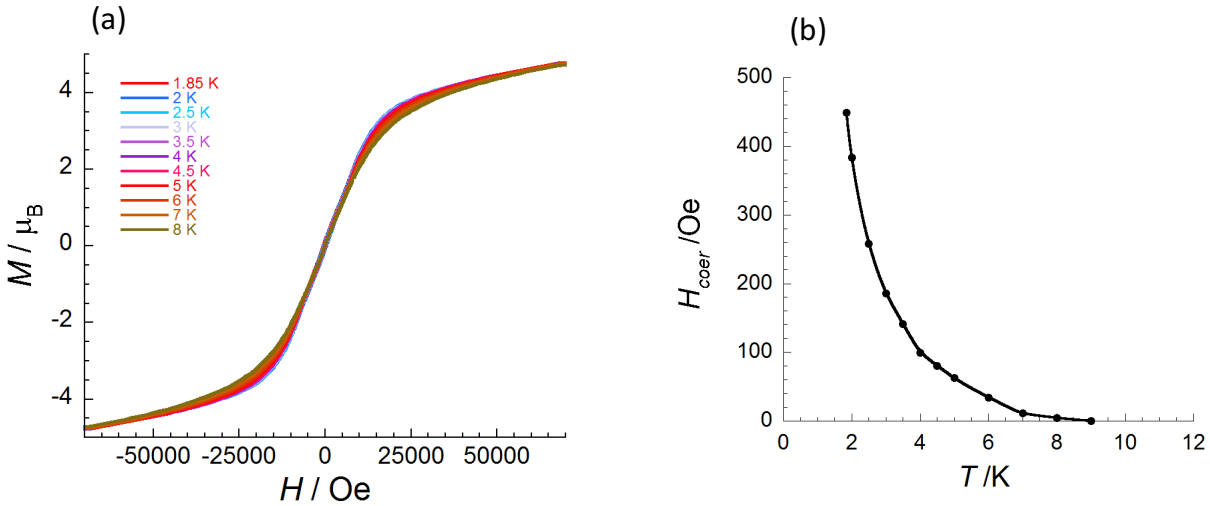

Figure IV.13. (a) The magnetic hysteresis $M = f(H)$ plots of **17** with the field sweep rate of 180 Oe/min below 8 K between -7 T and 7 T. Inset: the expanded view of same parameters at 1.85 K between -1.5 T and 1.5 T. (b) The temperature variation of the coercive field (H_{coer}) of **17** between 1.85-9 K.

In order to probe the magnetic dynamics of **17**, we have further performed *ac* magnetization measurements between 1.8-12 K and 1-10000 Hz. At zero applied field ($H_{dc} = 0$), the *ac* magnetic susceptibilities χ' (in-phase) and χ'' (out-of-phase) of **17** are found to be frequency dependent below 8

K. In the low temperature region, $\chi'(T)$ starts to decrease (figure IV.14a) and $\chi''(T)$ starts to increase (figure IV.14b), indicating slow relaxation of the magnetization. Furthermore, to study the relaxation time of the system $\chi'(\nu)$ (figure IV.14c) and $\chi''(\nu)$ (figure IV.14d) were measured below 4.4 K. The $\chi''(\nu)$ (figure IV.14d) curves exhibit temperature dependent maxima. The relaxation time (τ) of **17** is deduced as a function of the temperature T ($\tau(T) = 1/(2\pi\nu)$) from the maximum of the $\chi''(\nu)$ curves at different temperatures. The semilog plot of τ vs. $1/T$ (figure IV.14e) exhibits the temperature dependence of the relaxation time. According to an Arrhenius law, the relaxation time is an exponential function of temperature having the relation $\tau(T) = \tau_0 \exp(\Delta_\tau/k_B T)$ where τ_0 is the pre-exponential constant and Δ_τ is the energy needed to reverse the magnetization. Therefore a linear fit of the experimental τ vs. $1/T$ data (figure IV.14e) clearly demonstrates the thermally activated behavior of **17** and gives $\Delta_\tau/k_B = 36.8$ K with $\tau_0 = 8.4 \times 10^{-10}$ s at zero field.

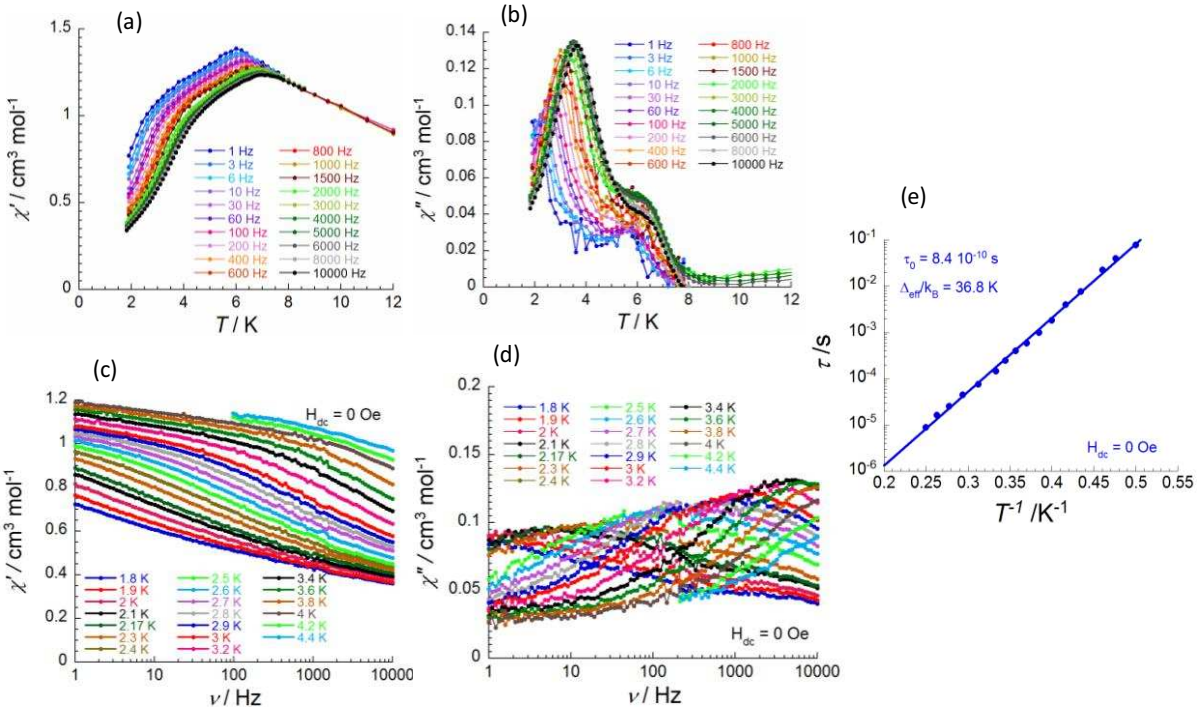

Figure IV.14. (a) to (d) Temperature and frequency dependence of the χ' (in-phase) and χ''(out-of-phase) parts of the *ac* magnetic susceptibility of **21** at $H_{dc} = 0$ Oe where $\chi'(T)$, $\chi''(T)$, $\chi'(\nu)$ and $\chi''(\nu)$ are represented in a, b, c, and d respectively. (e) Thermal variation of τ fitted to an Arrhénius law $\tau(T) = \tau_0 \exp(\Delta_\tau/k_B T)$.

Therefore in this $Re^{IV}Fe^{II}$ chain compound, we found the canted antiferromagnetic ground state exhibiting slow relaxation dynamics introduced by the one dimensional $Re^{IV}Fe^{II}$ object.

IV.4. Conclusions and perspectives

In this chapter we have discussed the structural and magnetic properties of newly synthesized one dimensional 3*d*-5*d* cyanido bridged 1:1 bimetallic systems. The cyclam-based compounds **14-16** displayed comparable crystal packing, as did the LN_3O_2-based compounds **17** and **18**.

We found all the M^{II} (M = Ni, Cu, Fe) ions in compounds **14-17** interact ferromagnetically with the Re^{IV} ions through the cyanido bridge. Comparing the Re^{IV}-Cu^{II} magnetic interaction through the cyanido bridge in **15** and **16** with that in the $(Bu_4N)[TpCuReCl_4(CN)_2]$ one-dimensional compound (Tp^{-}: hydrotris(pyrazol-1-yl)borate)[2] it is clear that the ferromagnetic exchange in **15** and **16** is much weaker. This likely results from the different coordination sites occupied by the cyanido groups on the Cu^{II} ion: axial in **15** and **16** versus equatorial for $(Bu_4N)[TpCuReCl_4(CN)_2]$ associated with long and shorter Cu-N bond distances, respectively. In **17**, the Re^{IV}-Fe^{II} interactions are found to be significantly ferromagnetic and also exhibit slow relaxation dynamics of magnetization in its canted antiferromagnetic ground state with a spin reversal barrier of 36.8 K.

We have also tried to build cyanido bridged M^{III}-Re^{IV} ($M = Fe^{III}$, Mn^{III}, Cr^{III}) compounds using molecular precursors based $[M^{III}(cyclam)]^{3+}$ having different counter anions (e.g, ClO_4^-, BF_4^-, CF_3CO^{2-} etc) using different solvent media (e.g, MeOH, MeCN, $MeNO_2$ etc). But unfortunately, we always found a pale green colored product (in the form of either a precipitate or small crystals) for all these attempts which was characterized as $(H_2cyclam)[Re^{IV}Cl_4(CN)_2]\cdot nS$ (nS = n number of solvent molecules) by single crystal X-ray diffraction. This observation implies that these 3*d* M^{III} ions, having a smaller ionic radius than the 3*d* M^{II} ions, are probably too small to be held in the cavity of cyclam in presence of the $[Re^{IV}Cl_4(CN)_2]^{2-}$ moiety. In case of the $Re^{IV}Mn^{II}$ compound even though we have not measured the magnetic properties, we can expect a Re^{IV}-Mn^{II} antiferromagnet exchange on the basis of of the $[Re^{IV}Cl_4(CN)_2][Mn^{II}(DMF)_4]$ chain reported earlier. [1]

In all these systems we have observed the interchain antiferromagnetic interactions leading to an AF or canted AF ground state. Furthermore, all the 1D network systems described in this chapter are individually neutral. So, no counter ions (ClO_4^-, Cl^- or Bu_4N^+) is found in the crystal packing that could separate the chains far from each other and this induce the minimization of interchain antiferromagnetic interactions. Therefore, in order to obtain such one dimensional heterometallic Re^{IV}-M systems with SCM properties the separation of the chains in their crystal packing is an obvious requirement.

IV.5. References

[1] T. D Harris, M.V. Bennett, R. Clérac, J. R. Long, *J. Am. Chem. Soc*., **2010,** 132, 3980.

[2] T. D. Harris, C. Coulon, R. Clérac, J. R. Long, *J. Am. Chem. Soc*., **2011**, 133, 123.

[3] B. Bosnich, M. L. Tobe, G. A. Webb, *Inorg Chem,* **1965**, 4, 1109.

[4] T. S. Venkatakrishnan, S. Sahoo, N. Bréfuel, C. Duhayon, C. Paulsen, A. L. Barra, S. Ramasesha, J. P. Sutter, *J. Am. Chem. Soc*., **2010**, 132, 6047.

[5] D. Zhang, H. Wang, Y. Chen, Z.-H. Ni, L. Tian, J. Jiang, *Inorg. Chem*., **2009**, 48, 12, 5488.

[6] L. J. Jongh, A. R. Miedena, Experiments on simple magnetic model systems. *Adv. In Physics*, **1974**, 23, 1.

[7] S. Chikazumi, *Physics of Ferromagnetism.* Clarendon Press: Oxford Science Publication: Oxford, **1997**, 521.

[8] C. Coulon, S. Moreau, Physique statistique et thermodynamique. **2000**, *Dunod Eds*., Paris, France, p.342-354.

[9] P. M. Chaikin, T. C. Lubensky, *Principles of Condensed Matter Physics*. **1995**, Cambridge University Press, Cambridge, UK, p. 146-151.

[10] (a) M. Drillon, E. Coronado, D. Beltran, R. Georges, *Chem. Phys.* **1983**, 79, 449. (b) R. Georges, J. J. Borras-Almenar, E. Coronado, J. Curely, M. Drillon, *Magnetism: Molecules to Materials I: Models and Experiments*; Miller, J. S., Drillon, M., Eds; Wiley-VCH: Weinheim, Germany, **2002**.

[11] (a) T. C. Stamatatos, V. Nastopoulos, A. J. Tasiopoulos, E. E. Moushi, W. Wernsdorfer, G. Christou, S. P. Perpeles, *Inorg. Chem*., **2008**, 47, 10081. (b) S. Hayami, G. Juhasz, Y. Maeda, T. Yokoyama, O. Sato, *Inorg. Chem*., **2005**, 44, 7289. (c) Y.-Z. Zhang, B.-W. Wang, O. Sato, S. Gao, *Chem.Comm*., **2010**, 46, 6959. (d) X.-Y. Wang, A. V. Prosvirin, K. R. Dunbar, *Angew. Chem. Int. Ed.*, **2010**, 49, 5081.

[12] (a) X. Feng, J. Liu, T. D. Harris, S. Hill, J. R. Long, *J. Am. Chem. Soc.*, **2012**, 134, 7521. (b) T. D. Harris, H. S. Soo, C. J. Chang, J. R. Long, *Inorg. Chim. Acta.*, **2011**, 369, 82.

CHAPTER V

Ru^{III}-Mn^{III}-Schiff base systems

V.1. Introduction

In order to obtain molecule based 3*d*-4*d* magnetic materials we have synthesized Mn^{III}-Ru^{III} heterometallic systems where the Mn^{III} ion has $3d^4$ electrons (S = 2) and Ru^{III} is low spin with $4d^5$ electronic configuration (S = 1/2). The magnetic interaction between Ru^{III} and Mn^{III} ions is known to be ferromagnetic from the example of one dimensional Ru^{III}-Mn^{III} compound $[Ru^{III}(salen)(CN)_2][Mn^{III}(L)]$ (L = *N, N′*-(1- methylethylene)bis(2-hydroxynaphthalene-1-carbaldehydene iminate) dianion).[1] In this chapter, we will discuss new molecular systems obtained from the reaction between the different types of Mn^{III}-Schiff base complexes[2,7] and *trans*-$(Ph_4P)[Ru^{III}(salen)(CN)_2]\cdot MeOH\cdot H_2O$[1,8] or *trans*-$(Bu_4N)[Ru^{III}(5\text{-Cl-saltmen})(CN)_2]$. Interestingly, depending upon the Mn^{III}-Schiff base precursor used, we have obtained Mn^{III}-Ru^{III} complexes with different nuclearity: from dinuclear to one dimensional compounds. The synthesis, crystal structure and the magnetic characterization of these Mn^{III} and Ru^{III} based molecular precursors have been thoroughly discussed in chapter II, thus we will discuss here only the obtained final materials.

V.2. Ru^{III}-Mn^{III}-Schiff base molecular systems

Based on the Mn^{III}-Schiff base complexes and the trans-$Ru^{III}(CN)_2$-Schiff base precursors, we have synthesized two Ru^{III}-Mn^{III} dinuclear (**19** and **20**), one Ru^{III}_2-Mn^{III}_4 hexanuclear (**21**) and one Ru^{III}-Mn^{III} one dimensional (**22**) systems. In all these compounds, the Mn^{III} and Ru^{III} ions are bridged with the cyanido group so that the Ru^{III} and Mn^{III} ions are respectively connected to the carbon and nitrogen atoms of the cyanido group. The following sections of this chapter present the synthesis, the single crystal X-ray structures, and the magnetic properties of these Ru^{III}-Mn^{III} compounds.

V.2.1. Synthesis

V.2.1.1. $[Mn^{III}(4\text{-OH-saltmen})][Ru^{III}(salen)(CN)_2]\cdot H_2O$ (19)

$[Mn^{III}(4\text{-HO-saltmen})(H_2O)_2](ClO_4)\cdot H_2O$ (0.0057 g, 0.01 mmol) was dissolved in 5 mL of methanol in a vial and a 2 mL methanol solution of *trans*-$(Ph_4P)[Ru^{III}(salen)(CN)_2]\cdot MeOH\cdot H_2O$ (0.0081 g, 0.01 mmol) was slowly added. After 6 hours small brown needle shaped crystals were collected by filtration. The yield of the product was about 75 % on the basis of the Mn^{III}-Schiff base precursor. Elemental analysis calculated (%) for $C_{38}H_{38}MnN_6O_7Ru$ (M = 846.76 g/mol): C 53.90, H 4.52, N 9.93; found (%) as C 54.06, H 4.61, N 9.89; IR: $\bar{\nu}$ = 2106 (bridging C≡N stretch), 2093 (non bridging C≡N stretch) 1596, 1604 (C=N stretch) cm^{-1}.

V.2.1.2. $[Mn^{III}(4\text{-MeO-saltmen})][Ru^{III}(5\text{-Cl-saltmen})(CN)_2]\cdot MeCN$ (20)

$[Mn^{III}(4\text{-MeO-saltmen})(H_2O)_2](ClO_4)\cdot 2H_2O$ (0.0061 g, 0.01 mmol) was dissolved in 2 ml of acetonitrile in a vial and a 2 mL methanol solution of *trans*-$(Bu_4N)[Ru^{III}(5\text{-Cl-saltmen})(CN)_2]$ (0.0079 g, 0.01 mmol) was slowly added. The vial opening was covered with the parafilm followed by making small holes in it with a needle in order to ensure the slow evaporation. The mixture was kept for slow evaporation at room temperature. After two days, small brown block-shaped crystals were collected by filtration. The yield of the product was about 60 % on the basis of the Mn^{III}-Schiff base precursor. Elemental analysis calculated (%) for $C_{46}H_{49}Cl_2MnN_7O_6Ru$ (M = 1022.83 g/mol): C 54.02, H 4.83, N 9.59; found (%) as C 54.12, H 4.78, N 9.64; IR: ν = 2104 (bridging C≡N stretch), 1598, 1611 (C=N stretch) cm^{-1}.

V.2.1.3. $[Mn^{III}(saltmen)]_4[Ru^{III}(salen)(CN)_2]_2.(ClO_4)_2\cdot 2H_2O$ (21)

To a 5 mL methanol solution of of $[Mn^{III}_2(saltmen)_2(H_2O)_2](ClO_4)_2$ (0.0099 g, 0.01mmol) a 2 mL methanol solution of *trans*-$(Ph_4P)[Ru^{III}(salen)(CN)_2]\cdot MeOH\cdot H_2O$ (0.0081 g, 0.01 mmol) was added dropwise, followed by the addition of 0.5 mL distilled water. The mixture was kept for slow evaporation at room temperature. After 2 days, brown block-shaped crystals appeared at the bottom of the vial. The crystals were collected by filtration. The yield of the product was 80 % on the basis of the Mn^{III}- Schiff base precursor. Elemental analysis calculated (%) for $C_{116}H_{120}Cl_2Mn_4N_{16}O_{22}Ru_2$ (M = 2583.83 g/mol): C 53.94, H 4.68, N 8.68; found (%) as C 53.99, H 4.60, N 8.60; IR : $\bar{\nu}$ = 2110 (C≡N stretch), 1590, 1613 (C=N stretch), 1089.1116 (Cl-O stretch) cm^{-1}.

Changing the reaction conditions (solvent medium), we obtained the same compound **21** when a 2 mL methanol solution of *trans*-$(Ph_4P)[Ru^{III}(salen)(CN)_2]\cdot MeOH\cdot H_2O$ (0.0081 g, 0.01 mmol) was added to a 3 mL acetonitrile solution of of $[Mn^{III}_2(saltmen)_2(H_2O)_2](ClO_4)_2$ (0.0099 g, 0.01 mmol) followed by the addition of 0.5 mL distilled water.

V.2.1.4. $[Mn^{III}(5\text{-Cl-saltmen})][Ru^{III}(salen)(CN)_2]\cdot 2MeCN$ (22)

A 2 mL acetonitrile solution of *trans*-$(Ph_4P)[Ru^{III}(salen)(CN)_2]\cdot MeOH\cdot H_2O$ (0.0161 g, 0.02 mmol) was added to a 3 mL acetonitrile solution of of $[Mn^{III}_2(5\text{-Cl-saltmen})_2(H_2O)_2](ClO_4)_2$ (0.0113 g, 0.01 mmol). The solution was then kept for slow evaporation at room temperature. After one day, tiny dark greenish brown needle-like crystals were found. The crystals were separated by filtration and the yield of the product was 70 % on the basis of the Mn^{III}-Schiff base precursor. Elemental analysis

calculated (%) for $C_{84}H_{80}Cl_4Mn_2N_{16}O_8Ru_2$ (M = 1895.46 g/mol): C 53.23, H 4.25, N 11.82; found (%) as C 53.41, H 4.40, N 11.63; IR (KBr): $\bar{\nu}$ = 2109 (C≡N stretch), 1596, 1615 (C=N stretch) cm^{-1}.

V.2.2. X-ray crystal structure

All the Ru^{III}-Mn^{III} systems crystallized in the triclinic crystal system and P-1 space group. The crystallographic parameters of **19-22** are summarized in table V.1.

Table V.1 Crystal data and structure refinement for compounds **19-22**.

Compounds	**19**	**20**	**21**	**22**
Sum formula	$C_{38}H_{38}MnN_6O_8Ru$	$C_{46}H_{49}Cl_2MnN_7O_6Ru$	$C_{116}H_{120}Cl_2Mn_4N_{16}O_{22}Ru_2$	$C_{84}H_{80}Cl_4Mn_2N_{16}O_8Ru_2$
MW (g/mol)	864.77	1022.83	2583.83	1895.46
Temp. (K)	120(2)	100(2)	120(2)	120(2)
Crystal System	Triclinic	Triclinic	Triclinic	Triclinic
Space group	P-1	P-1	P-1	P-1
a (Å)	11.464(5)	12.869(5)	11.337(5)	13.458(3)
b (Å)	12.284(5)	13.752(5)	13.434(5)	16.098(3)
c (Å)	13.208(5)	14.055(5)	19.371(5)	20.760(4)
α (°)	87.621(5)	86.008(5)	72.449(5)	74.89(3)
β (°)	83.396(5)	64.684(5)	79.733(5)	79.68(3)
γ (°)	82.694(5)	83.265(5)	83.720(5)	75.49(6)
Volume ($Å^3$)	1832.0(13)	2232.5(4)	2763.0(17)	4172.3(17)
Z	2	2	1	2
Density ($g.cm^{-3}$)	1.568	1.522	1.550	1.509
$\mu_{MoK\alpha}$ (mm^{-1})	0.819	0.798	0.838	0.845
F_{000}	862	1050	1322	1932
GooF	0.990	1.030	1.069	1.042
[a]R_1 ($I > 2.00\sigma(I)$)	0.1375	0.0712	0.0674	0.0486
[b]wR_2	0.4029	0.2260	0.1936	0.1888

[a]$R_1 = \Sigma ||F_0| - |F_C|| / \Sigma|F_0|$, [b]$wR_2 = [\Sigma w(F_0^2 - F_C^2)^2 / \Sigma w(F_0^2)^2]^{1/2}$, $w = 1/[\sigma^2 F_0^2 + (0.0313P)^2 + 1.5564P]$; where $P = (F_0^2 + 2F_C^2)/3$

In **19**, one $[Mn^{III}(4\text{-HO-saltmen})]^+$ and one $[Ru^{III}(salen)(CN)_2]^-$ moiety are connected to each other via one of the cyanido groups of the $[Ru^{III}(salen)(CN)_2]^-$ anion (figure V.1a). Compound **20** is also a dinuclear compound composed also of $[Mn^{III}(4\text{-MeO-saltmen})]^+$ and one $[Ru^{III}(5\text{-Cl-saltmen})(CN)_2]^-$ moiety which are connected via one of the cyanido groups of the Ru^{III}-based fragment (figure V.2a). In both molecules, the Ru^{III} and Mn^{III} ions are in a distorted octahedral and distorted square pyramidal environment, respectively. The four equatorial coordination sites of the hexacoordinated Ru^{III} ion are occupied with two imino nitrogen and two phenoxido oxygen atoms of the salen ligand in **19** and the 5-Cl-saltmen ligand in **20**; and axially coordinated with the carbon atoms of two cyanido groups. The nitrogen atom of one of these cyanido groups is connected with the pentacoordinated Mn^{III} ion. The other equatorial coordination sites of the Mn^{III} ion are occupied respectively by the nitrogen and oxygen atoms of 4-HO-saltmen for **19** and 4-MeO-saltmen in **20**. In **19,** the equatorial Mn^{III}-N distances are 1.97(1) Å and 1.94(1) Å, the equatorial Mn^{III}-O distances are 1.86(1) Å and 1.85(2) Å, the Mn^{III}-$N_{cyanido}$ distance is 2.15(1) Å. In the salen plane of **19** the Ru^{III}-N

distances are 2.02(1) Å and 1.97(1) Å and the Ru^{III}-O distances are 2.02(1) Å. In case of **20**, the equatorial Mn^{III}-N distances are 1.99(8) Å and 1.98(1) Å, the equatorial Mn^{III}-O distances are 1.89(1) Å and 1.89(8) Å, the Mn^{III}-$N_{cyanido}$ distance is 2.16(1) Å, the equatorial Ru^{III}-N distances are 1.99(5) Å and 1.98(8) Å and the Ru^{III}-O distances are 2.01(7) Å and 2.00(1) Å.

In **19** the Mn-N-C angle is 157.9(1) ° which is quite non-linear and provides a bent geometry to the molecule around the molecular axis. This angle is 175.4(7) ° in **20** and therefore the Mn-N-C-Ru molecular axis is much closer to linearity in **20**.

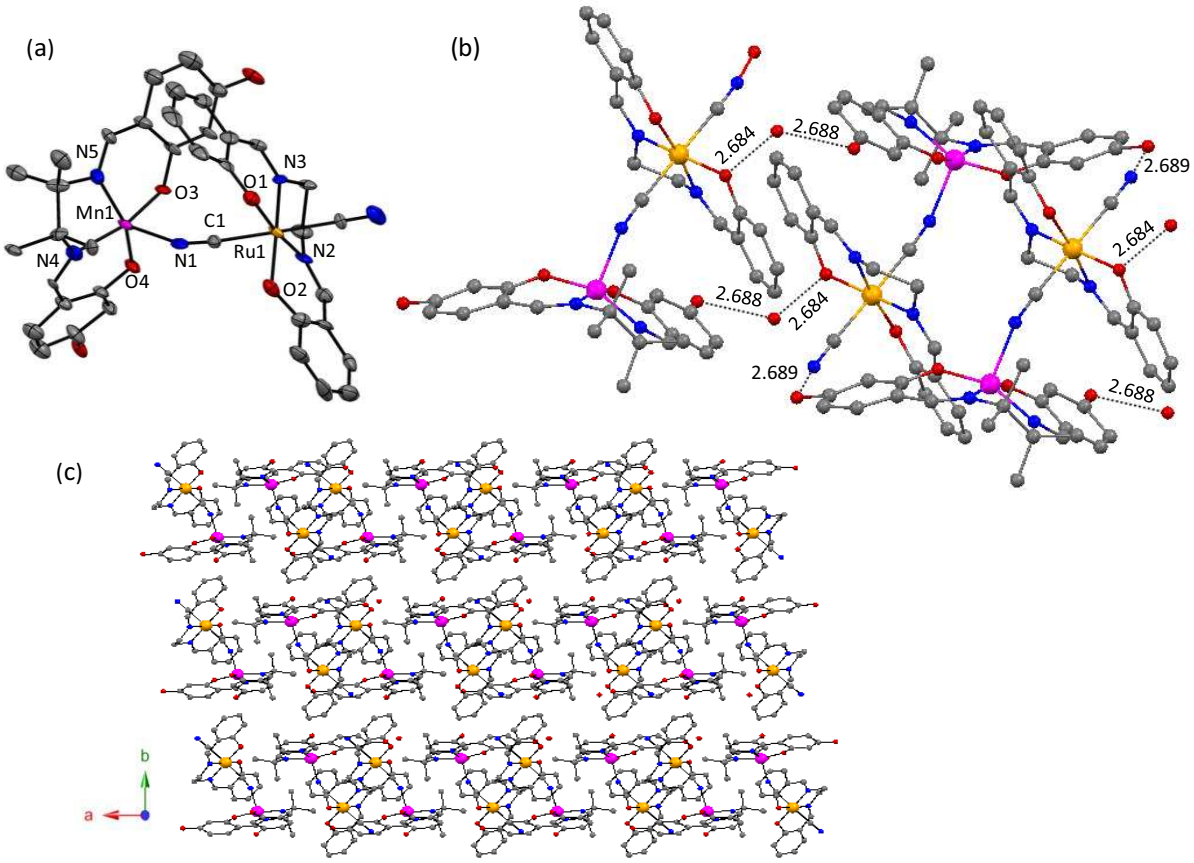

Figure V. (a) ORTEP type view of the discrete molecule of **19**, where the grey, blue, red, magenta and orange spheres (shown in 50 % thermal ellipsoids) represent the C, N, O, Mn and Ru atoms respectively. The H atoms and solvent molecules (water) are omitted for clarity (b) View of the hydrogen bonding supramolecular interactions. (c) View of the crystal packing in the *ab* plane.

In **19**, a number of intermolecular hydrogen bonding interactions are found in the packing structure (figure V.1b). The non-bridging cyanido nitrogen atom is involved in a hydrogen bonding short contact with one of the OH groups of the 4-HO-saltmen of a neighboring molecule, with an average distance of *ca.* $d_{O...O}$ = 2.689 Å. Cocrystallizing water molecules in **19** not only fill the void in the crystal packing but also mediate the H-bonding interactions (*ca.* $d_{O...O}$ = 2.684-2.688 Å) between an OH group of one molecule and a phenoxido oxygen atom of a neighboring molecule (figure V.1b).

These supramolecular interactions result in the close packing of the molecules; the molecular packing of **19** in *ab* plane is displayed in figure V.1c.

In the crystal structure of **20**, the $[Mn^{III}(4\text{-MeO-saltmen})][Ru^{III}(5\text{-Cl-saltmen})(CN)_2]$ pairs are in close contact; two $[Mn^{III}(4\text{-MeO-saltmen})]$ moieties orient face to face forming a dinuclear $[Mn^{III}(4MeO\text{-saltmen})]_2$ unit sandwiched in the middle of two $[Ru^{III}(5\text{-Cl-saltmen})(CN)_2]$ fragments (figure V.2b). In this dinuclear unit, the Mn^{III}-O^*_{phen} distance; i.e., the distance between the Mn^{III} ion of one $[Mn^{III}(4\text{-MeO-saltmen})]$ group and the phenoxido oxygen atom of the nearest $[Mn^{III}(4\text{-MeO-saltmen})]$ group is about 3.09 Å. Compared to the Mn^{III}-Schiff base complexes in the literature[2] and also described in chapter II, section II.3.1 of this thesis, this Mn^{III}-O^*_{phen} distance in $[Mn^{III}(4\text{-MeO-saltmen})]_2$ unit is too high to claim that the Mn^{III} ion has an octahedral crystal field with an axial Mn^{III}-O^*_{phen} bond. The π-stacking interactions (~ 3.48 Å) between these $[Mn^{III}(4\text{-MeO-saltmen})]^+$ groups is another driving force causing them to pack in a dinuclear fashion (figure V.2b). The void in the crystal structure of **20** is filled with acetonitrile molecules. In these acetonitrile molecules, the nitrogen and the methyl carbon occupy the same position with an almost 50 % statistical distribution. Due to this disorder, the acetonitrile molecules were not refined anisotropically.

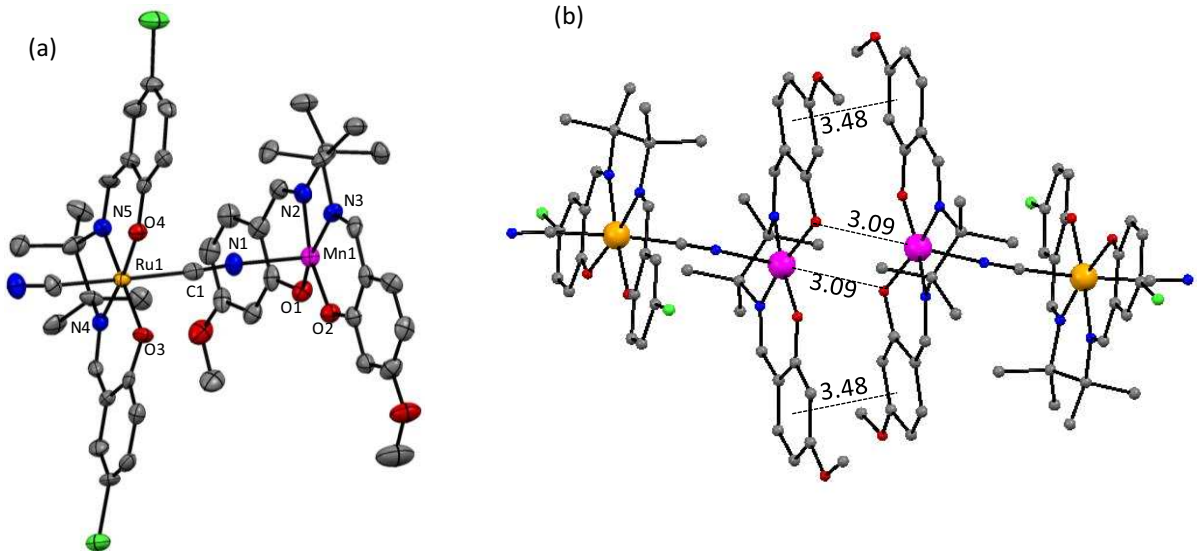

Figure V.2. (a) ORTEP type view of the molecular view of **20**; where the grey, blue, red, green, magenta and orange spheres (shown as 50 % thermal ellipsoids) represent the C, N, O, Cl, Mn and Ru atoms respectively. H atoms and the solvent molecules are omitted for clarity (b) The Mn^{III}-O^*_{phen} and the π-stacking interactions found in the crystal packing of **20**.

Compound **21** is an interesting hexanuclear complex having four $[Mn^{III}(saltmen)]^+$ and two $[Ru^{III}(salen)(CN)_2]^-$ units in each molecule (figure V.3). The two Ru^{III} ions in **21** are in an octahedral environment where the salen ligand occupies the equatorial coordination sites and the axial positions are connected to the carbon atoms of two cyanido groups. In the center of complex **21** there is a dinuclear $[Mn^{III}_2(saltmen)_2]^{2+}$ motif formed via interactions with the phenoxido oxygen atoms as previously observed.[2] These two Mn^{III} ions are in an octahedral ligand environment where they are

equatorially coordinated to the N and O atoms of the saltmen ligand and the remaining axial position the Mn^{III} ions are connected to the cyanido nitrogen atoms of two $[Ru^{III}(salen)(CN)_2]^-$ units. The other cyanido groups of the $[Ru^{III}(salen)(CN)_2]^-$ units are connected to another pentacoordinated Mn^{III} ion via the N atoms; thus forming a Mn^{III}-Ru^{III}-Mn^{III}_2-Ru^{III}-Mn^{III} hexanuclear unit. On the other hand, this hexanuclear unit may be considered as a dimer of a Mn^{III}-Ru^{III}-Mn^{III} fragment connected to each other via the phenoxido oxygen bridge. The terminal Mn^{III} ions are in distorted square pyramidal ligand environment where the square plane contains the Schiff base saltmen ligand having two nitrogen donor atoms and the two oxygen donor atoms.

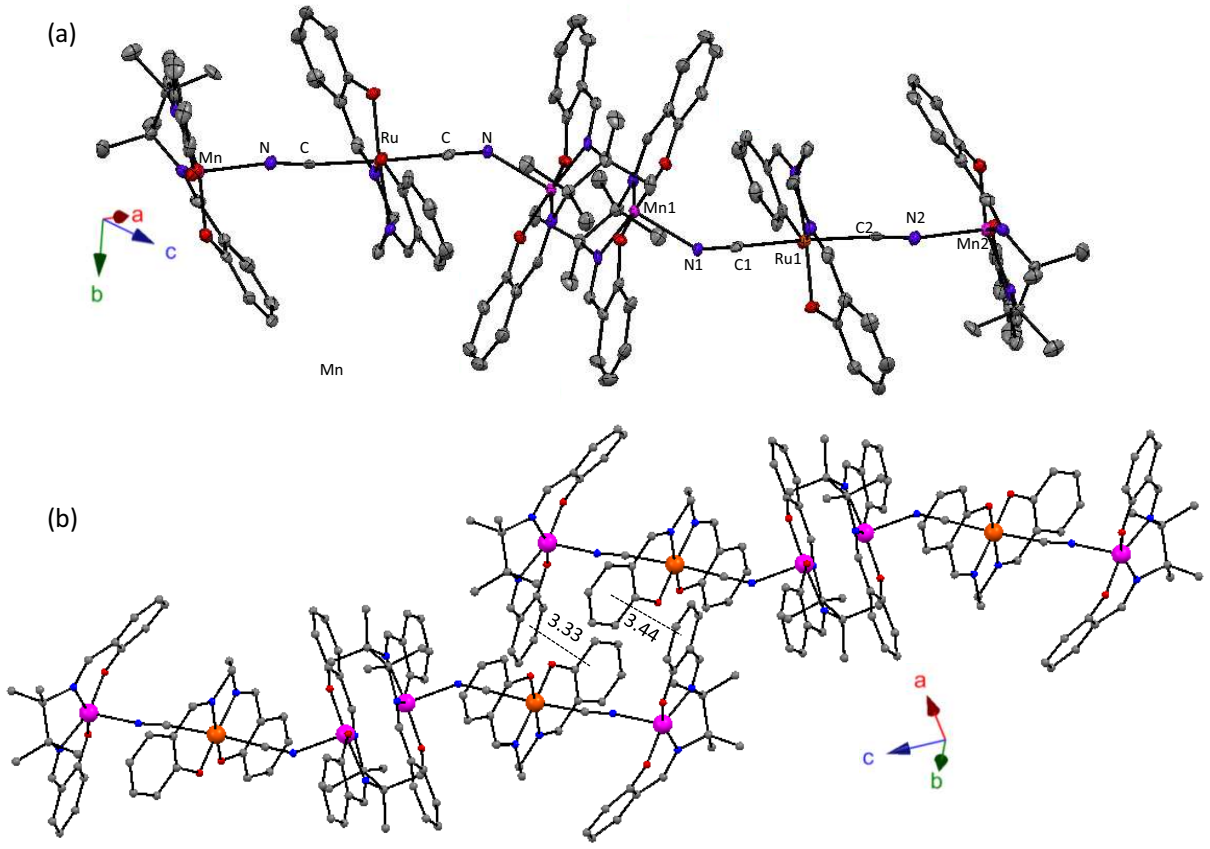

Figure V.3. (a) OTTEP type view of the molecular structure of **21**, where the grey, blue, red, green, magenta and orange spheres (shown as 50 % thermal ellipsoids) represent the C, N, O, Cl, Mn and Ru atoms respectively. H atoms, solvent molecules(water) and counter ions (ClO_4^-) are not shown for clarity (b) View of the structure emphasizing the π-stacking interactions between the neighboring hexanuclear units in **21**.

Two perchlorate ions neutralize the charge of the hexanuclear unit. The Mn-Mn distance of the central dinuclear Mn^{III}-Schiff base moiety is about 3.408 Å with a Mn-O*$_{Phen}$ distance of 2.578(2) Å. The inversion center of this hexanuclear moiety resides in the middle of the core Mn^{III}_2 unit. In **21** the equatorial Mn^{III}-N distances lies between 1.977(6) and 1.994(5) Å, whereas the equatorial Mn^{III}-O distances range from 1.867(5) to 1.891(5) Å. The equatorial Ru^{III}-N distances are 2.018(6) Å and 2.000(5) Å, the equatorial Ru^{III}-O distances are 2.015(4) Å and 2.007(6) Å. The Mn-N-C angle

belonging to the inner dinuclear Mn^{III}-Schiff base is 144.8(5)° and that belonging to the outer pentacoordinated Mn^{III}-Schiff base is 170.7(6)°. Water molecules fill the gap in the crystal packing and have H-bonding interactions with the perchlorate anions of about 3.19 Å. The π-stacking interactions between the aromatic rings of neighboring hexanuclear units as displayed in figure V.3b also contribute to close packing of the molecules in the crystal structure.

The hexanuclear compound **21** is quite comparable with the $Re^{IV}Mn^{III}$ hexanuclear compound **7** (chapter III, section III.2.3). In **7** the terminal Mn^{III} ions are hexacoordinated and the $Re^{IV}_2Mn^{III}_4$ units are terminated with the water molecules axially coordinated to the Mn^{III} ions. Similar to **7** in case of **21** there is two kinds of Mn-N-C angle, where the terminal one is more linear compared to the one linked to Mn^{III}_2 unit. The overall charge of a $Ru^{III}_2Mn^{III}_4$ unit in **21** is +2, whereas in **7** the $Re^{IV}_2Mn^{III}_4$ units are neutral in charge.

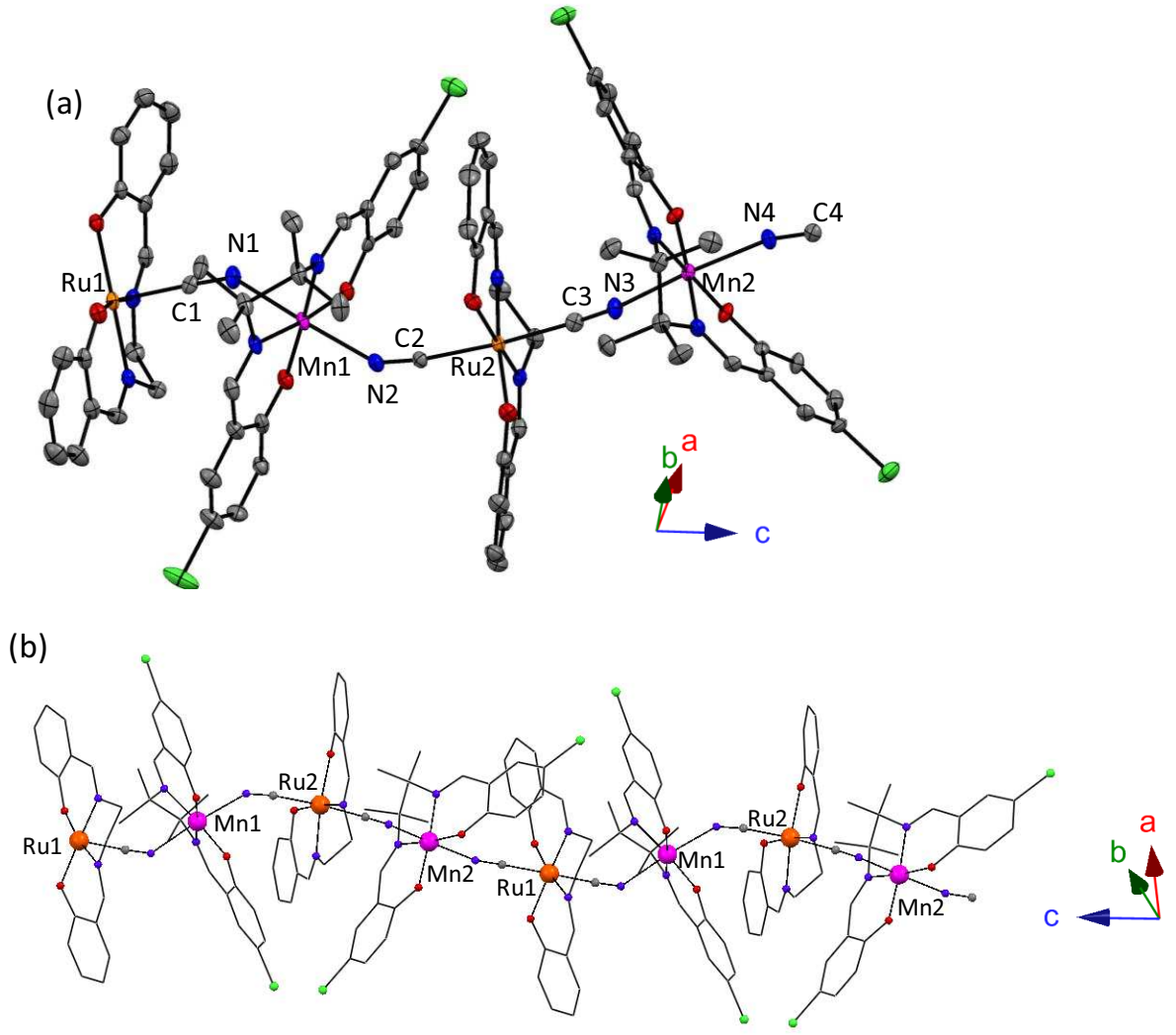

Figure V.4. (a) ORTEP type view of the crystal structure of **22**; where the grey, blue, red, green, magenta and orange spheres (shown as 50 % thermal ellipsoids) represent the C, N, O, Cl, Mn and Ru atoms respectively. H atoms and solvent molecules are not shown for clarity (b) View emphasizing the alternative arrangement of the two different kinds of Ru^{III} and Mn^{III} ions in the chain in **22** exhibiting a zigzag pattern.

Compound **22** is a one dimensional heterometallic coordination polymer where the Ru^{III} and Mn^{III} ions are alternatively arranged in one dimension through cyanido bridge (figure V.4). All the metal ions are in an octahedral environment, where the Mn^{III} and the Ru^{III} ions respectively are embraced by 5-Cl-saltmen and salen with four equatorial bonds to the two imino nitrogen and the two phenoxido oxygen atoms of the Schiff base ligands. The axial coordination sites of the Ru^{III} ions are occupied by to the carbon atoms of the bridging cyanido. The nitrogen atoms of these cyanido groups are connected to the Mn^{III} ions. Two acetonitrile molecules fill the void spaces in the crystal packing. Due to slightly different coordination sphere, two kinds of Mn^{III} ions (Mn1 and Mn2 in figure V.4b) and also two kinds of Ru^{III} ions (Ru1 and Ru2 in figure V.4b) are present in the structure. Therefore the tetranuclear Ru1-Mn1-Ru2-Mn2 motif acts as the repeating unit along the chain (figure V.4b). In this tetranuclear Ru1-Mn1-Ru2-Mn2 fragment, all the Mn-N-C angles are mutually different. Mn1 is involved in Mn-N-C angles of 140.1(4)° and 147.2(4)° with the cyanido group connected to the Ru1 and Ru2; while the Mn2-N-C angles are 171.1(5)° and 166.0(4)° with the cyanido group connected to Ru2 and Ru1 respectively, resulting in a zigzag chain pattern.

The equatorial Mn^{III}-O distances are ranging between the 1.897(3) Å and 1.905(4) Å, Mn^{III}-N distances are found between 1.998(4) Å and 2.009(4) Å. In the equatorial Ru^{III} center, the Ru^{III}-O distances are found between 2.014(4) Å and 2.034(3) Å, whereas the Ru^{III}-N distances range between 1.994(4) Å and 2.009(5) Å.

V.2.3. Magnetic properties

Due to the time limitation of our research work, we were able to measure the magnetic properties of only compounds **21** and **22** using polycrystalline samples.

V.2.1.1. $[Mn^{III}(saltmen)]_4[Ru^{III}(salen)(CN)_2]_2\cdot(ClO_4)_2\cdot 2H_2O$ (21)

The magnetic susceptibility of **21** as a function of temperature at an applied *dc* field of 1000 Oe is plotted as χT vs. T (figure V.5a) between 270-1.8 K. At 270 K the χT values is 12.9 cm^3K/mol which is in very good agreement with the theoretical value (12.75 cm^3K/mol) for a system having four Mn^{III} (S =2) and two Ru^{III} (S = 1/2) ion with g = 2 for both metal ions. With lowering of temperature, the χT product remains almost the same until 100 K and then this product rapidly increases to 34.9 cm^3K/mol at 1.8 K. This behavior of the magnetic susceptibility indicates the presence of a significant ferromagnetic interaction between the Mn^{III} and Ru^{III} ions whereas the interaction between the core dinuclear Mn^{III} unit is already known to be weakly ferromagnetic.[2] In order to probe the magnetic

exchange between the Mn^{III} and Ru^{III} ions (*J*), the χT vs. *T* data was modeled with a Mn^{III}-Ru^{III}-Mn^{III} trinuclear model (neglecting the Mn^{III}-Mn^{III} ferromagnetic exchange) using the following isotropic Heisenberg Hamiltonian

$$\boldsymbol{H = -2J\,(S_{Mn}.S_{Ru} + S_{Ru}.S_{Mn})} \qquad \textbf{Eq. V.1}$$

where S_{Mn} = 2, S_{Ru} = 1/2, and *J* is the Ru^{III}-Mn^{III} magnetic interaction (figure V.5b). Using this trinuclear model in the Van Vleck equation, [3] the expression of the magnetic susceptibility χ of the Mn^{III}-Ru^{III}-Mn^{III} trimer becomes:[4, 5]

$$\chi_{\text{trimer}} = \frac{Ng_{av}^2\mu_B^2}{4k_BT}\left[\frac{\text{A}}{\text{B}}\right] \qquad \textbf{Eq.V.2}$$

where, g_{av} is the average Landé factor corresponding to individual Mn^{III} and Ru^{III} ions

A = 165 + [*exp*(-6*x*) + *exp*(-4*x*)] + 10[*exp*(-7*x*) + *exp*(-3*x*)] + 35[*exp*(-8*x*) + *exp*(-2*x*)] + 84[*exp*(-9*x*) + *exp*(-*x*)]

and

B = 5 + [*exp*(-6*x*) + *exp*(-4*x*)] + 2[*exp*(-7*x*) + *exp*(-3*x*)] + 3[*exp*(-8*x*) + *exp*(-2*x*)] + 4[*exp*(-9*x*) + *exp*(-*x*)]

with $x = J/k_BT$. This trinuclear model nicely corresponds to the experimental data above 15 K (the red solid line in figure V.5b) and yields g_{av} = 2.81(6) and J/k_B = + 5.4(1) K, leading to a spin ground state of S_T = 9/2 for the coupling Mn^{III}-Ru^{III}-Mn^{III} trinuclear unit. In order to estimate the Mn^{III}-Mn^{III} magnetic below 15 K, the magnetic interaction was treated in the frame of the mean field approximation according to the following equation,

$$\boldsymbol{\chi T = \chi_{trimer} T/(1 - cJ'\chi_{trimer})} \qquad \textbf{Eq.V.3}$$

where $c = 2/Ng^2\mu_B^2$. This mean field model fits the experimental χT data above 6 K (given by the solid red line in figure V.5c) and yields g_{av} = 2.81(2), J/k_B = + 4.2(2) K and zJ'/k_B = + 0.06(1) K. This set of magnetic interaction implies that the hexanuclear complex possess an S_T= 9 spin ground state.

The low temperature magnetization of **21** has also been measured between 1.86-8 K as a function of applied field until 7 T (figure V.6). At 1.86 K the magnetization curve reaches the value 17.2 μ_B which is close to the expected magnetization at saturation for an S_T = 9 complex (theoretically the magnetization value should be 18 μ_B at saturation). In the present case there are two Mn^{III}-Ru^{III}-Mn^{III} units (*S* = 9/2) interacting ferromagnetically and therefore the nature of magnetization curves are consistent with the spin ground state of the Mn^{III}-Ru^{III}-Mn^{III}_2-Ru^{III}-Mn^{III} hexanuclear unit.

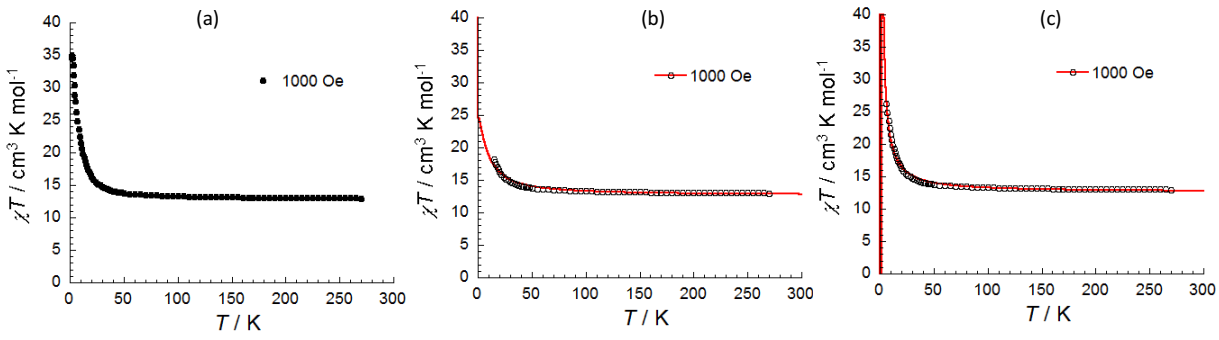

Figure V.5. (a) The plot of χT vs. T for **21** at 1000 Oe *dc* applied field. (b) The solid red line corresponds to the fit of χT vs. T experimental data at 1000 Oe (shown in black hollow circles) above 15 K with the trinuclear Mn^{III}-Ru^{III}-Mn^{III} model using the Heisenberg Hamiltonian $\boldsymbol{H = -2J\,(S_{Mn}.S_{Ru} + S_{Ru}.S_{Mn})}$. (c) The solid red line is the extended fit of the experimental data using the mean field approximation over the Mn^{III}-Ru^{III}-Mn^{III} trinuclear model using the expression $\boldsymbol{\chi T = \chi_{trimer} T/(1 - cJ'\chi_{trimer})}$.

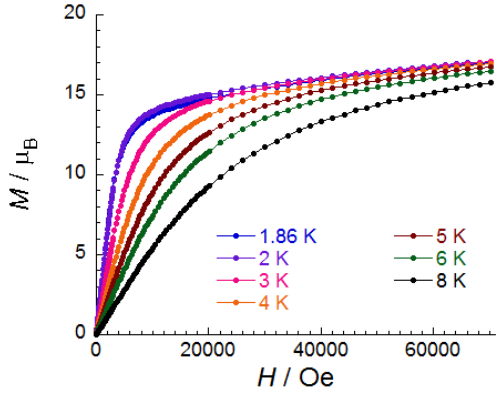

Figure V.6. The plot of M vs. H for **21** at multiple temperatures between 1.86 and 8 K.

In order to probe the magnetic dynamics of **21**, we have further performed *ac* magnetization measurements between 1.8-7 K and 1-1500 Hz. At zero applied field (H_{dc} = 0), the magnetic susceptibilities χ' (in-phase) and χ'' (out-of-phase) of **21** are found to be frequency dependent below 3 K which is the indication of single-molecule magnet behavior. For **21**, the plots of $\chi'(T)$, and $\chi''(T)$ at different *ac* frequency and the $\chi'(\nu)$ and $\chi''(\nu)$ at different temperatures are displayed at figure V.7.

According to the *ac* magnetic measurements below 2.5 K, $\chi'(T)$ starts to decrease (figure V.7a) and $\chi''(T)$ starts to increase (figure V.7b), indicating slow relaxation of magnetization. As additional evidence of the slow relaxation, a clear frequency dependent maxima in the $\chi''(\nu)$ plot at 1.83 K and 1.9 K (figure V.7d) is observed. Nevertheless above 1.9 K, the maxima have the characteristic frequency higher than 1500 Hz, i.e., beyond our experimental *ac* frequency window. Therefore the characteristic frequency up to 2.4 K has been deduced using a classical scaling method[6] adapted to the *ac* susceptibility measurements. It is worth mentioning that the $\chi''(\nu)$ have been normalized to $\chi_0'(10\ \text{Hz})$ before scaling in order to compensate the temperature dependence of the χ''

intensity at the characteristic frequency. In figure V.7e, the relaxation time, $\tau(T) = 1/(2\pi\nu_{ac})$, of **21** was plotted as a function of the increase of the temperature. The experimental data as the τ vs. $1/T$ plot are well fitted to an Arrhenius law (figure V.7e): $\tau(T) = \tau_0\, exp(\Delta_A/k_BT)$ where $\tau_0 = 1.9 \times 10^{-9}$ s is the pre-exponential constant and $\Delta_A/k_B = 21.2$ K estimates the energy required to reverse the magnetization.

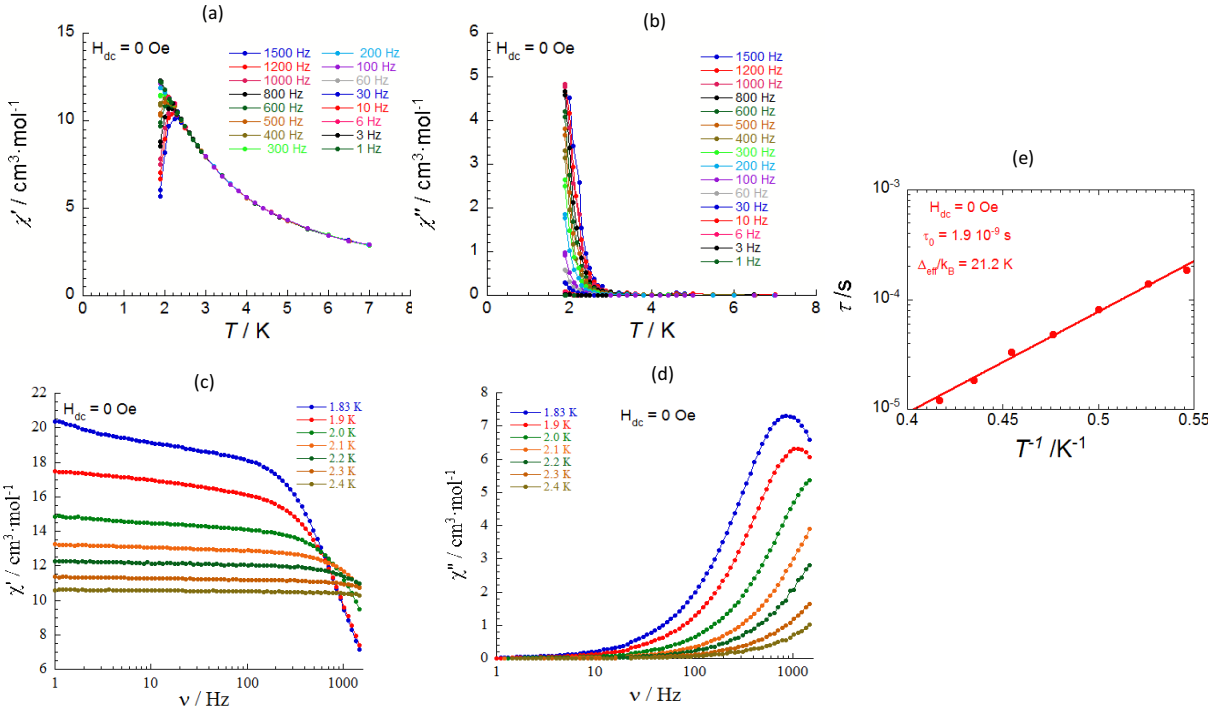

Figure V.7. Temperature (a, b) and frequency dependence(c, d) of the χ' (in-phase; a, c) and χ''(out-of-phase; b, d) parts of the *ac* magnetic susceptibility of **21** at $H_{dc} = 0$ Oe where $\chi'(T)$, $\chi''(T)$, $\chi'(\nu)$ and $\chi''(\nu)$ are represented in the figures a, b, c, and d respectively. (e) Thermal variation of τ plotted as τ vs. $1/T$, the solid line is the best fit obtained using an Arrhenius law: $\tau(T) = \tau_0\, exp(\Delta_A/k_BT)$ (see text).

V.2.1.2. $[Mn^{III}(5\text{-Cl-saltmen})][Ru^{III}(salen)(CN)_2]\cdot 2MeCN$ (22)

The temperature dependence of the magnetic susceptibility of **22** was measured in the presence of a 1000 Oe *dc* magnetic field and in the temperature range of 270-1.8 K (figure V.8a). At 270 K, the χT value is 3.48 cm^3K/mol which is close to the theoretical Curie constant value (3.375 cm^3K/mol) for a Mn^{III} ($S = 2$) and Ru^{III} ($S = 1/2$) considering $g = 2$ for both ions. As the temperature is lowered, χT slowly increased to 3.52 cm^3K/mol at 100 K and thereafter decreased slowly to 3.40 cm^3K/mol at 32 K, followed by a rapid decrease of χT to 1.47 cm^3K/mol at 1.8 K. This kind of temperature variation of the magnetic susceptibility of **22** indicates very weak ferromagnetic interaction between the Ru^{III} and the Mn^{III} ions which at low enough temperature are masked by the anisotropy of the metal ions or the interchain antiferromagnetic interactions, resulting in a steep decrease of χT below 30 K.

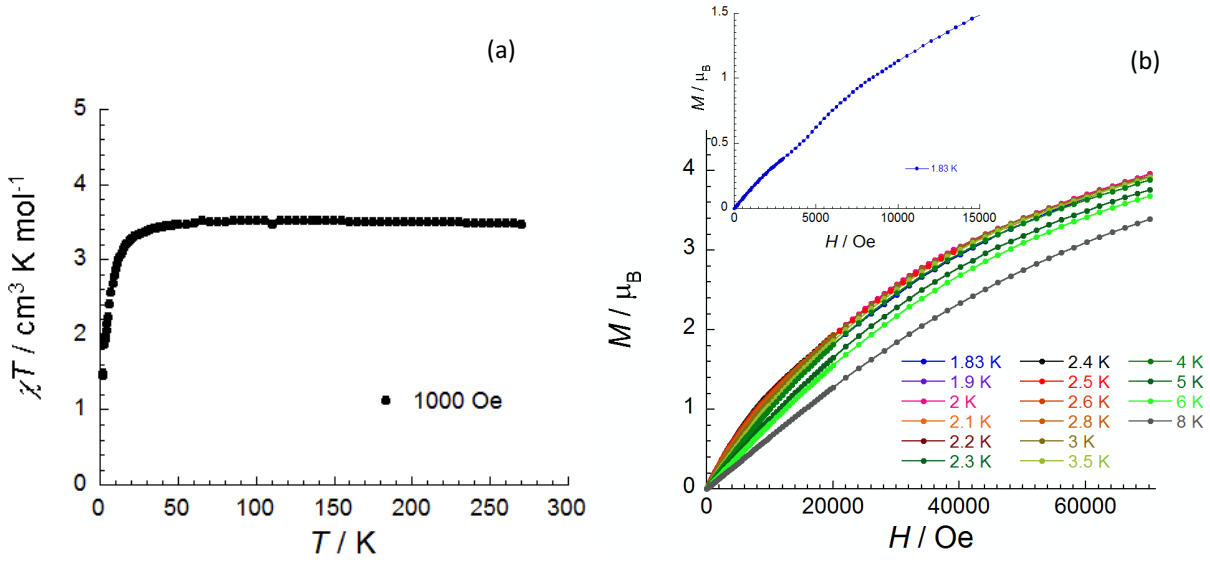

Figure V.8. (a) The χT vs. T plot of **22** at 1000 Oe *dc* applied field. (b) The M vs. H plot for **22** at multiple temperatures between 1.83 and 8 K.

The M vs. H data were collected for **22** below 7 T at multiple temperatures below 8 K (figure V.8b). Each magnetization curve below 2.5 K exhibits a typical "*S*" shape. This feature reveals the presence of antiferromagnetic interactions between chains which are overcome by the applied magnetic field at H_C. In order to quantify the temperature dependence of this characteristic field, dM/dH was plotted vs. H (figure V.9a). At low temperature χT vs. T data were also collected for **22** at different applied magnetic field (figure V.9b). The experimental data, that exhibit a clear maximum of the susceptibility around 2.5 K at low field, further emphasize the presence of a three dimensional antiferromagnetic order below 2.5 K. Therefore, extracting the maximum susceptibilities found in the χ vs. T and dM/dH vs. H curves, we built the H vs. T phase diagram for **22** (figure V.9c). The characteristic field H_C extrapolates at zero around 2.5 K. This result supports the presence of a 3D ordered antiferromagnetic system. If this line is extrapolated to the absolute zero temperature the critical field H_C (0 K) of **22** is found to be 4800 Oe.

From the H_C (0 K), the interchain antiferromagnetic interactions zJ'/k_B for **22** is calculated as -0.13 K, $g\mu_B H_C(0\text{ K})S_T = 2|zJ'|S_T^2$ with $g = 2$ and $S_T = 5/2$ for one Mn^{III} and one Ru^{III} center interacting ferromagnetically. Using these zJ'/k_B values the calculated Néel temperature (T_N^{cal}) of this system is 2.3 K from the relation $T_N = 2|zJ'|S_T(S_T+1)/3k_B$, which is comparable with the experimental Néel temperature (= 2.5 K) of **22** found from its phase diagram (figure V.9c).

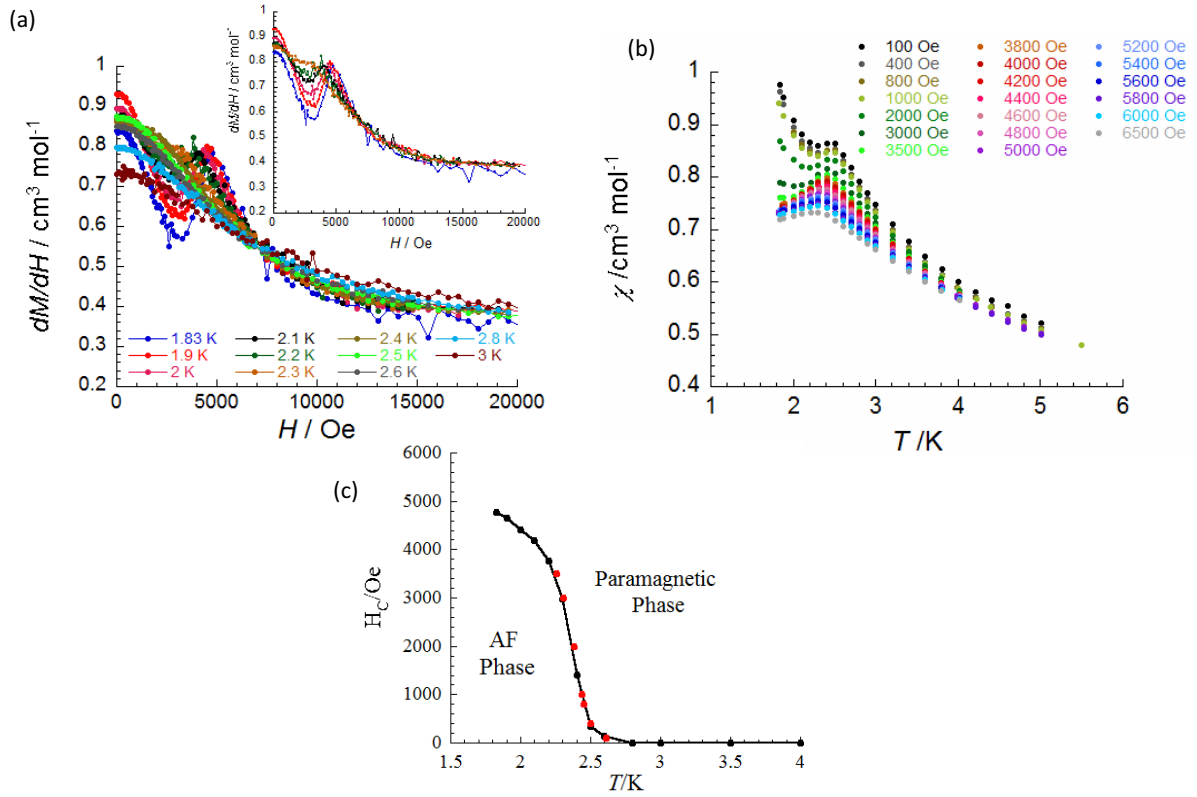

Figure V.9. (a) Plot of the derivative of magnetization for **22**, χ (*viz. dM/dH*), as a function of field at multiple temperatures to investigate characteristic field H_C at the maximum susceptibility (b) The temperature dependence of the magnetic susceptibility of **22** at multiple applied *dc* fields. (c) Magnetic phase diagram (*T, H*) of **22** constructed from maxima of χ vs. *T* (red circles) and *dM/dH* vs. *H* curves (black circles).

V.3. Conclusions and perspectives

In this chapter, we have discussed new cyanido-based Ru^{III}-Mn^{III} systems. Unfortunately due to the time limitation of this PhD work, we have not been able to undertake an extensive study and analysis of the magnetic properties. But the magnetic studies for the compound **21** and **22** clearly demonstrate the ferromagnetic exchange between the Mn^{III} and Ru^{III} ions. The hexanuclear compound **21** exhibits slow magnetic relaxation behavior at zero *dc* field although the molecules are not well separated from each other in the crystal packing. Moreover the Ru^{III}-Mn^{III} ferromagnetic exchange in **21** is much stronger than that in **22** due to the geometry of the cyanido bridge.

An interesting observation of such systems is that the change of Mn^{III}-Schiff bases complexes significantly impacts the nuclearity of the final compound. For example, the dinuclear complex **19** is an example of the smallest possible heterometallic system built with the Mn^{III} and Ru^{III} ions. Compound **20** seems to be a pair of a dinuclear Mn^{III}-Ru^{III} moiety which may also be classified as a quasi-tetranuclear unit. The $[Mn^{III}(saltmen)]^+$ unit results in the hexanuclear compound **21**, which

resembles a pair of Mn^{III}-Ru^{III}-Mn^{III} units. When 5-Cl-saltmen was used, the one dimensional 1:1 compound **22** was obtained. Notably in all the compounds **19-21** we have observed the Mn^{III}-Schiff base units to possess a square pyramidal geometry which we never found in the Re^{IV}-Mn^{III} systems (chapter III).

We have tried several other Mn^{III}-Schiff base complexes to react with these $Ru^{III}(CN)_2$-Schiff base systems and obtained two more compounds **28** and **29** which are described in the Annex section II. The crystal quality of these two compounds was not very good for X-ray crystallographic characterization, but sufficient to understand their crystal packing. Compound **29** is comparable to **21**, a hexanuclear Mn^{III}-Ru^{III}-Mn^{III}_2-Ru^{III}-Mn^{III} compound built with the $[Mn^{III}(5\text{-Me-saltmen})]^+$ and $[Ru^{III}(salen)(CN)_2]^-$ moiety, but the crystal packing pattern is much different. Compound **28** is an interesting pentanuclear Mn^{III}-Ru^{III}-Mn^{III}-Ru^{III}-Mn^{III} molecule composed from $[Mn^{III}(5\text{-}^t\text{Bu-saltmen})]^+$ and $[Ru^{III}(salen)(CN)_2]^-$ molecules (see Annex, section II). The ^{t}Bu group on the saltmen ligand imports a significant impact to the crystal packing pattern of this molecule.

The reaction between some of the Mn^{III}-Schiff base complexes with the $Ru^{III}(CN)_2$-Schiff base precursor are kinetically very fast and thus we frequently faced the problem of precipitation of the final product or the formation of extremely tiny crystals, unsuitable for X-ray analysis. Therefore in order to synthesize this Ru^{III}-Mn^{III} molecular systems it is very important to optimize the reaction conditions in terms of solvents (MeOH was found to be most efficient to avoid the precipitation in most cases) and the crystallization method as well.

V.4. References

[1] J. H. Yoon, H. S. Yoo, H. C. Kim, S. W. Yoon, B. J. Suh, C. S. Hong, *Inorg. Chem*., **2009**, 48, 816.

[2] (a) H. Miyasaka, R. Clérac, T. Ishii, H. –C. Chang, S. Kitagawa, M. Yamashita, *J. Chem. Soc. Dalton Trans*, **2002,** 1528. (b) H. Miyasaka, R. Clérac, W. Wernsdorfer, L. Lecren, C. Bonhomme, K.-i. Sugiura, M. Yamashita, *Angew. Chem. Int. Ed.,* **2004**, 43, 2801.

[3] (a) J. H. Van Vleck, *The Theory of Electric and Magnetic Susceptibilities,* Oxford university Press, Oxford, **1965**; (b) C. J. O'Connor, *Prog . Inorg. Chem*., **1982**, 29, 203.

[4] M. Ferbinteanu, H. Miyasaka, W. Wernsdorfer, K. Nakata, K. Sugiura, M. Yamashita, C. Coulon, R. Clérac, *J. Am. Chem. Soc.*, **2005**, 127, 3090.

[5] K. S. Pedersen, J. Dreiser, J. Nehrkorn, M. Gysler, M. Schau-Magnussen, A. Schnegg, K. Holldack, R. Bittl, S. Piligkos, H. Weihe, P. Tregenna-Piggott, O. Waldmann J. Bendix, *Chem. Commun*., **2011**, 47, 6918.

[6] A. Labarta, O Iglesias, L. I. Barcells, F. Badia, Phys. Rev. B, **1993**, 48, 10240.

[7] (a) Thèse "*Systematic Studies on Ferromagnetism and Magnetization Relaxation Dynamics in Dimeric Mn(III) Tetradentate Schiff-Base Complexes*" C. Kachi, Department of Chemistry Graduate School of Science Tokyo Metropolitan University, **2006**. (c) H. Miyasaka, A. Saitoh, S. Abe, *Coord. Chem. Rev*., **2007**, 251, 2622.

[8] (a) W. H. Leung, C. M. Che, *Inorg. Chem*., **1989**, 28, 4619. (b) J. A. Duimstra, C. L. Stern, T. J. Meade, *Polyhedron*, **2006**, 25, 2705.

GENERAL CONCLUSIONS AND FUTURE PERSPECTIVES

We herein summarize all the results we obtained during this thesis work followed by a discussion of future perspectives for this project.

In the first chapter, we discussed the general theoretical aspects of molecule-based magnets and their potential applications in information storage. Literature examples of Single-Molecule Magnets and Single-Chain Magnets were used to illustrate the properties of the low dimensional magnetic materials. This theoretical background helps chemists to design molecules with enhanced magnetic properties. From a chemical point of view, coordination chemistry using selected metal-organic precursors appear to be a powerfull tool to design new magnetic materials. We have also mentioned the reason for using *d*-block transition metal ions for the synthesis of magnetic molecules. Moreover our preference on the cyanido group as a bridging ligand between the different metal ions was emphasized in chapter I.

In the second chapter, we thoroughly discussed the molecular precursors used in this research work along with several literature examples. Our synthetic strategy to design molecule-based magnets was described upon donor-acceptor type coordination chemistry. The Mn^{III}-salen type compounds and M^{II}-macrocycles (M = Ni^{II}, Cu^{II}, Fe^{II}, Mn^{II}) were depicted as acceptor type building blocks, where the two axial coordination sites of the metal ions were available to accept electron density from the donor moiety. On the other hand, the used donor *trans*-dicyanido type compounds: *trans*-$(Bu_4N)_2[Re^{IV}Cl_4(CN)_2]$, *trans*-$(Ph_4P)[Ru^{III}(salen)(CN)_2]$ and *trans*-$(Bu_4N)[Ru^{III}(5\text{-Cl-saltmen})(CN)_2]$ were used. The cyanido nitrogen ends of these donor units can donate electron density to the acceptor metal ions. We decided to the use $Re^{IV}(5d^3)$ and $Ru^{III}(4d^5)$ precursors due to their known large magnetic anisotropy. Chapter II also contains the synthesis, infrared characteristics, single crystal X-ray data and magnetic properties of all these molecular precursors.

Chapter III was dedicated to the newly synthesized $[Re^{IV}Cl_4(CN)_2]$-Mn^{III}-Schiff base molecular systems and their characterization. In this chapter, we described a total of twelve compounds and showed how the modifications of the Schiff base ligand influence the coordination mode of Mn^{III} ions towards the cyanido nitrogen donor. In compounds **1-3**, the Mn^{III} ions preferred solvent molecules over the cyanido nitrogen atom to fulfill their axial coordination sites and thus we obtained Mn^{III}/Re^{IV} salts. Compounds **4-6** are trinuclear Mn^{III}-Re^{IV}-Mn^{III} systems where the Mn^{III} ions coordinate with one cyanido nitrogen atom in one of the two axial sites, and the remaining axial coordination is fulfilled by solvent molecules. Compound **7** was found to be an interesting hexanuclear compound which can be seen a double phenoxido bridged pair of Mn^{III}-Re^{IV}-Mn^{III} trinuclear units. Using different Mn^{III}-Schiff base compounds we have obtained a series of one dimensional $Mn^{III}{}_2$-Re^{IV} systems (compounds **8-12**). In these one dimensional compounds, close crystallographic packing of the chains results in ordered antiferromagnetic ground state. In the compound **8** and **9**, we observed the presence of slow relaxation of magnetization (magnetic hysteresis behavior) in their canted

antiferromagnetic phase. When the interchain interactions are overcome with the applied *dc* field (2400 Oe for **8** and 1700 for **9**) the chains are like decoupled and we observed significant magnetic susceptibility responds to the *ac* frequency. Therefore we found the most important way to improve the magnetic properties of these Re^{IV}-Mn^{III} systems is to separate more efficiently the Mn^{III}-Re^{IV}-Mn^{III} trinuclear complex or Mn^{III}_2-Re^{IV} chains in their crystal packing in order to minimize the inter-object magnetic interactions and thus to lower the probability of an ordered antiferromagnetic ground state.

Chapter IV represents new $[Re^{IV}Cl_4(CN)_2]$-M^{II}(macrocycle) one dimensional systems. Interestingly all the cyclam based compounds (**14-16**) have very similar crystal structures as well as the LN_3O_2 based compounds (**17-18**) that are also crystallographically very similar. We found that the Ni^{II}, Cu^{II} and Fe^{II} ions interact ferromagnetically with the Re^{IV} ion through the cyanido bridge. The $Re^{IV}Fe^{II}$ chain compound **17** possesses slow magnetic relaxation behavior in its antiferromagnetically ordered ground state as observed in **8** and **9**.

We have synthesized and characterized several Ru^{III}-Mn^{III} cyanido bridged compounds, which were described in chapter V. The heterometallic interaction was found to be ferromagnetic. We have shown that the modulation of the Schiff base ligands for both Mn^{III} and Ru^{III} ions results in compounds of different nuclearity. For these systems, we unfortunately could not find enough time to vary the ligands in order to bring much more structural diversity. Finally, the Annex contains many interesting outcomes of our research work. This part is included to have a complete view of whatever we obtained during our research work even if these compounds were only partially characterized and not always reproducible manner.

In terms of future perspectives, we would like to emphasize the diversity and versatility of the new systems studied in this thesis. The obtained materials during our research work, represent just a few examples, with respect of the numerous possible parameters that could be changed. In both Re^{IV}-Mn^{III} and Ru^{III}-Mn^{III} systems, we have observed that a change of the Mn^{III}-Schiff base complexes significantly impacts its bonding to the cyanido nitrogen atoms and thus the nuclearity of final product varies remarkably.

In the $[Re^{IV}Cl_4(CN)_2]$-Mn^{III}-Schiff base compounds, the low temperature antiferromagnetic order of the systems affected the desired magnetic relaxation (i. e. SCM properties). In order to overcome this problem, we have tried few possible solutions, such as the use of bigger solvent molecules and larger substituents on the Schiff base ligands. Although we were not successful in reaching our goal, we believe that further work on this project will achieve optimized $[Re^{IV}Cl_4(CN)_2]$-Mn^{III}-Schiff base single molecule magnets and single chain magnets. In the $[Re^{IV}Cl_4(CN)_2]$-Mn^{III}-Schiff base one dimensional systems (compound **8-12**), the chains are individually neutral in charge. So if we can synthesize a one dimensional compound where one $[Re^{IV}Cl_4(CN)_2]^{2-}$ and one Mn^{III}-Schiff base moiety resides alternatively along the chain direction, the overall charge of the chain will be

negative. In this case the $(Bu_4N)^+$ counter cation must be present in the crystal packing and the chains must be mutually more separated in a magnetic point of view. To obtain such a 1:1 chain, we need to find the right Mn^{III}-Schiff base precursor and proper reaction conditions. Not only Mn^{III} ions, but also other transition metal ions can be used to link the $[Re^{IV}Cl_4(CN)_2]^{2-}$ group through the cyanido bridge. In the chapter IV, we have shown a few examples of possible Re^{IV} heterometallic systems using Ni^{II}, Cu^{II}, Fe^{II} and Mn^{II} ions and also few examples are available in the literature.[1,2] Moreover, we have tried to make the bromido analogue of $[Re^{IV}Cl_4(CN)_2]^{2-}$ building block, but unfortunately we did not succeed in optimizing the reaction conditions. The Br^- is bigger in ionic radii than Cl^- and therefore we might be able to introduce more anisotropy to the system.[3] By changing the Cl^- to Br^- in this Re^{IV} precursor, we wanted to further synthesize the heterometallic magnetic materials; thus compare the coordination capability and magnetic properties of both Re^{IV} precursors and obtained heterometallic systems. This $[Re^{IV}Br_4(CN)_2]^{2-}$ molecule may be an interesting building block, but challenging to synthesize. On the other hand, even though we were not able to reproduce the synthesis of the $[Re^{IV}Cl_5(CN)]^{2-}$ building block (discussed in the Annex, section III), our findings establishes its existence. Thus the controlled synthesis of $[Re^{IV}Cl_5(CN)]^{2-}$ is also a future aspect of this research to synthesize new SMMs.

We know that the dinuclear Mn^{III}-Schiff base moiety itself is a Single-Molecule Magnet with a spin ground state $S_T = 4$.[4] In our work, we have seen that the Re^{IV}-Mn^{III} compounds containing the dinuclear Mn^{III}-schiff base moiety exhibited interesting magnetic properties. For example the chains in **8-12** have shown some slow magnetic relaxation behavior, while the hexanuclear compound **7** has magnetic hysteresis behavior. Therefore, the dinuclear Mn^{III}-Schiff base precursor could be replaced by other acceptor type SMM moiety with a higher spin ground state, and thus the magnetic properties of the resulting system may be enhanced. In this context $[Mn_4(hmp)_6]^{2+}$ moiety having $S_T = 9$ may be a good choice.[5]

In the $[Ru^{III}(salen)(CN)_2]$-Mn^{III}-Schiff base series, a number of compounds could be synthesized with a variety of magnetic properties. In chapter V, we have shown that compound **21** has SMM like properties. Therefore if we could synthesize a one dimensional polymer of the repeating hexanuclear unit of **21**, the compound would be expected to behave like a SCM. Thus varying the Schiff base ligands on both Ru^{III} and Mn^{III} ions, we could synthesize many more new magnetic molecules. It is also possible to use many other transition metal building blocks in order to connect the metal ion with Ru^{III} via the cyanido bridge. Indeed, an Os^{III} analogue of the Ru^{III}-Schiff base precursor would also be an interesting paramagnetic building block to synthesize molecule based magnets. In 2010, Guo et al. reported the *trans*-$Ph_4P[Os^{III}(salen)(CN)_2]$ moiety which made a one dimensional zigzag chain with $[Cu(Me_3tacn)]$ having heterometallic ferromagnetic interactions.[6] In the $[Os^{III}(salen)(CN)_2]^-$ moiety the Os^{III} has low spin $5d^5$ electronic configuration, thus a spin ground state of $S = 1/2$, similar to the Ru^{III}. Moreover, Os^{III} has a larger magnetic anisotropy than Ru^{III} which could

be advantageous in the design of new SMMs or SCMs.[7] Following the method of Guo et al.[6] we tried to synthesize the *trans*-$Ph_4P[Os^{III}(salen)(CN)_2]$ molecular precursor, but unfortunately the compound is not reproducibly obtained according to that method.

[1] T. D Harris, M.V. Bennett, R. Clérac, J. R. Long, *J. Am. Chem. Soc*., **2010,** 132, 3980.

[2] T. D. Harris, C. Coulon, R. Clérac, J. R. Long, *J. Am. Chem. Soc*., **2011**, 133, 123.

[3] H. I. Karunadasa, K. D. Arquero, L. A. Berben, J. R. Long, *Inorg. Chem*., **2010**, 49, 4738.

[4](a) H. Miyasaka, R. Clérac, T. Ishii, H. –C. Chang, S. Kitagawa, M. Yamashita, *J. Chem. Soc. Dalton Trans*, **2002,** 1528. (b) H. Miyasaka, R. Clérac, W. Wernsdorfer, L. Lecren, C. Bonhomme, K.-i. Sugiura, M. Yamashita, *Angew. Chem. Int. Ed.,* **2004**, 43, 2801.

[5] References [22, 23] in chapter I of this thesis.

[6] J. F. Guo, W. F. Yeung, P. H. Lau, X. T. Wang, S. Gao, W. T. Wong, S. Sin-Yin Chui, C. M. Che, W. Y. Wong, T. C. Lau, *Inorganic Chemistry*, **2010**, 49, 4.

[7] K. S. Pedersen, J. Dreiser, J. Nehrkorn, M. Gysler, M. Schau-Magnussen, A. Schnegg, K. Holldack, R. Bittl, S. Piligkos, H. Weihe, P. Tregenna-Piggott, O. Waldmann J. Bendix, *Chem. Commun*., **2011**, 47, 6918.

ANNEX

This ANNEX is describing all the byproducts and partially characterized compounds obtained during this research work. Specifically, we synthesized five new Re^{IV}-Mn^{III}-Schiff base compounds (compound **23-27**) besides those described in chapter III (**1-12**), as well as two Ru^{III}-Mn^{III}-Schiff base compounds (**28-29**) beyond those described in chapter V (**19-22**). In the time frame of this PhD work, we could not perform complete structural and magnetic characterization of these compounds (**23-29**) due different reasons as mentioned below. During our research work, we always gave priority to those compounds which were fully characterised by X-ray crystallography and were synthetic reproducible. For example, during the synthesis of the *trans*-$(Bu_4N)_2[Re^{IV}Cl_4(CN)_2]$ molecular precursor, we discovered a new building block $[Re^{IV}Cl_5(CN)]^{2-}$ from which we obtained three new interesting compounds **30-32**; unfortunately the synthesis of the Re^{IV} precursor was not reproducible and therefore we did not proceed to the magnetic characterization of **30-32**. In another case, after collecting crystals of *trans*-$(Bu_4N)_2[Re^{IV}Cl_4(CN)_2]\cdot 2DMA$ we recovered a new molecular precursor *trans*-$(Bu_4N)_2[Re^{V}(CN)_4(O)(OH)]\cdot 2DMA$ from the remaining mother liquor. Using this diamagnetic Re^{V} compound and the $[Ni^{II}(cyclen)(H_2O)_2](ClO_4)_2$ a large aggregated complexes was made (compound **33**). According to the above mentioned different types of molecules obtained, this annex is subdivided in four sections as following :

Section I. Re^{IV}-Mn^{III}-Schiff base systems (**23-27**).

Section II. Ru^{III}-Mn^{III}-Schiff base systems (**28**, **29**).

Section III. $[Re^{IV}Cl_5(CN)]^{2-}$ based systems (**30-32**).

Section IV. A giant cyanido based Re^{V}-Ni^{II} complex (**33**)

Section I.

Re^{IV}-Mn^{III}-Schiff base systems (23-27)

In this section, we will describe five partially characterized Re^{IV}-Mn^{III}-Schiff base systems (**23-27**). Among them **23** is a Re^{IV}/Mn^{III} salt having the molecular formula $[\{Mn^{III}(5\text{-}^{t}Bu\text{-saltmen})(H_2O)\}_2]_2[Re^{IV}Cl_4(CN)_2](ClO_4)_2\cdot 4H_2O$, **24** is a Mn^{III}-Re^{IV}-Mn^{III} trinuclear compound $[Mn^{III}(4\text{-MeO-saltmen})(H_2O)]_2[Re^{IV}Cl_4(CN)_2]$ and **25-27** are one dimensional systems with respective molecular formulae $[Mn^{III}(5\text{-Me-saltmen})]_2[Re^{IV}Cl_4(CN)_2]\cdot 3MeNO_2$ (**25**), $[Mn^{III}(5\text{-Cl-saltmen})]_2[Re^{IV}Cl_4(CN)_2]$ (**26**) and $[Mn^{III}(5\text{-Br-saltmen})]_2[Re^{IV}Cl_4(CN)_2]$ (**27**). The synthesis of these compounds is described below. The single crystal X-ray diffraction parameters are summarized in table A.I (even if all these X-ray data are not always of good quality) and figure A.I.1 and A.I.2 display the crystal structures of **23-27**.

Synthesis:

(a) ***$[\{Mn^{III}(5\text{-}^{t}Bu\text{-saltmen})(H_2O)\}_2]_2[Re^{IV}Cl_4(CN)_2](ClO_4)_2\cdot 4H_2O$*** **(23)**: To a 3 mL methanol solution of $[Mn^{III}_2(5\text{-}^{t}Bu\text{-saltmen})_2(H_2O)_2](ClO_4)_2\cdot 2H_2O$ (0.0125 g, 0.01 mmol) a 1 mL methanol solution of *trans*-$(Bu_4N)_2[Re^{IV}Cl_4(CN)_2]\cdot 2DMA$ (0.0103 g, 0.01 mmol) was added dropwise, followed by the addition of 0.5 mL distilled water. The solution slowly evaporated at room temperature by covering the vial opening with parafilm and making a small hole in it. After two days brown block-shaped crystals were found in the bottom of the vial and separated by filtration. The yield of the product was *ca.* 60 % on the basis of the Mn^{III}-Schiff base precursor used. IR: $\bar{\nu}$ = 2127 (C≡N stretch), 1601 (C=N stretch) cm^{-1}.

(b) ***$[Mn^{III}(4\text{-MeO-saltmen})(H_2O)]_2[Re^{IV}Cl_4(CN)_2]$*** **(24)**: To a 4 mL acetonitrile solution of $[Mn^{III}(4\text{-MeO-saltmen})(H_2O)_2](ClO_4)\cdot 2H_2O$ (0.0120 g, 0.02 mmol) a 2 mL acetonitrile solution of 0.0103 g (0.01 mmol) *trans*-$(Bu_4N)_2[Re^{IV}Cl_4(CN)_2]\cdot 2DMA$ was added drop wise. The reaction mixture was allowed to evaporate slowly at ambient temperature. After few days red needle-shaped crystals were separated by filtration. The yield of the product was 50 % on the basis of the Mn^{III}-Schiff base precursor used. IR: $\bar{\nu}$ = 2132 (C≡N stretch), 1599 (C=N stretch) cm^{-1}.

(c) ***$[Mn^{III}(5\text{-Me-saltmen})]_2[Re^{IV}Cl_4(CN)_2]\cdot 3MeNO_2$*** **(25)**: $[Mn^{III}(5\text{-Me-saltmen})(H_2O)]_2(ClO_4)_2$ (0.0104 g, 0.01 mmol) and *trans*-$(Bu_4N)_2[Re^{IV}Cl_4(CN)_2]\cdot 2DMA$ (0.0103 g, 0.01 mmol) were separately dissolved in 2 mL of nitromethane. The solution of Mn^{III} was poured into a thin tube of 1.5 cm diameter and then layered with 2 mL of pure nitromethane. Over the pure solvent the $(Bu_4N)_2[Re^{IV}Cl_4(CN)_2]\cdot 2DMA$ solution was very carefully layered to avoid fast mixing of the reactants. The tube opening was closed with parafilm. After one day a few brown crystals were found

at the wall of the tube and collected by filtration. The yield of the product was 70 % on the basis of the Mn^{III}-Schiff base precursor. IR: $\bar{\nu}$ = 2142 (C≡N stretch), 1596 (C=N stretch) cm^{-1}.

(d) ***$[Mn^{III}(5\text{-}Cl\text{-}saltmen)]_2[Re^{IV}Cl_4(CN)_2]$*** **(26):** To a 3 mL acetonitrile solution of of $[Mn^{III}_2(5\text{-}Cl\text{-}saltmen)_2(H_2O)_2](ClO_4)_2$ (0.0113 g, 0.01 mmol) a 2 mL acetonitrile solution of *trans*-$(Bu_4N)_2[Re^{IV}Cl_4(CN)_2]\cdot 2DMA$ (0.0103 g, 0.01 mmol) was slowly added. After one day tiny brown crystals were found at the bottom of the vial in 80 % yield on the basis of the Mn^{III} precursor. IR: $\bar{\nu}$ = 2139 (C≡N stretch), 1598 (C=N stretch) cm^{-1}.

(e) ***$[Mn^{III}(5\text{-}Br\text{-}saltmen)]_2[Re^{IV}Cl_4(CN)_2]$*** **(27):** To a 3 mL acetonitrile solution of $[Mn^{III}_2(5\text{-}Br\text{-}saltmen)_2(H_2O)_2](ClO_4)_2$ (0.0131 g, 0.01 mmol) a 2 mL acetonitrile solution of 0*trans*-$(Bu_4N)_2[Re^{IV}Cl_4(CN)_2]\cdot 2DMA$ (0.0103 g, 0.01 mmol) was slowly added. After one day tiny brown crystals were found at the bottom of the vial in 80 % yield on the basis of the Mn^{III}-Schiff base precursor. IR: $\bar{\nu}$ = 2141 (C≡N stretch), 1600 (C=N stretch) cm^{-1}.

Crystallography:

Table.A.I. Crystal data and structure refinement of **23-27**

Compounds	**23**	**24**	**25**	**26**	**27**
Sum formula	$C_{114}H_{176}Cl_6Mn_4N_{10}O_{30}Re$	$C_{48}H_{44}Cl_4Mn_2N_6O_{10}Re$	$C_{49}H_{61}Cl_4Mn_2N_9O_{10}Re$	$C_{42}H_{40}Cl_8Mn_2N_6O_4Re$	$C_{42}H_{40}Cl_4Br_4Mn_2N_6O_4Re$
MW (g/mol)	2785.34	1302.78	1373.97	1272.89	1450.29
Temp. (K)	120(2)	150(2)	150(2)	120(2)	120(2)
Crystal System	Triclinic	Triclinic	Monoclinic	Triclinic	Triclinic
Space group	P-1	P-1	$P2_1/c$	P-1	P-1
a (Å)	11.988(5)	9.4013(19)	11.440(2)	8.090(5)	8.140(2)
b (Å)	16.805(5)	12.554(3)	17.448(4)	12.826(5)	12.985(3)
c (Å)	17.794(5)	12.553(3)	13.980(3)	13.039(5)	13.304(3)
α (°)	99.017(5)	110.54(3)	90	67.649(5)	68.374(5)
β (°)	96.434(5)	102.19(3)	93.30(3)	72.051(5)	73.691(7)
γ (°)	105.189(5)	102.20(3)	90	76.413(5)	76.463(5)
Volume ($Å^3$)	3372(2)	1288.5(7)	2785.9(10)	1179.7(10)	1241.1(5)
Z	1	1	2	1	1
Density ($g.cm^{-3}$)	1.362	1.679	1.634	1.791	1.940
$\mu_{MoK\alpha}$ (mm^{-1})	1.448	3.095	2.868	3.587	6.414
F_{000}	1427	647	1376	627	699
GooF	1.060	2.009	1.061	1.967	0.875
[a]R_1 ($I > 2.00\sigma(I)$)	0.0484	0.1500	0.0465	0.2484	0.0291
[b]wR_2	0.1437	0.4055	0.1322	0.5877	0.0768

[a]$R_1 = \Sigma ||F_0| - |F_C|| / \Sigma|F_0|$, [b]$wR_2 = [\Sigma w(F_0^2 - F_C^2)^2 / \Sigma w(F_0^2)^2]^{1/2}$, $w = 1/[\sigma^2F_0^2 + (0.0313P)^2 + 1.5564P]$; where $P = (F_0^2 + 2F_C^2)/3$

The crystal structure of **23** (figure A.I.1a) is similar to compound **2** in chapter III, with the exception that in **23** two ClO_4^- counter ions and one $[Re^{IV}Cl_4(CN)_2]^{2-}$ are present to neutralize the charge of the two $[Mn^{III}_2(5\text{-}^tBu\text{-}saltmen)_2(H_2O)_2]^{2+}$ units. Like in **2**, here the $[Mn^{III}_2(5\text{-}^tBu\text{-}saltmen)_2(H_2O)_2]^{2+}$ cation does not interact with the $[Re^{IV}Cl_4(CN)_2]^{2-}$ unit. This observation indicates that Mn^{III} ions coordinated with the 5-^{t}Bu-saltmen ligand prefers solvent molecules to the cyanido nitrogen as axially coordinating atoms. We did not perform the magnetic measurements of this species

due to the crystallographic similarity with **2** and absence of the Mn^{III}-Re^{IV} cyanido bonding interactions.

In chapter III, we showed that, using $[Mn^{III}(3\text{-MeO-saltmen})]^+$ and $[Mn^{III}(5\text{-MeO-saltmen})]^+$ molecular precursors we could synthesize the cocrystallized compound **1** and the one dimensional compound **11**, respectively. Interestingly in **24**, the $[Mn^{III}(4\text{-MeO-saltmen})]^+$ building block interacts with the $[Re^{IV}Cl_4(CN)_2]^{2-}$ moiety to form a Mn^{III}-Re^{IV}-Mn^{III} trimer (figure A.I.1b). Therefore, MeO substitution on the 4 and 4′ positions of the saltmen ligand implies a tendency towards the formation of Mn^{III}-Re^{IV} cyanido bridges, but not enough to form a one dimensional Mn^{III}-Re^{IV} cyanido bridged polymer. Thus, we have observed that changing the position of the MeO substituent on the aromatic ring exhibits a significant impact on the coordination capability of the Mn^{III}-Schiff base ligands. We did not proceed to the magnetic studies of **24** due to its poor crystal quality.

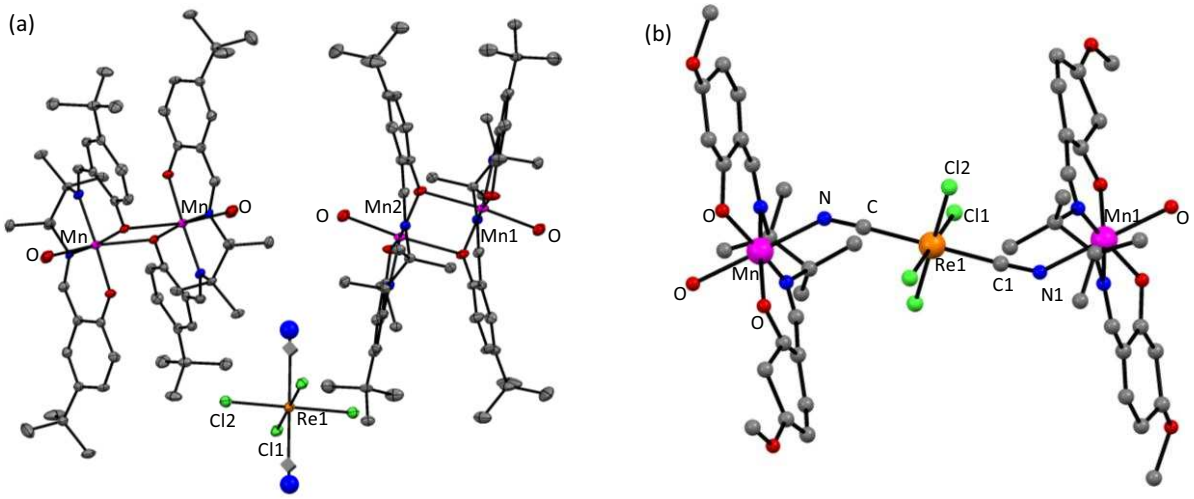

Figure A.I.1. (a) ORTEP type diagram of **23** with 50% thermal probability ellipsoids. (b) The crystal structure of **24** in ball and stick because the thermal ellipsoid are not good. The grey, blue, red, green, magenta and orange spheres represent the C, N, O, Cl, Mn, and Re atoms. In figure (a) The N atoms of $[Re^{IV}Cl_4(CN)_2]$ moiety were refined isotropically. The H atoms and the solvent molecules are omitted for clarity.

Compound **25** is similar to **8**, except that the solvent of crystallization is nitromethane instead of acetonitrile (figure A.I.2a). This change of solvent has a minimal impact on the crystal packing of both one dimensional compounds. The magnetic properties of **25** are similar to those of **8**. However, during the magnetic measurements of **25** we observed systematically, the presence of a small amount of a byproduct that interfered with the magnetic characterization. Unfortunately, the re-synthesis of **25** preserves this interfering component and we could neither identify this impurity, nor wash it away with different solvents (for example, nitromethane, acetonitrile).

Compound **26** (figure A.I.2b) and **27** (figure A.I.2c) are one dimensional Re^{IV}-Mn^{III}-Schiff base compounds having a crystal structure comparable to **10** (discussed in chapter III); only the halide atoms are changed from F (in **10**) to Cl (in **26**) and Br (in **27**). The magnetic properties of these compounds have not been measured due to the time limitation of the present research work.

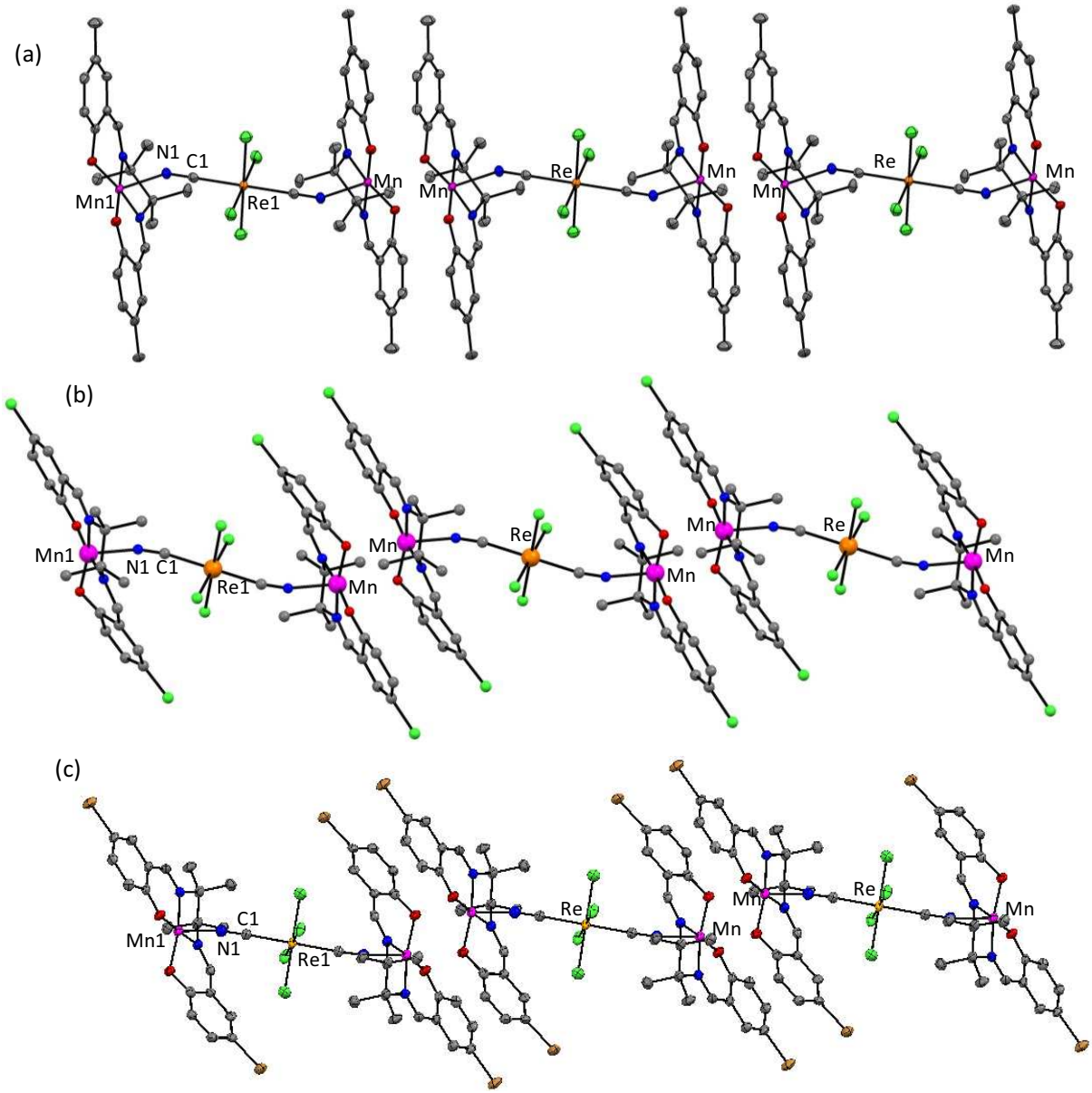

Figure A.I.2. ORTEP type views of crystal structure of **25** (a) and **27** (c) with 50% thermal probability ellipsoids. (b) The crystal structure view of **26** in ball and stick model as its crystal structures quality was not good. The grey, blue, red, green, magenta and orange spheres represent the C, N, O, Cl, Mn, and Re atoms. In figure (c) the brown spheres represents the Br atoms. The H atoms and solvent molecules (nitromethane in of compound **25**) are omitted for clarity.

Section II.

Ru^{III}-Mn^{III}-Schiff base systems (28, 29)

We synthesized two additional Ru^{III}-Mn^{III}-Schiff base compounds **28** and **29** and partially characterized them by single crystal X-ray diffraction. Compound **28** is a pentanuclear molecule having the approximate molecular formula $[Mn^{III}(5\text{-}^{t}Bu\text{-saltmen})][Ru^{III}(salen)(CN)_2]_2[Mn^{III}(5\text{-}^{t}Bu\text{-saltmen})(H_2O)]_2(OH)\cdot 2CH_3CN\cdot 7H_2O$. Compound **29** is a hexanuclear molecule having the molecular formula $[Mn^{III}_2(5\text{-Me-saltmen})_2][Ru^{III}(salen)(CN)_2]_2[Mn^{III}(5\text{-Me-saltmen})(H_2O)]_2\cdot(ClO_4)_2\cdot CH_3CN\cdot H_2O$. The synthesis of **28** and **29** are described below. The single crystal X-ray diffraction parameters are summarized in table A.II, while figure A.II.1a and A.II.2a display an ORTEP type view of the structures. For both compounds the single crystals were of poor quality. We did not proceed with the magnetic characterization of these compounds due to the absence of sufficient crystallographic characterization and lack of time at the end of this work.

Synthesis:

(a) ***$[Mn^{III}(5\text{-}^{t}Bu\text{-saltmen})][Ru^{III}(salen)(CN)_2]_2[Mn^{III}(5\text{-}^{t}Bu\text{-saltmen})(H_2O)]_2(OH)\cdot 2CH_3CN\cdot 7H_2O$*** **(28)**: To a 3 mL acetonitrile solution of $[Mn^{III}_2(5\text{-}^{t}Bu\text{-saltmen})_2(H_2O)_2](ClO_4)_2\cdot 2H_2O$ (0.0125 g, 0.01 mmol) a 1 mL MeOH solution of *trans*-$(PPh_4)[Ru^{III}(salen)(CN)_2]\cdot MeOH\cdot H_2O$ (0.0081 g, 0.01 mmol) was added drop wise followed by the addition of 0.2 mL distilled water. The solution slowly evaporated at room temperature by covering the vial opening with parafilm and making a small hole in it. After two days, brown needle-shaped crystals were found in the bottom of the vial and separated by filtration. The yield of the product was *ca.* 40 % on the basis of the Mn^{III}-Schiff base precursor used. IR: $\bar{\nu}$ = 2112 (C≡N stretch), 1595, 1608 (C=N stretch) cm^{-1}.

(b) ***$[Mn^{III}_2(5\text{-Me-saltmen})_2][Ru^{III}(salen)(CN)_2]_2[Mn^{III}(5\text{-Me-saltmen})(H_2O)]_2\cdot(ClO_4)_2\cdot CH_3CN\cdot H_2O$*** **(29)**: $[Mn^{III}(5\text{-Me-saltmen})(H_2O)]_2(ClO_4)_2$ (0.0104 g, 0.01 mmol) was dissolved in 3 mL of acetonitrile followed by the addition of a 1 mL MeOH solution of *trans*-$(PPh_4)[Ru^{III}(salen)(CN)_2]\cdot MeOH\cdot H_2O$ (0.0081 g, 0.01 mmol) and 0.5 mL distilled water. The reaction mixture was allowed to evaporate slowly at ambient temperature. After few days, very dark colored crystals were found at the bottom of the vial. Yield of the product was 60 % on the basis of the Mn^{III}-Schiff base precursor. Most of the crystals were very small and of poor quality. IR: $\bar{\nu}$ = 2114 (C≡N stretch), 1599, 1610 (C=N stretch), 1075, 1098 (Cl-O stretch) cm^{-1}.

Crystallography:

Table.A.II. Crystal data and structure refinement of **28** and **29**

Compounds	**28**	**29**
Sum formula	$C_{124}H_{190}Mn_3N_{16}O_{21}Ru_2$	$C_{126}H_{141}Cl_2Mn_4N_{10}O_{10}Ru_2$
MW (g/mol)	2607.88	2612.23
Temp. (K)	120(2)	120(2)
Crystal System	Monoclinic	Triclinic
Space group	Cm	P-1
a (Å), b (Å), c (Å)	17.6320(13), 31.504(2), 13.0773(5)	11.626(6), 15.900(9), 37.69(2)
α (°), β (°), γ (°)	90, 75.400(5), 90	89.91(2), 89.96(2), 69.439(17)
Volume (Å^3)	7029.6(10)	6523(6)
Z	2	2
Density (g.cm^{-3})	1.206	1.409
$\mu_{MoK\alpha}$ (mm^{-1})	0.536	0.713
F_{000}	2646	2562
GooF	0.970	0.987
$^aR_1$ ($I > 2.00\sigma(I)$)	0.0874	0.1303
$^bwR_2$	0.2528	0.3373

$^aR_1 = \Sigma ||F_0| - |F_C|| / \Sigma|F_0|$, $^bwR_2 = [\Sigma w(F_0^2 - F_C^2)^2 / \Sigma w(F_0^2)^2]^{1/2}$, $w = 1/[\sigma^2 F_0^2 + (0.0313P)^2 + 1.5564P]$; where $P = (F_0^2 + 2F_C^2)/3$

Compound **28** is a Mn^{III}-Ru^{III} pentanuclear species (figure AII.1) composed of three $[Mn^{III}(5\text{-}^tBu\text{-saltmen})]^+$ groups and two *trans*-$[Ru^{III}(salen)(CN)_2]^-$ groups forming Mn^{III}-N-C-Ru^{III} bridges. The overall charge of this $Mn^{III}_3Ru^{III}_2$ moiety is +1, but we could not identify a suitable counter anion in the crystal structure (expected to be ClO_4^-). Moreover we found a number of cocrystallizing water molecules along with cocrystallizing acetonitrile molecules in the crystal structure, which fill the voids in the crystal packing. Therefore we suspect that one hydroxide anion is present for each $Mn^{III}_3Ru^{III}_2$ pentamer in order to form the neutral final compound **28**. In the middle of the pentamer complex one $[Mn^{III}(5\text{-}^tBu\text{-saltmen})]^+$ moiety is connected with two $[Ru^{III}(salen)(CN)_2]^-$ moieties via a cyanido bridge, and the remaining cyanido groups of the Ru^{III} ions are connected to another $[Mn^{III}(5\text{-}^tBu\text{-saltmen})(H_2O)]^+$ fragment where a water molecule satisfies the remaining axial positions of the terminal Mn^{III} ions. Each of these peripheral water molecules display hydrogen bonding short contacts (ca. $d_{O\cdots O}$ = 2.66-2.82 Å) with the phenoxido oxygen of a $[Ru^{III}(salen)(CN)_2]^-$ fragment of a neighboring pentanuclear unit (figure A.II.1c). Besides these supramolecular interactions, within the pentanuclear unit one of the ^{t}Bu groups of each terminal $[Mn^{III}(5\text{-}^tBu\text{-saltmen})(H_2O)]^+$ moiety exhibits Van der Waals attraction causing a bent U-shaped geometry to the Mn^{III}-Ru^{III}-Mn^{III}-Ru^{III}-Mn^{III} pentamer axis. [1] Thus in the *ab* plane the crystal packing of **28** exhibits an interesting fish-scale type motif as shown in figure A.II.1b. The magnetic analysis of **28** was not done because of the uncertainty about its molecular formula.

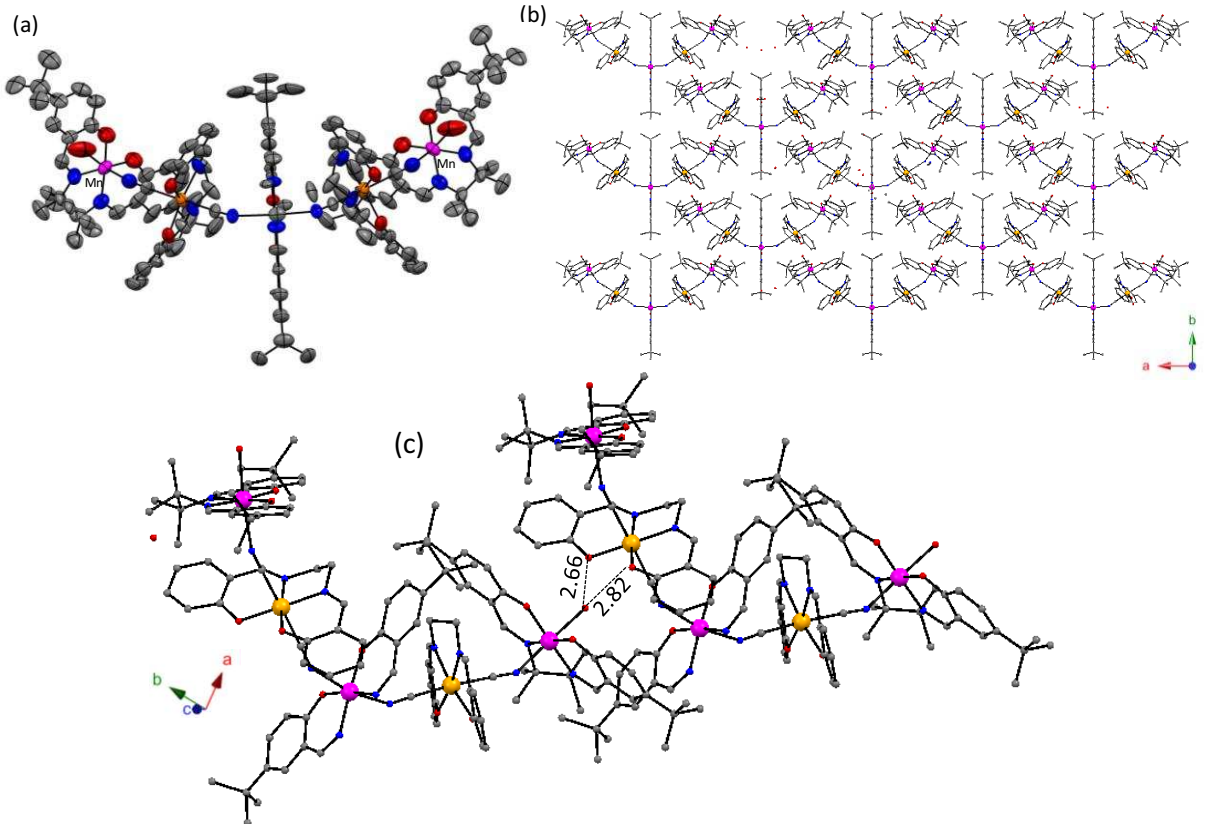

Figure A.II.1 (a) The ORTEP type view of the crystal structure of **28** with 50% thermal probability ellipsoids. The grey, blue, red, magenta and orange spheres represent the C, N, O, Mn, and Ru atoms. The H atoms and solvent molecules are omitted for clarity.(b) Crystallographic packing of the molecules in the *ab* plane. (c) The H-bonding interactions between the neighboring molecules of **28**.

The hexanuclear compound **29** is composed of $[Mn^{III}(5\text{-Me-saltmen})]^{+}$ and $[Ru^{III}(salen)(CN)_2]^{-}$ building blocks, arranged in a similar fashion to those found in **21** (in Chapter V) . Similar to **21**, a dinuclear phenoxido bridged $[Mn^{III}_2(5\text{-Me-saltmen})_2]^{2+}$ unit resides in the middle of the hexamer **29**, and is connected to two $[Ru^{III}(salen)(CN)_2]^{-}$ moieties via a cyanido bridge. The nitrogen end of the other cyanido group of each Ru^{III} ion is connected to another $[Mn^{III}(5\text{-Me-saltmen})]^{+}$ unit. The ligand field of these terminal Mn^{III} ions in **29** differs from that in **21** and exhibit octahedral coordination with a water molecule in the axial position. There are one water and one acetonitrile molecules in the void spaces of the crystal packing of **29** as well. The packing of these $Mn^{III}_4Ru^{III}_2$ hexanuclear moieties in the crystal structure of **29** is much different than that of **21**. In **29** two kinds of orientations are observed for the $Mn^{III}_4Ru^{III}_2$ hexamer (figure A.II.2b). H-bonding interactions are observed between the terminal oxygen of $[Mn^{III}(5\text{-Me-saltmen})(H_2O)]^{+}$ of $Mn^{III}_4Ru^{III}_2$ unit and the phenoxido oxygen of the $[Ru^{III}(salen)(CN)_2]^{-}$ fragments of a neighboring differently oriented $Mn^{III}_4Ru^{III}_2$ unit (figure A.II.2c). Since we did not have a good single crystal X-ray characterization of **29**, we did not progress towards the magnetic analysis.

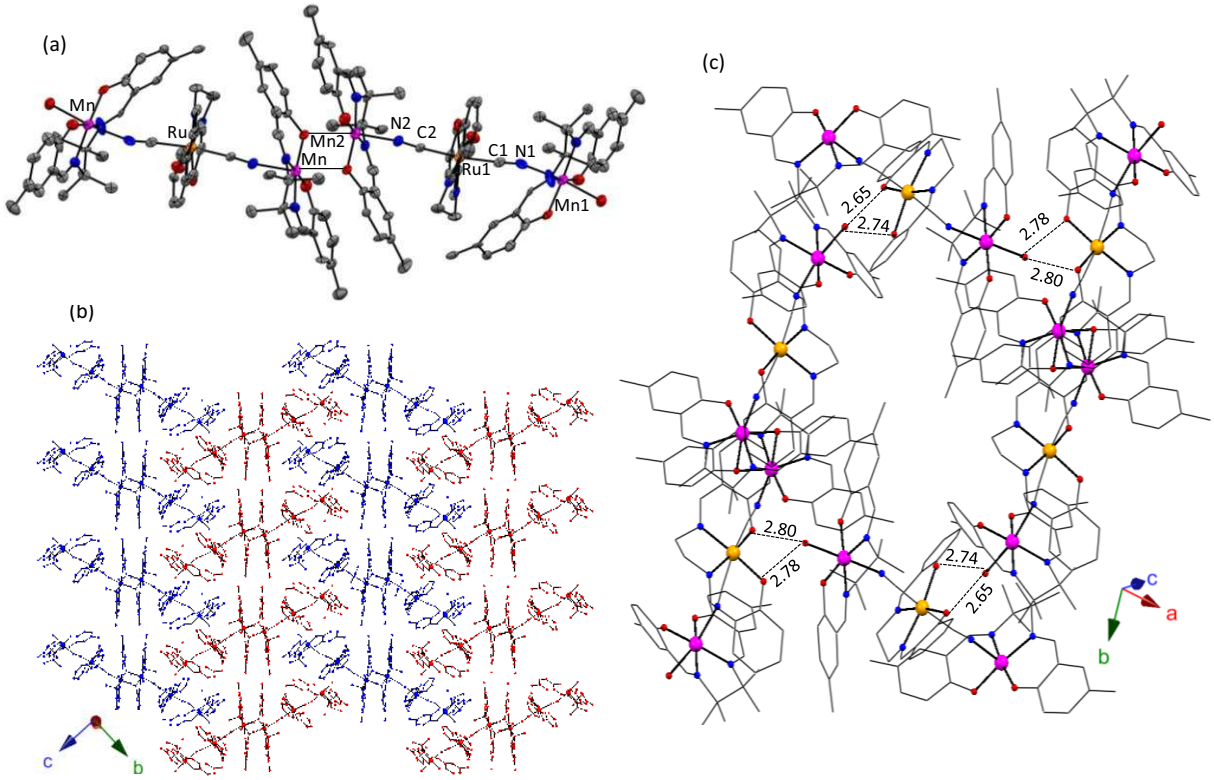

Figure A.II.2 (a) The ORTEP type view of the crystal structure of **29** with 50% thermal probability ellipsoids. The grey, blue, red, magenta and orange spheres represent the C, N, O, Mn, and Ru atoms. The H atoms, solvent molecules (water and acetonitrile) and counter anion (ClO_4^-) are omitted for clarity. (b) Crystallographic packing of the molecules in the *ac* plane. Two different kinds of orientations are observed for the $Mn^{III}_4Ru^{III}_2$ hexanuclear units that displayed in blue and red respectively. (c) The H-bonding interactions between the neighboring molecules of **29**. The $d_{O...O}$ distances are shown in Å.

Section III

$[Re^{IV}Cl_5(CN)]^{2-}$ based molecules (30-32)

During the synthesis of *trans*-$(Bu_4N)_2[Re^{IV}Cl_4(CN)_2]\cdot 2DMA$, we discovered a new building block $[Re^{IV}Cl_5(CN)]^{2-}$ which we tried to characterize crystallographically as the Bu_4N salt, but the crystal quality was too poor. Unfortunately, we were unable to re-synthesize the compound with a rational reaction scheme. The reaction between this Re^{IV} compound and $[Mn^{III}(5\text{-X-saltmen})]^+$ (X = F, Cl) molecular precursors yielded two new tetranuclear compounds $\{[Mn^{III}_2(5\text{-X-saltmen})_2][Re^{IV}Cl_5(CN)]_2\}^{2-}$ cocrystallized with two $[Mn^{III}(5\text{-X-saltmen})(MeOH)(H_2O)]^+$ moieties (**30** for X = F and **31** for X = Cl). Using the $Mn^{II}(ClO_4)_2$ salt, Hhmp ligand (Hhmp = Hydroxymethylpyridine) and this $[Re^{IV}Cl_5(CN)]^{2-}$ compound we also obtained a new hexanuclear compound $[Mn^{II}_2Mn^{III}_2(hmp)_6(Hhmp)_2][Re^{IV}Cl_5(CN)]\cdot 2CH_3CN$ (**32**) in a basic reaction medium. The

synthesis of **30-32** are described in the following section and single crystal X-ray diffraction parameters are summarized in table A.III. Figure A.III.1 and A.III.2a display their ORTEP type view of the crystal structure.

Synthesis:

(a) ***{[Mn^{III}_2(5-F-saltmen)$_2$][$Re^{IV}Cl_5$(CN)]$_2$}[Mn^{III}(5-F-saltmen)(MeOH)(H_2O)]$_2$·4CH_3OH*** **(30)**: To a 3 mL MeOH solution of [Mn^{III}(5-F-saltmen)(H_2O)$_2$](ClO_4) (0.0110 g, 0.02 mmol) a 1 mL MeOH solution of (Bu_4N)$_2$[$Re^{IV}Cl_5$(CN)] (0.010 g, ~0.01 mmol) was added dropwise. The solution slowly evaporated at room temperature. In one day, brown crystals were found in the bottom of the vial and separated by filtration. The yield of the product was *ca.* 60 % on the basis of the Mn^{III}-Schiff base precursor.

(b) ***{[Mn^{III}_2(5-Cl-saltmen)$_2$][$Re^{IV}Cl_5$(CN)]$_2$}[Mn^{III}(5-Cl-saltmen)(MeOH)(H_2O)]$_2$·4CH_3OH*** **(31)**: To a 5 mL methanol solution of [Mn^{III}_2(5-Cl-saltmen)$_2$(H_2O)$_2$](ClO_4)$_2$ (0.0113 g, 0.01 mmol) a 1 mL MeOH solution of (Bu_4N)$_2$[$Re^{IV}Cl_5$(CN)] (0.010 g, ~0.01 mmol) was added dropwise. The reaction mixture slowly evaporated at room temperature. In one day, brown crystals were found in the bottom of the vial and separated by filtration. The yield of the product was *ca.* 60 % on the basis of the Mn^{III}-Schiff base precursor.

(c) ***[$Mn^{II}_2Mn^{III}_2$(hmp)$_6$(Hhmp)$_2$][$Re^{IV}Cl_5$(CN)]·2CH_3CN*** **(32)**: To a 2 mL acetonitrile solution of $Mn^{II}(ClO_4)_2·6H_2O$ (0.0145 g, 0.04 mmol), Hhmp (0.0088 g, 0.08 mmol) was added followed by the addition of one drop of a 40 % aqueous solution of tetrabutylammonium hydroxide (Bu_4NOH). The reaction mixture was allowed to stir for one hour. The final brown solution was poured into a long thin glass tube (0.5 cm diameter) and layered with a 2 mL acetonitrile solution of (Bu_4N)$_2$[$Re^{IV}Cl_5$(CN)] (0.010 g, ~0.01 mmol). The tube was closed with parafilm. After two weeks a few red crystals were found at the wall of the tube. The crystals were collected by breaking the glass tube. IR: $\bar{\nu}$ = 2143 (C≡N stretch).

Crystallography:

Compounds **30** and **31** possess a similar type of crystal structure where a phenoxido bridged dinuclear [Mn^{III}_2(5-X-saltmen)$_2$]$^{2+}$ (X = F, Cl) unit is connected to two [$Re^{IV}Cl_5$(CN)]$^{2-}$ units via the cyanido bridge. Thus a tetranuclear anionic Re^{IV}-Mn^{III}-Mn^{III}-Re^{IV} complex is formed with the formula {[Mn^{III}_2(5-X-saltmen)$_2$][$Re^{IV}Cl_5$(CN)]$_2$}$^{2-}$. Interestingly the charge of this tetranuclear species is neutralized by two [Mn^{III}(5-X-saltmen)(MeOH)(H_2O)]$^+$ moieties which are themselves in a hydrogen bonding close contact between the axial water molecule of one unit and the phenoxido oxygen of the other. The cocrystallizing methanol molecules not only fill up the void spaces in the crystal packing

but also participate in the H-bonding supramolecular interactions with the $[Mn^{III}$(5-X-saltmen)(MeOH)$(H_2O)]^+$ moieties.

Table.A.III. Crystal data and structure refinement of **30-32**

Compounds	**30**	**31**	**32**
Sum formula	$C_{88}H_{108}Cl_{10}F_8Mn_4N_{10}O_{16}Re_2$	$C_{88}H_{108}Cl_{18}Mn_4N_{10}O_{16}Re_2$	$C_{54}H_{57}Cl_{10}Mn_4N_{12}O_8Re_2$
MW (g/mol)	2644.4	2844.3	1948.80
Temp. (K)	150(2)	150(2)	150(2)
Crystal System	Triclinic	Triclinic	Triclinic
Space group	P-1	P-1	P 1
a (Å)	12.3426(6)	12.575(3)	12.064(2)
b (Å)	12.6948(6)	13.258(3)	13.171(3)
c (Å)	17.7564(6)	18.766(4)	17.293(4)
α (°)	83.393(3)	87.56(3)	108.67(3)
β (°)	79.302(3)	70.76(3)	101.77(3)
γ (°)	68.198(2)	99.08(3)	98.95(3)
Volume (Å^3)	2535.1(7)	2685.2(14)	2475.0(9)
Z	1	1	1
Density(g.cm^{-3})	1.732	1.728	1.308
$\mu_{MoK\alpha}$ (mm^{-1})	3.205	3.213	3.241
F000	1310	1386	949
GooF	1.064	1.042	1.040
[a]R_1 (I > 2.00σ(I))	0.0545	0.0783	0.0830
[b]wR_2	0.1938	0.2380	0.2698

[a]$R_1 = \Sigma ||F_0| - |F_C|| / \Sigma|F_0|$, [b]$wR_2 = [\Sigma w(F_0^2 - F_C^2)^2 / \Sigma w(F_0^2)^2]^{1/2}$, $w = 1/[\sigma^2 F_0^2 + (0.0313P)^2 + 1.5564P]$; where $P = (F_0^2 + 2F_C^2)/3$

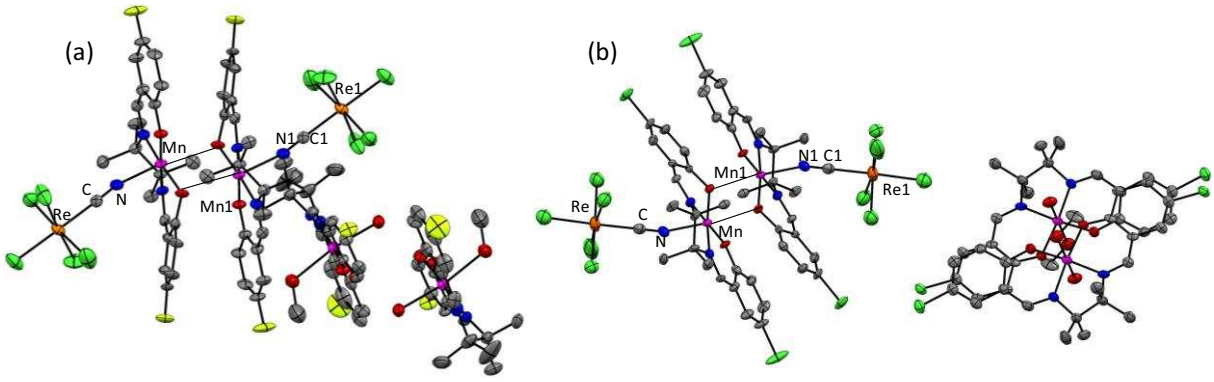

Figure A.III.1. ORTEP type view of the crystal structures of **30** (a) and **31** (b) with 50% thermal probability ellipsoids. The grey, blue, red, green, magenta and orange ellipsoids represent the C, N, O, Cl, Mn, and Re atoms. The light green ellipsoids in (a) represent the F atoms. The H atoms and the solvent molecules (MeOH) are omitted for clarity.

Compound **32** is a hexanuclear Re^{IV}-Mn^{II}-Mn^{III}_2-Mn^{II}-Re^{IV} complex (figure A.III.2) having the molecular formula $[Mn^{II}_2Mn^{III}_2(hmp)_6(Hhmp)_2][Re^{IV}Cl_5(CN)]$ which cocrystallizes with two acetonitrile molecules. All of the metal ions of this compound are in an octahedral ligand environment. The hmp^- ligand has a N donor atom on the aromatic ring and an alcoxido oxygen. This alcoxido oxygen atom from the ligand bridges two Mn^{III} ions and also links the Mn^{III}/Mn^{II} ions. The core of the hexanuclear unit contains two Mn^{III} ions whose coordination sites are occupied by the N atom in axial positions and equatorial sites by μ- type bridging O atoms of the six hmp^- ligands. Each of these two Mn^{III} ions is connected to one Mn^{II} ion via the alcoxido linkages such that the hmp^- ligands occupy

three coordination sites of each Mn^{II} ion. Two of the remaining coordination sites of the Mn^{II} ion are satisfied with a bidentate Hhmp ligand via Mn^{II}-N and Mn^{II}-OH bonds. Finally, each of the Mn^{II} ions are coordinated to the cyanido group of a $[Re^{IV}Cl_5(CN)]^{2-}$ unit. Acetonitrile molecules fill the void spaces in the crystal packing. The hexanuclear moieties are quite well separated in the crystal packing as illustrated in the *bc* plane by figure A.III.2b.

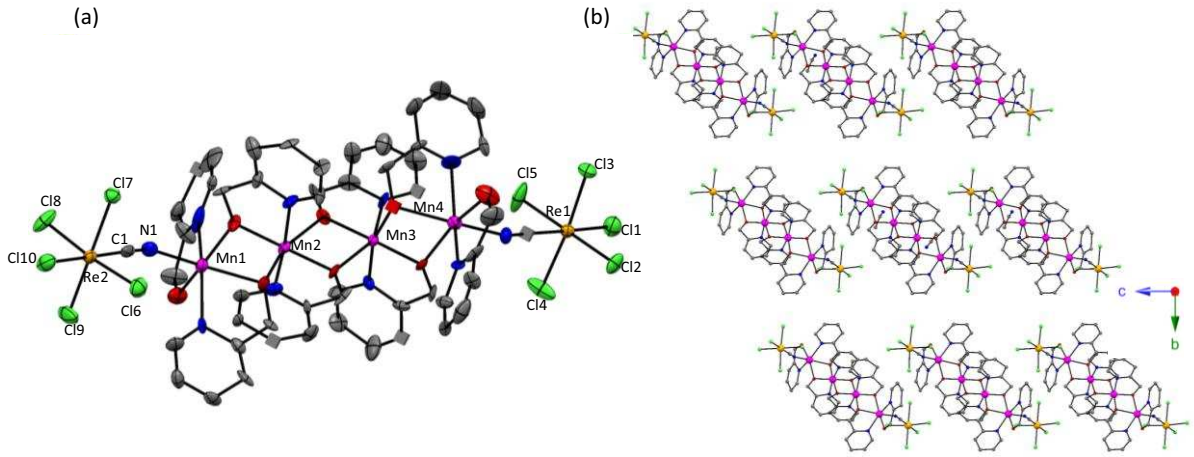

Figure A.III.2. (a) ORTEP type view of the crystal structure of **32** with 50% thermal probability ellipsoids. The grey, blue, red, green, magenta and orange ellipsoids represent the C, N, O, Cl, Mn, and Re atoms. The H atoms and solvent molecules (acetonitrile) are omitted for clarity. (b) Crystallographic packing of **32** in the *bc* plane.

Section IV

A giant cyanido based Re^{V}-Ni^{II} complex (33)

We have observed that the synthesis of the *trans*-$(Bu_4N)_2[Re^{IV}Cl_4(CN)_2]\cdot 2DMA$ molecular precursor gives one minor byproduct $(Bu_4N)_2[Re^{V}(CN)_4(OH)O]\cdot 2DMA$ (figure A.IV.1a). This compound reacts with $[Ni^{II}(cyclen)(H_2O)_2](ClO_4)_2$ (cyclen = 1,4,7,10-tetraazacyclododecane) resulting the large cyanido bridged Re^{V}-Ni^{II} molecular complex **33**. The isolation of the Re^{V} compound and synthesis of **33** are given as following and table A.IV contains their single crystal X-ray diffraction parameters.

Synthesis

(a) ***$(Bu_4N)_2[Re^{V}(CN)_4(OH)O]\cdot 2DMA$:*** After removing all of the crystals of *trans*-$(Bu_4N)_2[Re^{IV}Cl_4(CN)_2]\cdot 2DMA$ from the DMA-Et_2O solvent mixture (described in chapter II section II.4.5), diethyl ether vapor was allowed to diffuse for long time (more than a week) in the rest of the solution which resulted into the formation of the deep blue crystals of

$(Bu_4N)_2[Re^V(CN)_4(OH)O]\cdot 2DMA$. IR: $\bar{\nu}$ = 2122, 2130 (C≡N stretch) cm^{-1}.

(b) ***Re^V-Ni^{II} molecular complex***: $[Ni^{II}(cyclen)(H_2O)_2](ClO_4)_2$ was prepared by adding one equivalent of $Ni^{II}(ClO_4)_2\cdot 6H_2O$ to a stirring EtOH solution of the macrocyclic ligand cyclen (cyclen = 1,4,7,10-tetraazacyclododecane). The reaction mixture was allowed to stir for 2 hours at 60 °C and then cooled to room temperature. The violet product was separated by filtration. The yield is more than 90 % based on the Ni^{II} stating material.

A 2 mL aqueous solution of $[Ni^{II}(cyclen)(H_2O)_2](ClO_4)_2$ (0.0047 g, 0.01 mmol) was poured into a thin glass tube which was layered with 2 mL pure acetonitrile. Over this pure solvent layer a 2 mL acetonitrile solution of $(Bu_4N)_2[Re^V(CN)_4(OH)O]\cdot 2DMA$ (0.0098 g, 0.01 mmol) was carefully poured and the tube was sealed with parafilm. After one week very small brown crystals of **33** were found on the wall of the tube. The yield is less than 30% based on the Ni^{II} precursor. IR: $\bar{\nu}$ = 2104, 2127 (C≡N stretch) cm^{-1}.

Crystallography and Magnetic properties:

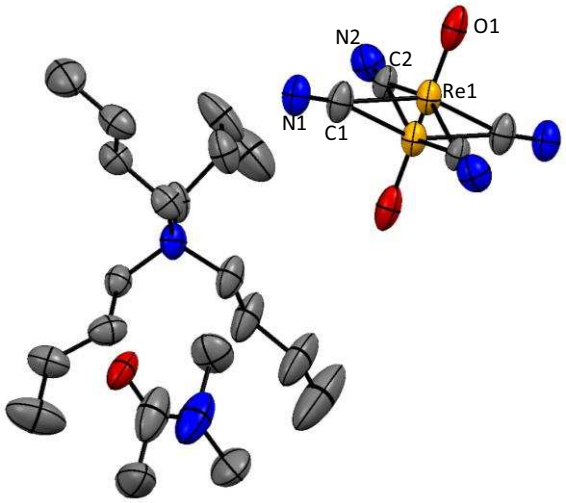

Figure A.IV.1. ORTEP type view of the crystal structure of $(Bu_4N)_2[Re^V(CN)_4(OH)O]\cdot 2DMA$ with 50 % thermal probability. The grey, blue, red and orange ellipsoids represent the C, N, O, and Re atoms. The Re^V ion is disordered over two positions. The H atoms are omitted for clarity.

In the $(Bu_4N)_2[Re^V(CN)_4(OH)O]\cdot 2DMA$ compound the Re^V ion is in an octahedral ligand environment with the equatorial plane containing four cyanido groups linked by Re^V-C bonds (figure A.IV.1a). One of the two axial positions is coordinated with one O^{2-} ion, while the other axial position is coordinated by a hydroxido group. The charge of this $[Re^V(CN)_4(OH)O]^{2-}$ unit is neutralized by two Bu_4N^+ groups. The Re^V ions in the $[Re^V(CN)_4(OH)O]^{2-}$ moiety are disordered over two positions with a 50 % occupancy and the O^{2-} and OH^- groups are also statistically disordered in the same position. Therefore we could not identify the H atoms belonging to the OH^- group. Thus we cannot be sure of

the oxidation state of the metal ions from the crystal structure of $[Re^{V}(CN)_4(OH)O]^{2-}$. In order to determine the oxidation state of the Rhenium site, the temperature dependence of the magnetic susceptibility was measured for $(Bu_4N)_2[Re^{V}(CN)_4(OH)O]\cdot 2DMA$ between 270-1.8 K in presence of a 1000 Oe applied *dc* field. The magnetic data confirmed the compound to be diamagnetic and thus the low spin Re^{V} ($5d^2$ electrons, $S = 0$) ground state of $(Bu_4N)_2[Re^{V}(CN)_4(OH)O]\cdot 2DMA$.

Table.A. IV. Crystal data and structure refinement $(Bu_4N)_2[Re^{V}(CN)_4(OH)O]\cdot 2DMA$ and **33**

Compounds	**$(Bu_4N)_2[Re^{V}(CN)_4(OH)O]\cdot 2DMA$**	**33**
Sum formula	$C_{44}H_{91}N_8O_4Re$	$C_{160}H_{340}N_{104}Ni_{12}O_{74}Re_{12}$
MW (g/mol)	982.46	7836.15
Temp. (T)	120(2)	120(2)
Crystal System	Triclinic	Rhombohedral
Space group	P-1	R-3
a (Å),b (Å), c (Å)	10.473(5), 11.766(5), 12.375(5)	35.6674(11), 35.6674(11), 20.3126(14)
α (°), β (°), γ (°)	65.442(5), 81.415(5), 74.892(5)	90, 90, 120
Volume ($Å^3$)	1337.6(10)	22379(2)
Z	1	3
Density ($g.cm^{-3}$)	1.214	1.727
$\mu_{MoK\alpha}$ (mm^{-1})	2.314	5.663
F_{000}	517	11328
GooF	1.073	1.111
[a]R_1 ($I > 2.00\sigma(I)$)	0.0548	0.0681
[b]wR_2	0.1518	0.2279

[a]$R_1 = \Sigma ||F_0| - |F_C|| / \Sigma |F_0|$, [b]$wR_2 = [\Sigma w(F_0^2 - F_C^2)^2 / \Sigma w(F_0^2)^2]^{1/2}$, $w = 1/[\sigma^2 F_0^2 + (0.0313P)^2 + 1.5564P]$; where $P = (F_0^2 + 2F_C^2)/3$

In the Re^{V}-Ni^{II} molecular complex **33** is an $\{[Ni^{II}_2(cyclen)_2][Re^{V}_2(CN)_8O_3]\}_6$ nano-object having a spherical type geometry where a number of water molecules and acetonitrile molecules fill the void spaces inside and outside of the cavity of the sphere. The compound crystallizes in a highly symmetrical R-3 space group. Six asymmetric $\{[Ni^{II}_2(cyclen)_2][Re^{V}_2(CN)_8O_3]\}$ units (figure A.IV.2) form the spherical shaped molecule $\{[Ni^{II}_2(cyclen)_2][Re^{V}_2(CN)_8O_3]\}_6$. All the metal ions are hexacoordinated and the cyclen acts as a tetradentate nitrogen donor capping ligand occupying four coordination sites of each Ni^{II} ion. The other two *cis* oriented coordination sites of the Ni^{II} ion are connected to two N atoms of the cyanido groups originating from two $[Re^{V}_2(CN)_8O_3]^{4-}$ moieties (figure IV.2). Thus each $[Ni^{II}(cyclen)]^{2+}$ fragment is cyanido bridged to two $[Re^{V}_2(CN)_8O_3]^{4-}$ moieties. The $[Re^{V}_2(CN)_8O_3]^{4-}$ moiety is a μ-oxido bridged $[Re^{V}]_2$ (Re1-O1-Re2 in figure A.IV.2a) moiety where each Re^{V} center possesses a $Re^{V}(CN)_4$ equatorial plane. The Re^{V} ions are connected to the carbon atoms of the cyanido groups. These two $Re^{V}(CN)_4$ planes in a $[Re^{V}_2(CN)_8O_3]^{4-}$ fragment are parallel to each other and possess mutually staggered conformation. One O^{2-} ion satisfies the remaining coordination position the Re^{V} ions in the $[Re^{V}_2(CN)_8O_3]^{4-}$ fragment. All four of the cyanido groups of one Re^{V} ion (Re1 in figure A.IV.2) in the $[Re^{V}_2(CN)_8O_3]^{4-}$ fragment are connected to four Ni^{II} ions and this Re^{V} ion reside on the inside of the spherical molecule (figure A.IV.2c). On the contrary, the other Re^{V} ion (Re2 in figure A.IV.2) of the $[Re^{V}_2(CN)_8O_3]^{4-}$ fragments exhibits no cyanido bridging and are positioned on the outside of the sphere (figure A.IV.2c). Thus in each molecule of **33** one $[Re^{V}_2(CN)_8O_3]^{4-}$ moiety is connected to four $[Ni^{II}(cyclen)]^{2+}$ fragments.

Some disorders on the terminal cyanido groups of the $[Re^{V}_{2}(CN)_{8}O_{3}]^{4-}$ unit is observed i.e., on the cyanido groups coordinated to the Re2 ions. The H atoms on the cocrystallized water molecules were not introduced while solving the crystal structure; but they have been calculated in the molecular weight of **33** given in table A.IV. In figure A.IV.3 the ORTEP type view of the crystal structure of **33** is displayed followed by the molecular view of this species in different crystallographic directions. The $\{[Ni^{II}_{2}(cyclen)_{2}][Re^{V}_{2}(CN)_{8}O_{3}]\}_{6}$ moieties are well separated in the crystal packing by the outer-sphere water molecules and this packing in *ab* plane is displayed in figure A.IV.3b.

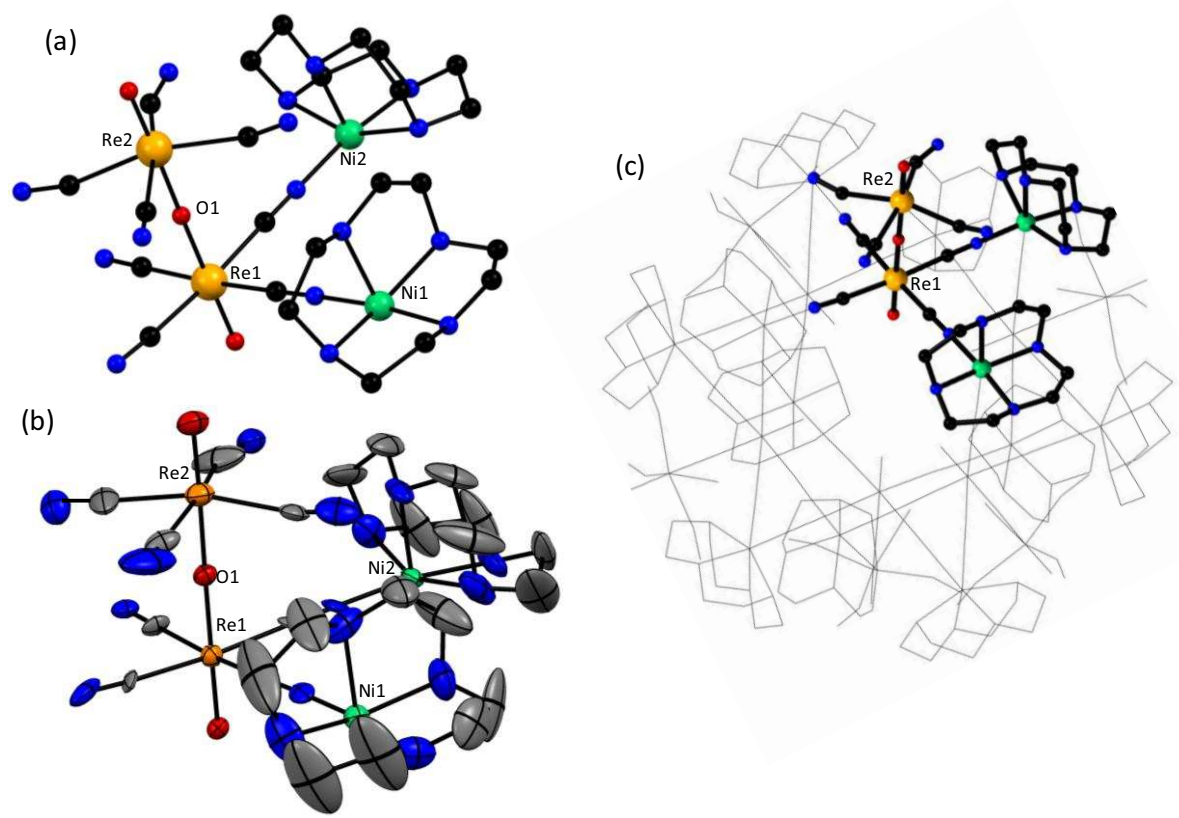

Figure A.IV.2. Asymmetric unit $\{[Ni^{II}_{2}(cyclen)_{2}][Re^{V}_{2}(CN)_{8}O_{3}]\}$ of **33** in ball and stick (a) and ORTEP type (b) view**.** The Re1 is cyanido bridged with the Ni^{II} ions and the cyanido groups of Re2 remains non-bridged. Six of such units make the spherical molecule $\{[Ni^{II}_{2}(cyclen)_{2}][Re^{V}_{2}(CN)_{8}O_{3}]\}_{6}$ (c) The spherical molecule $\{[Ni^{II}_{2}(cyclen)_{2}][Re^{V}_{2}(CN)_{8}O_{3}]\}_{6}$ highlighting the asymmetric units. The Re1 and Re2 ions respectively reside in the inner and outer side of the spherical moiety.

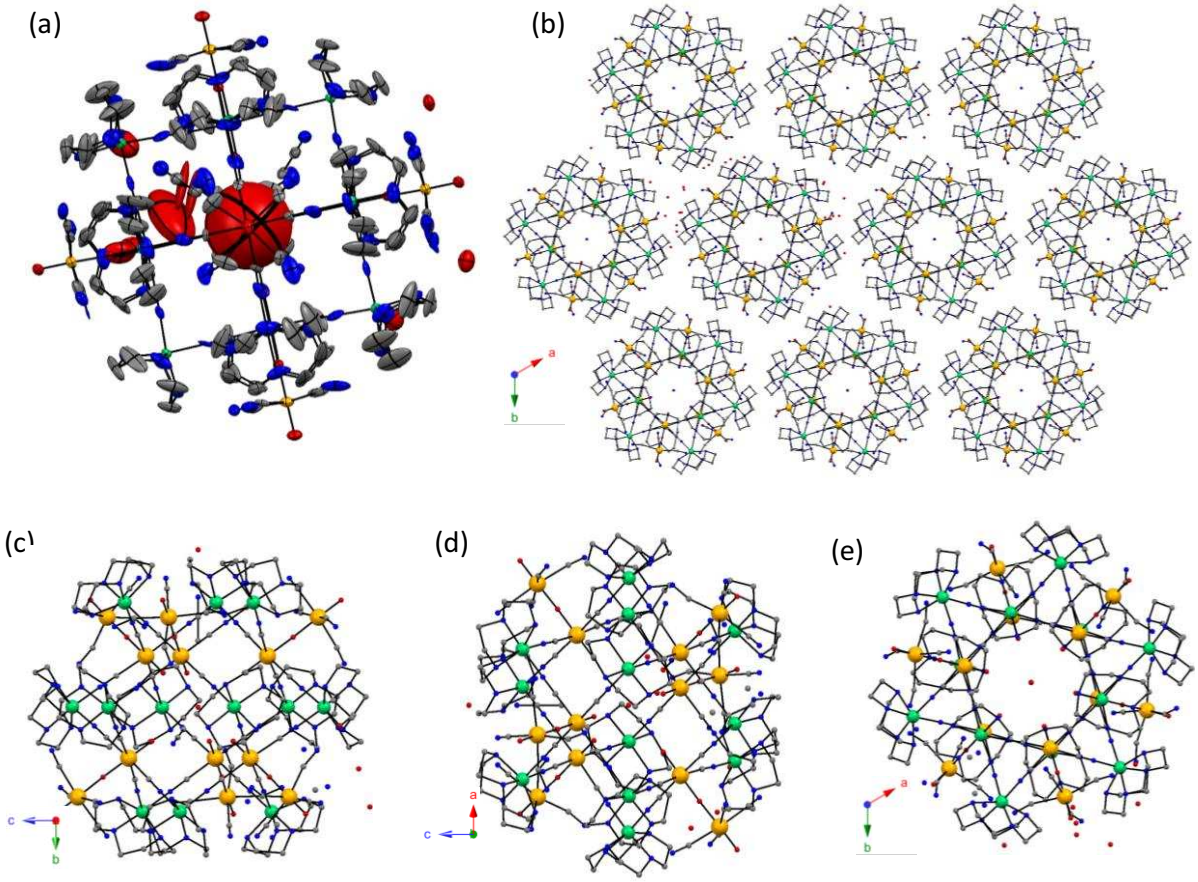

Figure A.IV.3. (a) ORTEP figures of **33** with 50% thermal probability ellipsoids. The grey, blue, red, green and orange ellipsoids represent the C, N, O, Ni and Re atoms. The H atoms are omitted for clarity. (b) Crystallographic packing of **33** in *ab* plane. (c), (d) and (e) The molecular view of **33** in the crystallographic direction *a* (c), *b* (d) and *c* (e).

References

[1] (a) U. Berg, T. Liljefors, C. Roussel, J. Sandstro, *Acc. Chem. Res*., **1985**, 18, 80. (b) N. L. Allinger, M. Frierson, F. A. Van-Catledge, *J . Am. Chem. Soc*., **1982**, 104, 4592.

SUPPORTING INFORMATION

I. PHYSICAL MEASUREMENTS:

Elemental Analysis

Elemental analyses (C, H, and N) were carried out by a FlashEATM 1112 automatic elemental analyzer at *Institut de Chimie de la Matière Condensée de Bordeaux* (ICMCB) to the determination of the mass fractions of carbon, hydrogen, nitrogen, and sulphur of a sample.

Fourier Transform Infra-red (FT-IR) analysis

Infrared spectra of the compounds **1-15**, **20**, **22** and **30-32** were recorded in the range 400-4000 cm^{-1} on a Nicolet750 Magna-IR spectrometer using KBr pellets. For the rest of the compounds the Infrared spectra were recorded in the same range on a Thermal Scientific Nicolet 6700 FT-IR spectrometer equipped with a Smart iTR diamond window.

Single Crystal X-ray Analysis

For single crystal X-ray diffraction data we have used either with a Nonius diffractometer Kappa CCD (at *Institut de Chimie de la Matière Condensée de Bordeaux* (ICMCB)) or with a Bruker APEX II diffractometer (at *Center de Recherche Paul Pascal* (CRPP)). Both apparatus are equipped with graphite monochromator centered on the path of MoKα (λ = 0.71073 Å). The single crystal was coated with Paratone N-oil and mounted on a fiber loop followed by data collection. The program Denzo-MNCH (for diffractometer Kappa CCD) and the program SAINT (for Bruker APEX II diffractometer) were used to integrate the data after an absorption correction with SADABS [1]. The structure was solved by direct methods and refined by least squares on F^2 in SHELX97 [2]. All non-hydrogen atoms were refined anisotropically by full-matrix least-squares (SHELXL-97). All hydrogen atoms were placed using a riding model. Their positions were constrained relative to their parent atom using the appropriate HFIX command in SHELXL-97.

[1] Sheldrick, G. M. SADABS, Version 2.03; Bruker Analytical X-Ray Systems, Madison, WI, **2000**.

[2] G. M. Sheldrick, SHELX-97. *Programs for Crystal Structure Solution and Refinement*; University of Göttingen: Göttingen, Germany, **1997**.

Magnetic Measurements

Magnetic susceptibility measurements were obtained using a Quantum Design MPMS-XL SQUID magnetometer and a PPMS susceptometer-9. The measurements were performed on the

polycrystalline samples introduced in a polyethylene bag (3 × 0.5 × 0.02 cm) and sealed. The available temperature range from 300 K to 1.8 K and the field can vary from -7 to 7 T (MPMS-XL) and -9 to 9 T (PPMS-9). In each measurement an *M vs H* measurement was performed at 100 K to confirm the absence of ferromagnetic impurities. The *ac* susceptibility experiments were performed at various frequencies ranging from 1 to 1500 Hz (in MPMS-XL) and 1 to 10000 Hz with an *ac* field amplitude of 3 Oe in zero *dc* field. Experimental data were corrected for the sample holder and for the diamagnetic contribution of the sample.

Heat Capacity Measurements

Heat capacity was measured on polycrystalline samples of **14-16** (1.0 mg) between 150 and 1.9 K by a thermal relaxation technique with a Quantum Design Physical Property Measurement System (PPMS-9) in zero-dc field. In each measurement, the blank heat capacity including a small amount of Apiezon N grease (1.5 mg) used for adhesion was measured prior to the sample mounting. The heat capacities of the compound were determined by subtracting the blank data from the measured total heat capacity.

II. LIST OF ABBREVIATIONS

SMM	Single-Molecule Magnet
ZFS	Zero Field Splitting
S_T	Spin ground state
T_B	Blocking temperature
QTM	Quantum Tunnelling of Magnetization
SCM	Single-Chain Magnets
HS	High Spin
LS	Low Spin
AF	Antiferromagnetic
T_N	Neel Temperature
T_C	Curie temperature
H_C	Critical field
dc	direct curent
ac	alternating curent
SQUID	Superconducting Quantum Interference Device
PPMS	Physical Properties Messurement System

ORTEP	Oak Ridge Thermal Ellipsoid
hmpH	2-hydroxymethylpyridine
SB	Schiff base
H_2salen	*N*,*N*'-bis(salicylidene)ethylenediamine
5-MeO-H_2salen	*N,N*'-bis(5-methoxy-salicylidene)ethylenediamine
H_2salpn	N,N'-bis(salicylidene)1,3-propylenediamine
5-MeO-H_2salpn	*N,N*'-bis(5-methoxy-salicylidene)-1,3-propylenediamine
5-Me-H_2salpn	*N,N*'-bis(5-methyl-salicylidene)-1,3-propylenediamine
5-Cl-H_2salmen	rac-*N,N'*-bis(5-chloro-salicylidene)-1-methylenediamine
H_2saltmen	*N,N*'-bis(salicylidene)-1,1,2,2-tetramethylethylenediamine
3-MeO-H_2saltmen	*N,N'*-bis(3-methoxy-salicylidene)-1,1,2,2-tetramethylethylenediamine
4-MeO-H_2saltmen	*N,N'*-bis(4-methoxy-salicylidene)-1,1,2,2-tetramethylethylenediamine
4-HO-H_2saltmen	*N,N'*-bis(4-hydroxy-salicylidene)-1,1,2,2-tetramethylethylenediamine
5-MeO-H_2saltmen	*N,N'*-bis(5-methoxy-salicylidene)-1,1,2,2-tetramethylethylenediamine
5-Me-H_2saltmen	*N,N'*-bis(5-methyl-salicylidene)-1,1,2,2-tetramethylethylenediamine
5-F-H_2saltmen	*N,N'*-bis(5-fluoro-salicylidene)-1,1,2,2-tetramethylethylenediamine
5-Cl-H_2saltmen	*N,N'*-bis(5-chloro-salicylidene)-1,1,2,2-tetramethylethylenediamine
5-Br-H_2saltmen	*N,N'*-bis(5-bromo-salicylidene)-1,1,2,2-tetramethylethylenediamine
5-^{t}Bu-H_2saltmen	*N,N'*-bis(5-tetra-^{n}butylammonium -salicylidene)-1,1,2,2-tetramethylethylenediamine
H_2salphen	N,N'-bis(salicylidene)-ortho-phenylene
LN_5	2,13-dimethyl-3,6,9,-12,18-pentaazabicicylo[12.3.1]octadeca-1(18),2,12,14,16-pentaene)
LN_3O_2	3,12,18-triaaza-6,9-dioxabicyclo[12.3.1]octadeca-1(18),14,16-triene)
Bu_4N^+	tetra-n-butylammonium
Ph_4P^+	tetraphenylphosphonium
DMF	dimethylformamide
DMA	dimethyleacetamide
EtOH	ethanol
Et_2O	diethylether
MeOH	methanol
MeCH	acetonitrile
$MeNO_2$	nitromethane

III. PHYSICAL CONSTANTS

	Symbol	Value	Units	
			SI	CGS
Avogadro constant	N_A	6.02217	10^{23} mol^{-1}	
Boltzmann constant	k_B	1.38062	10^{-23} J·K^{-1}	10^{-21} erg·G^{-1}
Bohr magneton	μ_B	9.27410	10^{-24} J·T^{-1}	10^{-16} erg·K^{-1}
vacuum permeability	μ_0		$4\pi\ 10^{-24}$ T·m·A^{-1}	10^{7} erg·mol^{-1}·K^{-1}

Thèse préparée au:
Centre de Recherche Paul Pascal UPR 8641 / CNRS - Université Bordeaux 1
115 av. Albert Schweitzer, 33600 PESSAC (France)
http://www.crpp-bordeaux.cnrs.fr/

Synthèse et caractérisation de matériaux moléculaires magnétiques incorporant des ions métalliques 3*d* et 4*d*/5*d* connectés par des ponts cyanures

Dans cette thèse, nous avons synthétisé de nouveaux matériaux moléculaires hétérométalliques pontés par des groupements cyanures en utilisant la chimie de coordination donneur-accepteur. Les précurseurs moléculaires basés sur un ion métallique 3*d* ($Mn^{II/III}$, Fe^{II}, Ni^{II}, Cu^{II}) agissent en tant qu'unités acceptrices, alors que les précurseurs 4*d* (Ru^{III}) et 5*d* (Re^{IV}) de type trans-cyanido ont été utilisés comme groupements donneurs.
Le chapitre I présente une approche théorique avec quelques exemples des matériaux magnétiques de basse dimensionnalité: molecule et chaîne aimant qui illustrent le rôle du ligand cyanido pour concevoir les matériaux magnétiques. En outre, nous avons sélectionné des précurseurs cyanido à base de métaux 4*d*/5*d* pour leur anisotropie magnétique plus élevée par rapport aux ions de métaux 3*d*. Le choix des précurseurs moléculaires, leur synthèse et leur caractérisation ont été largement décrits dans le chapitre II. Au cours de ce travail de recherche, nous avons obtenu de nombreux systèmes moléculaires hétérométalliques mais également des systèmes unidimensionnels. Les chapitres III, IV et V décrivent la synthèse, la structure cristallographique et la caractérisation magnétique de tous les complexes synthétisés. L'empilement cristallin compact des molécules conduit à un état fondamental antiferromagnétique pour la plupart des complexes ce qui perturbe souvent les phénomènes de relaxation magnétique. Nous avons donc établi les diagrammes de phases magnétiques pour la plupart de ces systèmes. De plus, certaines des chaînes Re^{IV}/Mn^{III} et une chaîne Re^{IV}/Fe^{II} présentent des comportements magnétiques de type "chaîne aimant" et donc une bistabilité magnétique.
Mot clés: *Ions métalliques 3d, 4d et 5d; Complexe de cyanure; Prospérités magnétique; Chaîne aimant; Relaxation de l'aimantation; diagramme de phase magnétique*

The synthesis and characterization of low dimensional molecule-based magnetic materials having a cyanido bridge between 3*d* and 4*d*/5*d* transition metal ions

In this thesis, we have synthesised new cyanido bridged heterometallic molecule-based magnetic materials with the tool of simple donor-acceptor coordination chemistry. The 3*d* metal ion ($Mn^{II/III}$, Fe^{II}, Ni^{II}, Cu^{II}) based molecular precursors acted as acceptor building blocks, whereas the 4*d* (Ru^{III}) and 5*d* (Re^{IV}) trans-cyanido type molecular precursors were used as donor moieties.
Chapter I contains a theoretical approach with examples of low dimensional magnetic materials: Single Molecule and Single Chain Magnets that illustrate the role of the cyanido ligand to design such magnetic materials. Furthermore, we emphasized the 4*d*/5*d* metal based cyanido precursors for their higher magnetic anisotropy over the 3*d* metal ions. The choice of molecular precursors, their synthesis and characterization were extensively described in chapter II. In this research work, we have obtained many heterometallic molecular complexes and also one dimensional systems. Chapter III, IV and V contain the synthesis, X-ray crystallographic and magnetic characterization of all the newly synthesized complexes. The close crystal packing of the molecules lead to an antiferromagnetic ground state for most of the complexes and this often perturbed the magnetic relaxation phenomena. As expected, we have found metamagnetic phase diagrams for most of these systems. Some of the Re^{IV}/Mn^{III} and a Re^{IV}/Fe^{II} one dimensional compounds exhibited Single-Chain magnet like properties and thus magnetic bistability.
Keywords: *3d, 4d and 5d metal ions; Cyanido complexes; Magnetic properties; Single Chain Magnet; Magnetic phase diagram*